Investigation of Multiphase Coupled-Inductor Buck Converters in Point-of-Load Applications

Yan Dong

Dissertation submitted to the Faculty of the
Virginia Polytechnic Institute and State University
in partial fulfillment of the requirements for the degree of

Doctor of Philosophy
in
Electrical Engineering

Fred C. Lee, Chairman
Dushan Boroyevich
Ming Xu
William T. Baumann
Carlos T. A. Suchicital

Jul.24, 2009
Blacksburg, Virginia

Keywords: multiphase buck, coupled-inductor

Investigation of Multiphase Coupled-Inductor Buck Converters in Point-of-Load Applications

Yan Dong

(ABSTRACT)

Multiphase interleaving buck converters are widely used in today's industrial point-of-load (POL) converters, especially the microprocessor voltage regulators (VRs). The issue of today's multiphase interleaving buck converters is the conflict between the high efficiency and the fast transient in the phase inductor design. In 2000, P. Wong proposed the multiphase coupled-inductor buck converter to solve this issue. With the phase inductors coupled together, the coupled-inductor worked as a nonlinear inductor due to the phase-shifted switching network, and the coupled-inductor has different equivalent inductances during steady-state and transient. One the one hand, the steady state inductance is increased due to coupling and the efficiency of the multiphase coupled-inductor buck converter is increased; on the other hand, the transient inductance is reduced and the transient performance of the multiphase coupled-inductor buck is improved. After that, many researches have investigated the multiphase coupled-inductor buck converters in different aspects. However, there are still many challenges in this area: the comprehensive analysis of the converter, the alternative coupled inductor structures with the good performance, the current sensing of converter and the light-load efficiency improvement. They are investigated in this dissertation.

The comprehensive analysis of the multiphase coupled-inductor buck converter is investigated. The n-phase (n>2) coupled-inductor buck converter with the duty cycle D>1/n hasn't been analyzed before. In this dissertation, the multiphase coupled-inductor buck converter is systematically analyzed for any phase number and any duty cycle condition. The asymmetric multiphase coupled-inductor buck converter is also analyzed.

The existing coupled-inductor has a long winding path issue. In low-voltage, high-current applications, the short winding path is preferred because the winding loss dominates the inductor

total loss and a short winding path can greatly reduce the winding loss. To solve this long winding path issue, several twisted-core coupled-inductors are proposed. The twisted-core coupled-inductor has such a severe 3D fringing effect that the conventional reluctance modeling method gives a poor result, unacceptable from the design point of view. By applying and extending Sullivan's space cutting method to the twisted core coupled inductor, a precise reluctance model of the twisted-core coupled-inductor is proposed. The reluctance model gives designers the intuition of the twisted-core coupled-inductors and facilitates the design of the twisted-core coupled-inductors. The design using this reluctance model shows good correlation between the design requirement and the design result. The developed space cutting method can also be used in other complex magnetic structures with the strong fringing effect.

Today, more and more POL converters are integrated and the bottleneck of the integrated POL converters is the large inductor size. Different coupled-inductor structures are proposed to reduce the large inductor size and to improve the power density of the integrated POL converter. The investigation is based on the low temperature co-fire ceramic (LTCC) process. It is found that the side-by-side-winding coupled-inductor structure achieves a smaller footprint and size. With the two-segment B-H curve approximation, the proposed coupled-inductor structure can be easily modeled and designed. The designed coupled-inductor prototype reduces the magnetic size by half. Accordingly, the LTCC integrated coupled-inductor POL converter doubles the power density compared to its non-coupled-inductor POL counterpart and an amazing 500W/in^3 power density is achieved.

In a multiphase coupled-inductor converter, there are several coupled-inductor setups. For example, for a six-phase coupled-inductor converter, three two-phase coupled inductors, two three-phase coupled-inductors and one six-phase coupled inductors can be used. Different coupled-inductor setups are investigated and it is found that there is a diminishing return effect for both the steady-state efficiency improvement and the transient performance improvement when the coupling phase number increases.

The conventional DCR current sensing method is a very popular current sensing method for today's multiphase non-coupled-inductor buck converters. Unfortunately, this current sensing method doesn't work for the multiphase coupled-inductor buck converter. To solve this issue,

two novel DCR current sensing methods are proposed for the multiphase coupled-inductor buck converter.

Although the multiphase coupled-inductor buck converters have shown a lot of benefits, they have a low efficiency under light-load working in DCM. Since the DCM operation of the multiphase coupled-inductor buck converter has never been investigated, they are analyzed in detail and the reason for the low efficiency is identified. It is found that there are more-than-one DCM modes for the multiphase coupled-inductor buck converter: DCM1, DCM2 …, and DCMn. In the DCM2, DCM3…, and DCMn modes, the phase-currents reach zero-current more-than-once during one switching period, which causes the low efficiency of the multiphase coupled-inductor buck converter in the light load. With the understanding of the low efficiency issue, the burst-in-DCM1-mode control method is proposed to improve the light load efficiency of the multiphase coupled-inductor buck converter. Experimental results prove the proposed solution.

TO MY PARENTS

GUOLIANG DONG
SHUXIAN LIU

TO MY SISTER

YUE DONG

ACKNOWLEDGMENTS

With sincere gratefulness in my heart, I would like to thank my advisor, Dr. Fred C. Lee for his continuous encouragement, guidance and support, especially during my depressed time. It is really an honor to pursue my Ph.D study under his supervision. His research attitude, an attitude for perfection, was and will be beneficial for my entire life. His great intuition, philosophical thinking and broad knowledge have been a source of inspiration for me throughout the last six years. Of many valuable things I have learned from him, the attitude in face of challenges is the most precious one for me, which is also applicable to my other aspects of life.

I am also thankful to my committee: Dr. Dushan Boroyevich, Dr. Ming Xu, Dr. William Baumann and Dr. Carlos Suchicital.

It has been a great pleasure to work in the Center for Power Electronics Systems (CPES), not only because of the talented colleagues but also the friendships. I would like to specially thank Dr. Julu Sun, who encouraged me a lot during his stay in CPES and I learned a tremendous amount from him both within and beyond the scope of research. In would also like to thank all the other PMC group members: Dr. Kaiwei Yao, Dr. Jia Wei, Dr. Yang Qiu, Dr. Juanjuan Sun, Mr. Yu Meng, Dr. Shuo Wang, Dr. Kisun Lee, Dr. Ching-Shan Leu, Dr. Bing Lu, Mr. Doug Sterk, Dr. Yan Jiang, Dr. Authur Ball, Mr. Chuanyun Wang, Mr. Dianbo Fu, Mr. Andrew Schmit, Mr. David Reusch, Dr. Jian Li, Mr. Bin Huang, Mr. Ya Liu, Mr. Yi Sun, Dr. Pengju Kong, Mr. Yucheng Ying, Mr. Qiang Li, Dr. Xu Yang, Dr. Yugang Yang, Dr. Yan Xing, Dr. Ke Jin, Mr. Pengjie Lai, Mr. Zijian Wang, Mr. Daocheng Huang, Mr. Qian Li, Mr. Zheng Luo, Mr. Feng Yu, Mr. Mingkai Mu, Mr. Yingyi Yan, Mr Haoran Wu and Mr. Chanwit Prasantanakorn. It was a pleasure to work with such a talented and creative group. I would also like to thank all of the other students I have met in CPES during my six-year study, especially to Dr. Qian Liu, Dr. Huiyu Zhu, Dr. Rengang Chen, Dr. Xigen Zhou, Dr. Michele Lim, Dr. Yan Liang, Dr. Jing Xu, Dr. Rixing Lai, Dr. Honggang Sheng, Mr. Xiao Cao, Mr. Tong Liu, and Mr. Dong Jiang, Mr. Ruxi Wang and Mr. Hua Lin for the delightful discussions, both related and non-related to power electronics.

I would also like to thank the wonderful members of the CPES staff who were always willing to help me out, Ms. Teresa Shaw, Ms. Linda Gallagher, Ms. Teresa Rose, Ms. Ann Craig, Ms. Marianne Hawthorne, Ms. Elizabeth Tranter, Ms. Michelle Czamanske, Ms. Linda Long, Mr. Steve Chen, Mr. Robert Martin, Mr. Jamie Evans, Mr. Dan Huff, and Mr. David Fuller. Specially, I would like to thank Ms. Keara Axelrod for her editing of this dissertation.

With much love, I would like to thank my great parents, and my elder sister. My parents pray for me every day as I am staying in a different country. They are happy for every small success I have made and encourage me during every frustration I have experienced. My sister is always proud of her younger brother and takes the duty of taking care of parents when I'm not around. I didn't realize how much a small accident happened to me can affect the whole family. I owe all of you too much and I will try my best to compensate for all my life.

There are also some friends outside CPES who made my life in Blacksburg enjoyable. You may never realize the value of your help to me. I will not list the names here; you already know who you are.

This work was primarily supported by Analog Devices, C&D Technologies, CRANE, Delta Electronics, HIPRO Electronics, Infineon, International Rectifier, Intersil, FSP-Group, Linear Technology, LiteOn Tech, Primarion, NXP, Renesas, National Semiconductor, Richtek, Texas Instruments. Also, this work made use of ERC shared facilities supported by the National Science Foundation under Award Number EEC-9731677.

Table of Contents

List of Figures

List of Tables

List of Symbols

f	Frequency
C	Capacitance
L	Inductance
R	Resistance
V	Voltage
I	Current
P	Power
B	Magnetic flux density
H	Magnetic field intensity
t	Time or thickness
$P_{winding}$	Winding loss
P_{core}	Core loss
α	Steinmetz exponent, alpha
β	Steinmetz exponent, beta
k	Steinmetz coefficient
μ_0	Permeability of free space
μ_r	Relative permeability
A	Area
w	Width
J	Current density
Q	Electrical charge

I_{DC}	DC current
D	Duty cycle
M	Mutual inductance
L_{self}	Self inductance
L_k	Leakage inductance
L_{ss}	Steady-state inductance
L_{tr}	Transient inductance
I_{pp}	Peak-to-peak current ripple
η	Efficiency
V_{in}	Input voltage
V_o	Output voltage

Chapter 1. Introduction

1.1. Multiphase Interleaving Buck Converters

1.1.1. The Multiphase Interleaving Buck Converter

Modern technologies such as computers, wireless communications, GPS units, and digital camcorders all started with the invention of integrated circuits. The more transistors are integrated into a single die, the more functions that die can perform. Just as Moore's Law predicts that transistor density doubles every eighteen months [1-4], the number of transistors per die has increased steadily in the last 50 years. The number of transistors per die will reach ten billion in 2010 [1] (Figure 1.1).

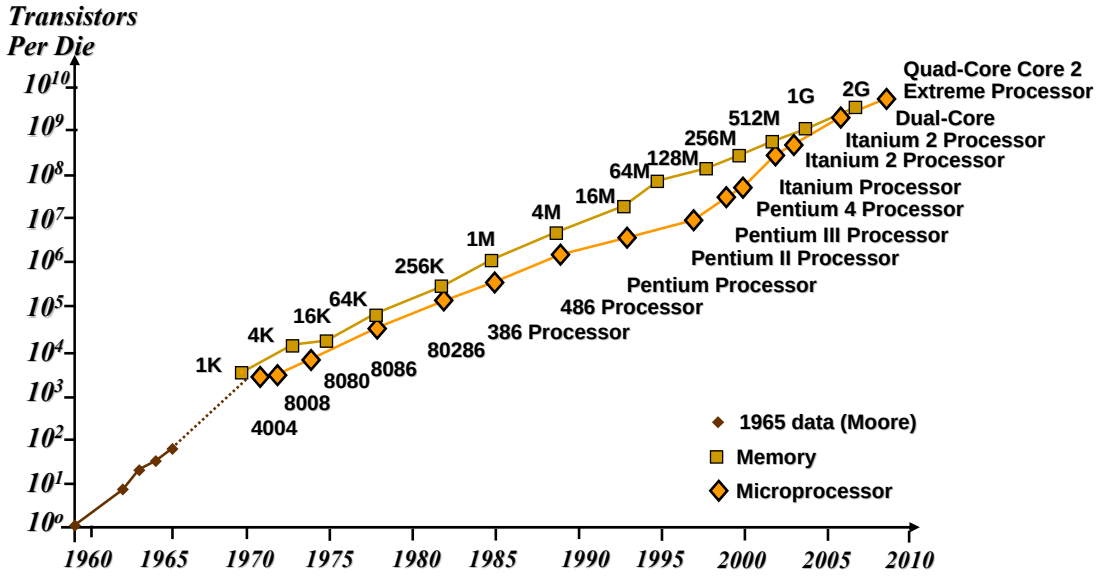

Figure 1.1 The historical trend of the transistors per die in microprocessors and memories

Transistor density is not the only factor that determines the performance of an integrated circuit. How fast a transistor can switch, or the clock frequency, represents the performance of the integrated circuit. For example, an i486 processor can run at 25MHz, while today's Quad-Core processor is running in the 3-4GHz range. The increases in the integrated circuit's speed

and number of transistors have resulted in an increase in power demand. Currently, for cost-performance CPUs in desktop applications, the power consumption is about 100W. For high-performance CPUs, such as the Itanium® processor used in server applications, power consumption goes up to 130W. It is no longer an easy task to deal with the losses in these applications.

In order to minimize the power consumption of the microprocessors, the supply voltage V_{dd} has to be decreased [5-6] so that the energy dissipated during one clock cycle, CV_{dd}^2, is reduced significantly. However, lower V_{dd} leads to an even higher supply current, because the CPU power is also increasing. Figure 1.2 shows the power roadmap of Intel's microprocessors [7].

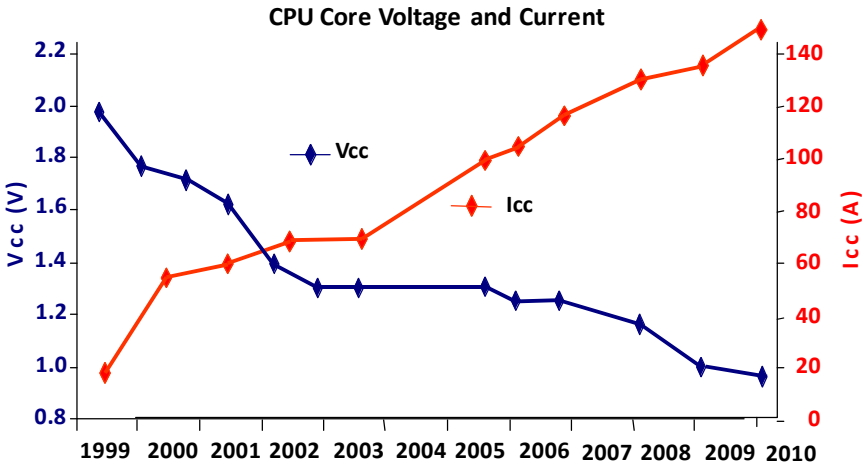

Figure 1.2 The road map of the voltage and the current of the Intel's microprocessors in the last ten years.
Used with permission of Kisun Lee, 2009

Moreover, due to high clock frequencies, the microprocessors' load transition speeds also increase. The microprocessor load current slew rates are also increasing. The low-voltage, high-current, and fast load-transition speeds are the challenges imposed on the dedicated microprocessor power supplies, known as microprocessor voltage regulators (VRs), and are physically located on the motherboard next to the microprocessors.

To meet these requirements, multiphase interleaving buck converters are adopted for today's microprocessor VRs[8-23]. Figure 1.3 shows the n-phase interleaving buck converter for microprocessor VR application. Figure 1.4 shows such a microprocessor VR in a motherboard.

Most of today's microprocessor VRs consist of four to ten phases, operating at a switching frequency of about 300-700KHz per phase.

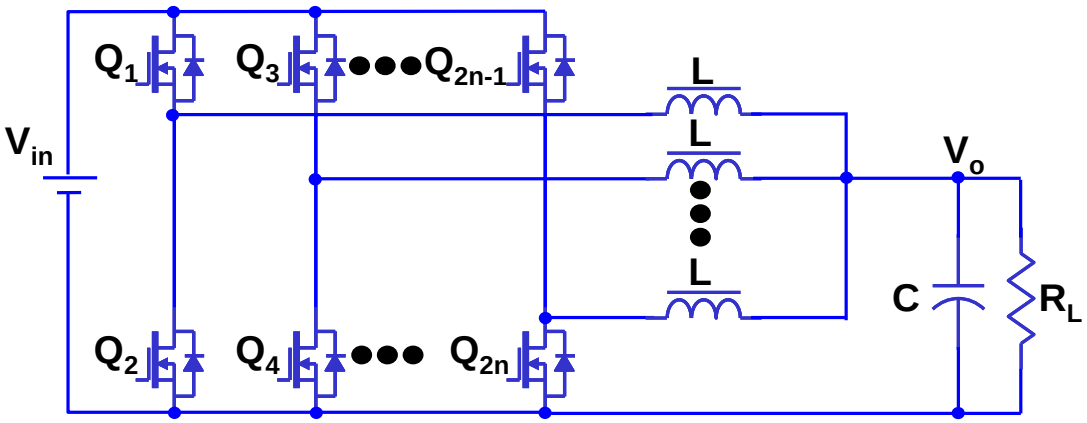

Figure 1.3 Schematic of the n-phase interleaving buck converter

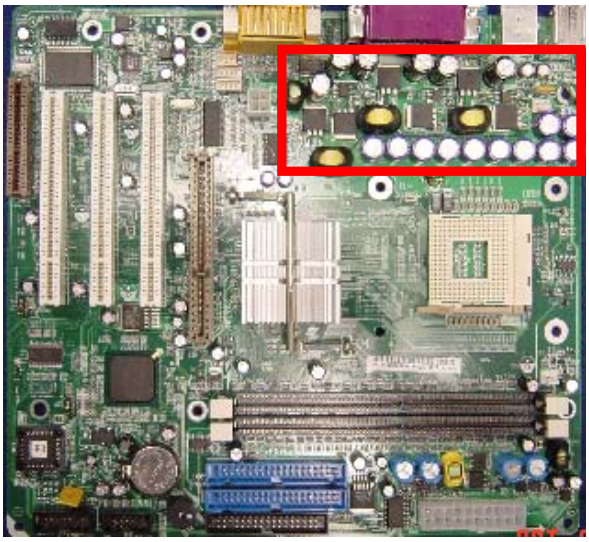

Figure 1.4 The multiphase buck converter in today's motherboard (desktop) [17]

Multiphase interleaving buck converters have several benefits. By paralleling several synchronous buck converters and phase-shifting their drive signals, the multiphase buck converter can reduce both the input and output current ripples and improve the transient response. Furthernore, the multiphase buck converters distribute the different buck phases. This will distribute the heat throughout the converter, avoid the hot spot and improve the thermal performance of the converter. With the low temperature in the power devices, the loss of these power devices also drop, which results in the efficiency increase of the multiphase buck converter. Moreover, with the multiphase buck, the inductor is separated into several small

inductors. Therefore, the profile of the inductors can be made to be very small. This will reduce one bottleneck of the low profile converter.

All the VRs built for today's Intel microprocessors need to meet stringent transient response requirements [24-31], the VR load line specification. The load line contains static and transient voltage regulation data as well as maximum and minimum voltage levels. The upper and lower load lines represent the allowable range of voltages that must be presented to the processor. The voltage must never exceed these boundaries for proper operation of the processor. However, in a CPU, the high clock speed circuits result in fast, unpredictable, and large magnitude changes in the supply current. The rate of change could be many amps per nanosecond. If not well-managed, these current transients may cause the VR output voltage to go outside the regulation band and manifest as power supply noise, which ultimately limits how fast the CPU can operate. This is further compounded by the reduced noise margin in the CMOS logic circuits that result from power supply voltage scaling. While voltage overshoots may cause the CPU reliability to degrade, undershoots may cause malfunctions of the CPU, often resulting in a blue screen indicating the PC is about to crash.

This is why output filter capacitors are so important for a processor to operate properly. In order to supply sufficient energy to the processor, sufficient energy storage capacitors have to be placed in different locations in the power delivery path to the processor. The closest capacitors to the microprocessor VR are so-called "bulk" capacitors. Oscon/Polymer capacitors or multi-layer ceramic capacitors (MLCCs) are widely used as the bulk capacitors in most of today's desktop designs or server designs, respectively. Following the bulk capacitors in the power path are the MLCC cavity capacitors, which are located in the socket cavity and have lower ESR and ESL compared to the bulk capacitors. The packaging capacitors are also ceramic capacitors with extremely low ESL, which are located in the CPU package. There is also an on-die capacitor just besides the CPU die (Figure 1.5 and Figure 1.6).

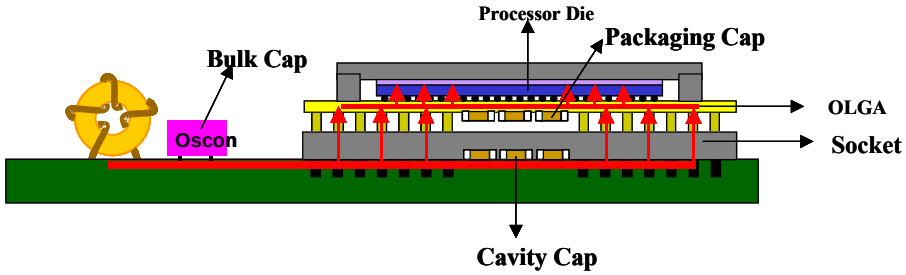

Figure 1.5. A typical power delivery path for today's microprocessors

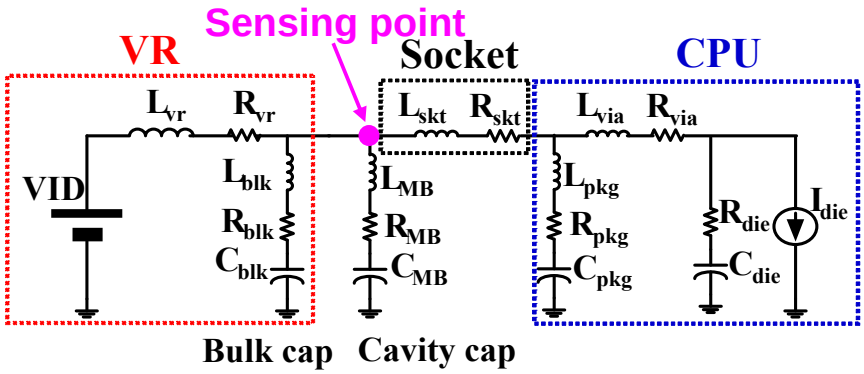

Figure 1.6 A lumped circuit model of the power delivery path of today's microprocessors

In the future, the transient requirements of VRs will be even more stringent than those of today's VRs. Therefore, a huge VR with a huge output capacitors are needed (Figure 1.7[18]). The huge output capacitors not only increase the cost of the VRs, but also consume a large real estate of the motherboard. Reduction of the huge output capacitors is worth investigating.

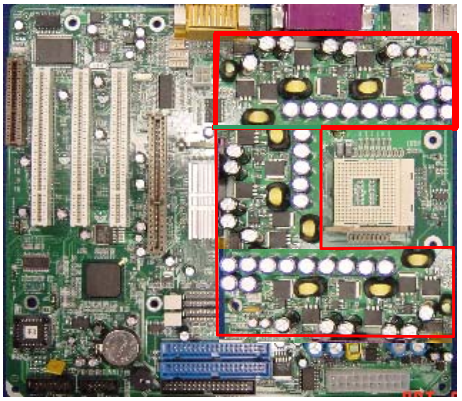

Figure 1.7 The conceptual drawing of the future microprocessor VR with huge output capacitors. ***Used with permission of Yuancheng Ren, 2009***

Besides the microprocessor VR for the CPU, other point-of-load (POL) converters, dedicated for components like memory cards, are gradually adopting multiphase interleaving buck converters as their performance requirements go higher and higher. Figure 1.8 shows another three-phase buck converter (VCN60/70BADJTU-1C) from the Murata Corp. dedicated for the memory array application [32]. Figure 1.9 shows a three-phase POL converter (PTV08T250W) for the wide-input POL application [33-34].

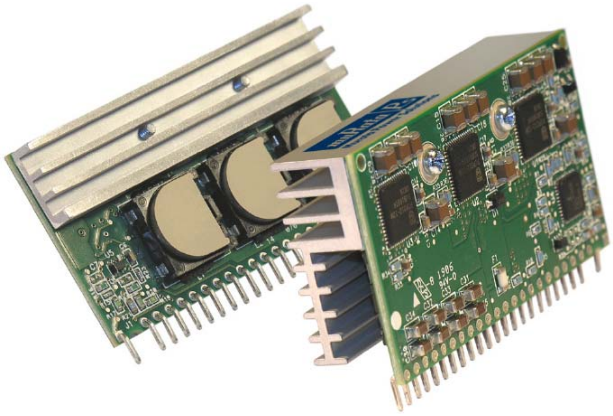

Figure 1.8 The multiphase buck converter for the memory array POL (VCN60/70BADJTU-1C). ***Used with permission of Murata company, 2009***

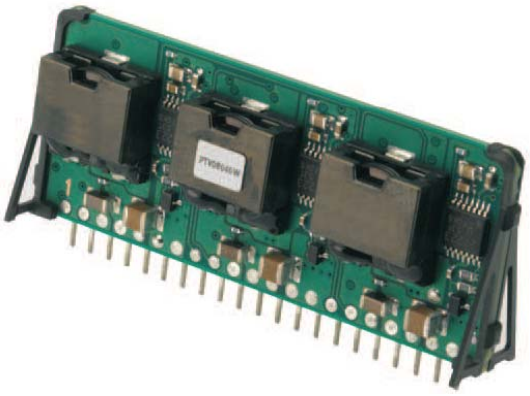

Figure 1.9 The multiphase buck converter for the wide-input POL application (PTV08T250W). ***Used with permission of Texas Instrument company, 2009***

Table 1.1 summarizes the multiphase buck converters in different applications. The input voltage, the output voltage and the duty cycle are shown in the table. It can be seen that the duty cycle range is quite wide. For example, in the wide input POL application, the duty cycle is 0.06-0.45.

Table 1.1 Multiphase buck converters in different applications

Application	V_{in}(V)	V_o(V)	Duty cycle D
CPU VR	10.8-13.2	0.8-1.6	0.06-0.15
DDR memory POL	10.2-13.2	0.6-3.5	0.05-0.34
Wide-input POL	8-14	0.8-3.6	0.06-0.45

1.1.2. Limitation of the Multiphase Interleaving Buck Converter

Figure 1.10 shows the efficiency vs. the phase inductance curve for a multiphase interleaving buck converter. It can be seen that when the phase inductance is increased, the efficiency of the multiphase interleaving buck converter will also increase. This is because when the phase inductance is increased, the phase current ripple will be reduced. Therefore, both the conduction loss and the switching loss will be reduced.

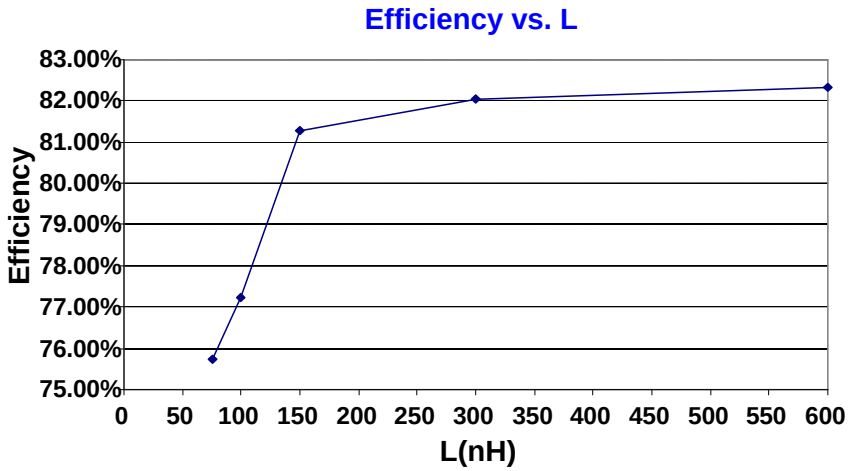

Figure 1.10 The efficiency vs. the phase inductance curve of the multiphase interleaving buck converter (the ISL6561 board)

However, when the phase inductance increases, the transient perormance of the multiphase interleaving buck converter will suffer [35]. Figure 1.11 shows the multiphase buck converter and Figure 1.12 shows the inductor current response during the output load current transient.

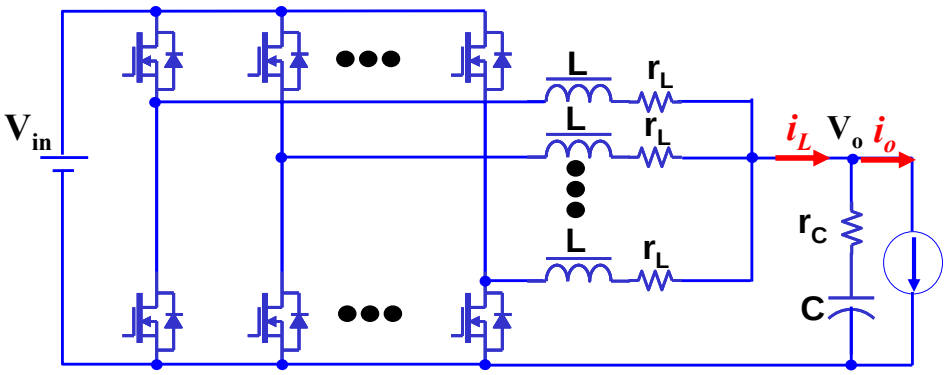

Figure 1.11 The multiphase interleaving buck converter with the inductor current i_L and the output current i_o marked

The transient voltage drops on the multiphase buck converter output voltage V_o occurs because the multiphase buck converter output capacitors need to provide current during the transient responses. The current demand of the load, i_o, has a much higher slew rate than that of the multiphase buck inductor current, i_L. The difference between the two currents determines the charges that need to be provided by the multiphase buck converter output capacitors. If the unbalanced charges can be reduced, the multiphase buck converter transient voltage spikes can also be reduced for the same multiphase buck converter output capacitors. The triangle part in Figure 1.12 shows the unbalanced charges. This part is affected by the output inductance design.

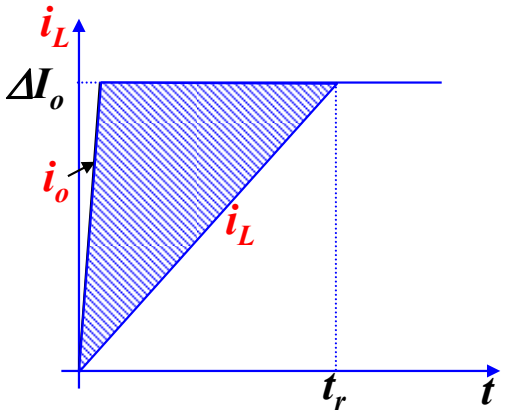

Figure 1.12 The transient inductor current i_L response of the multiphase interleaving buck converter under the output current i_o transient

The triangle part in Figure 1.12 of the unbalanced charges is determined by the inductor current slew rate and the magnitude of the current step. The current step magnitude is determined by the applications, which cannot be changed. The only way to reduce the unbalanced charges is

to increase the current slew rate flowing into the multiphase buck converter output capacitors so that the transient voltage spike on the capacitors can be reduced.

From the viewpoint of control system, the transient unbalanced charges shown in Figure 1.12 are actually a function of how well the inductor current i_L can follow the changes of load current i_o, as shown in Figure 1.11.

To describe the ability of the inductor current to follow the load current, the average current transfer function $G_{ii}(s)$ is defined as follows:

$$G_{ii}(s) = \frac{\tilde{i}_L(s)}{\tilde{i}_o(s)} \tag{1.1}$$

where $\tilde{i}_L(s)$ and $\tilde{i}_o(s)$ are the perturbations added to the inductor current i_L and load current i_o, respectively. The transfer function can be derived from the circuit shown in Figure 1.11, as follows:

$$G_{ii}(s) = \frac{\tilde{i}_L(s)}{\tilde{i}_o(s)} = \frac{s \cdot r_C \cdot C + 1}{s^2 \cdot L \cdot C / n + s \cdot (r_C + r_L / n) \cdot C + 1} \tag{1.2}$$

where r_c, C and L are shown in Figure 1.11.

This transfer function is determined only by the passive component parameters. The duty cycle, the load current and the input voltage do not affect it. If linear parameters are assumed, the equation (1.2) is also valid for the large-signal perturbations as long as the duty cycle is not saturated.

The bode plot of the current transfer function $G_{ii}(s)$ is shown in Figure 1.13. Here, ω_o is the resonant frequency.

$$\omega_o = \frac{1}{\sqrt{L \cdot C / n}} \tag{1.3}$$

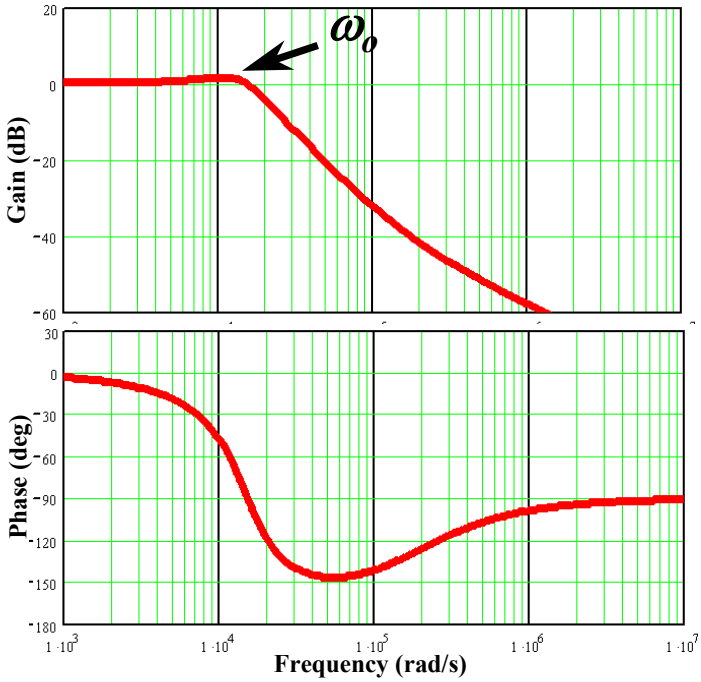

Figure 1.13 The open-loop inductor current to the output current transfer function $G_{ii}(s)$ in a multiphase buck converter [35]. ***Used with permission of Pit-Leong Wong, 2009***

Feedback control is used in multiphase buck converter to regulate output voltages. The following discussion attempts to identify how the feedback control affects both the rise time and the transient response of the multiphase buck converter. In order to do so, the closed-loop current transfer function must be derived.

With voltage feedback control, the closed-loop current transfer function $G_{iic}(s)$ is as follows:

$$G_{iic}(s) = G_{ii}(s) - G_{id}(s) \cdot G_c(s) \cdot \frac{Z_O(s)}{1 + T(s)} \tag{1.4}$$

where $G_{id}(s)$ is the duty-cycle-to-inductor-current transfer function, $G_c(s)$ is the transfer function of the compensator, $Z_o(s)$ is the converter output impedance, and $T(s)$ is the loop gain. The loop gain is described as follows:

$$T(s) = K \cdot G_{vd}(s) \cdot G_c(s) \tag{1.5}$$

where $G_{vd}(s)$ is the duty-cycle-to-output-voltage transfer function, and K is the gain of the compensator. During load transient responses, the duty cycle changes. However, the duty cycle

change does not affect the closed-loop current transfer function $G_{iic}(s)$. In load transient responses, as long as the duty cycle is not saturated, the small-signal model transfer function is also valid for large signal analysis. Thus, $G_{iic}(s)$ can be used to accurately analyze the large-signal load transient responses.

For a certain feedback control loop design, the open-loop and closed-loop current transfer functions, $G_{ii}(s)$ and $G_{iic}(s)$, and the loop gain $T(s)$ are shown in Figure 1.14.

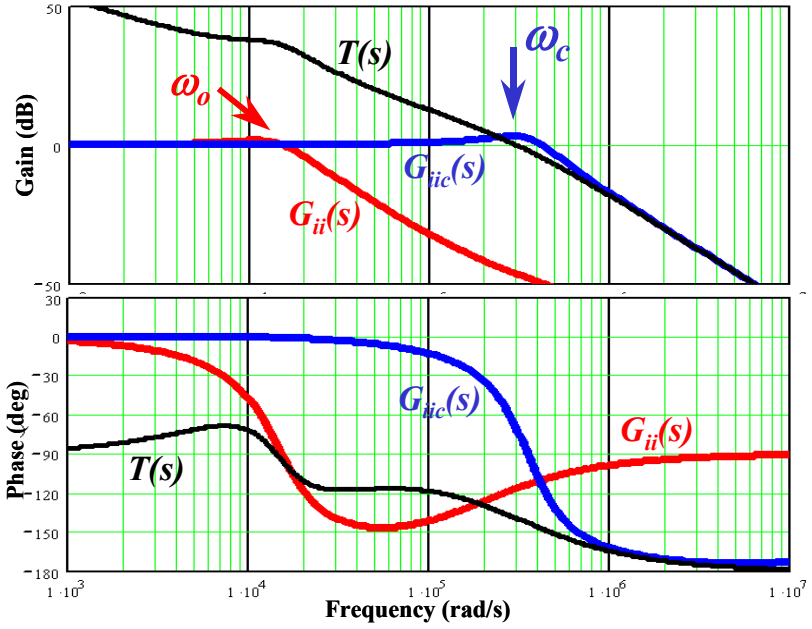

Figure 1.14 The open loop and closed loop inductor current to the output current transfer functions: $G_{ii}(s)$, $G_{iic}(s)$ and the loop gain transfer function $T(s)$ [35]. *Used with permission of Pit-Leong Wong, 2009*

As shown in Figure 1.14, the closed-loop current transfer function has the same shape as its open-loop counterpart unless the corner frequency moves to ω_c, which is the feedback control bandwidth. The control bandwidth ω_c is much higher than the power stage double poles' frequency ω_o.

The open-loop and closed-loop current transfer functions are both second-order systems. The difference lies is the frequencies of their double poles, which results in different time domain performances of the two transfer functions. The time domain step responses of the two transfer functions are compared in Fig. 3.9.

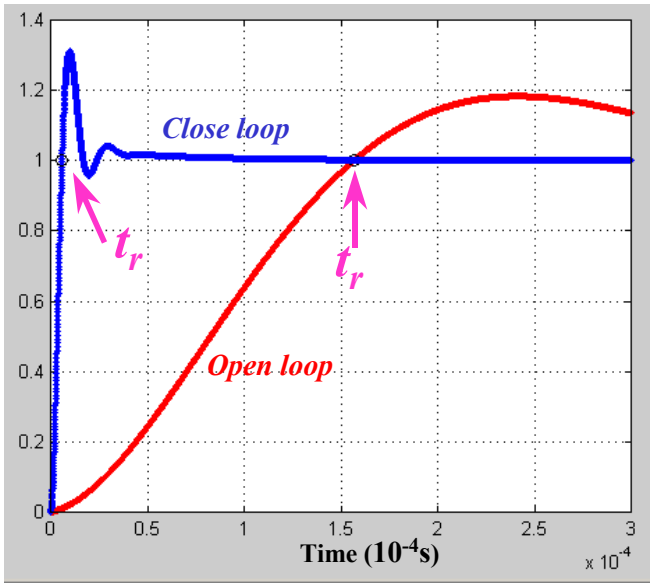

Figure 1.15 Step responses of the inductor current in the open-loop and closed-loop multiphase buck converters [35]. ***Used with permission of Pit-Leong Wong, 2009***

The rise time of the closed-loop step response is much smaller than that of the open-loop step response. The unbalanced charge area is greatly reduced. Much faster transient response can be expected with feedback control. Our interest is to quantify this improvement.

The relationship between rise time and control bandwidth can be approximated as follows:

$$t_r = \frac{T_c}{4} = \frac{\pi/2}{\omega_c} \tag{1.6}$$

The only factor that determines the inductor current rise time during transient responses is the feedback control bandwidth. Therefore, the inductor current slew rate can be easily derived, as follows:

$$\left.\frac{di}{dt}\right|_{avg} = \frac{\Delta I_o}{t_r} = \frac{\Delta I_o \cdot \omega_c}{\pi/2} \tag{1.7}$$

Figure 1.16 shows the transfer functions of the duty cycle to the output voltage (G_{vd}) in multiphase interleaving buck converters. It can be seen that when the phase inductance increases, the corner frequency of the G_{vd} transfer function decreases. Therefore, the loop bandwidth ω_c of the multiphase buck converter with a smaller phase inductance will potentially be larger than that of the multiphase buck converter with a larger phase inductance.

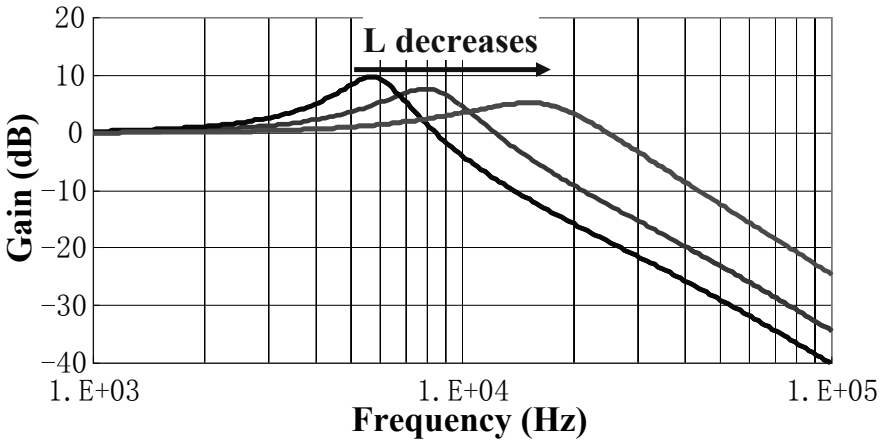

Figure 1.16 The gain of the duty cycle to the output voltage transfer function $|G_{vd}|$ vs. frequency in the multiphase buck converter

Figure 1.18 shows the average current slew rate of the multiphase buck converter with different inductances. When the phase inductance decreases, the closed loop bandwidth ω_c can be designed to be higher. Therefore, the average current slew rate of the multiphase buck converter is higher. Accordingly, the unbalanced charges in the triangle part are reduced and the transient output voltage change will be smaller.

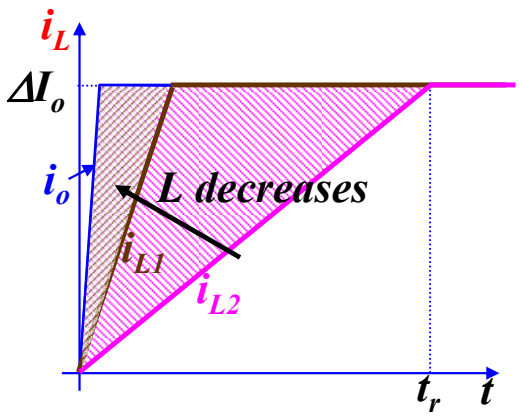

Figure 1.17 The effect of the phase inductance on the unbalanced charge provided by the output capacitors of the multiphase buck converter

From the above analysis, it can be seen that the efficiency of the multiphase buck converter increases when the phase inductance increases; and that transient performance of the multiphase buck converter improves when the phase inductance decreases. Therefore, there is a conflict for the phase inductor design in the multiphase interleaving buck converter. Figure 1.18 shows the conflict in the phase inductor design.

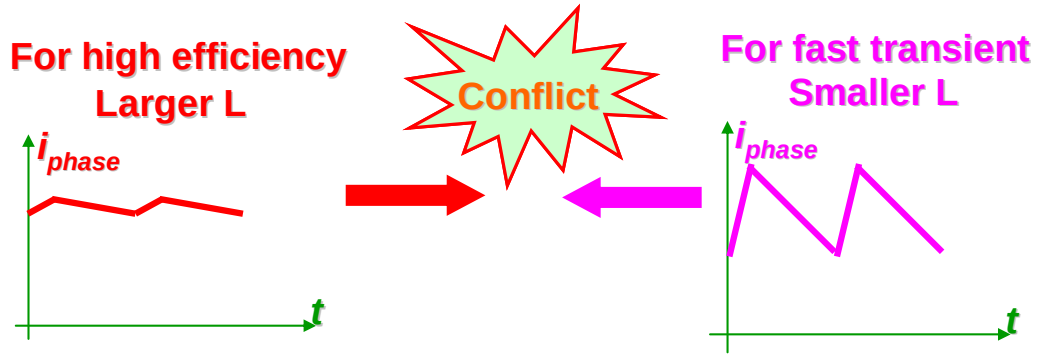

Figure 1.18 The design conflict of the phase inductance in the multiphase interleaving buck converter

To satisfy both the high efficiency requirement and the fast transient response requirement of a multiphase buck converter, a nonlinear inductor is needed. The nonlinear inductor should have a high inductance for the steady state operation to achieve the high efficiency of the converter; and it should also have a low inductance in the transient for a fast response of the converter. To achieve such a nonlinear inductor, the coupled inductor is proposed.

1.2. Multiphase Coupled-inductor Buck Converters

To solve the conflict of today's multiphase interleaving buck converters, P.Wong proposed the multiphase coupled inductor buck converter in 1999 [35-39].

Figure 1.19 shows the schematics of the two-phase non-coupled-inductor buck converter and the two-phase coupled-inductor buck converter. The L in Figure 1.19 (b) is the self-inductance of the coupled-inductor; the M in Figure 1.19 (b) is the mutual inductance of the coupled-inductor. The M can be positive (M>0, non-inverse coupling) or negative (M<0, inverse coupling). The relationship of M to L can be expressed as

$$M = \alpha L \tag{1.8}$$

where α is the coupling coefficient between the two inductors ($-1<\alpha<1$). Figure 1.20 shows the integrated two-phase non-coupled-inductor structure and the integrated two-phase coupled-inductor structure. In the integrated two-phase non-coupled-inductors, the flux generated by one phase current doesn't link to the other phase and the two phase currents are not coupled. In the integrated two-phase coupled-inductors, the flux generated by one phase current links to the other phase and the two phase currents are coupled.

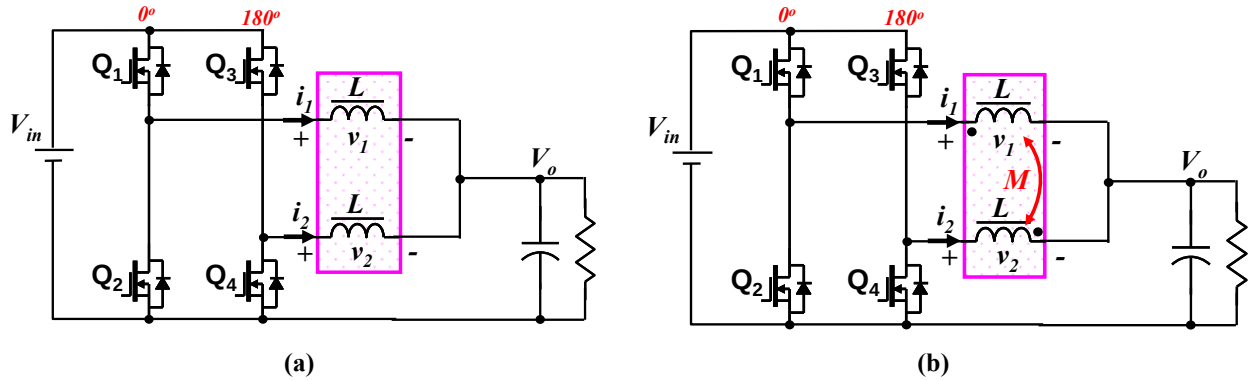

Figure 1.19 The two-phase non-coupled inductor and coupled-inductor buck converters
(a) The two-phase non-coupled-inductor buck converter (b) The two-phase coupled-inductor buck converter

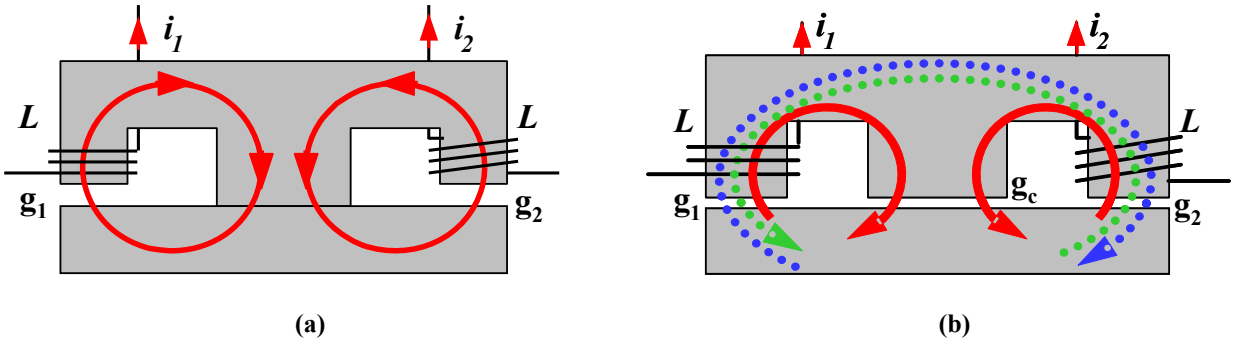

Figure 1.20 The two-phase non-coupled-inductors and coupled-inductors and their magnetic flux flow paths
(a) The two-phase non-coupled-inductors and their flux flow paths (b) The two-phase coupled-inductors and their flux flow paths

P. Wong found that the coupled-inductors work as a nonlinear inductor within a phase-shifted switching network. With the proper design, the multiphase coupled-inductor buck converter can have a higher steady-state inductance for a higher efficiency and/or a smaller transient inductance for a faster transient response.

The basic equations for the two-phase coupled-inductors are shown below.

$$\begin{cases} v_1 = L \cdot \dfrac{di_1}{dt} + M \cdot \dfrac{di_2}{dt} \\ v_2 = M \cdot \dfrac{di_1}{dt} + L \cdot \dfrac{di_2}{dt} \end{cases} \tag{1.9}$$

The two-phase coupled-inductor buck converter has different equivalent inductances during different time intervals in one switching cycle. This is because of the different inductor voltage combinations from the phase-shifted switching network. Figure 1.21 shows the waveforms when D<0.5 and Figure 1.22 for D>0.5.

After derivation, it is found that

$$L_{eq1} = \frac{L_s^2 - M^2}{L_s + \frac{D}{D'} \cdot M} \tag{1.10}$$

$$L_{eq2} = L_s + M \tag{1.11}$$

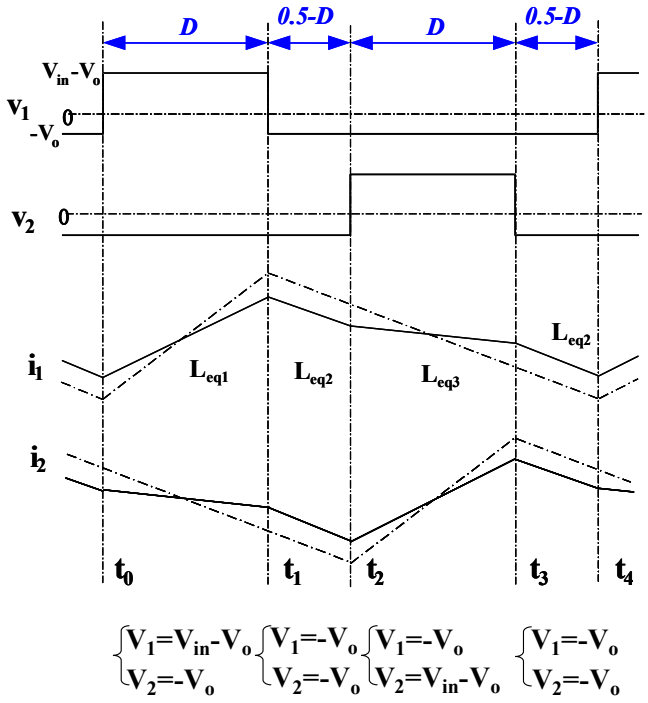

Figure 1.21 The steady-state inductor voltage and current waveforms for two-phase non-coupled-inductor and coupled-inductor buck converters (D<0.5)

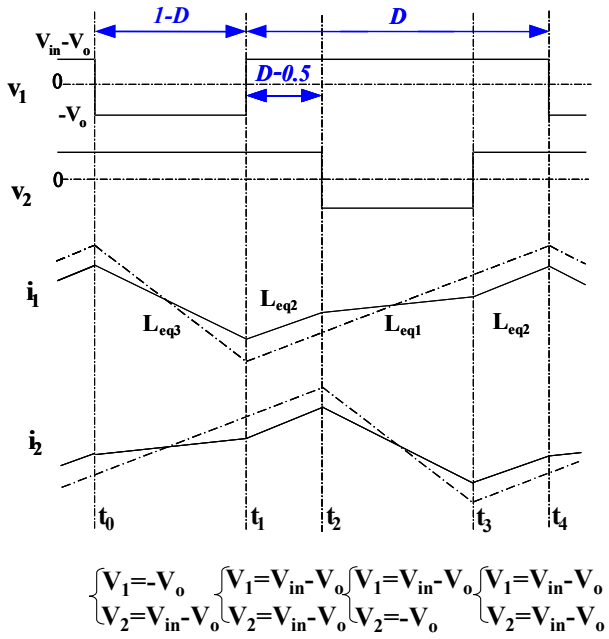

Figure 1.22 The steady-state inductor voltage and current waveforms for two-phase non-coupled-inductor and coupled-inductor buck converters (D>0.5)

$$L_{eq3} = \frac{L_s^2 - M^2}{L_s + \frac{D'}{D} \cdot M} \tag{1.12}$$

Based on the equivalent inductances, we can analyze the effects of the coupled-inductors on the converter performance both in steady-state operation and during transient responses. The steady-state criterion is the current ripple because it has a direct impact on the converter efficiency. From Figure 1.21 and Figure 1.22, it can be seen that the L_{eq1} and L_{eq3} determine the converter steady-state current ripple when D<0.5 and when D>0.5, respectively. Therefore, the steady state inductance L_{ss} is defined as

$$L_{SS} = L_{eq1} \text{ (D<0.5)} \tag{1.13}$$

$$L_{SS} = L_{eq3} \text{ (D>0.5)} \tag{1.14}$$

The transient criterion is the current slew rate during transient responses. Figure 1.23 shows the phase-current response with a perturbation ΔD in the duty cycle D. It can be derived that

$$\Delta i = \frac{V_{in}}{L_{eq2} \cdot f_s} \cdot \Delta D \tag{1.15}$$

where f_s is the switching frequency of the coupled buck converter. Therefore, it is L_{eq2} that determines the transient response of the converter phase-current. Based on this, the transient inductance L_{tr} is defined as

$$L_{tr} = L_{eq2} = L_s + M < L_s \tag{1.16}$$

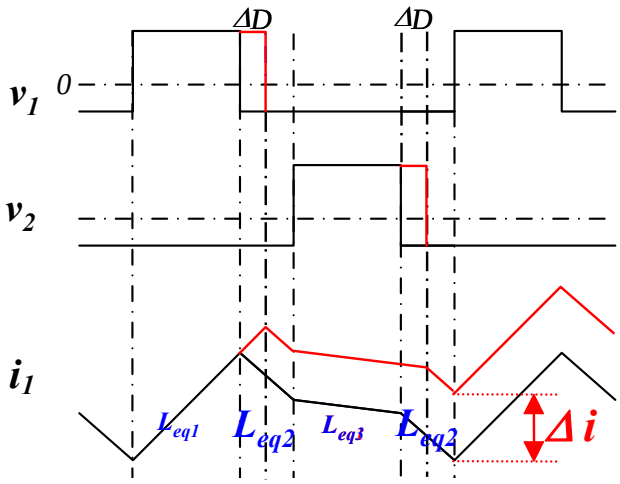

Figure 1.23 The transient inductor voltage and current waveforms for the two-phase coupled-inductor buck converter

From the equation (1.16), the inverse coupled inductor (M<0) can reduce the transient inductance. Therefore, the inverse coupled inductor can increase the bandwidth (Figure 1.24 [21]) and improve the transient performance of the multiphase buck converter.

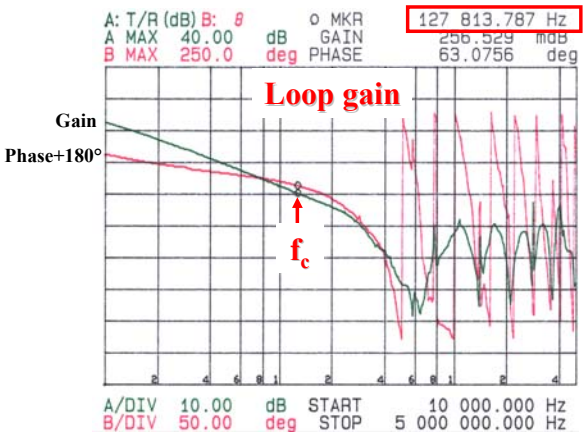

(a)

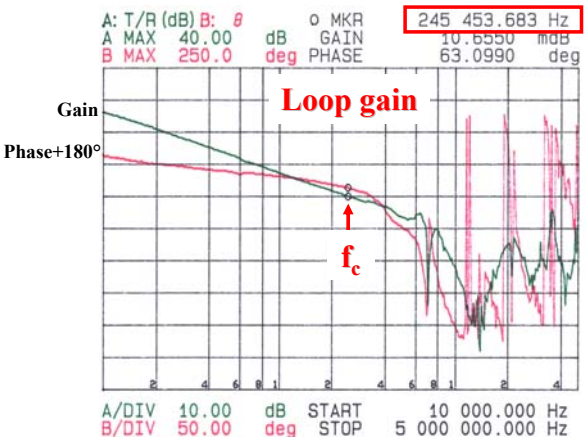

(b)

Figure 1.24 The bandwidth improvement of the multiphase coupled-inductor buck converter compared to the multiphase non-coupled-inductor buck converter (a) the bandwidth of the non-coupled-inductor buck converter: 127kHz (b) the bandwidth of the coupled-inductor buck converter: 245kHz [21]

From the equations (1.10), (1.13), (1.14) and (1.16), it can be seen that the non-inverse coupled-inductors (M>0) can increase the transient inductance and may decrease the steady-state inductance; the inverse coupled-inductors (M<0) can reduce the transient inductance and may increase the steady-state inductance. Therefore, the inverse coupled-inductor is preferred. (In the following discussion, references to the coupled-inductor are about the inverse coupled-inductor, unless otherwise specified.)

Based on the same transient equivalent inductance, the relationship between the steady-state inductor peak-to-peak currents of non-coupled and coupled-inductors can be determined and compared as follows:

$$\frac{I_{pp\_cp}}{I_{pp\_nc}} = \frac{L_{nc}}{L_{ss}} = \frac{L_{tr}}{L_{ss}} = \begin{cases} \dfrac{1+\dfrac{D}{D'}\cdot\alpha}{1-\alpha} & (D<0.5) \\ \dfrac{1+\dfrac{D'}{D}\cdot\alpha}{1-\alpha} & (D>0.5) \end{cases} \tag{1.17}$$

where I_{pp_cp} is the peak-to-peak current ripple of the coupled-inductor, I_{pp_nc} is the peak-to-peak current ripple of the non-coupled-inductor, and L_{nc} is the inductance of the non-coupled-inductor. The relationship shown in the equation (1.17) is plotted in Figure 1.25.

When the steady-state duty-cycle is closer to 0.5, the current ripple reduction is more effective. Stronger coupling effects give smaller current ripples. The conclusion of P. Wong's study is that the coupled-inductors should be designed to have a larger $|\alpha|$ while maintaining the same L_{eq2} (L_{tr}) in order to have the same transient responses and to achieve smaller steady-state current ripples.

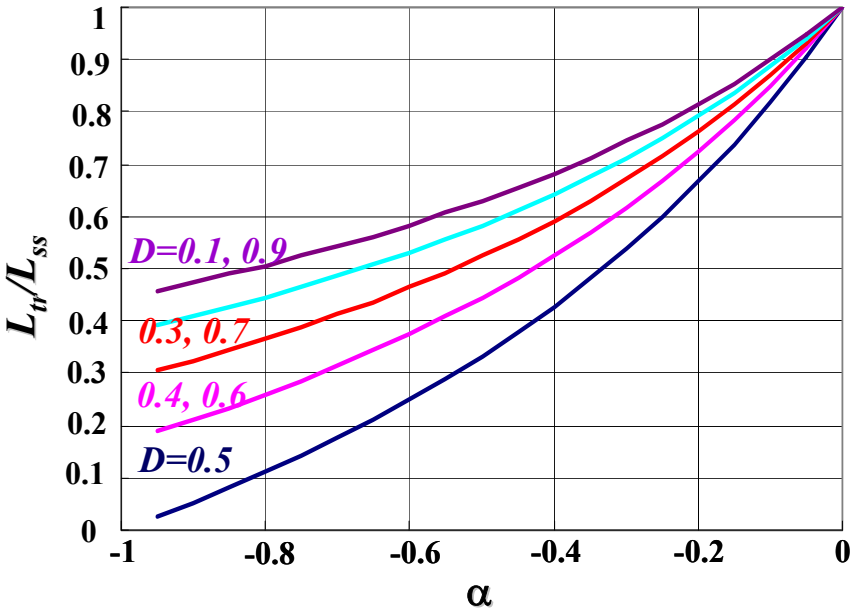

Figure 1.25 The ratio of the transient inductance to the steady-state inductance L_{tr}/L_{ss} vs. the coupling coefficient α and the duty cycle D in two-phase coupled-inductor buck converters

Figure 1.26 shows the two-phase and four-phase inverse coupled-inductor structures proposed by P.Wong [38]. In this four-phase coupled-inductor, the magnetic fluxes generated from any two-phase currents are inversely coupled.

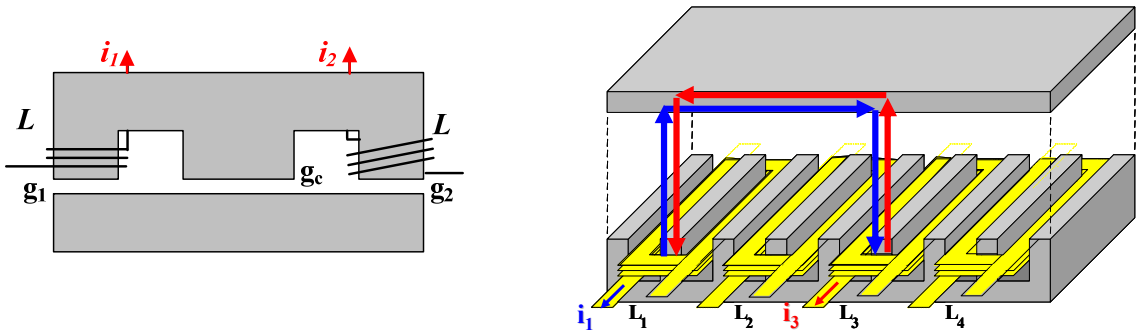

(a) (b)

Figure 1.26 P.Wong's two-phase and four-phase inverse coupled-inductor structures (a) P. Wong's two-phase coupled-inductor structure (b) P.Wong's four-phase coupled-inductor structure [35]. ***Used with permission of Pit-Leong Wong, 2009***

From Figure 1.25, the stronger the coupling, the better the performance of the multiphase coupled-inductor buck converter. This can be achieved by reducing the middle leg of the coupled-inductor structure in Figure 1.26(a). Figure 1.27 shows the extreme case (α=-1) by reducing the middle leg. This will reduce the leakage inductance almost to zero and Figure 1.28 shows the output voltage waveform of the coupled inductor buck converter with such an no-leakage coupled inductor. The output voltage is not regulated and the converter doesn't work!

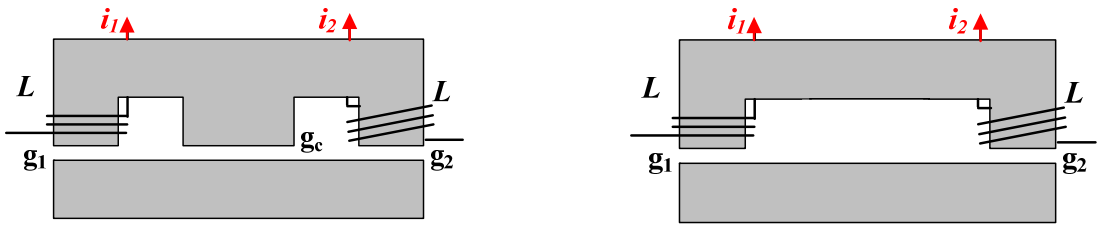

(a) (b)

Figure 1.27 The extreme case of P.Wong's two-phase coupled-inductor structure (α=-1, no leakage inductance) (a) P. Wong's coupled-inductor structure (b) P.Wong's coupled inductor structure with α=-1

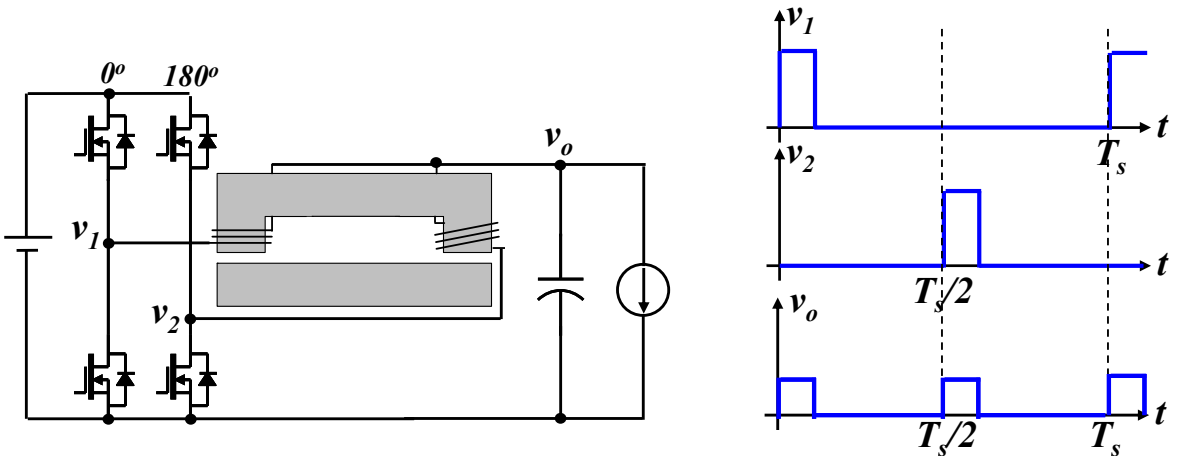

(a) (b)

Figure 1.28 The coupled inductor buck conveter with the P.Wong's no-leakage coupled-inductor (α=-1) (a) The coupled inductor buck circuit with α=-1 (b) The switching point voltage waveforms and the output voltage waveform

C. Sullivan proposed one solution to solve this issue. Figure 1.29 shows the C. Sullivan's two-phase coupled-inductor structure [39-42]. The main difference between P.Wong's two-phase coupled-inductor structure and C. Sullivan's two-phase coupled-inductor structure is that C. Sullivan's structure greatly reduces the middle leg to achieve a strong coupling. To compensate

the leakage inductance decrease due to the middle leg reduction, two wings are added to increase the leakage inductance of this structure.

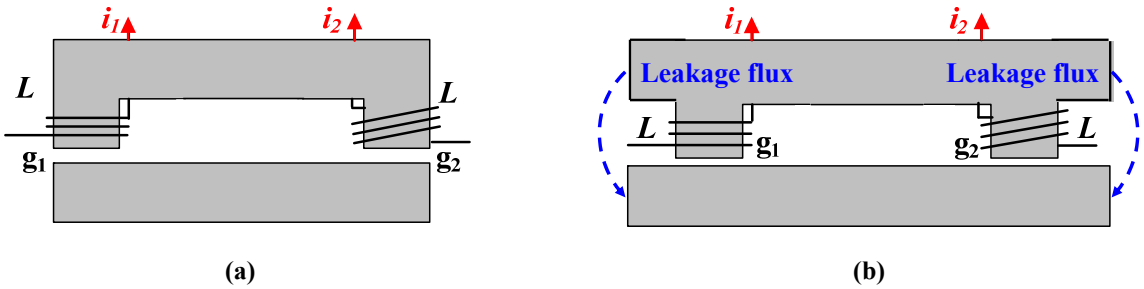

Figure 1.29 C. Sullivan's 2-phase coupled-inductor structure by providing additional leakage flux paths (a) P.Wong's coupled inductor structure in the extreme case (α=-1) (b) C. Sullivan's 2-phase coupled-inductor structure with additional leakage flux paths

Figure 1.30 shows C. Sullivan's two-phase coupled-inductor product and its detailed winding path structure [40-42]. It can be seen that the winding path of C. Sullivan's coupled-inductor is quite long, which is not good for low–voltage, high-current applications.

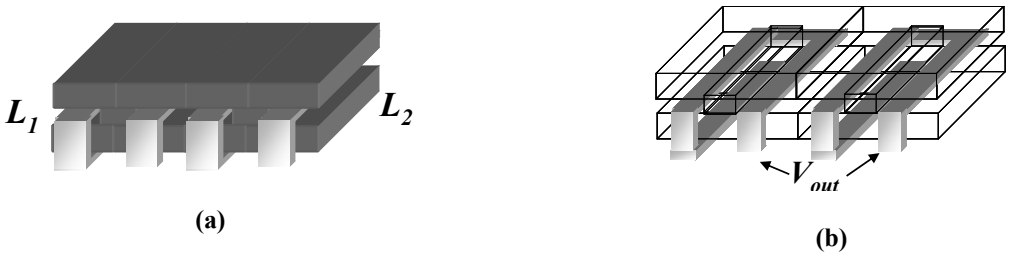

Figure 1.30 C. Sullivan's two-phase coupled-inductor product and its winding pattern. (a) C. Sullivan's two-phase coupled-inductor product (b) The winding pattern of the coupled inductor in (a)

Figure 1.31 shows C. Sullivan's three-phase coupled-inductor and its magnetic paths between Phase 1 and Phase 2, and between Phase 1 and Phase 3. It can be seen that the magnetic path between Phase 1 and Phase 2 is different from the magnetic path between Phase 1 and Phase 3. Different too are the magnetic path from Phase 1 to Phase 3 and the magnetic path from Phase 2 to Phase 3. The magnetic path differences in the three-phase coupled-inductor will result in the asymmetry of the inductor.

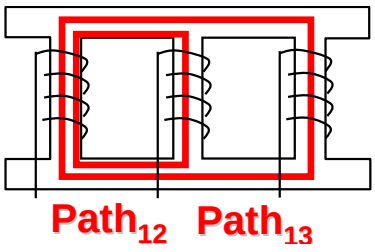

Figure 1.31 C. Sullivan's three-phase coupled-inductor structure and its asymmetric magnetic flux flow paths

For the n-phase coupled-inductor, the asymmetry means the self-inductances of different phases and mutual inductances between different phases are not always the same, i.e. $L_1 \neq L_2 \neq \cdots \neq L_n$, $M_{12} \neq M_{13} \neq \cdots \neq M_{n(n-1)}$.

Unlike the symmetric coupled inductor case (Figure 1.32), the asymmetric coupled-inductors will result in a difference in the phase-current ripples (Figure 1.33), and will also result in an increase of the output voltage ripple of the coupled-inductor buck converter (Figure 1.34). These will the burden the control and degrade the coupled-inductor buck converter's performance. Therefore, it is desirable to eliminate the asymmetry or attenuate the n-phase coupled-inductors.

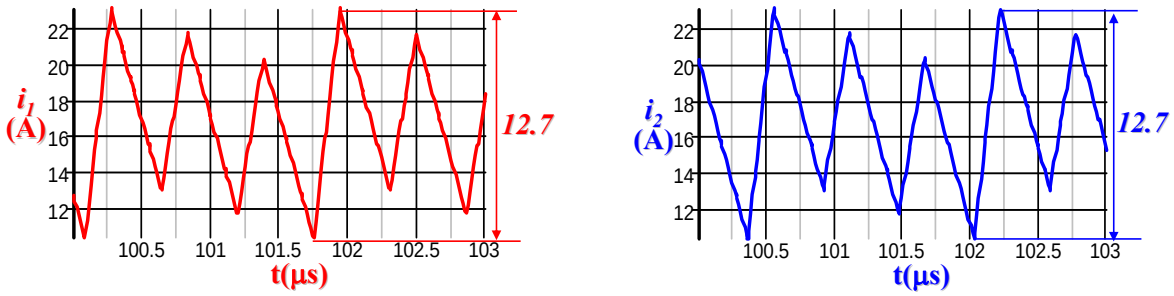

Figure 1.32 The phase-current ripples in a three-phase symmetric coupled-inductor buck converter (a) The steady-state phase 1 inductor current waveform (b) the steady-state phase 2 inductor current waveform

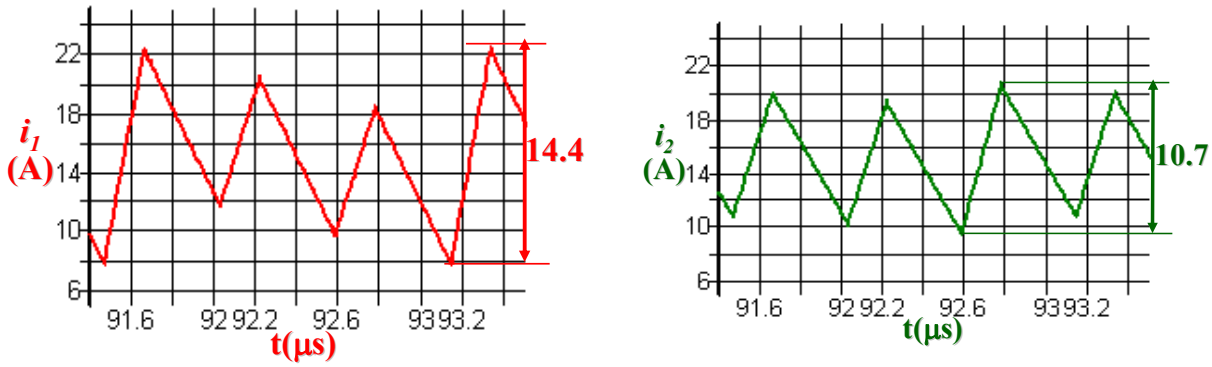

Figure 1.33 The difference of the phase-current ripples in a three-phase asymmetric coupled-inductor buck converter (a) The steady-state phase 1 inductor current waveform (b) the steady-state phase 2 inductor current waveform

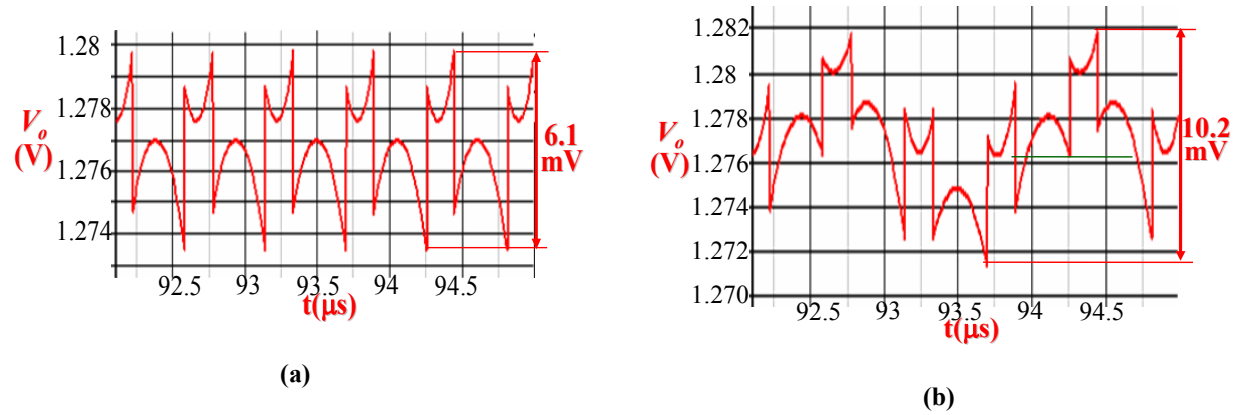

Figure 1.34 The output voltage ripples of the three-phase asymmetric coupled-inductor buck converter and the three-phase symmetric coupled-inductor buck converter (a) The three-phase symmetric coupled-inductor buck converter (b) The three-phase asymmetric coupled-inductor buck converter

A. Ledenev at Advanced Energy proposed another method to increase the leakage inductance. He added an additional discrete inductor to realize the function of the leakage inductance [43] (Figure 1.35). With the additional discrete inductor, the output voltage can be regulated at a fixed voltage and the circuit can work.

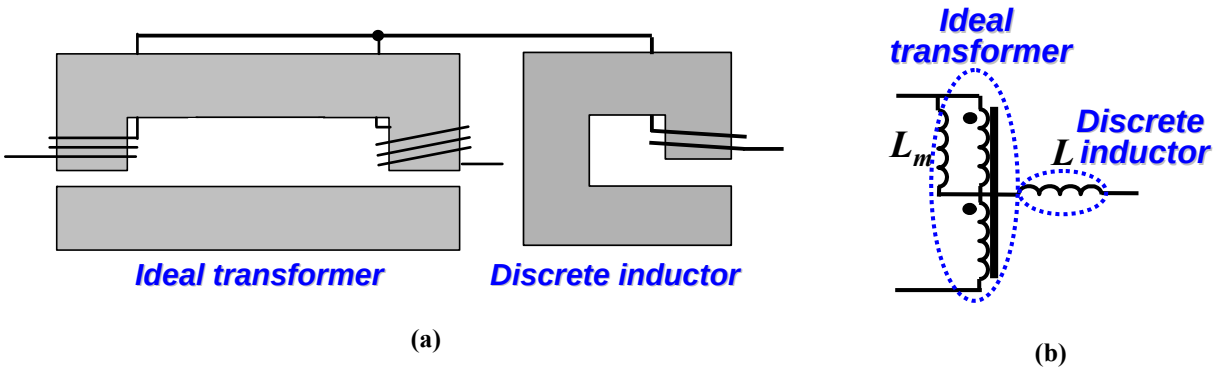

Figure 1.35 Advanced Energy's two-phase coupled-inductor structure (a) The coupled-inductor structure with an ideal transformer plus a discrete inductor (b) the circuit representation of the advanced Energy's two-phase coupled-inductor

This coupled-inductor structure is equivalent to P. Wong's and C. Sullivan's coupled-inductors (Figure 1.36) with the relationship

$$L_m = (L_s + |M|)/2 \tag{1.18}$$

$$L = (L_s - |M|)/2 \tag{1.19}$$

Therefore, Advanced Energy's coupled-inductor is exactly the same as the P. Wong's and C. Sullivan's coupled-inductors in terms of electrical performance.

Figure 1.36 Two transformation of the two types of coupled-inductors (a) Representation of Advanced Energy's two-phase coupled-inductor (b) Representation of P. Wong and C. Sullivan's two-phase coupled-inductor

Figure 1.37 shows Advanced Energy's four-phase coupled-inductor buck converter. It can be seen that in this structure, the coupled-inductor is also not symmetric. The relationship between the Phase 1 inductor and the Phase 2 inductor is different from the relationship between the Phase 1 inductor and the Phase 3 inductor.

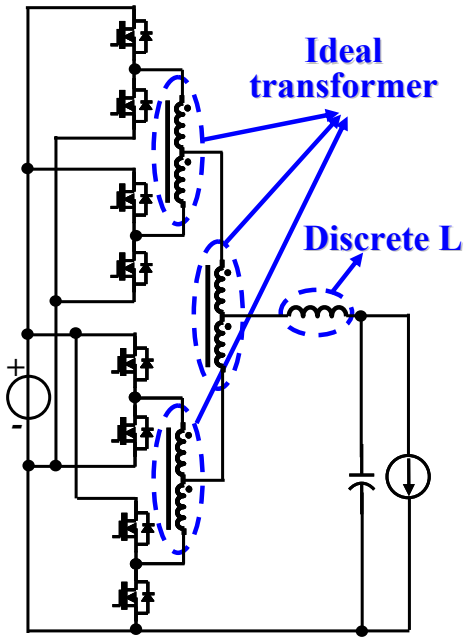

Figure 1.37 Advanced Energy's four-phase asymmetric coupled-inductor buck converter

To solve the asymmetry issue in C. Sullivan's and Advanced Energy's n-phase (n>2) coupled-inductors, many researchers have proposed several n-phase (n>2) symmetric coupled-inductor structures.

J. Cobos proposed an n-phase (n>2) symmetric coupled-inductor structure [44-45] (Figure 1.38). The basic concept is that the different phases are coupled by two-phase coupled-inductor cells, since the two-phase coupled-inductors are symmetric. Every two phases are coupled by the same two-phase coupled-inductor cell to build an n-phase symmetric coupled-inductor. Since the topology of this structure, shown in Figure 1.38, looks like a full matrix, this symmetric coupled-inductor structure is also called the full matrix symmetric coupled-inductor structure. The drawback of this symmetric coupled-inductor is that there are many separate magnetic components, and the magnetic component number increases rapidly when the phase number increases (C_n^2). Moreover, the winding path of each phase inductor is quite long, since each phase inductor needs to go through n-1 coupled-inductor cells.

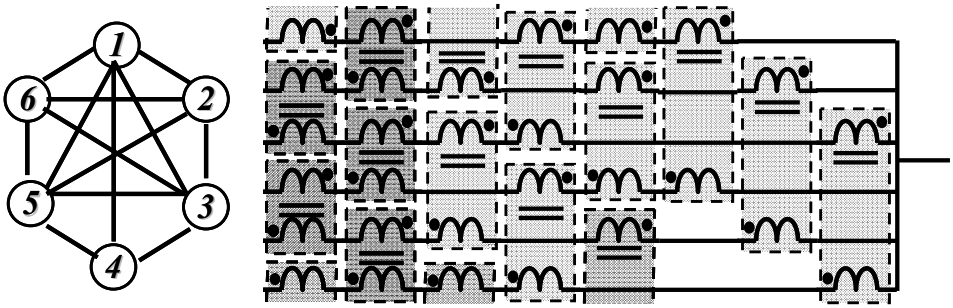

Figure 1.38 J. Cobos' n-phase full-matrix symmetric coupled-inductor structure by coupling any two phases with an identical two-phase coupled-inductor:

Besides J. Cobos, J. Zhou proposed another set of symmetric coupled-inductor structures. Figure 1.39 shows the three-phase coupled-inductor structure and the four-phase coupled-inductor structure. Figure 1.40 summarizes this set of symmetric coupled-inductor structures and illustrates the generic symmetric coupled-inductor topology.generic topology of this type of single-magnetic n-phase symmetric coupled-inductors. The concept is that all the magnetic paths, which are wrapped with the phase-currents need to be connected to two common points and the magnetic paths are evenly distributed around the two common points. The dotted line in Figure 1.40 represents the leakage flux path of the coupled-inductor. The drawback of this type of symmetric coupled-inductors is that the magnetic core is too complex and costly to be used in industry.

(a) **(b)**

Figure 1.39 The symmetric three-phase and four-phase coupled-inductor structures (a) The three-phase coupled-inductor structure (b) The four-phase coupled-inductor structure

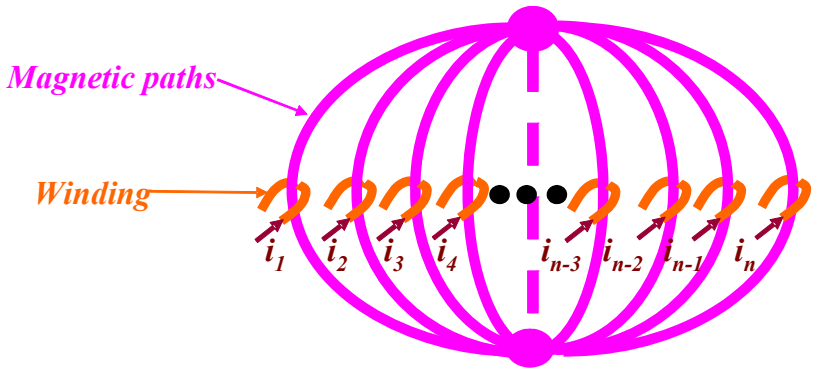

Figure 1.40 The generalized n-phase symmetric coupled-inductor structure (the solid magnetic line: the main magnetic paths; the dotted magnetic line: the leakage magnetic flux path)

M. Xu [46] and W. Chen [47] each proposed an n-phase (n>2) symmetric coupled-inductor structure (Figure 1.41). In this structure, a secondary winding is introduced to couple the different phase inductors. The secondary windings of different phase inductors are connected in series to form a loop. The advantage of this structure is that it is very flexible, though it also has drawbacks. There are many magnetic components, which is not desired, and the secondary windings increase the complexity of the inductors.

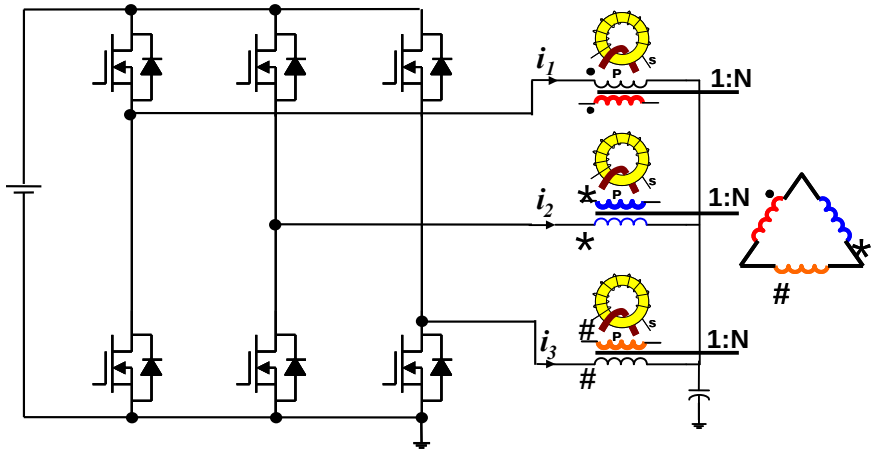

Figure 1.41 M. Xu's and W. Chen's n-phase symmetric coupled-inductor buck converter (the secondary sides of each transformer are in series to form a loop)

In [36], P.Wong analyzed the two-phase coupled-inductor buck converter, but he didn't analyze the n-phase (n>2) phase buck converter. After P. Wong published his work, C. Sullivan continued to investigate this area. He did the analysis of n-phase (n>2) coupled-inductor buck converter when the converter duty cycle D is less than 1/n [41].

Figure 1.42 shows the n-phase symmetric inverse coupled-inductor buck converter when the duty cycle D<1/n. The V_{x0}, V_{x1},…, $V_{x(n-1)}$ are the switching point voltages; L_M is the equivalent total magnetizing inductance; L_l is the leakage inductance; and V_o is the output voltage of the converter. Figure 1.43 shows the voltage and current waveforms of the n-phase coupled-inductor buck converter when D<1/n.

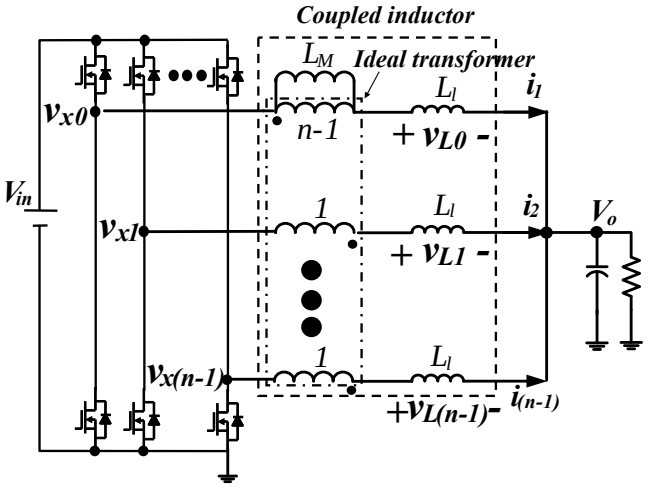

Figure 1.42 The representation of the n-phase symmetric coupled-inductor buck converter

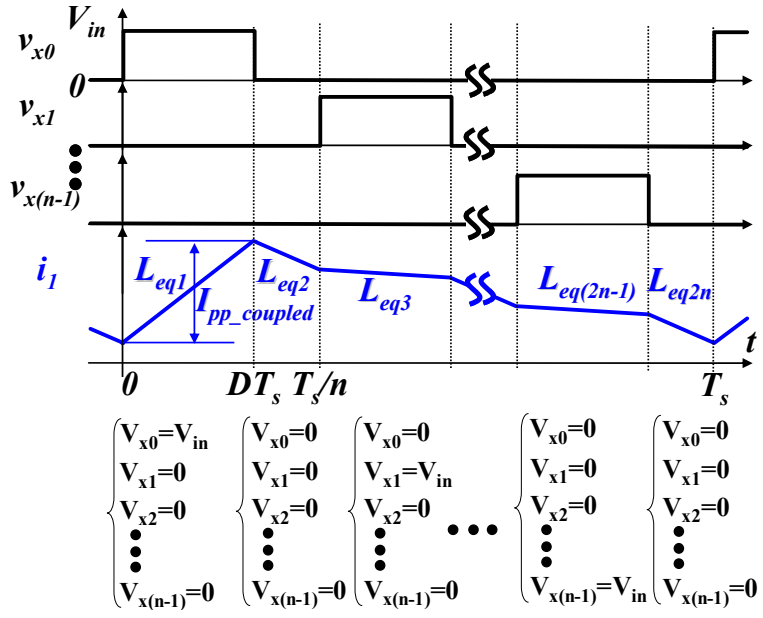

Figure 1.43 The voltage and current waveforms of the n-phase coupled-inductor buck converter (D<1/n)

The electrical equations of n-phase inverse coupled-inductors when D<1/n, are

$$\begin{cases} v_{x0} = L_M \cdot \dfrac{d(i_1 - i_2)}{dt} + L_l \cdot \dfrac{di_1}{dt} + V_o \\ v_{x1} = -\dfrac{1}{n-1} L_M \cdot \dfrac{d(i_1 - i_2)}{dt} + L_l \cdot \dfrac{di_2}{dt} + V_o \\ \cdots \\ v_{x(n-1)} = -\dfrac{1}{n-1} L_M \cdot \dfrac{d(i_1 - i_2)}{dt} + L_l \cdot \dfrac{di_{(n-1)}}{dt} + V_o \end{cases} \tag{1.20}$$

After derivation, C. Sullivan found that the relationship between the steady-state inductor peak-to-peak currents of n-phase non-coupled and n-phase coupled-inductors with the same leakage inductances is

$$\frac{I_{pp\_coupled}}{I_{pp\_non-coupled}} = \frac{\dfrac{n-1+\rho}{n-1+n\rho} - D}{1-D} \quad (D < 1/n) \tag{1.21}$$

where ρ is the ratio of the magnetizing inductance to leakage inductance L_M/L_l, and T_s is the switching period of the converter. If the coupling coefficient α is defined as

$$\alpha = \frac{(n-1)M}{L} \tag{1.22}$$

where M is the mutual inductance between any two phase inductors, and L is the self inductance of any phase inductor, then the equation (1.21) can be rewritten as

$$\frac{I_{pp\_coupled}}{I_{pp\_non-coupled}} = \frac{L_{tr}}{L_{ss}} = \frac{1 + [\dfrac{n-2}{n-1} + \dfrac{D}{D'}] \cdot \alpha}{1 - \dfrac{\alpha}{n-1}} \quad (D < 1/n) \tag{1.23}$$

The current ripple reductions by the coupled-inductors are functions of the steady-state duty cycle D and the coupling coefficient α and the phase number n. The relationship shown in the equation (1.23) is plotted in Figure 1.44, where D=0.1. It can be seen from Figure 1.44 that the larger phase number n (n<1/D) results in more effective current ripple reduction, and the stronger coupling effect gives smaller current ripples. Comparing Figure 1.25 and Figure 1.44, it can also be seen that there are two choices for improving the effect of the two-phase current ripple reduction: either make the duty cycle nearer to 0.5, or increase the number of coupling phases.

The conclusion of C. Sullivan's study is that in order to have the same transient responses and to achieve smaller steady-state current ripples, more phase inductors should be coupled while maintaining the same L_{eq2} (L_{tr}).

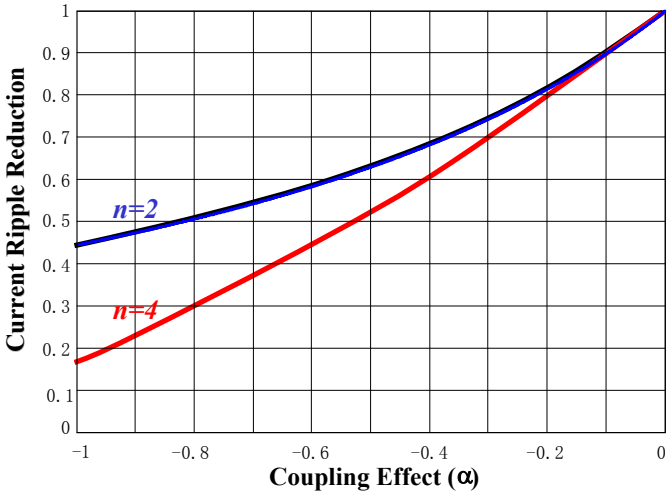

Figure 1.44 The steady-state phase-current ripple reduction in n-phase symmetric coupled-inductor buck converters (D<1/n, D=0.1)

Although many researchers have done a lot of investigation of multiphase coupled-inductor buck converters [35-49], there are still many topics about multiphase coupled-inductor buck converters to be investigated.

1.3. Challenges in Multiphase Coupled-inductor Buck Converters

The multiphase coupled-inductor buck converter has shown many benefits compared to the multiphase non-coupled-inductor buck, but there are still many challenges unsolved in this area.

1) Extending the analysis of multiphase coupled-inductor buck converters to the n-phase, D>1/n cases

P. Wong analyzed the two-phase coupled-inductor buck converter for the whole duty cycle range. C. Sullivan extended P. Wong's analysis and analyzed the n-phase (n>2) symmetric coupled-inductor buck converter when the duty cycle D is less than 1/n. However, the n-phase

(n>2) coupled-inductor buck when the duty cycle D is larger than 1/n, is never analyzed and its performance is never clear. This challenge needs to be addressed.

Furthermore, both P. Wong's and C. Sullivan's analyses assume that the multiphase coupled-inductors are symmetric. However this is not always true in reality as shown prevously. How to analyze the asymmetric multiphase coupled-inductor buck converter and what's the effect of asymmetric coupled-inductors on the multiphase coupled-inductor buck converter are two additional issues to be addressed before multiphase coupled-inductor buck converters can be widely used.

2) Searching for alternative coupled-inductor structures to reduce the winding path

Figure 1.45 shows the commercial non-coupled-inductors and coupled-inductors. Their winding paths are also shown in detail. The LS represents the low-side switch and the HS represents the high-side switch. It can clearly be seen that the existing coupled-inductors have quite a long winding path compared to that of the non-coupled-inductors, around 3 times longer. This is not good for the low-voltage high-current applications, such as the microprocessor VR and the graphic card VR. This is because the winding loss is dominant in the inductor total loss in these applications and the long winding path means the large inductor winding loss and total loss.

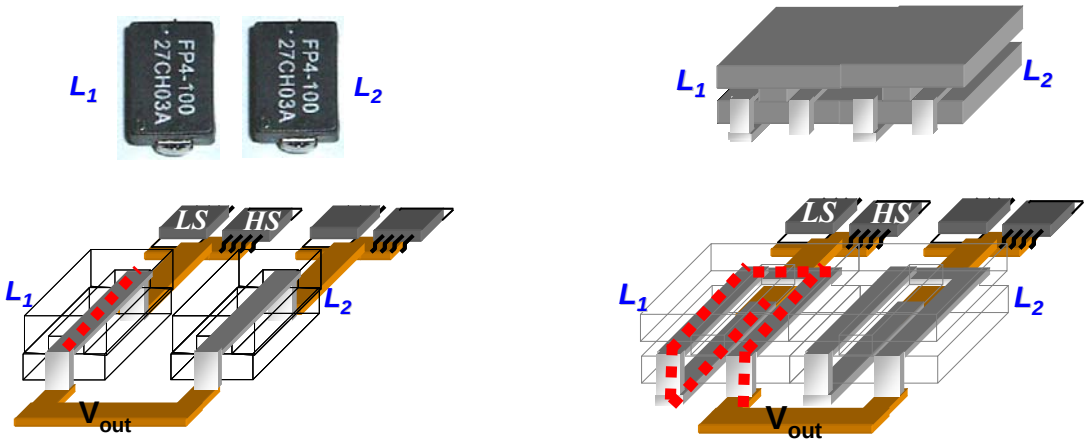

Figure 1.45 The winding path comparison between the commercial non-coupled-inductors and coupled-inductors (a) The commercial non-coupled-inductors and their winding paths (picture by author, 2005) (b) The commercial coupled-inductors and their winding paths

To address this issue, the alternative coupled-inductor structures with the short winding paths need to be investigated.

3) Searching for a better coupled inductor structure based on the LTCC integration process to reduce the inductor size

Today the converter is more and more integrated to improve its power density. The LTCC (Low Temperature Co-fire Ceramic) process is a low-cost, promising integration process for the future integrated converters. The large inductor size is the bottleneck for the high power density of today's LTCC integrated power converter. Coupled-inductor is a possible solution to reduce the inductor size and improving the power density of the multiphase integrated buck converter. Searching for a better LTCC coupled-inductor structure to reduce the inductor size and improve the power density of the multiphase coupled-inductor buck converter is another challenge.

4) Evaluating the benefits of coupling in the n-phase coupled-inductor buck converters

Multiphase coupled inductor buck has been claimed to have benefits in both increasing the converter efficiency and improving the converter transient response. However, how much benefits can multiphase coupled inductor bucks achieve in the real applications in terms of increased efficiency percentage, and the output capacitor reduction in size and cost are never clear. They should be addressed based on a real commercial multiphase interleaving buck converter, e.g. the 6-phase interleaving buck converter in Figure 1.46 for the CPU VR application.

Figure 1.46 The commercial 6-phase non-coupled-inductor buck converter for the CPU VR application (picture by author, 2006)

Moreover, in a multiphase interleaving buck converter, there are normally several coupled inductor combinations. For example, in a six-phase interleaving buck converter, 3* 2-phase coupled inductors, 2*3-phase coupled inductors and 1*6-phase coupled inductor can be used to replace the original 6 non-coupled inductors. Which combination can achieve the best benefits in practice is unclear and addressing this is a challenge.

5) Novel current sensing techniques for the multiphase coupled inductor buck converters

Current sensing is mandatory in almost every DC-DC converters for the current protection, the current sharing and control for current mode converters. However, the current sensing has never been investigated in detail in multiphase coupled inductor buck converters

Figure 1.47 shows the most popular current sensing method, the DCR current sensing method, in today's multiphase interleaving non-coupled inductor buck converters. When the sensing network time constant satisfy

$$R_{cs}C_{cs} = L_{self} / DCR \tag{1.24}$$

the sensing signal v_{cs} is proportional to the inductor current i_L (Figure 1.48)

$$v_{cs} = DCR \cdot i_L \tag{1.25}$$

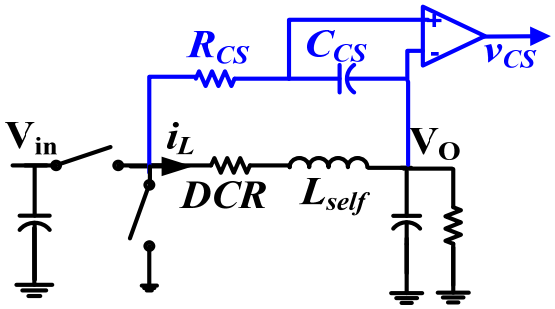

Figure 1.47 The conventional DCR current sensing network in a simple buck converter

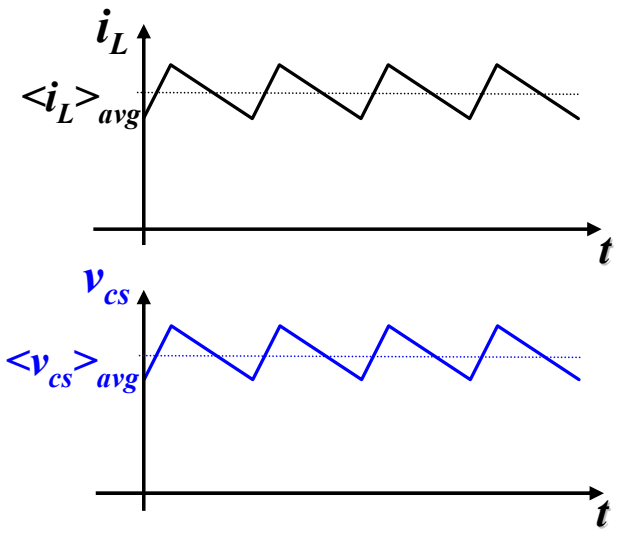

Figure 1.48 The inductor current i_L and the current sensing signal v_{cs} waveforms in a simple buck converter with the conventional DCR current sensing method

However, it is found that the DCR current sensing method doesn't work in the multiphase coupled inductor buck converter. Figure 1.49 shows the conventional DCR current sensing method in the 2-phase coupled inductor buck. Figure 1.50 shows the phase current and the sensing signal waveforms. In Figure 1.50, i_1 is the inductor current of the phase 1, v_{cs1} is the sensed signal of the phase 1 from the DCR current sensing network. It can be seen that even the shape of the phase current sensing signal and the shape of the real phase current are different.

Inventing a novel DCR current sensing method for multiphase coupled inductor bucks is a challenge.

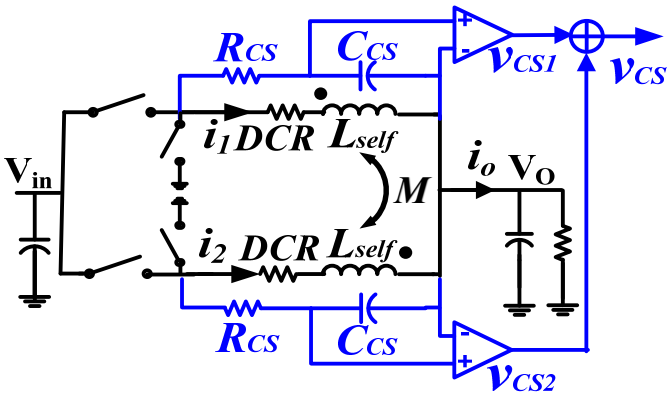

Figure 1.49 The direct use of the conventional DCR current sensing method to the multiphase coupled inductor buck converter

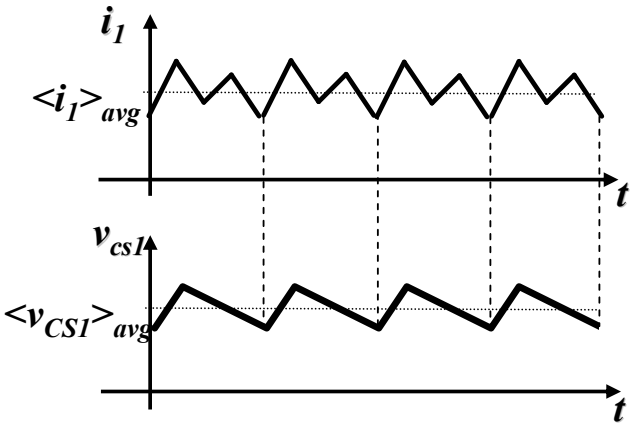

Figure 1.50 The inductor phase current waveform and the phase current sensing signal waveform of the conventional DCR current sensing method in the multiphase coupled inductor buck converter

6) Improving the light load efficiency of the multiphase coupled inductor buck converters

All the previous research focused on the Continuous Current Mode (CCM) of multiphase coupled inductor bucks in the heavy load condition. The Discontinuous Current Mode (DCM) of multiphase coupled inductor bucks has never been investigated.

However, DCM is used in the light load condition for some multiphase non-coupled inductor bucks. In these converters, the switching frequency is decreased to improve the efficiency in the light load. The constant-on time control method is a well-known and very popular control method to reduce the switching frequency in the light load in the multiphase non-coupled buck industry. Figure 1.51 shows the phase current waveforms for a multiphase non-coupled inductor buck (Figure 1.19 (a)) with the constant-on time control in the light load. In the heavy load, the circuit works in the CCM (Continuous Current Mode) and the switching frequency is fixed because of the fixed duty cycle D. In the light load, the circuit works in the DCM (Discontinuous Current Mode) and the switching frequency is decreased to increase the converter efficiency.

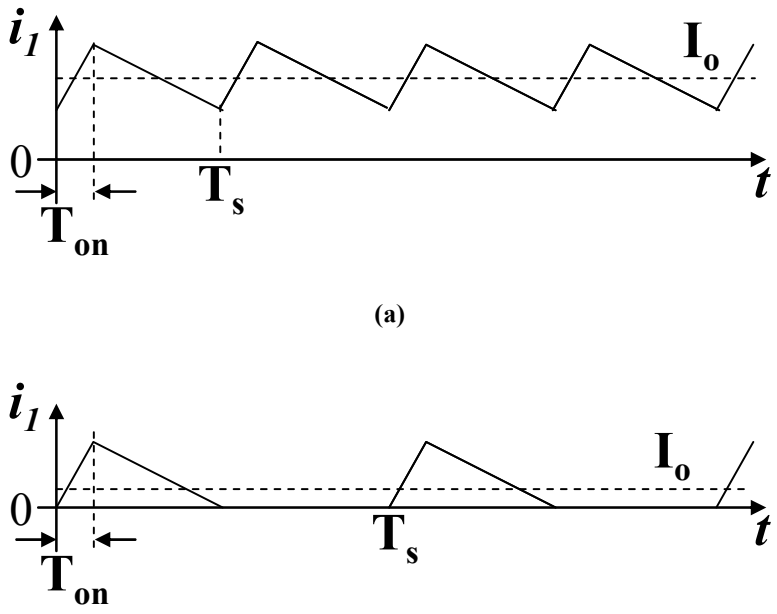

Figure 1.51 The inductor phase current waveforms under different load conditions of a multiphase non-coupled inductor buck with the constant-on time control to improve the light load efficiency (a) under the heavy load condition (CCM) (b) under the light load condition (DCM)

If the constant-on time control method is directly used in the multiphase coupled inductor buck, to improve the efficiency in the light load, there is an issue. Figure 1.52 shows the efficiency of the multiphase coupled inductor buck with the constant-on time control, based on a commercial multiphase interleaving buck converter for the CPU VR application. In Figure 1.52, the efficiency of the multiphase non-coupled inductor buck with the constant-on time control is

also shown. The assumption here is that both the 2-phase non-coupled inductor buck and the 2-phase coupled inductor buck have the same steady state inductance in the CCM mode. It can be seen that the multiphase coupled inductor buck has a much lower efficiency in the light load than the multiphase non-coupled inductor buck. The DCM analysis of the multiphase coupled inductor buck and how to improve the light load efficiency of the multiphase coupled inductor buck in DCM is another challenge.

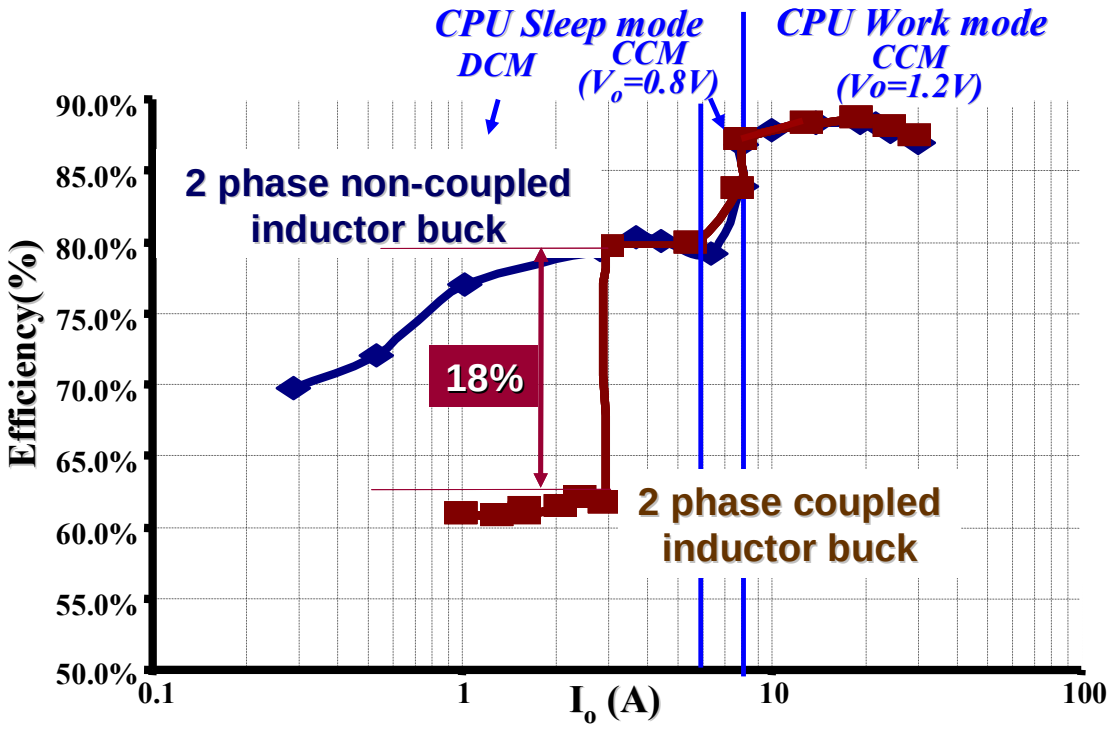

Figure 1.52 The efficiency comparison of the multiphase non-coupled-inductor and coupled-inductor buck converters under the light load condition based on the Max1545 multiphase VR demo board (V_{in}=12V, T_{on}=330ns, L=L_{ss}=600nH)

All the above challenges in the multiphase coupled-inductor buck converters are investigated in this dissertation.

1.4. Dissertation Outline

In this dissertation, Chapter 1 gives an introduction of the research background. The multiphase coupled-inductor buck converter is introduced and the prior research work in this

area is illustrated. The remaining challenges in this area are then highlighted, and the research goal is determined: to investigate the solutions for the outlined challenges.

In Chapter 2, the comprehensive analysis of multiphase coupled-inductor buck converters in CCM (Continuous Current Mode) is developed. P. Wong developed the two-phase coupled-inductor buck converter analysis, and C. Sullivan developed the n-phase coupled-inductor buck converter analysis when the duty cycle D is less than 1/n. The n-phase coupled-inductor buck converter analysis for the whole duty cycle range will be investigated in this section. Moreover, of the prior work done in this area, only the symmetric coupled-inductor buck converter has been analyzed. In this section, the asymmetric coupled-inductor buck converter will be analyzed as well.

In Chapter 3, alternative coupled-inductor structures intended to minimize the inductor loss are investigated. For the existing coupled-inductor structures, the inductor winding path is long. Therefore, the inductor winding loss is high, which is bad for low-voltage, high-current applications. To solve this issue, one twisted-core coupled-inductor is proposed. Although the twisted-core coupled-inductor can reduce the inductor winding loss, it increases the inductor core loss, and the inductor total loss is not minimized. To minimize the inductor total loss, the low profile twisted-core coupled-inductor is proposed. In the low profile twisted-core coupled-inductor, a trade-off is made between the winding loss and the core loss to achieve an even smaller total loss for the inductor.

The modeling and design of coupled-inductor structures are also investigated in this section. For the complex inductor structures, such as the twisted-core coupled-inductors, the 3D fringing flux effects are so strong that a simple model that doesn't consider the 3D fringing flux effects is very imprecise. C. Sullivan modeled the 3D fringing effect for the simple E-E core. By applying and extending C. Sullivan's space-cutting method, the 3D fringing fluxes in twisted-core coupled-inductors are modeled, and the reluctance model of the twisted-core coupled-inductor is built. The reluctance model is very accurate. Based on the reluctance model, the design of the twisted-core coupled-inductors is shown in detail. Additionally, the reluctance model built for twisted-core coupled-inductors can be modified to be used for low profile twisted-core coupled-inductors, thereby facilitating the design of the low profile twisted-core coupled-inductors. The

space-cutting method developed in the modeling of the twisted-core coupled-inductor can also be extended to other complex inductor structures with strong 3D fringing flux effects.

Nowadays, the POL converters are more and more integrated for the higher power density. In Chapter 4, two integrated coupled-inductor structures based on the low temperature co-fire ceramic (LTCC) process are proposed to further improve the converter power density. The inductor characteristics of these two integrated LTCC coupled-inductor structures are analyzed, and reluctance models based on the analyses are built and verified by 3D FEA simulation results. Based on the reluctance models, simple design methods are developed. The designed integrated LTCC coupled-inductors are customized and tested to verify the design processes. A better LTCC coupled-inductor structure with a smaller footprint is implemented with the active stage to build the high-power-density coupled-inductor integrated POL converter. It is found that the integrated LTCC coupled-inductor POL converter doubles the power density compared to the integrated non-coupled-inductor POL converter. The amazing power density 500W/in^3 is achieved.

In Chapter 5, the benefits of multiphase coupled-inductor buck converters are evaluated based on a commercial multiphase interleaving buck converter. In the multiphase buck converter, there are six phases. Therefore, there are several coupled-inductor setups. There are the three two-phase coupled-inductor setup, the two three-phase coupled-inductor setup, and the one six-phase coupled-inductor setup. The performances of the coupled-inductor buck converters with different coupled-inductor setup s are investigated systematically.

In Chapter 6, novel DCR current sensing methods for coupled-inductor buck converters are investigated. The conventional DCR current-sensing method is a very popular current-sensing method for multiphase buck converters. However, the conventional DCR current-sensing method doesn't work for the multiphase coupled-inductor buck converter. Novel DCR current sensing methods are proposed to solve this issue.

In Chapter 7 the discontinuous current mode (DCM) of multiphase coupled-inductor buck converters under light-load conditions is investigated. Although the prior research shows that the multiphase coupled-inductor buck converter has a lot of benefits from the CCM, it is found in this dissertation for the first time that the multiphase coupled-inductor buck converter with a DCM has a lower efficiency under a light-load. The DCM operation of the multiphase coupled-

inductor buck converter is investigated in detail to identify the reason for the low light-load efficiency. The reason for this is found to be the fact that the inductor phase-current reaches zero twice in a specific DCM mode of the multiphase coupled-inductor buck converter. With the understanding of the reason, the solution of the low light-load efficiency issue of the multiphase coupled-inductor buck converter is proposed. Experiments are implemented, and the results verify the proposed solution..

Chapter 8 provides a summary of the dissertation and the possible future research topic.

Chapter 2. Comprehensive Analysis of N-phase Coupled-inductor Buck Converters

Figure 2.1 shows the n-phase coupled-inductor buck converter. In Figure 2.1, $M_{ij}<0$, j>i, i=1…, n-1, j=2…, n. When the M_{ij} are the same, the n-phase coupled-inductor buck converter is symmetric. When the M_{ij} are not the same, the n-phase coupled-inductor buck converter is asymmetric.

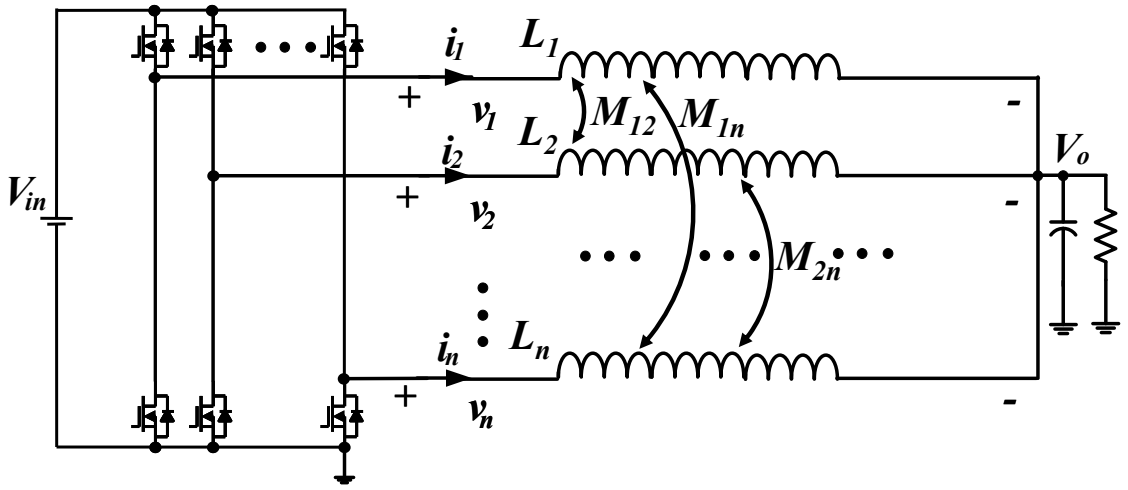

Figure 2.1 The circuit representation of the n-phase coupled-inductor buck converter

In [36], P. Wong analyzed the two-phase symmetric coupled-inductor buck converter. C. Sullivan analyzed the n-phase (n>2) symmetric coupled-inductor buck converter when the duty cycle D is less than 1/n [41]. Figure 2.2 shows the curve of L_{tr}/L_{ss} vs. the duty cycle D when the coupling coefficient α=-0.8, based on their analysis results. It can be seen that the performance of the n-phase (n>2) symmetric coupled-inductor buck converter with D>1/n is still unclear.

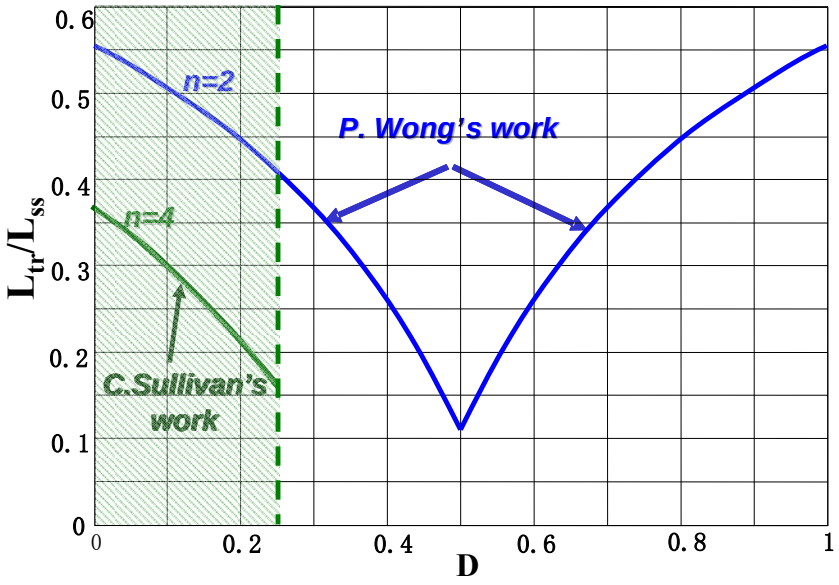

Figure 2.2 The incomplete curve of L_{tr}/L_{ss} vs. the duty cycle D of the symmetric coupled-inductor buck converter (α=-0.8)

The performance of the above multiphase coupled-inductor buck converter is needed if the phase inductors are coupled to improve the multiphase buck converter performance in the wide duty range applications (Table 2.1)[29-30]. Figure 2.3 shows one wide input multiphase buck POL converter from Texas Instrument. In these applications, the duty cycle D is quite wide. Therefore, the previous P. Wong's and C Sullivan's analyses are not valid any more. The quantitative analysis of the n-phase symmetric coupled-inductor buck converter with the whole duty cycle range needs investigating.

Table 2.1 Wide duty cycle range multiphase buck converters

Application	V_{in}(V)	V_o(V)	Duty cycle D
DDR memory POL	10.2-13.2	0.6-3.5	0.05-0.34
Wide-input POL	8-14	0.8-3.6	0.06-0.45

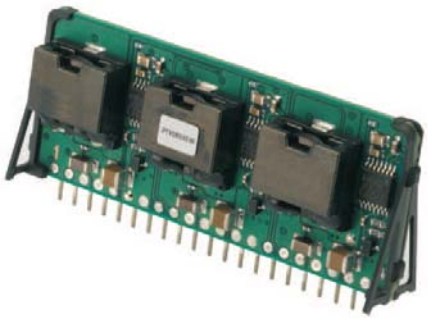

Figure 2.3 The wide-input three-phase buck POL converter with a large duty cycle range (PTV08T250W).
Used with permission of Texas Instrument company, 2009

In this section, the generalized analysis of the n-phase coupled-inductor buck converter with the duty cycle D>1/n is illustrated. Some special characteristics of the n-phase coupled-inductor buck converter during large duty-cycle conditions are shown. After that, the asymmetric effects of multiphase coupled-inductor buck converters are analyzed quantitatively.

2.1. Generalized Analysis of N-phase Coupled-inductor Buck Converters

In this section, the three-phase coupled-inductor buck converter with the duty cycle D>1/3 is analyzed first. Then, the analysis is extended to the N-phase, whole duty cycle range coupled-inductor buck converter.

2.1.1. Generalized Analysis of Three-phase Coupled-inductor Buck Converters

Figure 2.4 shows the three-phase coupled-inductor buck converter. The converter needs further analysis when the duty cycle D>1/3. The analyses for 1/3≤D<2/3 and 2/3≤D<1 according to the phase inductor current waveform difference are discussed in the following sections.

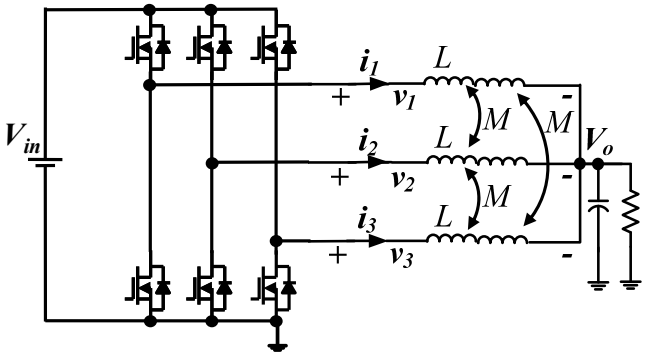

Figure 2.4 The circuit represenstation of a three-phase symmetric coupled-inductor buck converter

The basic electrical equations for the three-phase coupled-inductor in Figure 2.4 are

$$\begin{cases} v_1 = L\cdot\dot{i}_1 + M\cdot\dot{i}_2 + M\cdot\dot{i}_3 \\ v_2 = M\cdot\dot{i}_1 + L\cdot\dot{i}_2 + M\cdot\dot{i}_3 \\ v_3 = M\cdot\dot{i}_1 + M\cdot\dot{i}_2 + L\cdot\dot{i}_3 \end{cases} \tag{2.1}$$

where L is the self-inductance for each phase and M is the mutual inductance between any two phase inductors. M<0 for the inverse coupling.

The steady-state inductor voltage waveforms v_1, v_2, v_3 and inductor current waveform i_1 when 1/3≤D<2/3 are shown in Figure 2.5. There are six switching intervals during one switching cycle. Due to the different inductor voltage combinations in these six intervals, the inductances equivalent to those in the non-coupled-inductor case are different for the six intervals: L_{eq1}-L_{eq6}.

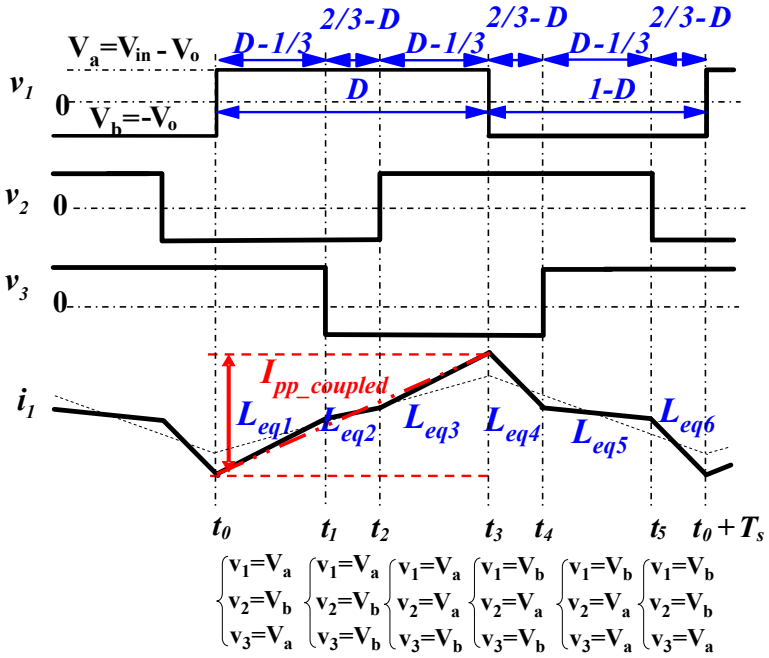

Figure 2.5 Steady-state inductor voltage and current waveforms for the three-phase coupled-inductor buck converter with 1/3≤D<2/3 (V_a=V_{in}-V_o, V_b=-V_o)

For the first time interval (t_0-t_1), the inductor voltage combination is

$$v_1 = V_{in} - V_o, v_2 = -V_o, v_3 = V_{in} - V_o \tag{2.2}$$

Substituting the equation (2.2) into the equation (2.1) and rearranging the terms, it can be derived that

$$v_1 = \frac{(L-M)(L+2M)}{L+\frac{D}{D'}\cdot M}\cdot\frac{di_1}{dt} \tag{2.3}$$

where D'=1-D. Therefore, the equivalent inductance for the first interval is

$$L_{eq1} = \frac{(L-M)(L+2M)}{L+\frac{D}{D'}\cdot M} \tag{2.4}$$

According to the different inductor voltage combinations shown in Figure 2.5, the equivalent inductances for the other five intervals can be derived similarly.

$$L_{eq2} = \frac{(L-M)(L+2M)}{L+(1+\frac{2D}{D'})\cdot M} \tag{2.5}$$

$$L_{eq3} = L_{eq1} = \frac{(L-M)(L+2M)}{L+\frac{D}{D'}\cdot M} \tag{2.6}$$

$$L_{eq4} = \frac{(L-M)(L+2M)}{L+\frac{D'}{D}\cdot M} \tag{2.7}$$

$$L_{eq5} = \frac{(L-M)(L+2M)}{L+(1+\frac{2D'}{D})\cdot M} \tag{2.8}$$

$$L_{eq6} = L_{eq4} = \frac{(L-M)(L+2M)}{L+\frac{D'}{D}\cdot M} \tag{2.9}$$

There are four different equivalent inductances: L_{eq1}, L_{eq2}, L_{eq4} and L_{eq5}.

From Figure 2.5, it can be seen that the peak-to-peak current ripple I_{pp_cp} is not determined by one of the four equivalent inductances, like the previous cases studied by P. Wong and C. Sullivan. The current ripple, I_{pp_cp}, is determined by the combination of two equivalent inductances: L_{eq1} and L_{eq2}. Since the steady-state inductance is determined by the total current ripple I_{pp_cp}, it can be defined as the inductance equivalent to that in the non-coupled-inductor buck converter, which results in the average current slope shown as the dotted line in Figure 2.5. Therefore, the steady-state inductance is

$$L_{ss} = \frac{1}{\frac{1}{L_{eq1}} \cdot \frac{2(D-1/3)}{D} + \frac{1}{L_{eq2}} \cdot \frac{2/3-D}{D}} = \frac{(L-M)(L+2M)}{L+(\frac{2}{3DD'}-1)M} \tag{2.10}$$

Figure 2.6 shows the transient inductor voltage and current waveforms for the three-phase coupled-inductor buck converter with 1/3≤D<2/3. The transient equivalent inductance is the equivalent inductance which determines the inductor current change Δi in one switching cycle when there is a duty cycle perturbation ΔD in the transient. Therefore, it is defined as

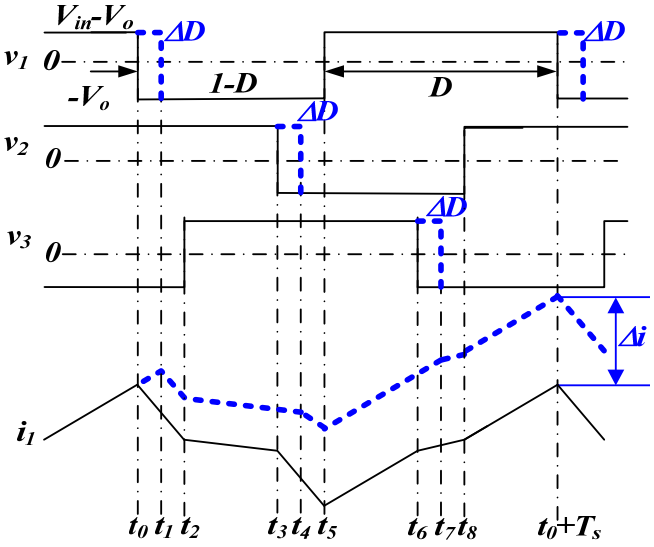

Figure 2.6 Transient inductor voltage and current waveforms for the three-phase coupled-inductor buck converter with 1/3≤D<2/3 under the duty cycle perturbation

$$(\frac{di_1}{dt})_{cp} = \frac{\Delta i}{T_s} \triangleq \frac{V_{in} \cdot \Delta D}{L_{tr}} \tag{2.11}$$

since

$$\Delta i = (L_{eq1} - L_{eq4})\Delta D \cdot T_s + (L_{eq5} - L_{eq4})\Delta D \cdot T_s + (L_{eq1} - L_{eq2})\Delta D \cdot T_s \tag{2.12}$$

Substituting the equation (2.12) into the equation (2.11), it can be derived that

$$L_{tr} = L + 2M \tag{2.13}$$

The steady-state inductor voltage waveforms v_1, v_2, v_3 and inductor current waveform i_1 when $2/3 \le D < 1$ are shown in Figure 2.7. There are six equivalent inductances: L_{eq1}-L_{eq6}. These inductances are different from those in the $1/3 \le D < 2/3$ case.

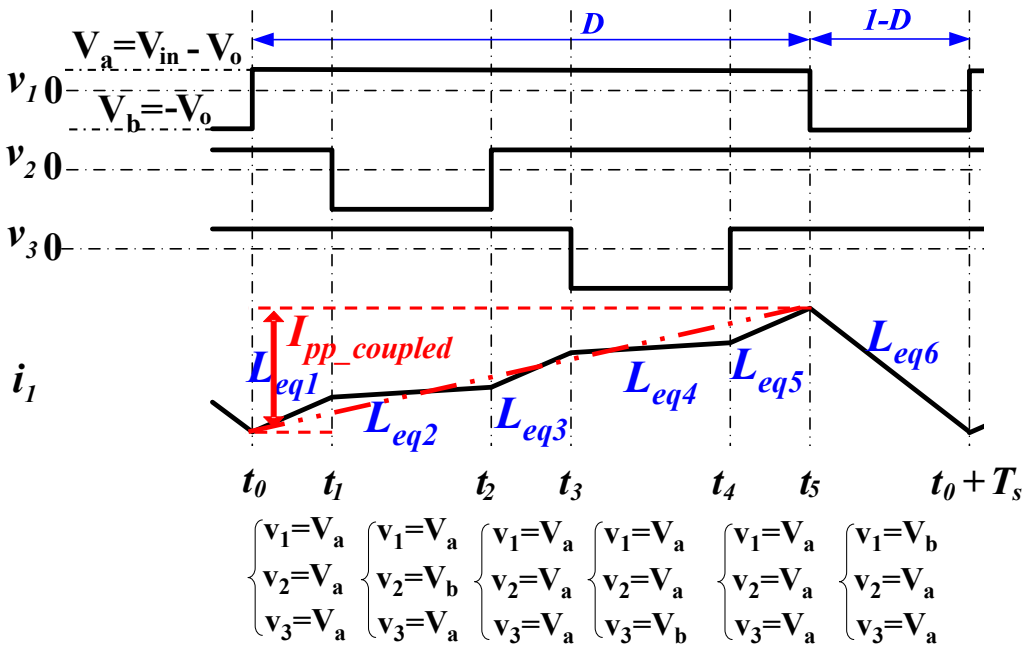

Figure 2.7 Steady-state inductor voltage and current waveforms for the three-phase coupled-inductor buck converter with $2/3 \le D < 1$ ($V_a=V_{in}-V_o$, $V_b=-V_o$)

Substituting the according inductor voltage combination into the equation (2.1), we can derive that

$$L_{eq1} = L_{eq3} = L_{eq5} = L + 2M \tag{2.14}$$

$$L_{eq2} = L_{eq4} = \frac{(L-M)(L+2M)}{L + \frac{D}{D'} \cdot M} \tag{2.15}$$

$$L_{eq6} = \frac{(L-M)(L+2M)}{L + (1 + \frac{2D'}{D}) \cdot M} \tag{2.16}$$

Since the phase-current ripple $I_{pp\_coupled}$ is determined by L_{eq6}, the steady-state inductance is

$$L_{ss} = L_{eq6} = \frac{(L-M)(L+2M)}{L+(1+\frac{2D'}{D})\cdot M} \tag{2.17}$$

In fact, the 2/3≤D<1 case is a duplicate of the 0≤D<1/3 case. If the D and D' are exchanged in the equation (2.17), the equation changes to the steady-state inductance equation for the 0≤D<1/3 case.

Figure 2.8 shows the transient inductor voltage and current waveforms for the three-phase coupled-inductor buck converter with 2/3≤D<1. Therefore,

$$\Delta i = (L_{eq1} - L_{eq6})\Delta D \cdot T_s + (L_{eq1} - L_{eq2})\Delta D \cdot T_s + (L_{eq1} - L_{eq2})\Delta D \cdot T_s \tag{2.18}$$

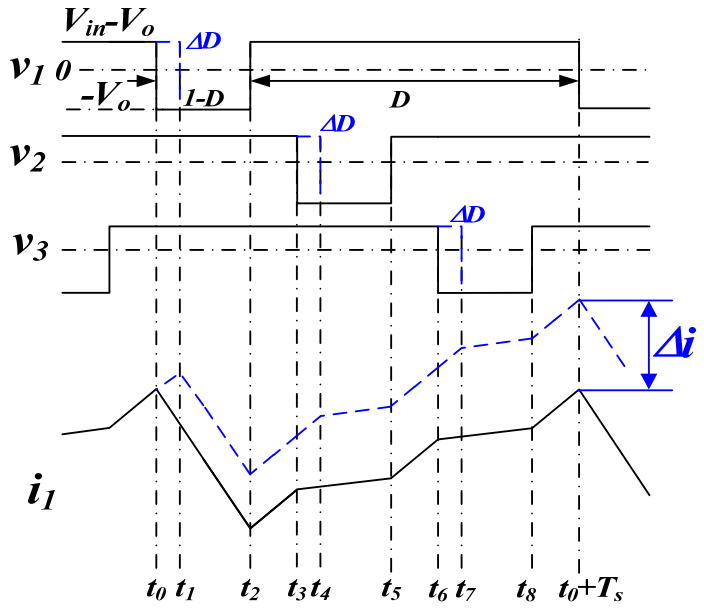

Figure 2.8 Transient inductor voltage and current waveforms for the three-phase coupled-inductor buck converter with 2/3≤D<1 under the duty cycle perturbation

Substituting the equation (2.18) into the equation (2.11), we get

$$L_{tr} = L + 2M \tag{2.19}$$

This is the same as the 1/3≤D<2/3 case. The reason for this is as follows. Figure 2.9 shows the equivalent coupled-inductor model as that in Figure 2.4. Figure 2.10 shows the small-signal model of the three-phase coupled-inductor buck converter and its derivation

($\hat{v}_{p1}=\hat{v}_{p2}=\hat{v}_{p3}=\hat{v}_p$). It can be seen that the total equivalent inductance for the converter is (L+2M)/3. Therefore, for each phase, the transient inductance is L+2M, which is the leakage inductance of the three-phase coupled-inductors. Since the transient performance of the three-phase coupled-inductor buck converter is determined by the leakage inductance of the coupled-inductor, the transient performance and the transient inductance of the three-phase coupled-inductor buck converter doesn't change with duty cycle D.

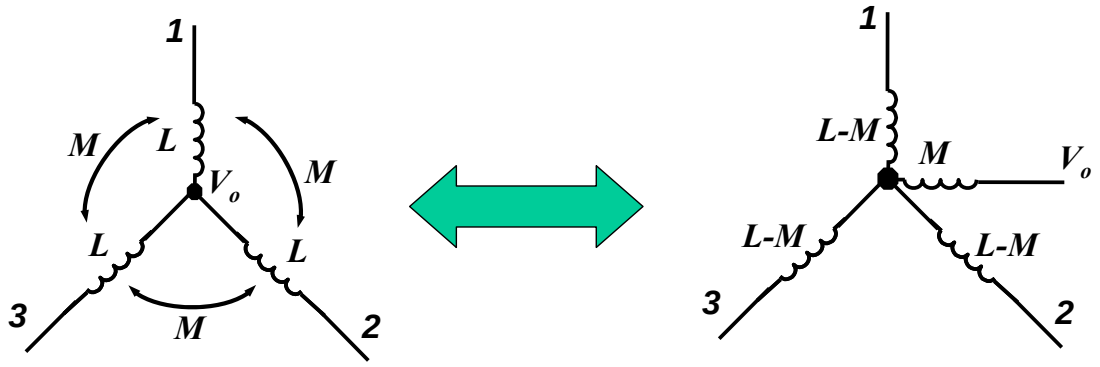

Figure 2.9 The equivalence between two three-phase coupled-inductor models (L: the self inductance of the coupled inductor; M: the mutual inductance of the coupled inductor, M<0)

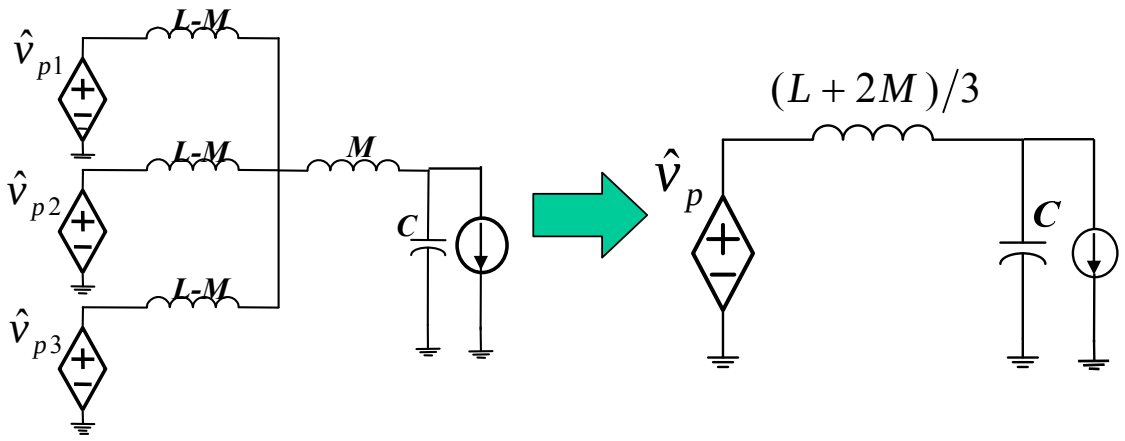

Figure 2.10 Transformation of the small-signal model of the three-phase coupled-inductor buck converter

For the three-phase non-coupled and coupled-inductors, if the transient equivalent inductances are the same ($L_{tr}=L_{nc}$), the transient responses are expected to be the same. The coupled-inductors can reduce the steady-state phase-current ripple. Based on the same transient equivalent inductance, the relationship between the steady-state, peak-to-peak inductor current ripples of non-coupled and coupled-inductors can be determined and compared as follows:

$$\frac{I_{pp\_coupled}}{I_{pp\_nc}} = \frac{L_{nc}}{L_{ss}} = \frac{L_{tr}}{L_{ss}} = \begin{cases} \dfrac{L + (\dfrac{2}{3DD'} - 1)M}{L - M} & 1/3 \le D < 2/3 \\ \dfrac{L + (1 + \dfrac{2D'}{D}) \cdot M}{L - M} & 2/3 \le D \le 1 \end{cases} \tag{2.20}$$

where $I_{pp\_coupled}$ is the peak-to-peak current ripple of the three-phase coupled-inductor, and I_{pp_nc} is the peak-to-peak current of the non-coupled-inductor. If the coupling coefficient α is defined as α=2M/L, then the equation (2.20) can be rewritten as

$$\frac{I_{pp\_coupled}}{I_{pp\_nc}} = \frac{L_{tr}}{L_{ss}} = \begin{cases} \dfrac{1 + (\dfrac{1}{3DD'} - \dfrac{1}{2}) \cdot \alpha}{1 - \dfrac{\alpha}{2}} & 1/3 \le D < 2/3 \\ \dfrac{1 + (\dfrac{1}{2} + \dfrac{D'}{D}) \cdot \alpha}{1 - \dfrac{\alpha}{2}} & 2/3 \le D \le 1 \end{cases} \tag{2.21}$$

The current ripple reductions by the three-phase coupled-inductors are functions of the steady-state duty cycle D and the coupling coefficient α. Since L_{tr}/L_{ss} can represent the performance improvement of coupled-inductor buck converters with respect to the non-coupled-inductor buck converters, L_{tr}/L_{ss} can be seen as the figure-of-merit (FOM) of coupled-inductor buck converters. The relationship shown in the equation (2.21) is plotted in Figure 2.11. It can be seen that when D is far from 0.5, e.g. 0.1, the three-phase coupled-inductor buck converter is better than the two-phase coupled-inductor buck converter and that when D is around 0.5, the two-phase coupled-inductor buck converter is better than the three-phase coupled-inductor buck converter.

The relationship shown in the equation (2.21) is also plotted in Figure 2.12. In Figure 2.12, the curve marked with n=2 is based on P. Wong's analysis; the red curve with D<1/3 is based on C. Sullivan's analysis; and the red curve with 1/3≤D<1 is based on the new analysis. It can be seen that the two-phase coupled-inductor is better when D is around 0.5. However, the three-phase coupled-inductor can achieve a larger current ripple reduction in a wider duty cycle range.

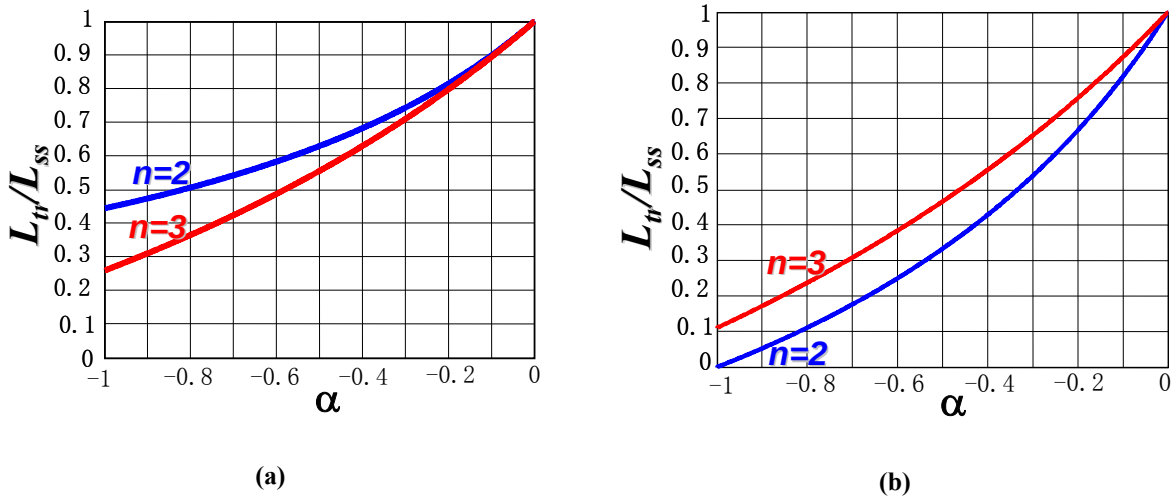

Figure 2.11 The two-phase and three-phase curves of the ratio of the transient inductance to the steady-state inductance L_{tr}/L_{ss} vs. the coupling coefficient α under the different duty cycles (a) the duty cycle D=0.1 (b) the duty cycle D=0.5

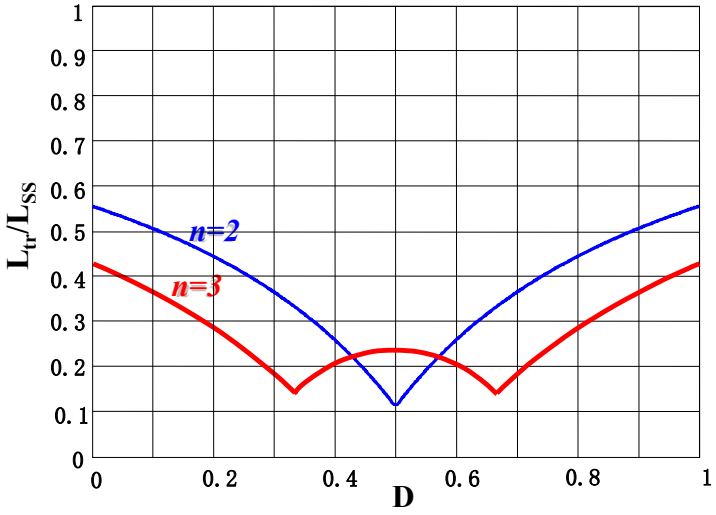

Figure 2.12 The two-phase and three-phase curves of the ratio of the transient inductance to the steady-state inductance L_{tr}/L_{ss} vs. the duty cycle D (the coupling coefficient α=-0.8)

Figure 2.13 shows the simulated phase-currents for the three-phase coupled-inductor buck converter (α=-0.85) and the three-phase non-coupled-inductor buck converter when V_{in}=400V, V_o=198V ($D=V_o/V_{in}$=0.495>1/3) in the PFC application. From the simulation, the phase-current ripple reduction of the coupled-inductor is 3.32A/16.63A=0.2. According to the new equation (2.21),

$$\frac{I_{pp\_coupled}}{I_{pp\_nc}} = \frac{1+(\frac{1}{3DD'}-\frac{1}{2})\cdot\alpha}{1-\frac{\alpha}{2}} = \frac{1-(\frac{1}{3\cdot 0.495\cdot 0.505}-0.5)\cdot 0.85}{1+\frac{0.85}{2}} = 0.2 \tag{2.22}$$

The calculation result matches the simulation result pretty well, which verifies the equation (2.21).

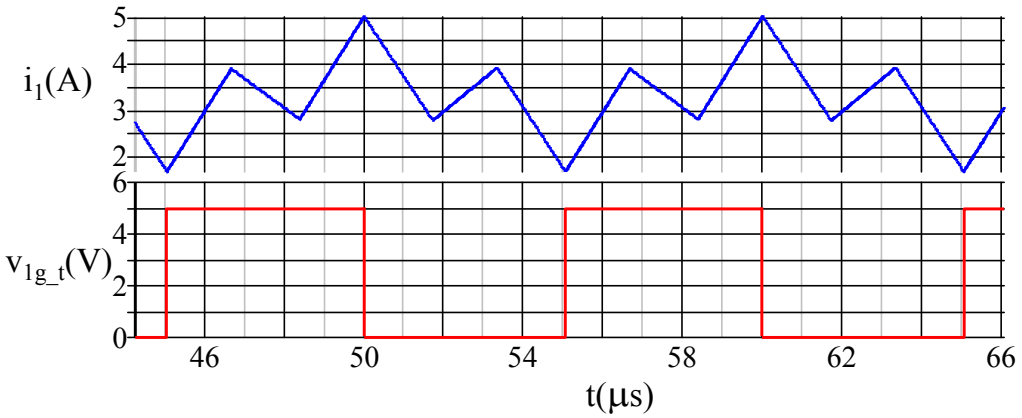

(a)

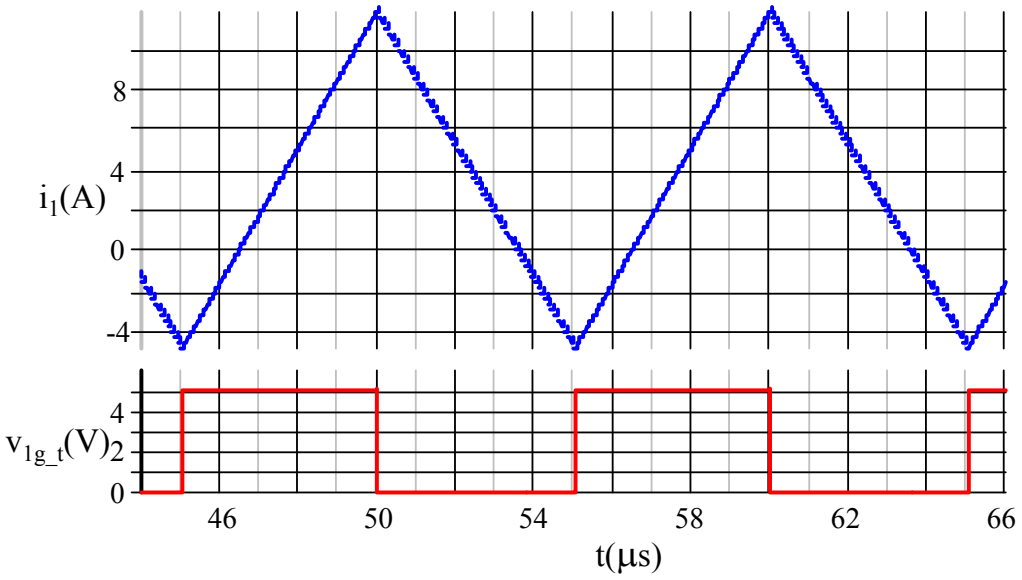

(b)

Figure 2.13 The simuated phase-current waveforms of the three-phase coupled-inductor buck converter and three-phase non-coupled-inductor buck converter when D>1/3 (a) The three-phase coupled-inductor buck converter (b) The three-phase non-coupled-inductor buck converter (i_1: the phase 1 inductor current; v_{1g_t}: the phase 1 top switch gate driving signal)

2.1.2. Extension to N-phase Coupled-inductor Buck Converters

The analysis in the above section can be extended to n-phase coupled-inductor buck converters. Figure 2.14 shows the n-phase coupled-inductor buck converter. The electrical equations for the n-phase coupled-inductor is

$$\begin{cases} v_1 = L\cdot\dot{i}_1 + M\cdot\dot{i}_2 + \ldots + M\cdot\dot{i}_{n-1} + M\cdot\dot{i}_n \\ v_2 = M\cdot\dot{i}_1 + L\cdot\dot{i}_2 + \ldots + M\cdot\dot{i}_{n-1} + M\cdot\dot{i}_n \\ \cdots \\ v_{n-1} = M\cdot\dot{i}_1 + M\cdot\dot{i}_2 + \ldots + L\cdot\dot{i}_{n-1} + M\cdot\dot{i}_n \\ v_n = M\cdot\dot{i}_1 + M\cdot\dot{i}_2 + \ldots + M\cdot\dot{i}_{n-1} + L\cdot\dot{i}_n \end{cases} \tag{2.23}$$

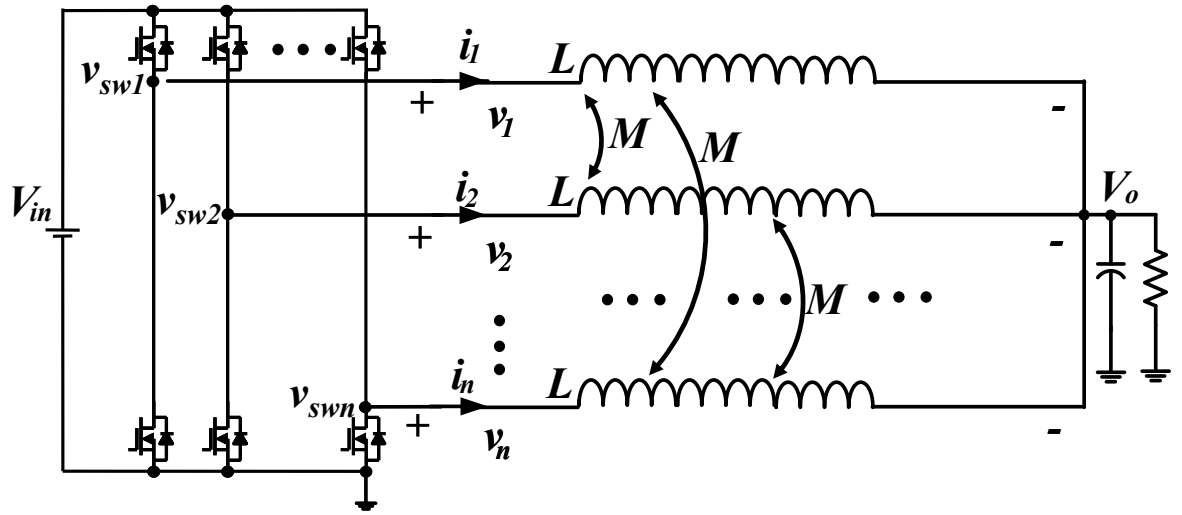

Figure 2.14 The circuit represenstation of an n-phase symmetric coupled-inductor buck converter

Figure 2.15 shows the steady-state inductor voltage waveforms v_1, v_2, $v_{(2n-1)}$, $v_{(2n)}$ and inductor current waveform i_1 when $1/n \le D < 2/n$. There are 2n switching intervals during one switching cycle. Due to the different inductor voltage combinations in these 2n intervals, the inductances equivalent to those in the non-coupled-inductor case are different for the 2n intervals: L_{eq1}-$L_{eq(2n)}$.

For the first time interval (t_0-t_1), the inductor voltage combination is

$$v_1 = V_{in} - V_o, v_2 = -V_o, ..., v_{n-1} = -V_o, v_n = V_{in} - V_o \tag{2.24}$$

Substituting the equation (2.24) into the equation (2.23) and rearranging the terms, it can be derived that

$$v_1 = \frac{(L-M)[L+(n-1)M]}{L+[\frac{n-3}{D'}+\frac{D}{D'}]\cdot M} \cdot \frac{di_1}{dt} \tag{2.25}$$

where D'=1-D. Therefore, the equivalent inductance for the first interval is

$$L_{eq1} = \frac{(L-M)[L+(n-1)M]}{L+[(n-3)+(n-2)\frac{D}{D'}]\cdot M} \tag{2.26}$$

According to the different inductor voltage combinations shown in Figure 2.15, the equivalent inductances for the other intervals can be derived similarly.

$$L_{eq2} = \frac{(L-M)[L+(n-1)M]}{L+[(n-2)+(n-1)\frac{D}{D'}]\cdot M} \tag{2.27}$$

$$L_{eq3} = L_{eq1} \tag{2.28}$$

$$L_{eq4} = L_{eq6} = ... = L_{eq(2n)} = \frac{(L-M)[L+(n-1)M]}{L+\frac{D'}{D}\cdot M} \tag{2.29}$$

$$L_{eq5} = L_{eq7} = ... = L_{eq(2n-1)} = \frac{(L-M)[L+(n-1)M]}{L+(1+\frac{2D'}{D})\cdot M} \tag{2.30}$$

There are four different equivalent inductances: L_{eq1}, L_{eq2}, $L_{eq(2n-1)}$ and $L_{eq(2n)}$.

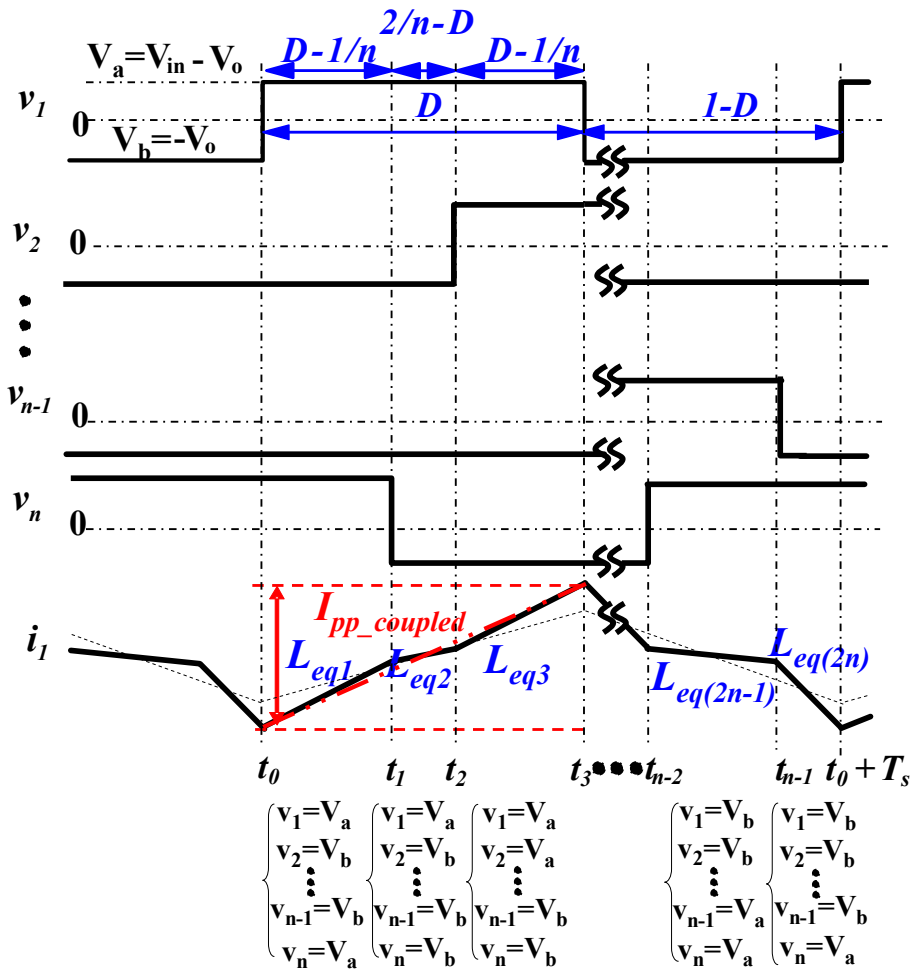

Figure 2.15 The steady-state inductor voltage and current waveforms for the n-phase coupled-inductor buck converter with 1/n≤D<2/n (V_a=V_{in}-V_o, V_b=-V_o)

From Figure 2.15, it can be seen that the peak-to-peak current ripple I_{pp_cp} is determined by the combination of two equivalent inductances: L_{eq1} and L_{eq2}. Therefore, the steady-state inductance is

$$L_{ss} = \frac{1}{\frac{1}{L_{eq1}} \cdot \frac{2(D-1/n)}{D} + \frac{1}{L_{eq2}} \cdot \frac{2/n-D}{D}} = \frac{(L-M)[L+(n-1)M]}{L+(\frac{2}{nDD'}+\frac{n-3}{D'}-1)\cdot M} \tag{2.31}$$

Figure 2.16 shows the transient inductor voltage and current waveforms for the n-phase coupled-inductor buck converter with 1/n≤D<2/n. Since the transient inductance is defined as

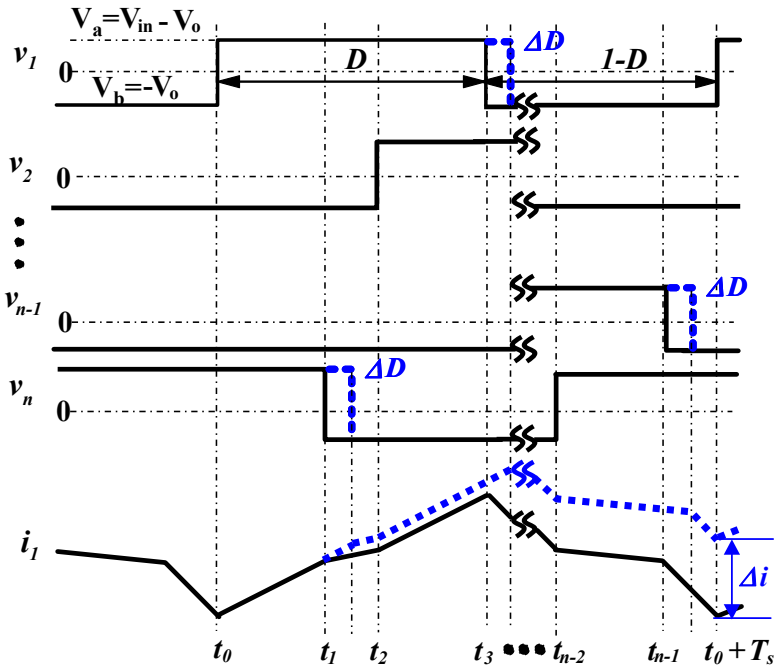

Figure 2.16 Transient inductor voltage and current waveforms of the n-phase coupled-inductor buck converter with 1/n≤D<2/n under the duty cycle perturbation

$$(\frac{di_1}{dt})_{cp} = \frac{\Delta i}{T_s} \triangleq \frac{V_{in} \cdot \Delta D}{L_{tr}} \tag{2.32}$$

and

$$\Delta i = (L_{eq1} - L_{eq2})\Delta D \cdot T_s + (L_{eq1} - L_{eq4})\Delta D \cdot T_s + \ldots + (L_{eq(2n-1)} - L_{eq(2n)})\Delta D \cdot T_s \tag{2.33}$$

then,

$$L_{tr} = L + (n-1)M \tag{2.34}$$

For the general case, when i/n≤D<(i+1)/n, 0≤i≤n-1, Figure 2.17 shows the steady-state inductor voltage waveforms v_1, v_i, v_{i+1}, v_n and inductor current waveform i_1. Due to the different inductor voltage combinations in these 2n intervals, the inductances equivalent to those in the non-coupled-inductor case are different for the 2n intervals L_{eq1}-$L_{eq(2n)}$.

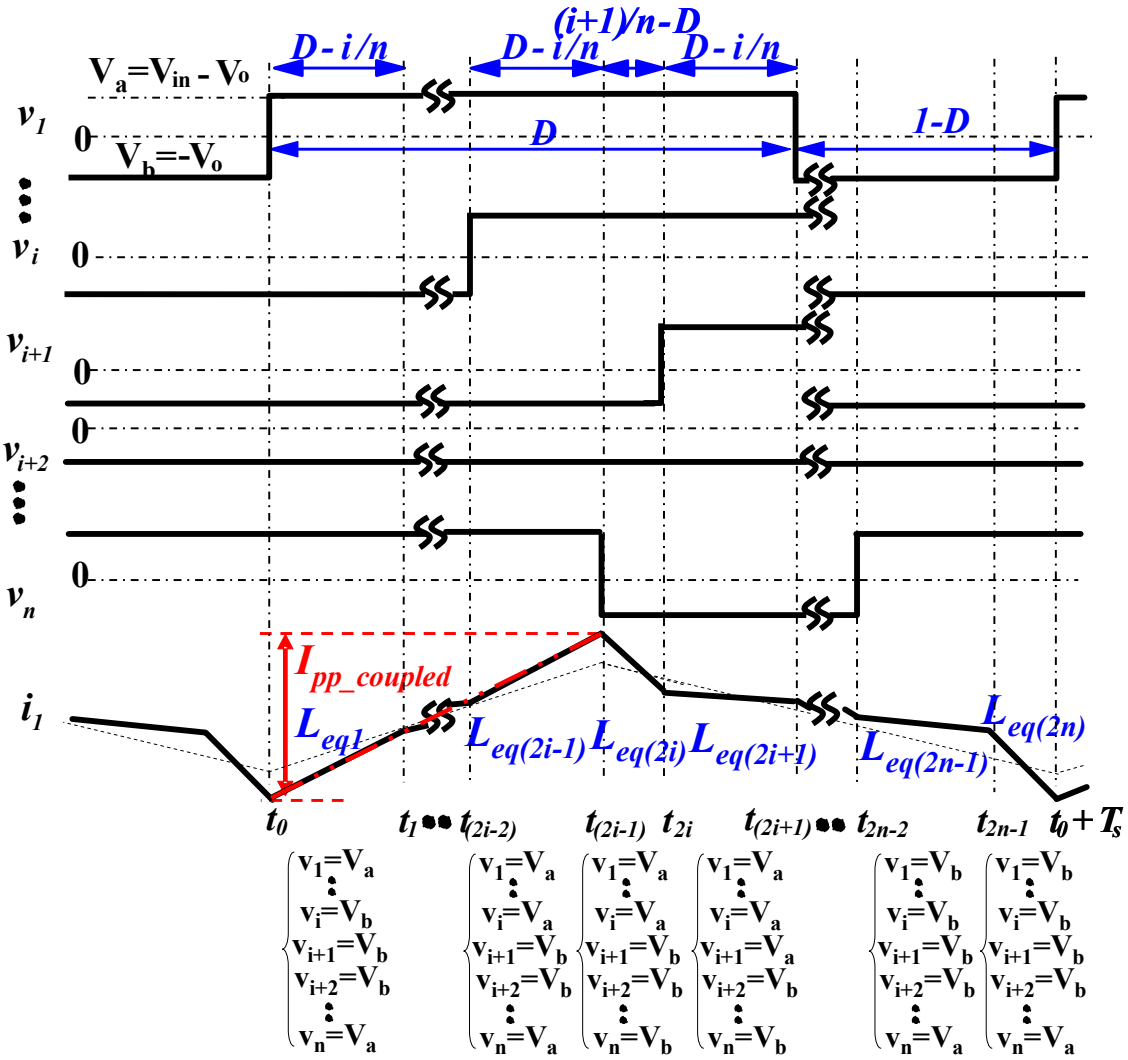

Figure 2.17 Steady-state inductor voltage and current waveforms for the n-phase coupled-inductor buck converter with i/n≤D<(i+1)/n (V_a=V_{in}-V_o, V_b=-V_o)

For the (2i-1) time interval (t_{2i-2}-t_{2i-1}), the inductor voltage combination is

$$v_1 = V_{in} - V_o, ..., v_i = V_{in} - V_o, v_{i+1} = V_{in} - V_o, ..., v_{n-1} = -V_o, v_n = -V_o \tag{2.35}$$

Substituting the equation (2.35) into the equation (2.23) and rearranging the terms, it can be derived that

$$v_1 = \frac{(L-M)[L+(n-1)M]}{L+[(n-i-2)+(n-i-1)\frac{D}{D'}]\cdot M} \cdot \frac{di_1}{dt} \tag{2.36}$$

where D'=1-D. Therefore, the equivalent inductance for the (2i-1) interval is

$$L_{eq(2i-1)} = \frac{(L-M)[L+(n-1)M]}{L+[(n-i-2)+(n-i-1)\frac{D}{D'}]\cdot M} \tag{2.37}$$

According to the different inductor voltage combinations shown in Figure 2.17, the equivalent inductances for the other intervals can be derived similarly.

$$L_{eq1} = \ldots = L_{eq(2i+1)} \tag{2.38}$$

$$L_{eq2} = \ldots = L_{eq(2i)} = \frac{(L-M)[L+(n-1)M]}{L+[(n-i-1)+(n-i)\frac{D}{D'}]\cdot M} \tag{2.39}$$

$$L_{eq(2i+3)} = \ldots = L_{eq(2n-1)} = \frac{(L-M)[L+(n-1)M]}{L+[i+(i+1)\frac{D'}{D}]\cdot M} \tag{2.40}$$

$$L_{eq(2i+2)} = \ldots = L_{eq(2n)} = \frac{(L-M)[L+(n-1)M]}{L+[(i-1)+i\frac{D'}{D}]\cdot M} \tag{2.41}$$

There are four different equivalent inductances: L_{eq1}, L_{eq2}, $L_{eq(2n-1)}$ and $L_{eq(2n)}$.

From Figure 2.17, it can be seen that the peak-to-peak current ripple I_{pp_cp} is determined by the combination of two equivalent inductances: L_{eq1} and L_{eq2}. Therefore, the steady-state inductance is

$$\begin{aligned} L_{ss} &= \frac{1}{\frac{1}{L_{eq1}}\cdot\frac{(i+1)(D-i/n)}{D}+\frac{1}{L_{eq2}}\cdot\frac{i[(i+1)/n-D]}{D}} \\ &= \frac{(L-M)[L+(n-1)M]}{L+[(n-2i-2)+\frac{i(i+1)}{nD}+\frac{nD(n-2i-1)+i(i+1)}{nD'}]\cdot M} \end{aligned} \tag{2.42}$$

Figure 2.18 shows the transient inductor voltage and current waveforms for the n-phase coupled-inductor buck converter with $i/n \le D < (i+1)/n$. Since the transient inductance is defined as

$$(\frac{di_1}{dt})_{cp} = \frac{\Delta i}{T_s} \triangleq \frac{V_{in}\cdot\Delta D}{L_{tr}} \tag{2.43}$$

and

$$\Delta i = (L_{eq1} - L_{eq2})\Delta D \cdot T_s + \ldots + [L_{eq(2i+1)} - L_{eq(2i+2)}]\Delta D \cdot T_s + \ldots + [L_{eq(2n-1)} - L_{eq(2n)}]\Delta D \cdot T_s \quad (2.44)$$

then,

$$L_{tr} = L + (n-1)M \quad (2.45)$$

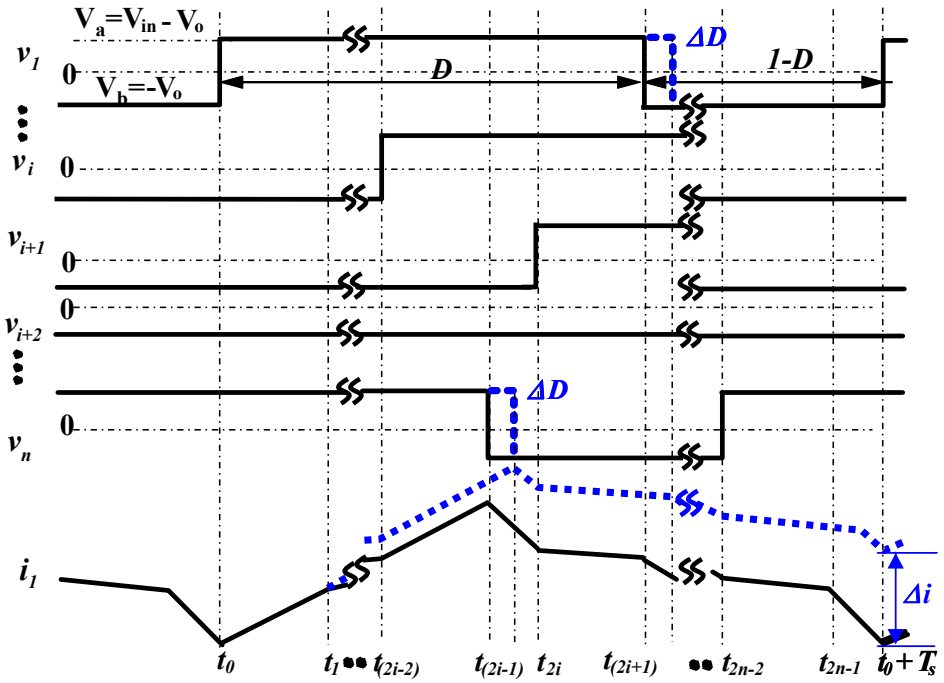

Figure 2.18 Transient inductor voltage and current waveforms of the n-phase coupled-inductor buck converter with i/n≤D<(i+1)/n under the duty cycle perturbation

This is expected since the transient inductance is not dependent on the duty cycle D. This result can also derived by the equivalent circuit method illustrated in the three-phase coupled-inductor buck converter case.

Table 2.2 shows the summary of steady-state inductances and transient inductances for the n-phase coupled-inductor buck converter.

Table 2.2 The steady-state inductances and transient inductances for the n-phase coupled-inductor buck converter

	0≤D<1/n	…	i/n≤D<(i+1)/n	…	(n-1)/n≤D<1
L_{ss}	$\frac{(L-M)[L+(n-1)M]}{L+[(n-2)+(n-1)\frac{D}{D'}]\cdot M}$	…	$\frac{(L-M)[L+(n-1)M]}{L+[(n-2i-2)+\frac{i(i+1)}{nD}+\frac{nD(n-2i-1)+i(i+1)}{nD'}]\cdot M}$	…	$\frac{(L-M)[L+(n-1)M]}{L+[(n-2)+(n-1)\frac{D'}{D}]\cdot M}$
L_{tr}	$L+(n-1)M$	…	$L+(n-1)M$	…	$L+(n-1)M$

According to the equation (2.42) and the equation (2.45), the FOM of n-phase coupled-inductor buck converters is:

$$\frac{L_{tr}}{L_{ss}}=\frac{I_{pp\_coupled}}{I_{pp\_nc}}=\frac{L+[(n-2i-2)+\frac{i(i+1)}{nD}+\frac{nD(n-2i-1)+i(i+1)}{nD'}]\cdot M}{L-M}$$
$$=\frac{1+[(n-2i-2)+\frac{i(i+1)}{nD}+\frac{nD(n-2i-1)+i(i+1)}{nD'}]\cdot\frac{\alpha}{n-1}}{1-\frac{\alpha}{n-1}} \quad (2.46)$$

where I_{pp_cp} is the peak-to-peak current of the n-phase coupled-inductor, I_{pp_nc} is the peak-to-peak current of the non-coupled-inductor with $L_{nc}=L_{tr}$, i/n≤D<(i+1)/n, 0≤i≤n-1, and the coupling coefficient α=-(n-1)M/L. The FOM is the function of the steady-state duty cycle D, the coupling phase number n and the coupling coefficient α. The relationship shown in the equation (2.46) is plotted in Figure 2.19 with L_{tr}/L_{ss} as a function of the coupling coeeficient α when the duty cycle D is 0.1. The relationship shown in the equation (2.46) is plotted in Figure 2.20 with L_{tr}/L_{ss} as a function of the coupling coefficient α when the duty cycle D is 0.33 and 0.5. It can be seen that when the duty cycle is very small, 0.1, the more-phase coupling is the best. When the duty cycle is close to 0.33, the three-phase coupling is the best when the duty cycle is close to 0.5, the two-phase coupling is the best.

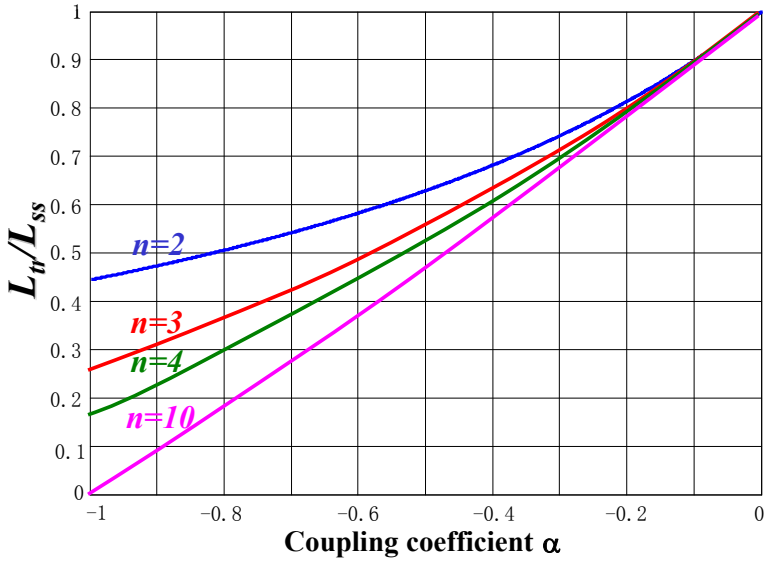

Figure 2.19 The two-phase, three-phase, four-phase and n-phase curves of the ratio of the transient inductance to the steady-state inductance L_{tr}/L_{ss} vs. the coupling coefficient α under the duty cycle D=0.1

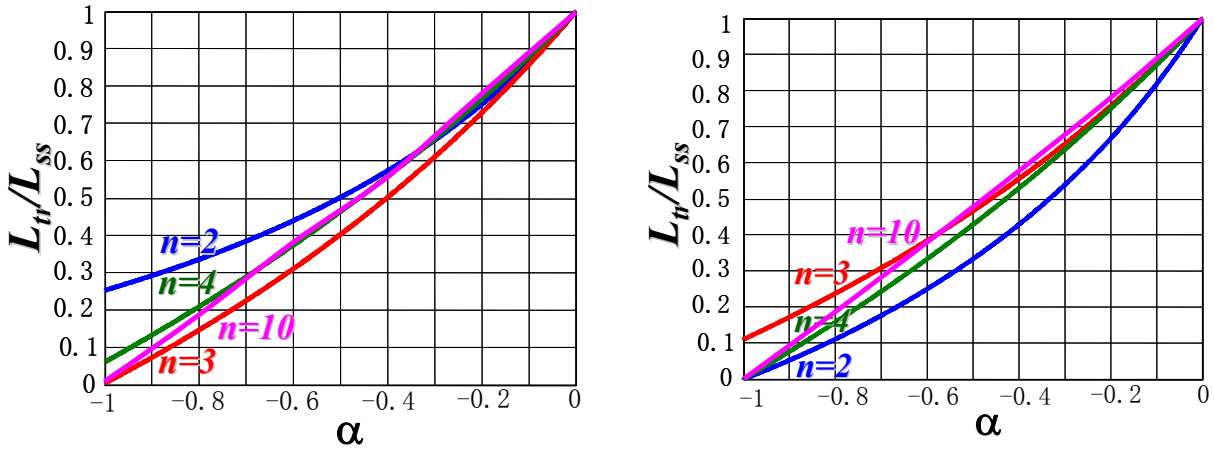

Figure 2.20 The two-phase, three-phase, four-phase and n-phase curves of the ratio of the transient inductance to the steady-state inductance L_{tr}/L_{ss} vs. the coupling coefficient α (a) the duty cycle D=0.33 (b) the duty cycle D=0.5

The relationship shown in the equation (2.46) is also plotted in Figure 2.21. Looking at the FOM curves for the whole duty cycle in Figure 2.21, it can be seen that the n-phase coupled-inductors are better when D is around 1/n, 2/n, …,(n-1)/n. Moreover, the more-phase coupled-inductor buck converter can achieve a smaller FOM in a wider duty cycle range. Therefore, to

achieve a better performance in the wide duty-cycle range multiphase buck converter, more phase coupling is preferred, such as the wide-input POL case and the multiphase PFC converter case. Table 2.3 shows the calculated efficiency comparison between the wide-input two-phase coupled-inductor POL and the wide-input ten-phase coupled-inductor POL in different input voltages. In the comparison, V_{in}=5-12V, V_o=2.5V, I_o=20A, f_s=2MHz, the top switch: 2168, the bottom switch: 2165 and ten phases for both cases. It can be seen that with the ten-phase coupled-inductor POL can increase 1.5 percent efficiency in 12V compared to the two-phase coupled-inductor POL converter, keeping the steady-state inductances in the 5V to be the same.

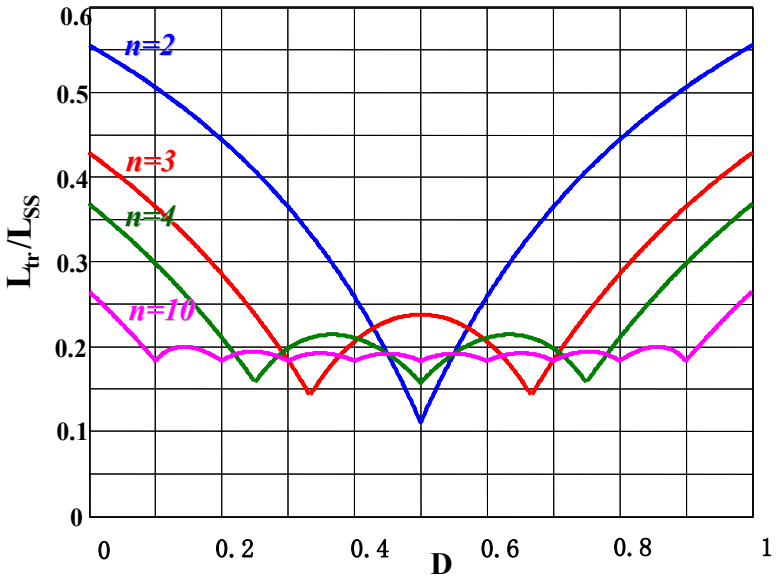

Figure 2.21 The two-phase, three-phase, four-phase and n-phase curves of the ratio of the transient inductance to the steady-state inductance L_{tr}/L_{ss} vs. the duty cycle D (the coupling coefficient α=-0.8)

Table 2.3 The efficiency comparision of the two-phase coupled-inductor POL converter and the ten-phase coupled-inductor POL converter in different input voltages

	two-phase coupled POL		10-phase coupled POL	
V_{in}(V)	5	12	5	12
L_{ss}(nH)	200	50	200	198
Efficiency(%)	88	83.5	88	85

Figure 2.21 also shows that at D=0.5, the two-phase coupled-inductor buck has a lower L_{tr}/L_{ss} than the four-phase coupled-inductor buck with the same coupling coefficient α=-0.8. This can be explained in the following. Figure 2.22 shows the two-phase coupled-inductor and the four-phase coupled-inductor with the same transient (leakage) inductance and the same coupling coefficient α=-0.8. According to the coupling coefficient definition, the two-phase coupling coefficient α_2 and the four-phase coupling coefficient α_4 are

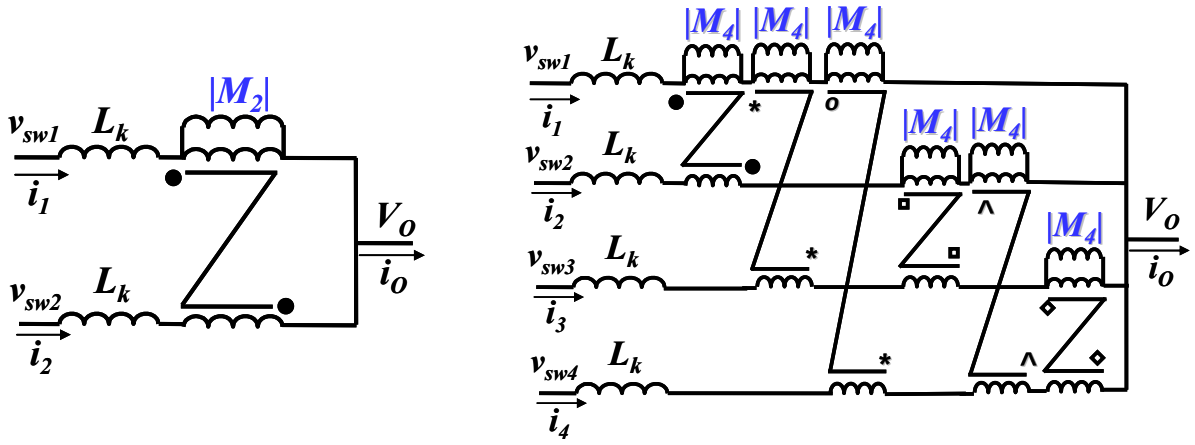

(a) **(b)**

Figure 2.22 The comparison of the two-phase coupled-inductor buck converter and the four-phase coupled-inductor buck converter with the same L_{tr} (L_k) and the same coupling coefficient α=-0.8 (a) the two-phase coupled inductor (b) the four-phase coupled inductor

$$\alpha_2 = M_2 / L_{self\,2} = -|M_2|/(|M_2|+L_k) \tag{2.47}$$

$$\alpha_4 = 3M_4 / L_{self\,4} = -3|M_4|/(3|M_4|+L_k) \tag{2.48}$$

With the same coupling coefficient,

$$\alpha_2 = \alpha_4 \tag{2.49}$$

Substituting the equations (2.47) and (2.48) into the equation (2.49), we can derive

$$|M_2| = 3|M_4| \tag{2.50}$$

The magnetizing inductance of the two-phase coupled-inductor is three times larger than the four-phase coupled-inductor. This large magnetizing inductance results in the smaller phase-current ripple and the larger steady-state inductance L_{ss} of the two-phase coupled-inductor.

2.2. Asymmetric Analysis of Multiphase Coupled-inductor Buck Converters

For all the above analyses for the multiphase coupled-inductor buck converter, the multiphase coupled-inductor is assumed to be symmetric. However, as shown in Figure 1.31, the practical n-phase (n>2) coupled-inductor is asymmetric. In this section, the effect of asymmetric coupled-inductors on the multiphase coupled-inductor buck converter will be investigated.

Figure 2.23 shows an example of the three-phase asymmetric coupled-inductor and the three-phase asymmetric coupled-inductor buck converter utilizing this coupled-inductor. For this asymmetric coupled-inductor, $L_1=L_3\neq L_2$, $M_{12}=M_{23}\neq M_{13}$.

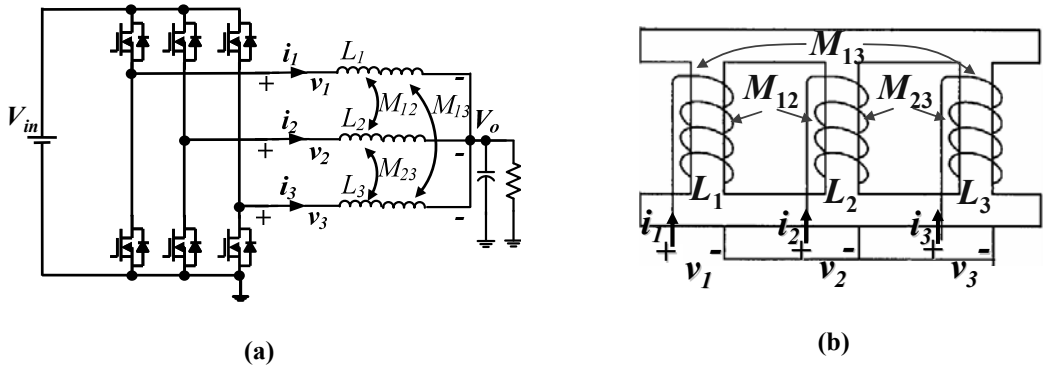

(a) (b)

Figure 2.23 The three-phase asymmetric coupled-inductor buck converter (a) The three-phase asymmetric coupled-inductor buck converter (b) The three-phase asymmetric coupled-inductor

The detail analysis of the asymmetric coupled-inductor buck converter is in the appendix. The steady state inductances and the transient inductances are listed here.

$$L_{ss1}=\frac{L_1(L_1L_2-M_{12}^2)-(L_1M_{12}^2-2M_{12}^2M_{13}+L_2M_{13}^2)}{L_1L_2-M_{12}^2+(L_1M_{12}-M_{12}M_{13}-M_{12}^2+L_2M_{13})\dfrac{D}{D'}} \quad (D<1/3) \tag{2.51}$$

$$L_{tr1}=\frac{L_1(L_1L_2-M_{12}^2)-(L_1M_{12}^2-2M_{12}^2M_{13}+L_2M_{13}^2)}{L_1L_2-L_1M_{12}+M_{12}M_{13}-L_2M_{13}} \quad (D<1/3) \tag{2.52}$$

To characterize the asymmetry of the asymmetric coupled-inductor, several parameters are defined.

$$k=\frac{L_1}{L_2},\ \alpha_1=\frac{M_{12}}{\sqrt{L_1L_2}},\ \alpha_2=\frac{M_{13}}{\sqrt{L_1L_3}}=\frac{M_{13}}{L_1} \tag{2.53}$$

k represents the difference in the phase self inductances. α_1 and α_2 are the coupled coefficients. The values k=1 and $\alpha_1 = \alpha_2$ represents the symmetric coupled-inductor.

With the equations (2.51), (2.52) and (2.53), the FOM for Phase 1 when D<1/3 can be derived

$$\frac{L_{tr1}}{L_{ss1}} = \frac{1-\alpha_1^2+(\alpha_1\sqrt{k}-\alpha_1\alpha_2\sqrt{k}-\alpha_1^2+\alpha_2)\dfrac{D}{D'}}{1-\alpha_1\sqrt{k}+\alpha_1\alpha_2\sqrt{k}-\alpha_2} \quad (D<1/3) \tag{2.54}$$

The relationship in the equation (2.54) is plotted in Figure 2.24 when D=0.1, and k=1. The FOMs of the two-phase symmetric coupled-inductor and three-phase symmetric coupled-inductor are also shown.

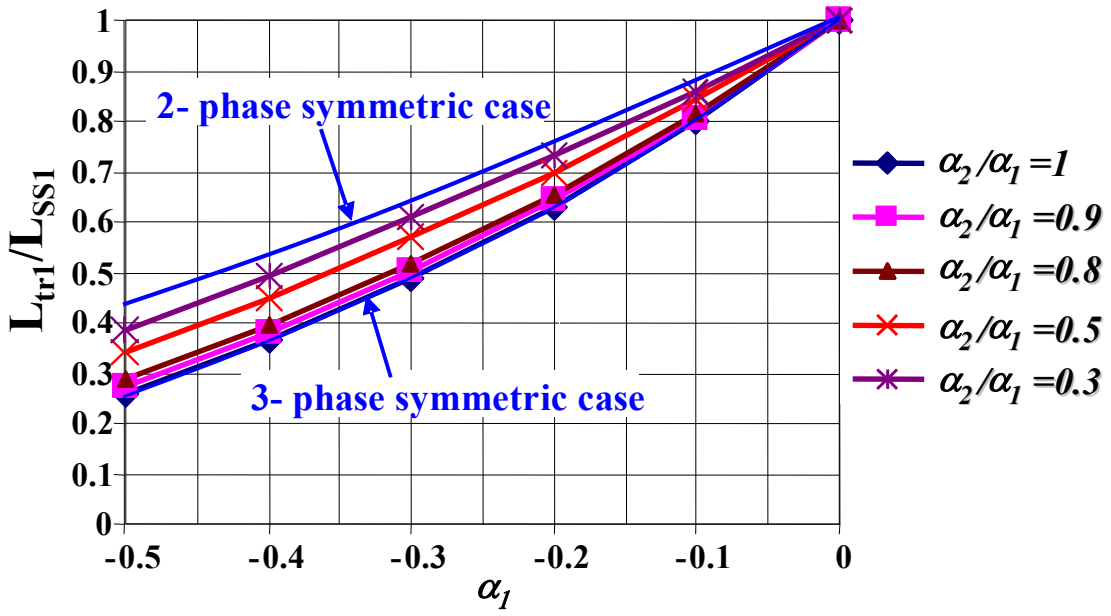

Figure 2.24 The effect of asymmetry α_2/α_1 on the curve of the L_{tr1}/L_{ss1} vs. the coupling coefficient α_1 in the three-phase asymmetric coupled-inductor buck converter (the duty cycle D=0.1)

It can be seen from Figure 2.24 that when the FOM of the three-phase asymmetric coupled-inductor is larger than that of the three-phase symmetric coupled-inductor; i.e. the benefits of the three-phase asymmetric coupled-inductor are degraded. The more asymmetric the inductor is, the more benefits it will degrade. When the asymmetry is very strong, the performance of the three-phase coupled-inductor is similar to that of the two-phase symmetric coupled-inductor.

When 1/3≤D<2/3 and 2/3≤D≤1, the FOMs for Phase 1 can be derived.

$$\frac{L_{tr1}}{L_{ss1}}=\frac{(1-\alpha_2-\alpha_1\sqrt{k}+\alpha_1\alpha_2\sqrt{k})+\frac{1}{3DD'}(\alpha_1\sqrt{k}+\alpha_2-\alpha_1^2-\alpha_1\alpha_2\sqrt{k})}{1-\alpha_1\sqrt{k}+\alpha_1\alpha_2\sqrt{k}-\alpha_2} \quad (1/3\leqslant D<2/3) \tag{2.55}$$

$$\frac{L_{tr1}}{L_{ss1}}=\frac{1-\alpha_1^2+(\alpha_1\sqrt{k}-\alpha_1\alpha_2\sqrt{k}-\alpha_1^2+\alpha_2)\frac{D'}{D}}{1-\alpha_1\sqrt{k}+\alpha_1\alpha_2\sqrt{k}-\alpha_2} \quad (2/3\leqslant D\leqslant 1) \tag{2.56}$$

The relationships in the equations (2.54), (2.55) and (2.56) are plotted in Figure 2.25 when α_1=-0.4, and k=1. The FOMs of the two-phase symmetric coupled-inductor and three-phase symmetric coupled-inductor are also shown. It can be seen that when the multiphase coupled inductor is more asymmetric, the FOM increases and the benefits from the more-phase coupling are degrading.

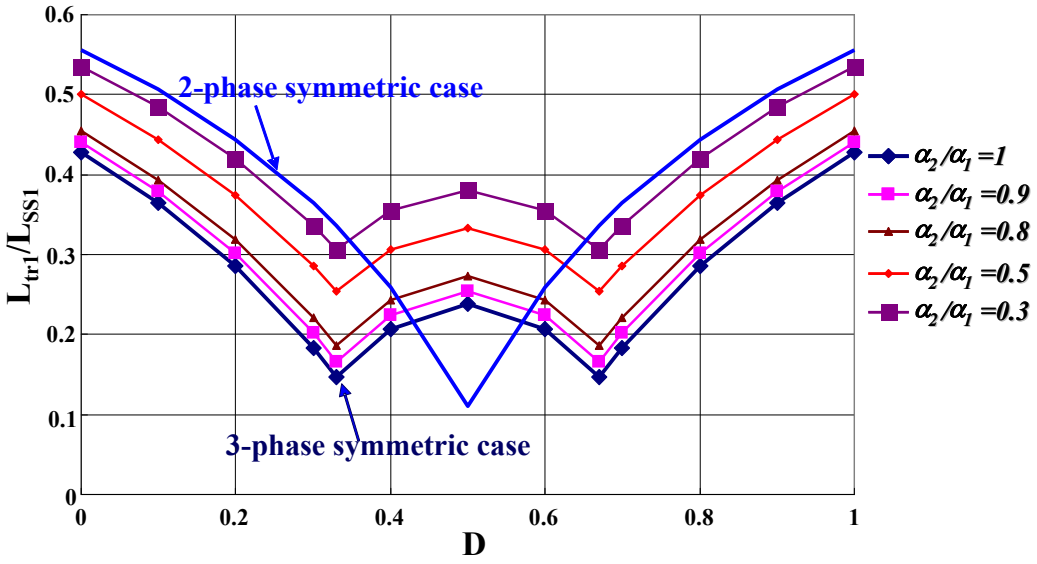

Figure 2.25 The effect of asymmetry α_2/α_1 on the curve of the L_{tr1}/L_{ss1} vs. the duty cycle D in the three-phase asymmetric coupled-inductor buck converter (the coupling coefficient α_1=-0.4)

2.3. Summary

In this section, previous analysis of multiphase coupled-inductor buck converters is extended, and there is a generalized analysis of the symmetric multiphase coupled-inductor buck converter. The results of the analysis show that coupling more phases can achieve a better performance in a wider duty cycle range. The effect of the asymmetric multiphase coupled-inductor on the buck converter performance is also investigated.

Chapter 3. Alternative Multiphase Coupled-inductor Structures

In Chapter 1, it is found that the winding path of today's existing coupled-inductor is quite long. Figure 3.1 shows the commercial non-coupled-inductor and coupled-inductor and their winding paths. The existing coupled-inductor's winding path is about three times longer than that of the non-coupled-inductor. Therefore, the winding loss of the existing coupled-inductor is much larger than that of the non-coupled-inductor. In high-current, low-voltage applications, such as the CPU and graphic card VRs, the winding loss is dominant in the inductor total loss. Therefore, a long winding path for the existing coupled-inductor is not preferred.

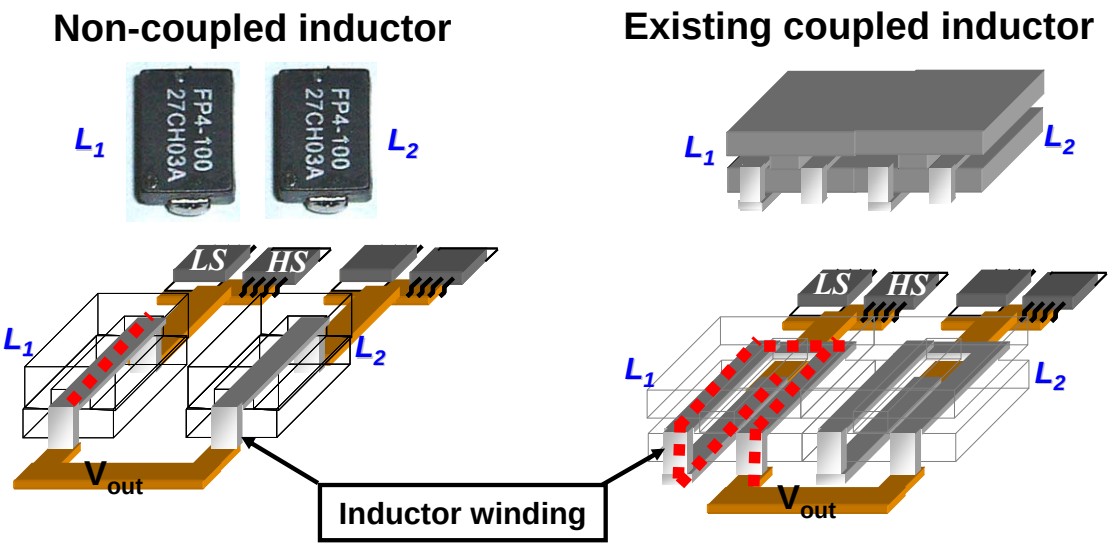

Figure 3.1 The winding path comparison between the commercial non-coupled inductors and the commercial coupled-inductors (LS: low-side switch; HS: high-side switch, picture by author, 2005)

In this section, several alternative coupled-inductor structures with short winding paths are proposed to solve this issue. Their reluctance models and design guidelines are established, and experiments are performed to verify the design guidelines.

3.1. Alternative Coupled-inductor Structures

3.1.1. Twisted-Core Coupled-inductors

To get rid of the long winding path, the reason why the existing coupled-inductor has a long winding path needs to be identified. Simplified in Figure 3.1, the existing coupled-inductor can be considered as a structure with a straight magnetic core with the winding wrapped around it. Since the winding is wrapped, it has a long winding path, although the magnetic core path is short.

If we think the opposite way, keeping the winding path straight and wrapping the magnetic core around the winding, the minimum winding path can be achieved. Since the magnetic core is twisted in this case, the resulting coupled-inductor is called the twisted-core coupled-inductor. Accordingly, the existing twisted-winding, straight-core coupled-inductor is called the twisted-winding coupled-inductor. Figure 3.2 shows the conceptual drawings of the twisted-winding coupled-inductor and the twisted-core coupled-inductor [50-52].

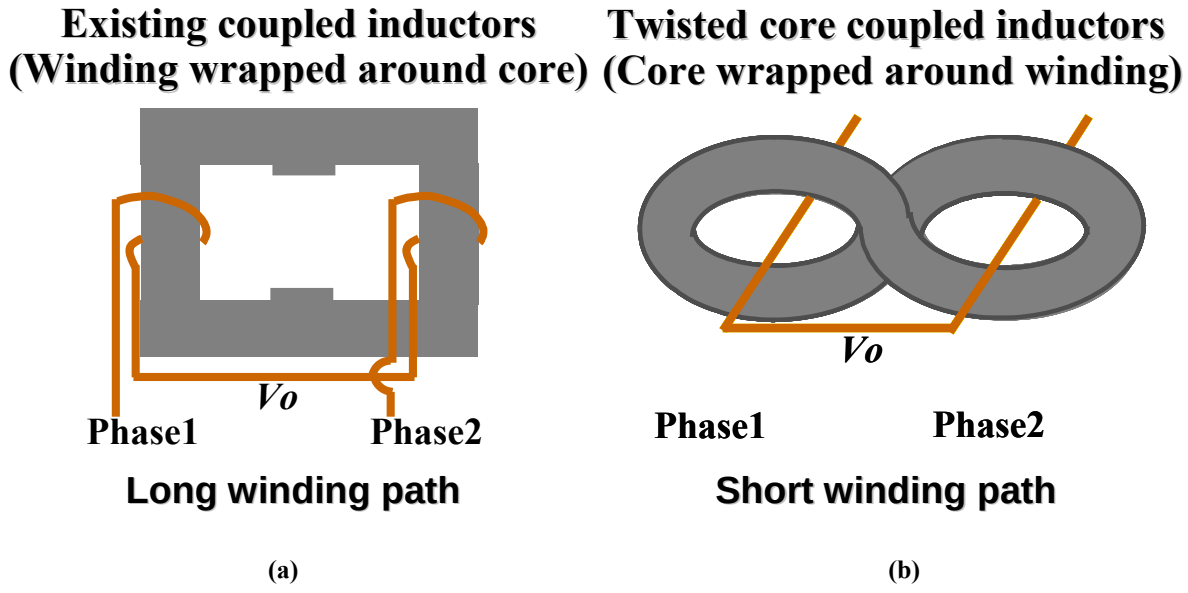

Figure 3.2 The conceptual drawing of the conventional twisted-winding coupled-inductors vs. the twisted-core coupled-inductors (a) the twisted-winding coupled inductor (b) the twisted-core coupled inductor

The twisted-core coupled-inductor has a minimized winding loss but a higher core loss, while the twisted-winding coupled-inductor has a minimized core loss but a higher winding loss.

In low-voltage, high-current applications, where the inductor winding loss is much more than the inductor core loss, the twisted-core coupled-inductors are preferred.

One example of twisted-core coupled-inductors is proposed by J. Zhou (Figure 3.3). This structure can be further improved by turning the left "L" shape core 90°. Figure 3.4 shows the compact twisted-core coupled-inductor structure. The compact twisted-core coupled-inductor structure is made of four magnetic parts, which are shown in Figure 3.4. Two magnetic parts are "I" shaped bars, and two are "L" shaped parts.

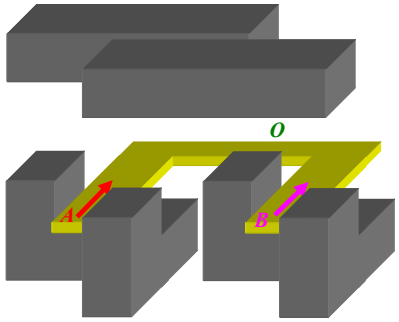

Figure 3.3 One twisted-core coupled-inductor example of the twisted-core coupled inductor concept in Figure 3.2

(a) **(b)**

Figure 3.4 Another twisted-core coupled-inductor example with the compact structure and its four magnetic parts (a) the compact twisted-core coupled-inductor (b) the four magnetic parts of (a)

Figure 3.5 shows the loss comparison of a twisted-core coupled-inductor and the existing twisted-winding coupled-inductor, which keeps the same footprint and inductances when the total output current I_o=40A, switching frequency f_s=1.2MHz, V_{in}=12V, and V_o=1.2V. In the

calculation, the coupled-inductor winding loss is approximately calculated by the following equation, which is verified by the Maxwell simulation result.

$$P_{winding} = NI_{phase}^{2} R_{L\_DC} \tag{3.1}$$

where N is the phase number, I_{phase} is the phase DC current, and R_{L_DC} is the inductor DC resistance. The coupled-inductor core loss is calculated according to the GSE (generalized Steinmetz equation) proposed in [53].

$$P_v = \frac{1}{T}\int_0^T k_1 \,|\, dB/dt \,|^{\alpha} |\, B(t) \,|^{\beta-\alpha}\, dt \quad , \quad k_1 = \frac{k}{(2\pi)^{\alpha-1}\int_0^{2\pi} |\cos\theta|^{\alpha} |\sin\theta|^{\beta-\alpha}\, d\theta} \tag{3.2}$$

where P_v is the time average core loss per unit volume, B(t) is the flux density function, T is the period of B(t), and k, α and β are constants given by the magnetic material manufacturer. The core loss densities for core parts with different values for B(t) are calculated separately, and the total core loss is obtained by summing the products of the core loss density and the core part volume. We can see that the total loss of the twisted-core coupled-inductors is 14% less than that of the twisted-winding coupled-inductors. This accounts for about a 0.5% efficiency increase in a CPU VR buck converter. From the data, we can also find that the twisted-core coupled-inductor reduces winding loss, and pays with core loss. Therefore, when the total output current is higher and the output voltage is lower, which is the trend of the CPU VR buck converter, the benefits of the twisted-core coupled-inductor are more pronounced.

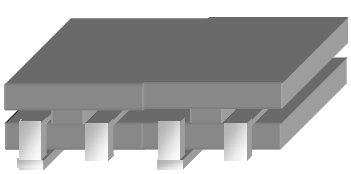

Twisted winding ***Twisted core***

$L_{winding}$=32mm (*per phase*) **$L_{winding}$=10mm (*per phase*)**

$P_{winding}$=0.72W P_{core}=0.425W **$P_{winding}$=0.225W P_{core}=0.7825W**

$P_{totloss}$=1.15W **$P_{totloss}$=1.01W**

Figure 3.5 The comparison of the winding loss, core loss and the inductor total loss between the twisted-winding coupled inductors and the twisted-core coupled-inductors with the same steady-state inductance L_{ss}=100nH and the transient inductance L_{tr}=50nH (picture by author, 2005)

3.1.2. Low Profile Twisted-core Coupled-inductors

Although the above twisted-core coupled-inductor minimizes the winding loss, it increases the core loss (Figure 3.5), which is not ideal. The twisted-winding coupled-inductor minimizes the core loss, but its winding loss is increased. Therefore, neither of these inductors can provide the minimum total loss. A structure with both a relatively low winding loss and a relatively low core loss is preferred to minimize the inductor total loss. With this concept, the low profile twisted-core coupled-inductor is proposed as a trade-off between the winding loss and the core loss. Figure 3.6 shows the evolution process of one low profile twisted-core coupled-inductor structure.

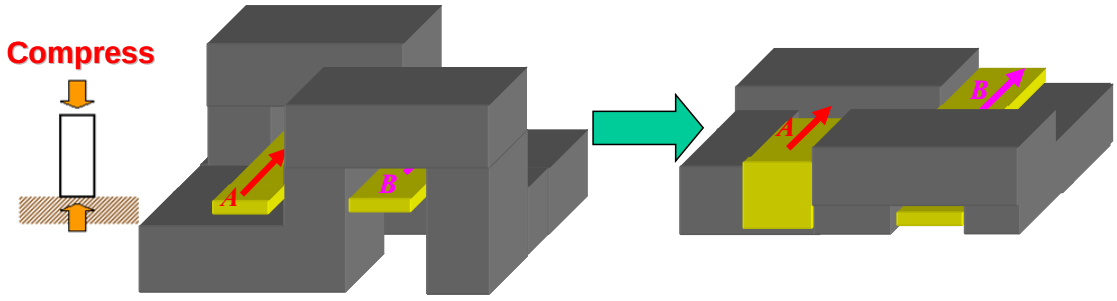

Figure 3.6 Evolution of the low profile twisted-core coupled-inductor structure from the twisted-core coupled inductor structure

The two-phase low profile twisted-core coupled-inductor structure shown in Figure 3.6 can't be easily extended to an n-phase coupled-inductor (Figure 3.7). However, if the winding position is changed a little bit, the resulting two-phase low profile twisted-core coupled-inductor can easily be extended to n-phase low profile twisted-core coupled-inductor (Figure 3.8). Figure 3.9 shows the proposed core and winding structures.

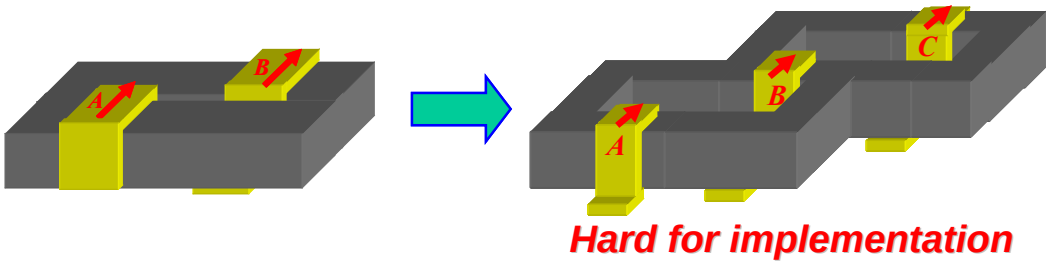

Figure 3.7 Direct extension of the 2-phase low-profile twisted-core coupled-inductor to the 3-phase low-profile twisted-core coupled-inductor

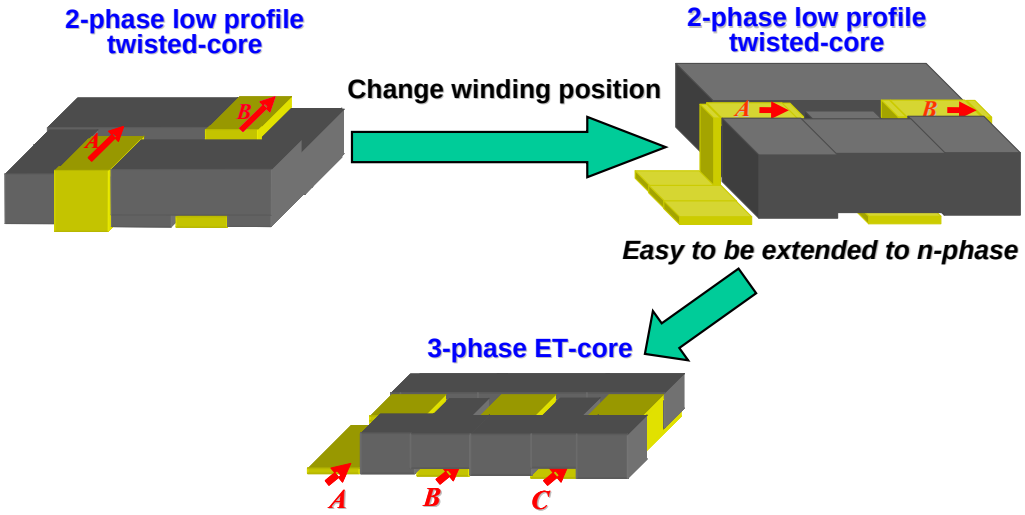

Figure 3.8 Step-by-step derivation of the three-phase low profile ET-core coupled-inductor from the 2-phase low profile twisted-core coupled inductor

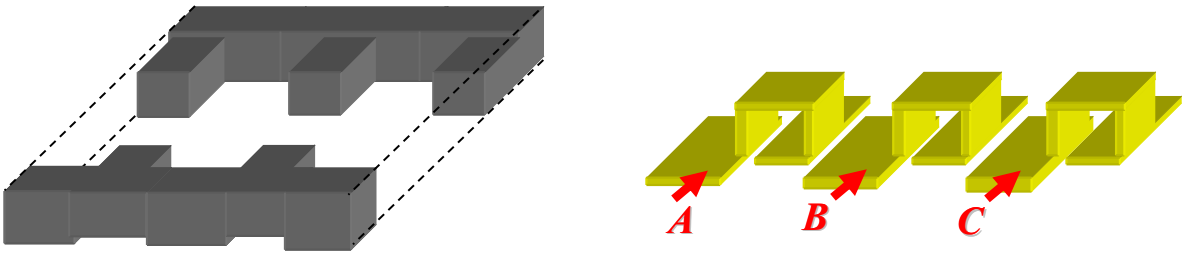

(a) **(b)**

Figure 3.9 The magnetic core structure and the winding structure of the three-phase ET-core coupled-inductor (a) the magnetic core structure (b) the winding structure

Another n-phase low profile twisted-core coupled-inductor structure, the Z-core coupled-inductor, is shown along with its evolution in Figure 3.10. In this structure, the magnetic core structure is tilted, which makes the core loss a little larger; additionally, the winding is not straight, which increases the winding loss a little bit. Although both the core loss and winding loss are not minimized, the total loss may be small with a trade-off between the winding loss and the core loss.

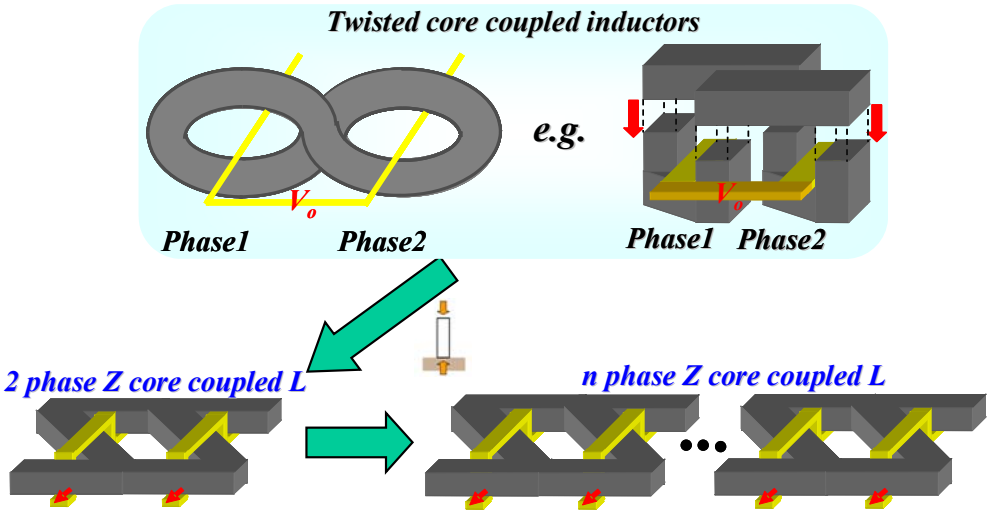

Figure 3.10 The step-by-step evolution of the low profile n-phase Z-core coupled-inductor from the twisted-core coupled-inductor concept

In the following sections, the twisted-core and low-profile twisted-core coupled-inductors are modeled and designed.

3.2. Twisted-core Coupled-inductors

3.2.1. Flux Flow Paths

To model the twisted-core coupled-inductor, the flux flow in the twisted-core coupled-inductor needs to be investigated. The main flux path of the twisted-core coupled-inductors is shown in Figure 3.11. From Figure 3.11, we can see that the main flux path follows the magnetic core itself. This figure also shows the small air gap, airgap1, which mainly controls the self inductance. The leakage flux path of the twisted-core coupled-inductor is quite complex. Figure 3.12 shows the two main leakage flux paths. Airgap1 is also marked in Figure 3.12. Figure 3.13 shows the dimension definition of twisted-core coupled- inductor. Figure 3.14 shows the precision of the conventional reluctance model, though it neglects the fringing flux. Here, the steady-state inductance and the transient inductance of the coupled-inductor buck (D<0.5) are

$$L_{ss} = \frac{L_{self}^2 - (L_{self} - L_k)^2}{L_{self} - \frac{D}{D'} \cdot (L_{self} - L_k)} \tag{3.3}$$

$$L_{tr} = L_{self} - M = L_k \tag{3.4}$$

according to the equations (1.10), (1.11), (1.13) and (1.16). It can be seen that the precision of the steady-state inductance and the transient (leakage) inductance are not acceptable. The fringing effect of air gaps must be considered.

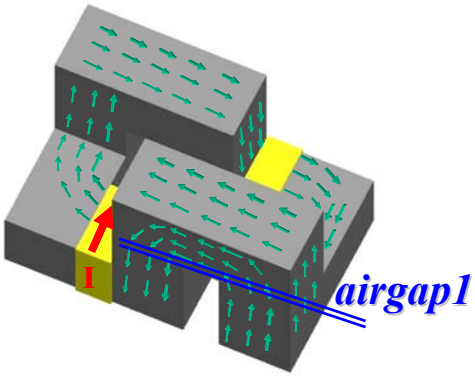

Figure 3.11 The main magnetic flux flow path of the twisted-core coupled-inductor: the magnetic-core-structure path

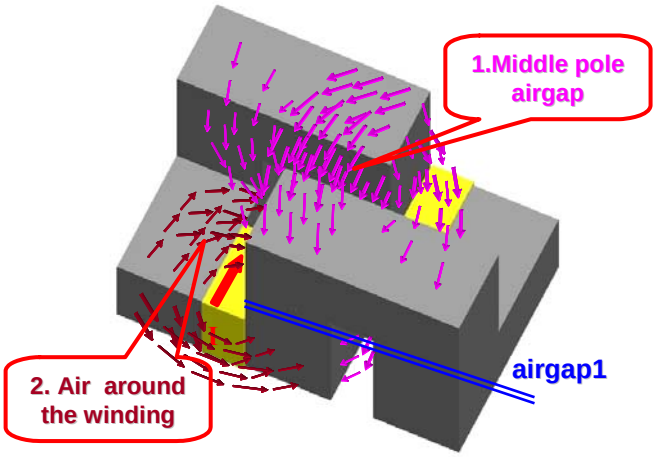

Figure 3.12 The two main leakage flux paths of the twisted-core coupled-inductors:the middle-pole-air-gap path and the air-around-the-winding path

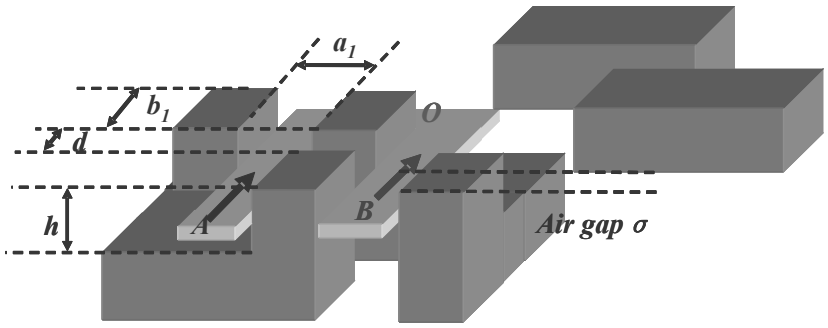

Figure 3.13 The dimension definition of the twisted core coupled inductor structure

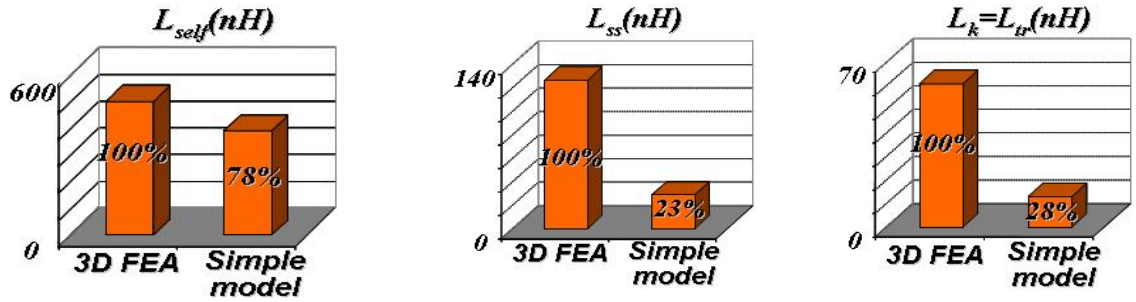

(a) (b) (c)

Figure 3.14 The L_{self}, L_{ss} and L_{tr}(L_k) precision of the conventional reluctance model without considering the fringing fluxes (h=2.5mm, b_1=4mm, a_1=2mm, d=2mm, and σ=0) (a) The L_{self} (b) the L_{ss} (c) the L_k=L_{tr}

3.2.2. Reluctance Model

To analyze and design the twisted-core coupled-inductors, the reluctance model of the twisted-core coupled-inductors is built in this section. In the following three subsections, the calculations of these three reluctances, the middle pole air gap reluctance R_{mid_airgap}, the reluatance of the air-around-the-winding R_{air}, the magnetic core reluctance R_{core} and the small air gap reluatance $R_{airgap1}$ are discussed. Here only the basic modeling concept is shown and the detail derivation of the equations is in the appendix.

3.2.2.1. The Middle-Pole Air Gap Reluctance R_{mid_airgap}

The 3D fringing effect related to the middle-pole air gap is very severe. Therefore, the 3D middle-pole air gap fringing effect must be considered when calculating the middle-pole airgap reluctance.

In [54], C. Sullivan investigated the 3D fringing effect for the E-E core structure, as shown in Figure 3.15. He separated the air gap flux cross-section into three areas: gap, face and corner. Gap is the area directly between the two poles, the face is the fringing fluxes between two parallel planes, and the corner is the remaining area.

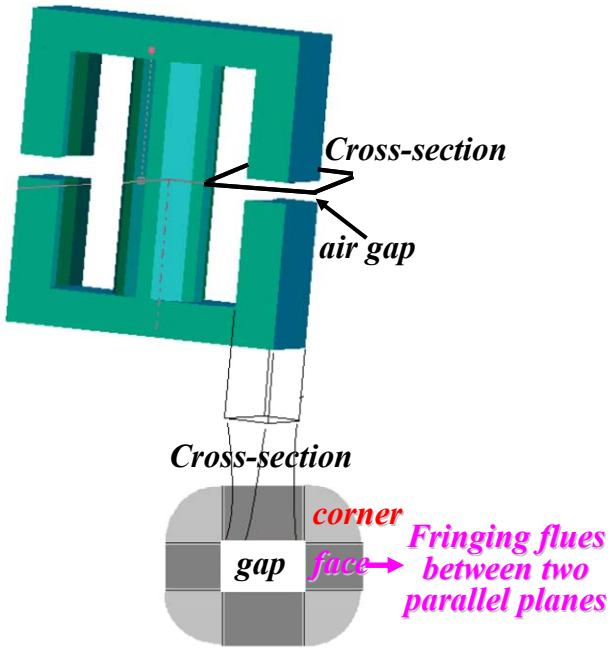

Figure 3.15 The air gap in the E-E magnetic core structure and the division of the air gap's 3D fringing fluxes mentioned in [54]

Following C. Sullivan's concept, a cut is made at the middle plane of the middle-pole air gap (Figure 3.16). The cross-section view after the cut is also shown in Figure 3.16, with half of the twisted-core as the reference. At the center of the middle-pole air gap cross-section view is the gap area, which represents the area just between the two middle-poles. The side areas of the gap area are the face areas, which represent the areas of the face fringing effect flux between two planes. The areas between the face areas are the corner areas, which represent the corner fringing effect flux areas.

However, the face area in the twisted-core coupled-inductor is not just the area between two parallel planes, but is actually quite complex. To find a method to deal with the complex face fringing flux area, 3D Maxwell simulations are done, and the fringing fluxes at the A_1, A_2, A_3 and A_4 planes shown in Figure 3.17 are illustrated in Figure 3.18.

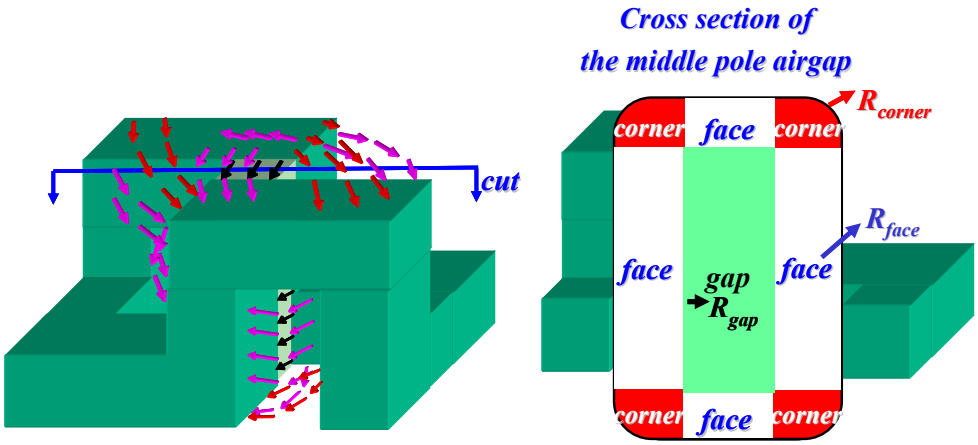

Figure 3.16 The cut at the middle pole air gap and the cross section view of the middle pole air gap after the cut

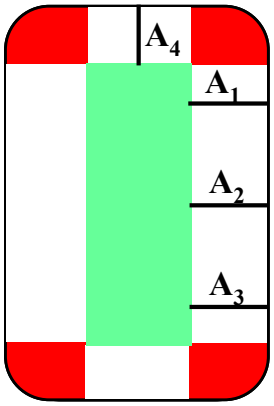

Figure 3.17 The different planes A_1, A_2, A_3 and A_4 with different face fringing flux conditions shown in the corss section view of the middle pole air gap

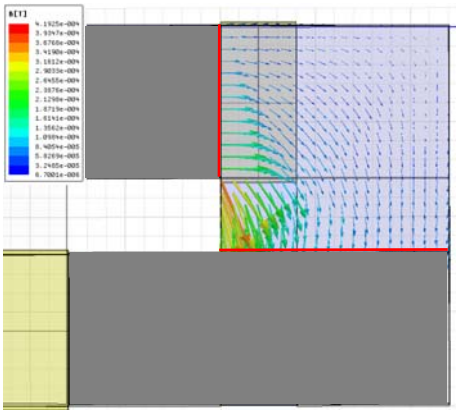

(a)

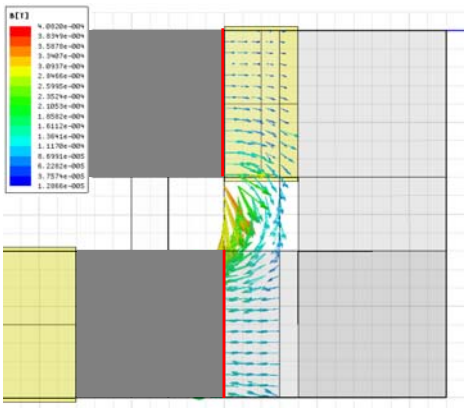

(b)

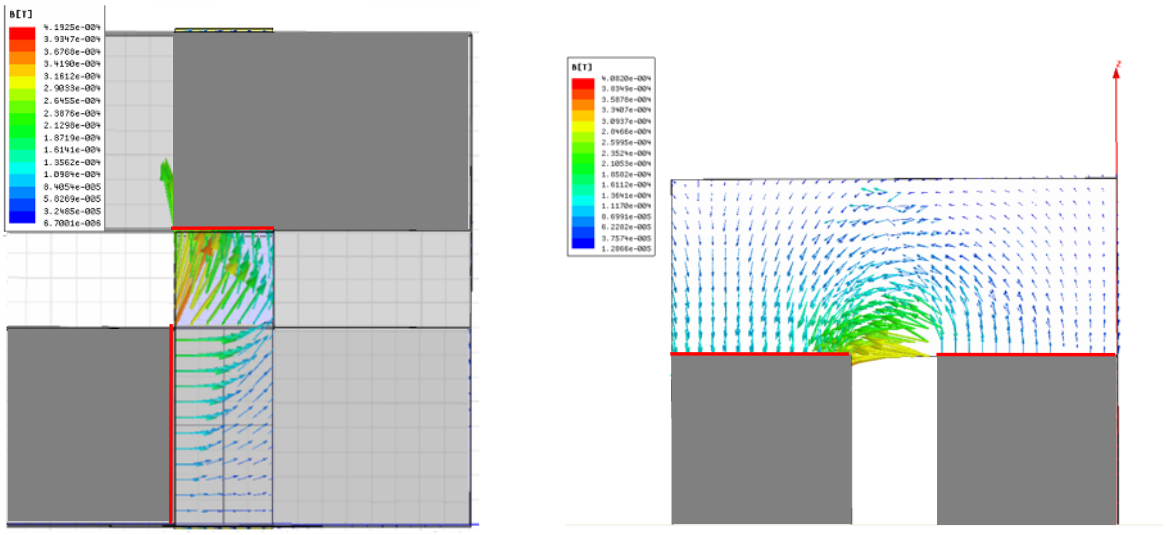

(c) **(d)**

Figure 3.18 The 3D FEA simulated fringing flux density distribution graphs at different planes in the face fringing flux area (a) The A_1 plane area (b) the A_2 plane area (c) the A_3 plane area (d) the A_4 plane area

The 3D Maxwell FEA simulation results show that the face fringing flux in A_1 is the fringing flux between two perpendicular planes; the face fringing flux in A_2 is the fringing flux between two parallel planes; the face fringing flux in A_3 is the fringing flux between two perpendicular planes; and the face fringing flux in A_4 is the fringing flux between two parallel planes.

According to the different face fringing flux conditions in the face area, two additional cuts are made, and the whole face area is further divided into three different face areas (Figure 3.19). The reluctances related to the face1 area, the face2 area and the face3 area are defined as R_{face1}, R_{face2} and R_{face3} respectively, and the reluctances related to the gap and corner areas are defined as R_{gap} and R_{corner}. Based on [55], the equations to calculate R_{face1}, R_{face2} and R_{face3} are derived. R_{gap} can be calculated with one-dimensional model and R_{corner} can be calculated based on [56]. (The detail derivations are in the Appendix).

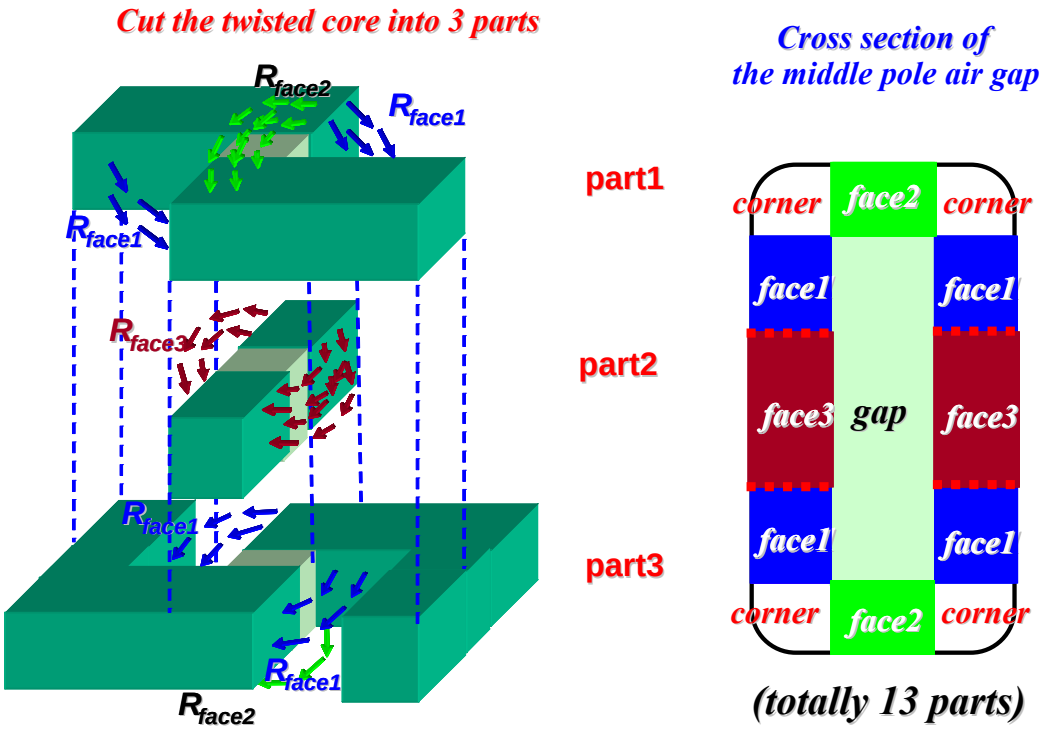

Figure 3.19 The three component parts of the twisted-core coupled-inductor after two horizontal cuts and the cross section view of the middle pole air gap after the two cuts

3.2.2.2. The Air-around-the-winding Reluctance R_{air}

Figure 3.20 shows the air-around-the-winding flux. It can be seen that this fringing flux can be looked as the fringing flux between two perpendicular planes. Therefore, it can be calculated similar as that in the middle-pole air gap.

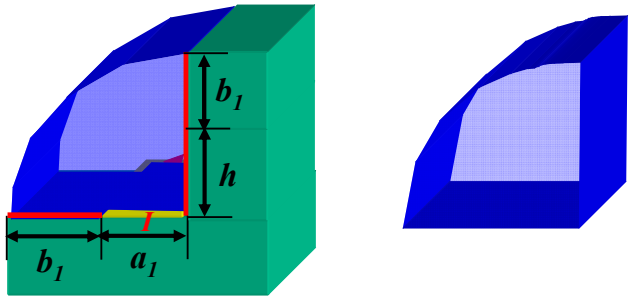

Figure 3.20 The air-around-the-winding fringing flux region in the twisted core coupled inductor and the air-around-the-winding fringing flux area

3.2.2.3. The Core Reluctance R_{core} and the Airgap1 Reluctance $R_{airgap1}$

For calculating R_{core}, we just use a one-dimensional reluctance model. $R_{airgap1}$ can be calculated based on the previous developed space cutting method. Figure 3.21 shows the different flux components in calculating $R_{airgap1}$.

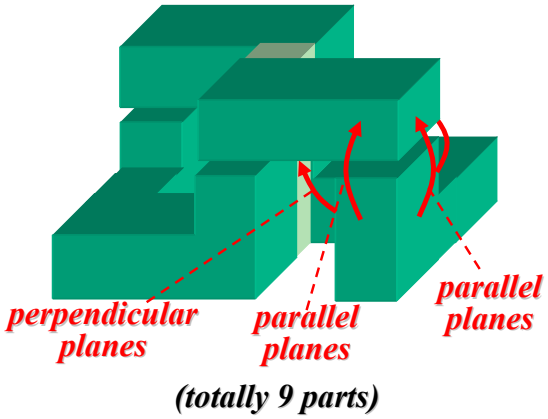

Figure 3.21 Different fringing flux components for the air gap 1 with the space cutting method developed for the middle pole air gap

Figure 3.22 shows the detail reluctance model with the fringing flux components marked. The dimensions of the twisted-core coupled-inductor are defined in Figure 3.23.

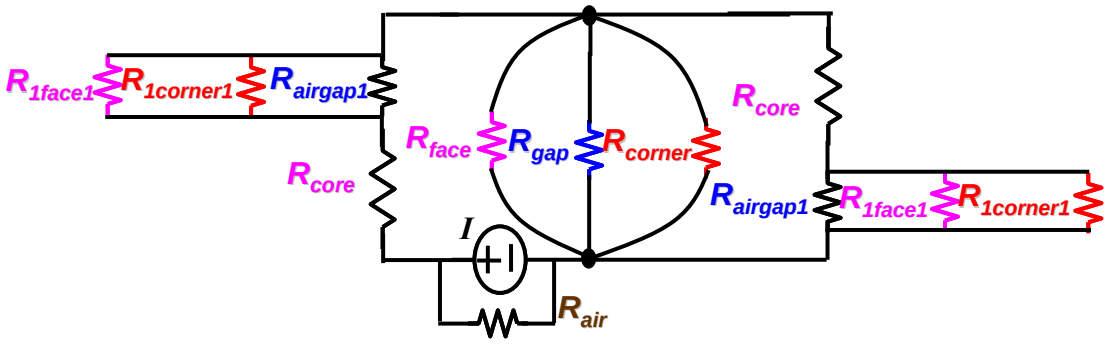

Figure 3.22 The detail new reluctance model of the twisted-core coupled-inductor considering the strong 3D fringing effect

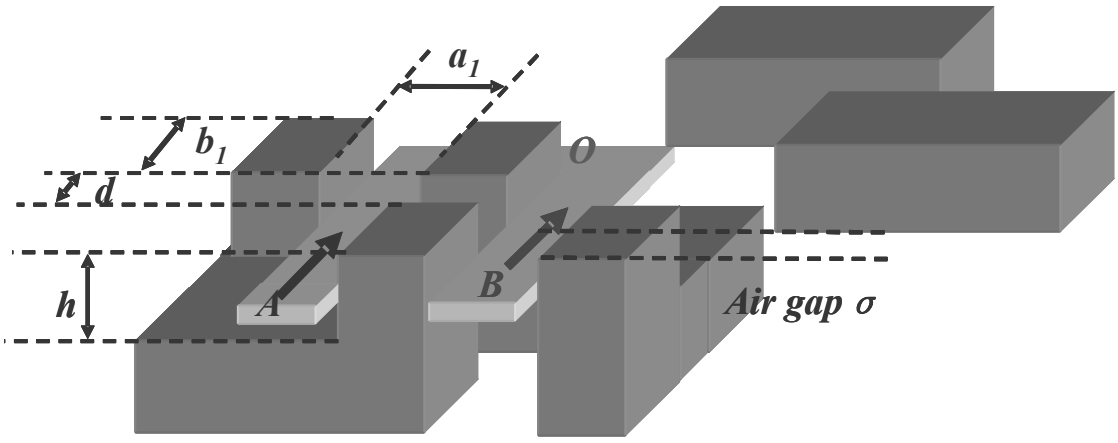

Figure 3.23 The dimensions of the twisted-core coupled-inductors: a_1, b_1, h, d and σ

According to the equations (1.10), (1.11), (1.13) and (1.16), the steady-state inductance and the transient inductance of the coupled-inductor buck (D<0.5) are

$$L_{ss} = \frac{L_{self}^2 - (L_{self} - L_k)^2}{L_{self} - \frac{D}{D'} \cdot (L_{self} - L_k)} \tag{3.5}$$

$$L_{tr} = L_{self} - M = L_k \tag{3.6}$$

The self-inductance L_{self} and leakage inductance L_k of the twisted-core coupled-inductors can be calculated based on the reluctance model.

$$L_{self} = \frac{R_{mid\_airgap}(b_1,d,h,\sigma) + R_{core}(b_1,a_1,d,h) + R_{airgap1}(b_1,h,\sigma)}{[R_{core}(b_1,a_1,d,h) + R_{airgap1}(b_1,h,\sigma)][2R_{mid\_airgap}(b_1,d,h,\sigma) + R_{core}(b_1,a_1,d,h) + R_{airgap1}(b_1,h,\sigma)]} + \frac{1}{R_{air}(b_1,a_1)} \tag{3.7}$$

$$L_k = \frac{1}{2R_{mid\_airgap}(b_1,d,h,\sigma) + R_{core}(b_1,a_1,d,h) + R_{airgap1}(b_1,h,\sigma)} + \frac{1}{R_{air}(b_1,a_1)} \tag{3.8}$$

$$R_{mid\_airgap}(b_1,d,h,\sigma) = R_{gap}(b_1,d,h,\sigma) // 0.25R_{face1}(b_1,d) // 0.5R_{face2}(b_1,d) // R_{face3}(b_1,d,h) // R_{corner}(b_1,d) \tag{3.9}$$

$$R_{gap}(b_1,d,h,\sigma) = \frac{d}{\mu_o b_1(2b_1 + h + \sigma)} \tag{3.10}$$

$$R_{face1}(b_1,d)\approx\frac{\pi}{b_1\mu_o[0.614+\ln(M^2(\frac{b_1}{d})+1)]} \tag{3.11}$$

$$R_{face2}(b_1,d)\approx\frac{2\pi}{b_1\mu_o(0.614+\ln(M^2(\frac{2b_1}{d})+1))} \tag{3.12}$$

$$R_{face3}(b_1,d,h)=\frac{\pi}{h\mu_o[0.614+\ln(M^2(\frac{2b_1}{d})+1)]} \tag{3.13}$$

$$M(\frac{b_1}{d})=\frac{\frac{\pi}{2}(1+\frac{b_1}{d})+\sqrt{\frac{\pi^2}{4}(1+\frac{b_1}{d})^2-2}}{2}) \tag{3.14}$$

$$R_{corner}(b_1,d)=\frac{1}{8}(\frac{1}{0.077\mu_o d}//\frac{4}{\mu_o b_1}) \tag{3.15}$$

$$R_{air}(b_1,a_1)=\frac{1}{\mu_o\frac{b_1}{\pi}\{0.614+\ln\{\frac{[\frac{\pi}{2}(1+\frac{b_1}{a_1})+\sqrt{\frac{\pi^2}{4}(1+\frac{b_1}{a_1})^2-2}]^2}{4}+1\}\}} \tag{3.16}$$

$$R_{core}(b_1,a_1,h,d)=\frac{2}{\mu_o\mu_r b_1}(\frac{h}{b_1}+\frac{\pi}{2})+\frac{1}{\mu_o\mu_r b_1}(\frac{d+2a_1}{b_1}+\frac{\pi}{4}) \tag{3.17}$$

$$R_{airgap1}(b_1,h,\sigma)=R_{1gap}(b_1,\sigma)//R_{1face}(b_1,h,\sigma)//R_{1corner}(\sigma) \tag{3.18}$$

$$R_{1gap}(b_1,\sigma)=\frac{2\sigma}{\mu_o b_1^2} \tag{3.19}$$

$$R_{1face}(b_1,h,\sigma)=2[R_{1face1}(b_1,h,\sigma)//0.5R_{1face21}(b_1,\sigma)//R_{1face22}(b_1,h,\sigma)] \tag{3.20}$$

$$R_{1face1}(b_1,h,\sigma)=\frac{\pi}{b_1\mu_o[0.614+\ln(M^2(\frac{h+b_1}{\sigma})+1)]} \tag{3.21}$$

$$R_{1face21}(b_1,\sigma)=\frac{2\pi}{b_1\mu_o(0.614+\ln(M^2(\frac{2b_1}{\sigma})+1))} \tag{3.22}$$

$$R_{1face22}(b_1,h,\sigma)=\frac{2\pi}{b_1\mu_o(0.614+\ln(M^2(\frac{2h}{\sigma})+1))} \tag{3.23}$$

$$R_{1corner}(\sigma) = \frac{1}{3}\left(\frac{1}{0.077\mu_o\sigma} // \frac{4}{\mu_o\sigma}\right) \tag{3.24}$$

Figure 3.24 shows the comparison between the calculation results with the above reluctance model and the 3D FEA simulation results made with Ansoft software for h=2.5mm, b_1=4mm, a_1=2mm, d=2mm, and σ=0. From Figure 3.24, we can see that the steady-state inductance has 83% precision, the self-inductance calculation result has about 92% precision, and that the leakage inductance calculation result has about 80% precision for the specific set of dimensions, compared with the 3D FEA simulation results. Figure 3.25 shows the approximate breakdown of the leakage inductance by covering the corresponding surfaces of the twisted-core with the low-permeability material proposed in [54]. The calculation precisions of the middle-pole airgap-related leakage inductance $L_{k\_mid\_airgap}$ and the air-around-the-corner-related leakage inductance L_{k_Rair} are also shown.

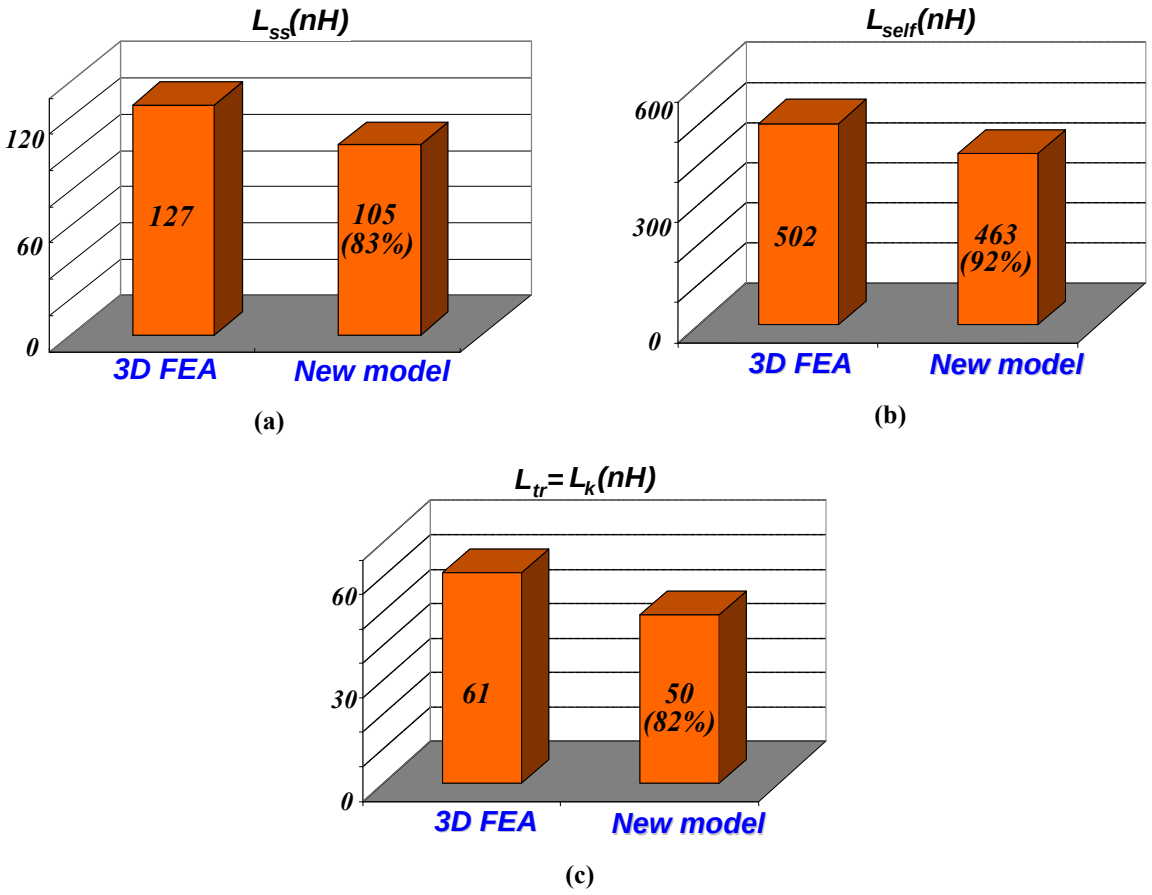

Figure 3.24 The precision of the new reluctance model considering the strong fringing effect (a) The L_{ss} precision (b) the L_{self} precision (c) the L_{tr}=L_k precison (h=2.5mm, b_1=4mm, a_1=2mm, d=2mm, and σ=0)

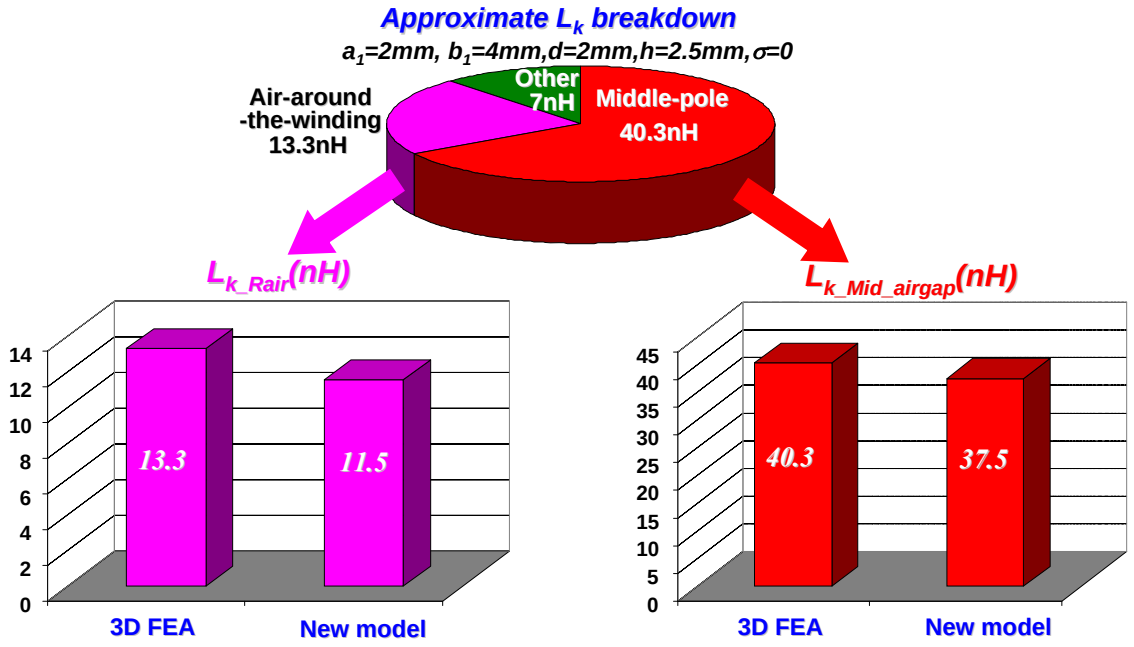

Figure 3.25 The approximate breakdown of the leakage inductance in the twisted-core coupled-inductor and the precision of the new reluctance model for different leakage inductance components

Figure 3.26 shows comparisons of the calculation results with the above reluctance model and of the 3D FEA simulation results with the Ansoft software for the different σ and d dimensions. From Figure 3.26, we can see that the reluctance model has a very good correlation for both the self-inductance and the leakage inductance.

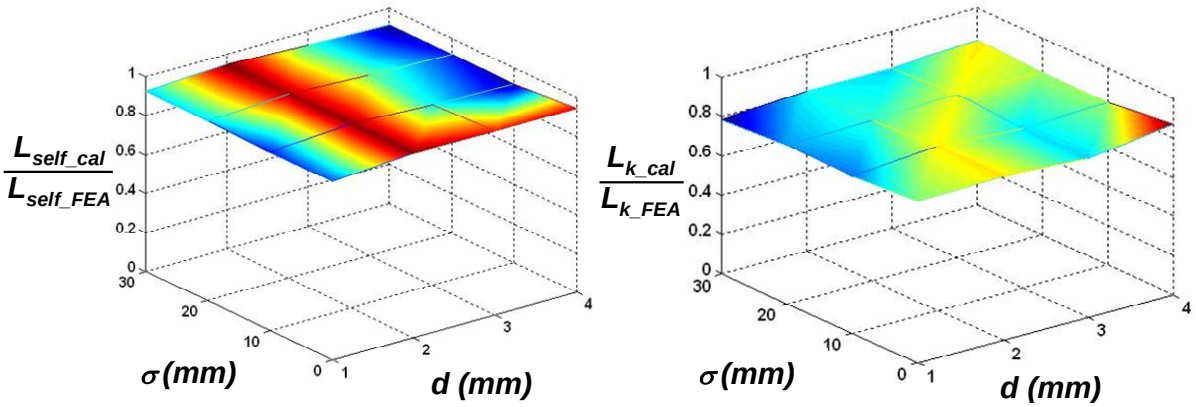

Figure 3.26 The ratio of the calculated self and leakage inductances based on the new model to the 3D FEA simulated self and leakage inductances vs. the dimension σ and d (a_1=2mm, b_1=4mm and h=2.5mm)

With the reluctance model, the effects of the different dimensions on L_{self} and L_k can be easily obtained. Figure 3.27 show the effects of σ, d and h on the L_{self} and L_k. It can be seen that L_{self} is very sensitive to σ, and L_k is very sensitive to d. Both L_{self} and L_k are not sensitive to h. This knowledge can be used in the twisted-core coupled-inductor design

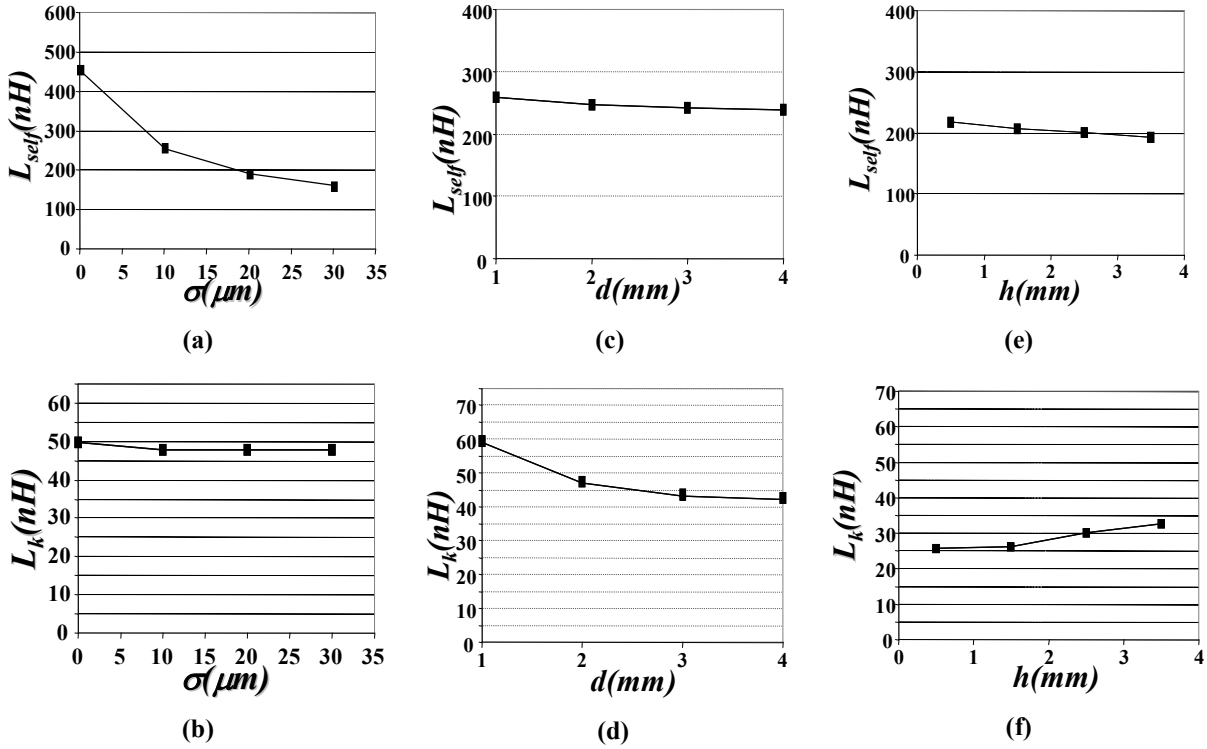

Figure 3.27 The curves of the L_{self} and L_k vs. σ, d and h (a) The L_{self} vs. σ (b_1=4mm, d=2mm, a_1=2mm, h=2.5mm) (b) the L_k vs. σ (b_1=4mm, d=2mm, a_1=2mm, h=2.5mm) (c) the L_{self} vs. d (b_1=4mm, σ=10um, a_1=2mm, h=2.5mm) (d) the L_k vs. d (b_1=4mm, σ=10um, a_1=2mm, h=2.5mm) (e) the L_{self} vs. h (a_1=2mm, d=2mm, σ=10um,b_1=3mm) (d) the L_k vs. h (a_1=2mm, d=2mm, σ=10um,b_1=3mm)

The following describes in detail the design procedure using the derived reluctance model, and a design example is provided.

3.2.3. Design Procedure

Assume that a two two-phase coupled-inductor for a four-phase buck converter with the targer:

V_{in}=12V,

V_o=1.2V,

f_s=1.2MHz,

I_o=100A,

With a fixed steady state inductance L_{ss}, a smaller transient inductance L_{tr} is preferred. The dimensions a_1, b_1, h, d, σ (Figure 3.28) will be designed step by step in the following.

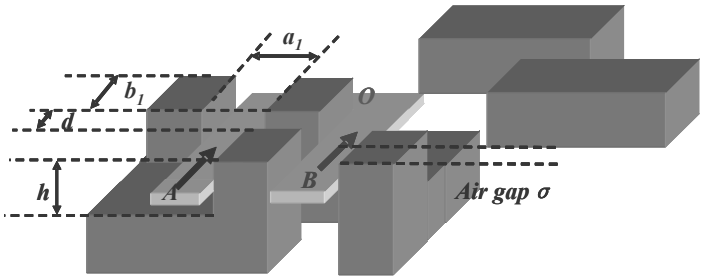

Figure 3.28 The dimensions of the twisted-core coupled-inductors: a_1, b_1, h, d and σ

Step 1: Calculate L_{self} and L_k

Assume the phase current ripple is 30 percent, then

$$L_{ss} = \frac{V_o(1-D)T_s}{0.3I_{phase}} \approx 107nH \tag{3.25}$$

Where V_o=1.2V, D=0.1, T_s=1/1.2MHz, I_{phase}=25A.

As mentioned in chapter, the coupled inductor buck circuit doesn't work when the coupling coefficient is -1. With a reasonable margin, choose the coupling coeffient α to be -0.8 (Figure 3.29),

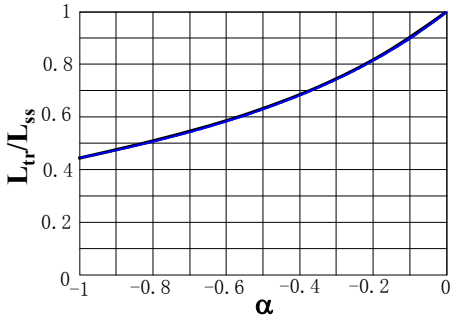

Figure 3.29 The curve of the L_{tr}/L_{ss} vs. the coupling coefficient α for the two-phase coupled-inductor buck converter (D=0.1)

$$L_{tr} = \frac{1+\frac{D}{D'}\alpha}{1-\alpha} L_{ss} \approx 55nH \tag{3.26}$$

where D is the duty cycle of the top switch of the buck converter and D' is 1-D.

The coupled-inductor's self-inductance L_{self} and leakage inductance L_k can be calculated based on the equations (1.13) and (1.16) to be

$$L_{self} = \frac{L_{tr}(D'L_{tr} + DL_{ss})}{2D'L_{tr} - (D'-D)L_{ss}} \tag{3.27}$$

$$L_k = L_{tr} \tag{3.28}$$

In this example, L_{self}=247nH and L_k=55nH.

Step 2: Select dimension h

In the previous reluctance model section, it is found that both L_{self} and L_k are not sensitive to h (Figure 3.27). Therefore, the dimension h should be chosen to be as similar as the inductor winding thickness. In our case, the PCB winding is adopted as the inductor winding. The thickness of the designed multiphase buck converter PCB board is about 2.3mm. Therefore we select h=2.5mm to leave some tolerance margin.

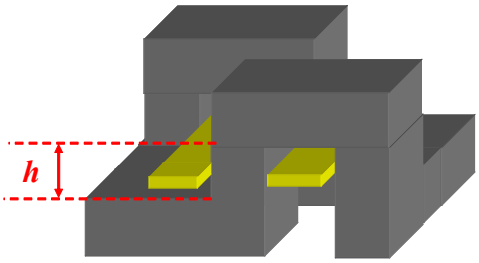

Figure 3.30 The dimension h in the twisted-core coupled-inductor structure

Step 3: Select dimension b_1

Dimension b_1 is shown in Figure 3.31. The b_1 is related to two things: thermal and magnetic core saturation.

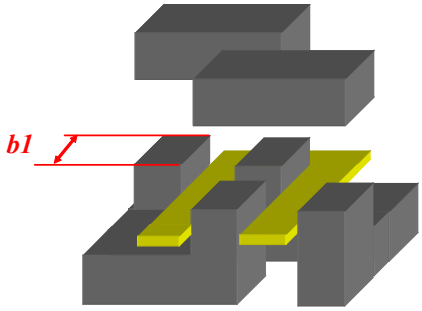

Figure 3.31 The dimension b_1 in the twisted-core coupled-inductor structure

To avoid thermal issues, we should design the b_1 so that the core loss density is acceptable. According to the Faraday's law

$$V_o = \frac{\Delta\Phi}{\Delta t} = \frac{2 \cdot \Delta B_{ac} \cdot A_c}{D' T_s} = \frac{2 \cdot \Delta B_{ac} \cdot A_c \cdot f_s}{D'} \tag{3.29}$$

where A_c is the cross-section of the twisted core, T_s is the switching period, f_s is the switching frequency and ΔB_{ac} is the suggested flux density value from the magnetic material datasheet. The across-section A_c is

$$A_c = b_1^2 \tag{3.30}$$

Substituting the equation (3.30) into the equation (3.29)

$$b_{1ac} = \sqrt{V_o D' / (2 \cdot f_s \cdot \Delta B_{ac})} \tag{3.31}$$

To avoid the magnetic core saturation, we should design b_1 so that the maximum flux density is less than B_{sat} of the magnetic material.

$$B_{\max} = B_{DC} + \Delta B_{ac} \tag{3.32}$$

Figure 3.32 shows the DC flux in the twisted core. It can be seen that

$$\Phi_{DC} = \Phi_{1DC} - \Phi_{2DC} \tag{3.33}$$

where Φ_{1DC} is the DC flux generated by I_1 and Φ_{2DC} is the DC flux generated by I_2.

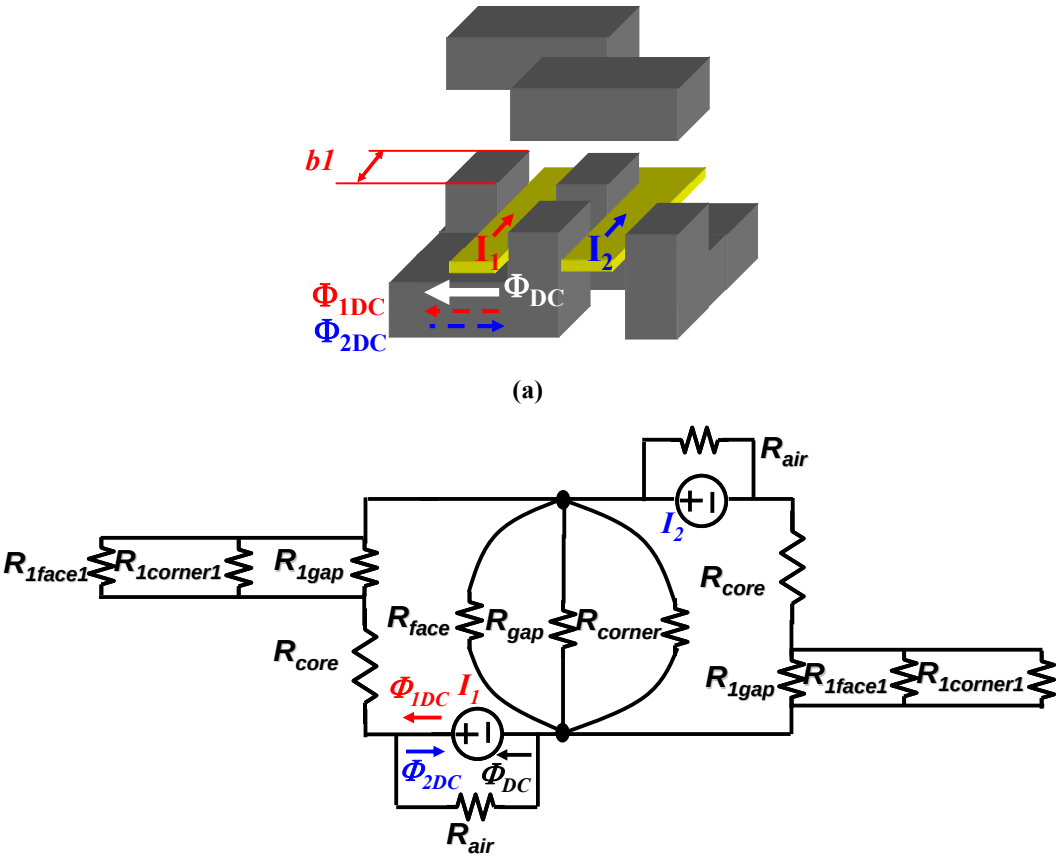

Figure 3.32 The DC flux in the phase current I_1 branch Φ_{DC} in the twisted-core coupled-inductor (Φ_{DC1}, the flux generated by the phase current I_1; Φ_{DC2}, the flux generated by the phase current I_2) (a) The fluxes in the twisted-core coupled-inductor structure (b) the fluxes in the twisted-core coupled-inductor reluctance model

$$\Phi_{1DC} = L_{self} \cdot I_1 \tag{3.34}$$

$$\Phi_{2DC} = | M | \cdot I_2 \tag{3.35}$$

Therefore

$$B_{DC} = \frac{\Phi_{DC}}{A_c} = \frac{L_{self} \cdot I_1 + M \cdot I_2}{b_1^2} \tag{3.36}$$

Substituting the equations (3.29) and (3.36) into the equation (3.32),

$$B_{\max} = [L_{self} I_1 + M I_2 + 0.5 V_o D' T_s] / b_1^2 \tag{3.37}$$

Since

$$B_{\max} \le B_{sat} \tag{3.38}$$

Therefore, the b_1 should be at least

$$b_{1\min} = \sqrt{[L_{self}(I_1 - I_2) + L_k I_2 + 0.5 V_o D' T_s] / B_{sat}} \tag{3.39}$$

where I_1 and I_2 are the maximum and minimum phase DC currents at the worst cases, and T_s is the switching period. In the design, the maximum value of b_{1ac} and b_{1min} should be chosen as b_1.

In this example, we choose 3F4 ferrite material. According to the core loss density curve from the datasheet, we choose B_{sat}=0.35T and from the datasheet, the recommended ΔB_{ac} is 50mT. We assume there are 40 percent DC current difference at the worst case. Therefore, I_1=30A and I_2=20A. According to the equations (3.31) and (3.39), b_{1ac}=4mm and b_{1min}=3.4mm, so we select b_1=4mm.

Step 4: Select dimension a_1

Dimension a_1 is shown in Figure 3.33. The a_1 can be calculated based on the winding current density

$$a_1 = I_o / (4 \cdot J \cdot t) \tag{3.40}$$

where I_o is the total output current, J is the winding current density and t is the winding thickness. We assume J=45A/mm^2, t=0.28mm, and a_1=2mm.

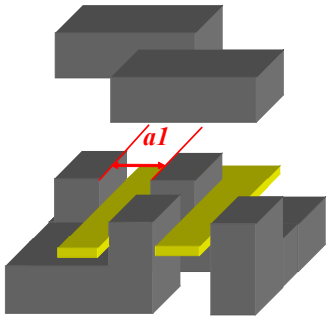

Figure 3.33 The dimension a_1 in the twisted-core coupled-inductor structure

Step 5: Select dimensions σ and d

Figure 3.34 shows the mimension d and σ. According to the equations (3.7) and (3.8),

$$L_{self}(\sigma,d) = 247nH = \frac{R_{mid\_airgap}(d,\sigma) + R_{core}(d) + R_{airgap1}(\sigma)}{[R_{core}(d) + R_{airgap1}(\sigma)][2R_{mid\_airgap}(d,\sigma) + R_{core}(d) + R_{airgap1}(\sigma)]} + \frac{1}{R_{air}} \tag{3.41}$$

$$L_k(\sigma,d) = 55nH * 0.85 = \frac{1}{2R_{mid\_airgap}(d,\sigma) + R_{core}(d) + R_{airgap1}(\sigma)} + \frac{1}{R_{air}} \tag{3.42}$$

Solving these equations, we get σ=10μm and d=2mm.

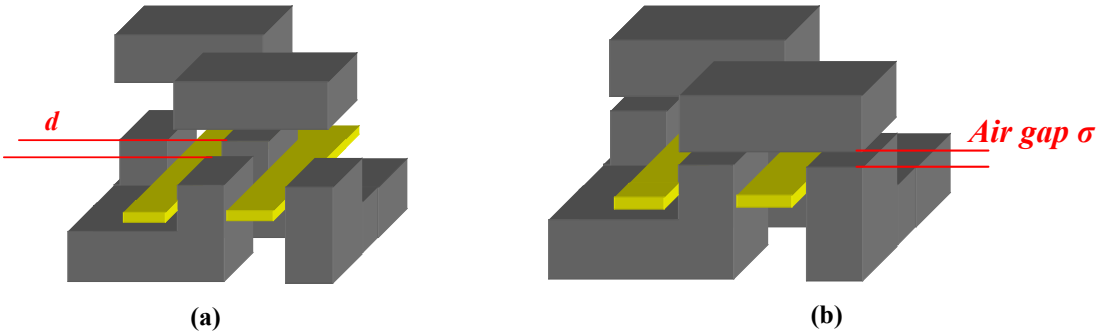

Figure 3.34 The dimensions d and σ in the twisted-core coupled-inductor structure (a) The middle pole air gap dimension d (b) the small air gap dimension σ

After 3D FEA simulation using the above dimensions (h=2.5mm, b_1=4mm, a_1=2mm, σ=10μm, d=2mm), it is found that L_{self}=262.2nH, L_k=57.45nH. Based on the equations (1.13) and (1.16), we have

$$L_{ss} = \frac{L_{self}^2 - (L_{self} - L_k)^2}{L_{self} - \frac{D}{D'}(L_{self} - L_k)} = 112nH \tag{3.43}$$

$$L_{tr} = L_k = 57nH \tag{3.44}$$

These 3D simulation results match the design requirement quite well.

3.2.4. Experimental results

According to the design results, real twisted-core coupled-inductors are customized, as shown in Figure 3.35. Table 3.1 shows the inductance testing results, the model results and the FEA simulation results for comparison. The testing results are pretty close to the 3D FEA simulation results and the design requirements.

Based on the twisted-core coupled-inductors, the twisted-core coupled-inductor VR is built with the values V_{in}=12V, V_o=1.2V, f_s=1.2MHz, and I_o=100A. Figure 3.36 shows the tested

phase-current waveforms. From the phase-current waveforms, we can see that the two phases are inversely coupled to each other.

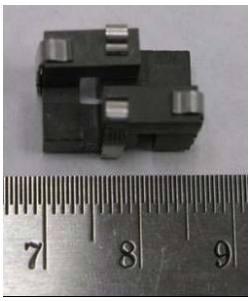

Figure 3.35 The customized 2-phase twisted-core coupled-inductors for the 2-phase coupled-inductor buck converter with V_{in}=12V, V_o=1.2V, f_s=1.2MHz, and I_{phase}=25A (picture by author, 2005)

Table 3.1 The comparison of the model, FEA and measurement results of the twisted-core coupled-inductor

	L_{self}(nH)	L_{ss}(nH)	$L_{tr}=L_k$(nH)
Simple model	222	36	16
New model	247	107	47
3D FEA simulation	262	112	57
Measurement	281	118	61

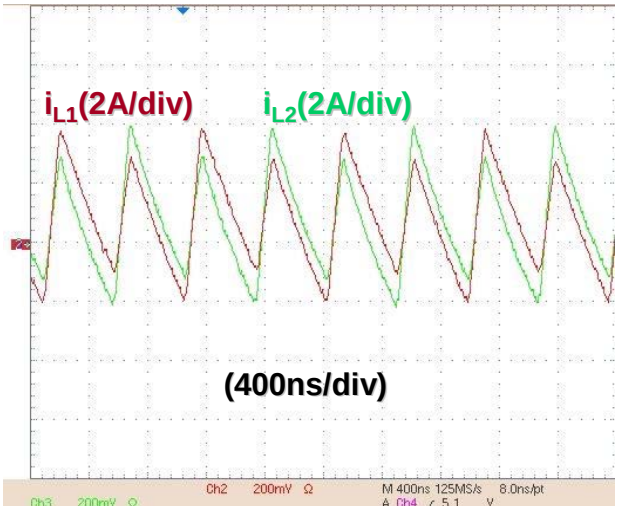

Figure 3.36 The phase-current waveforms of the two-phase twisted-core coupled-inductor buck converter with V_{in}=12V, V_o=1.2V, f_s=1.2MHz, and I_{phase}=25A

In this section, the twisted-core coupled-inductor is modeled by extending C. Sullivan's space cutting method and cutting the space with the strong fringing effect into the gap area, the corner area, the face areas between two perpendicular planes and the face areas between two parallel planes. This space-cutting method can also be used in other complex magnetic structures with strong fringing effects. The reluctance model illustrates the design procedure of the twisted-core coupled-inductors. Based on the design result, the twisted-core coupled-inductor is customized, and the twisted-core coupled-inductor buck converter prototype is built. The measurement results verify the twisted-core coupled-inductor, its reluctance model, and the design procedure.

However, the profile of the twisted-core coupled-inductor is high and not easy to be used. The low-profile twisted-core coupled-inductor is proposed to solve this issue. In the next section, the low-profile twisted-core coupled-inductor will be investigated.

3.3. Low Profile Twisted-core Coupled-inductor

3.3.1. Two-phase Low Profile Twisted-core Coupled-inductor

Figure 3.37 shows the low profile twisted-core coupled-inductor. It is the simplified version of the twisted-core coupled-inductor. Like the twistd-core coupled inductor, the 3D fringing effect is also very strong in this structure and the precise reluctance model considering the strong 3D fringing flux is necessary to design the low profile twisted-core coupled inductor.

Figure 3.37 The low profile twisted-core coupled-inductor

Since the two-phase low profile twisted-core coupled-inductor is a simplified twisted-core coupled-inductor, we can get a precise reluctance model of the two-phase low profile twisted-core coupled-inductor from the reluctance model for the twisted-core coupled-inductor, which is discussed in the previous section. Figure 3.38 the middle-pole airgap reluctance in the low profile twisted-core coupled inductor. Only the face2 fringing effect is needed to be calculated in

this case. The detail equations for the low profile twisted-core coupled-inductor are in the appendix.

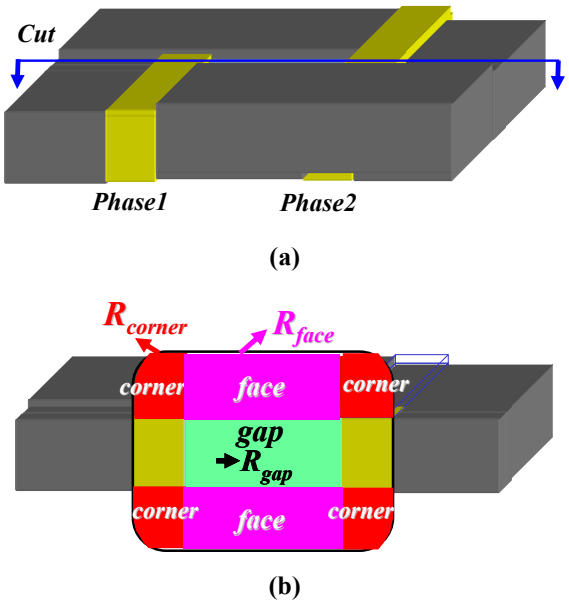

Figure 3.38 The separation of the middle-pole airgap fringing fluxes (a) Cut at the middle of the middle-pole airgap (b) The gap, face and corner flux areas in the cutting cross section of the middle-pole air gap

The dimension definition of the low profile twisted-core coupled-inductor is shown in Figure 3.38. The new reluctance model's precision is shown in Figure 3.40, when w=2mm, b_1=4mm, w_1=4mm, d=0.5mm, h=4.0mm, σ=30μm, and t=0.3mm. We can see that the precise reluctance model has around 80% precision for steady-state inductance and transient inductance.

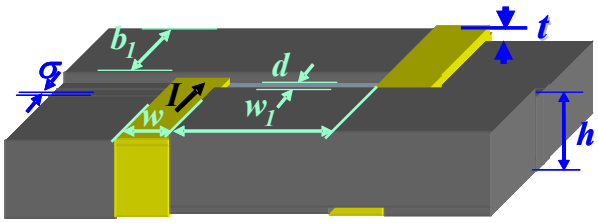

Figure 3.39 The dimension definition of the low profile twisted-core coupled-inductor structure

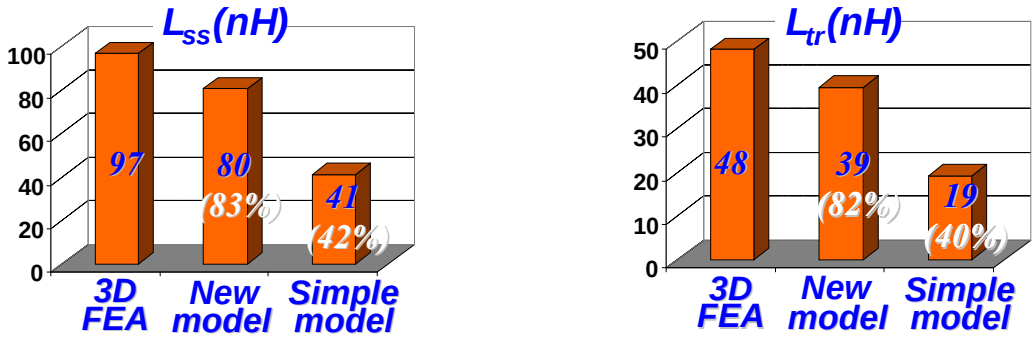

(a) (b)

Figure 3.40 The precision of the new reluctance model of the low-profile twisted-core coupled-inductor (w=2mm, b_1=4mm, w_1=4mm, d=0.5mm, h=4.0mm, σ=30μm, and t=0.3mm)

With the precise reluctance model of the low profile twisted-core coupled-inductor, we can design the low profile twisted-core coupled-inductor according to a given specification. In the following discussion, one design example is illustrated.

The design target is two-phase coupled-inductor for a 12V to 1.2 V, 1.2MHz, 20A/phase, buck VR.

Step 1: Calculating L_{self} and L_k

Assume the phase current ripple is 40 percent, then

$$L_{ss} = \frac{V_o(1-D)T_s}{0.4I_{phase}} \approx 89nH \tag{3.45}$$

Where V_o=1.2V, D=0.1, T_s=1/1.5MHz, I_{phase}=20A.

With a reasonable margin, choose the coupling coeffient α to be -0.8,

$$L_{tr} = \frac{1+\frac{D}{D'}\alpha}{1-\alpha} L_{ss} \approx 44.5nH \tag{3.46}$$

The coupled-inductor's self-inductance L_{self} and leakage inductance L_k can be calculated based on the equations (1.13) and (1.16) to be

$$L_{self} = \frac{L_{tr}(D'L_{tr} + DL_{ss})}{2D'L_{tr} - (D'-D)L_{ss}} \tag{3.47}$$

$$L_k = L_{tr} \tag{3.48}$$

In this example, L_{self}=245nH and L_k=44.5nH.

Step 2: Selecting dimension b_1

We preselect h=4.3mm firstly. In the following, the h will be iterated to find the best design.

Two aspects are related to dimension b_1: the magnetic core loss density and core saturation. The design equation for the magnetic core loss density is

$$b_{1ac} = V_o D' / [2 f_s \cdot h \cdot \Delta B_{ac}] \tag{3.49}$$

based on the Faraday's law. To avoid the magnetic core saturation, b_1 is to be at least

$$b_{1sat} = [L_{self}(I_1 - I_2) + L_k I_2 + 0.5 V_o D' T_s] / (h B_{sat}) \tag{3.50}$$

where I_1 and I_2 are the maximum and minimum phase DC currents at the worst case, respectively. T_s is the switching period.

In the design, the maximum value of b_{1ac} and b_{1sat} should be chosen as the b_1 value to avoid both the core loss density issue and the saturation issue.

In this example, we choose 3F4 ferrite material. According to the core loss and B-H characteristics in the 3F4 material datasheet, we choose B_{sat}=0.3T, ΔB_{ac}=30mT. We assume I_1=24A and I_2=16A at the worst case (maximum 40% phase DC current difference for both the steady-state condition and the transient condition). Then b_{1ac}=3mm and b_{1sat}=2.5mm, so we select b_1=3mm.

Step 3: Selecting dimensions w and d

Dimension w can be calculated based on the winding current density

$$w = I_o / (2 \cdot J \cdot t_{copper}) \tag{3.51}$$

where I_o is the total output current, J is the winding current density and t_{copper} is the winding thickness. We assume J=40A/mm^2, $t_{copper} \approx 4\delta$=0.2mm and w=2mm. Here, δ is the skin depth.

Dimension d is chosen to be as small as possible to minimize the footprint. $d=t_{copper}+t_{margin}$. We assume t_{margin}=0.2mm and d=0.4mm.

Step 4: Selecting dimensions σ and w_1

Now only dimensions σ and w_1 are left. They can be used to achieve the appropriate L_{self} and L_k. According to the equations (1.13) and (1.16),

$$L_{self}(\sigma, w_1) = 245nH \tag{3.52}$$

$$L_k(\sigma, w_1) = 44.5nH * 0.8 \tag{3.53}$$

Solving these equations numerically, we can get σ=20μm, w_1=3.5mm.

Step 5: Selecting h=5mm, 6mm, 7mm and repeat the design process 2-5

When the h=5mm, the design process 2-5 are repeated, and the design result is h=5mm,b_1=2.4mm,w_1=3.2mm, σ=20μm,d=0.4mm,w=2mm. When the h=6mm, the design process 2-5 are repeated, and the design result is h=6mm,b_1=2mm,w_1=3mm, σ=25μm,d=0.4mm,w=2mm. When the h=7mm, the design process 2-5 are repeated, and the design result is h=7mm,b_1=1.71mm,w_1=2.8mm, σ=25μm,d=0.4mm,w=2mm.

The winding loss, core loss and total loss of the above four designs are calculated and plotted in Figure 3.41. It can be seen that the design with h=5mm has the lowest inductor total loss. Therefore, it is the final design result.

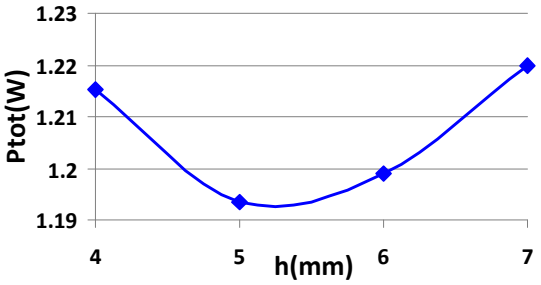

Figure 3.41 The graph of the inductor total loss vs. the h dimension

After 3D FEA simulation with the above dimensions (h=5mm,b_1=2.4mm,w_1=3.2mm, σ=20μm,d=0.4mm,w=2mm), it is found that L_{ss}=84nH and L_{tr}=42nH. We can see that the 3D simulation results match the design requirement quite well.

3.3.2. N-phase Low Profile Twisted-core Coupled-inductors

Figure 3.42 shows the three-phase ET-core coupled-inductor. The three-phase ET-core coupled-inductor can be modeled in a similar way to the two-phase low-profile twisted-core coupled-inductor.

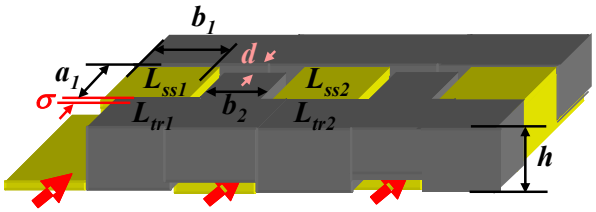

Figure 3.42 The three-phase ET-core coupled-inductor structure and its dimension definition

Figure 3.43 shows the reluctance model of the three-phase ET-core coupled-inductor. The equations for the reluctance model can be derived similarly as those of the two-phase low profile twisted-core coupled-inductor. The R_{mid_airgap} is shown in Figure 3.44. The R_{air} and R_{air1} are shown in Figure 3.45.

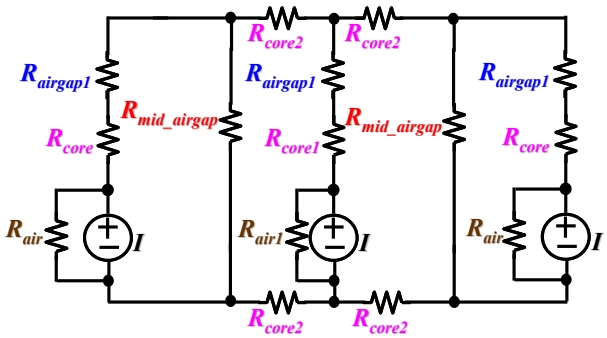

Figure 3.43 The reluctance model of three-phase ET-core coupled-inductor structure

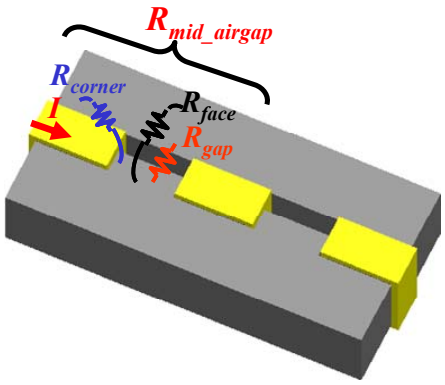

Figure 3.44 The middle-pole air gap reluctance R_{mid_airgap} and its reluctance components: the air gap reluctance R_{gap}, the face fringing flux reluctance R_{face} and the corner fringing flux reluctance R_{corner}

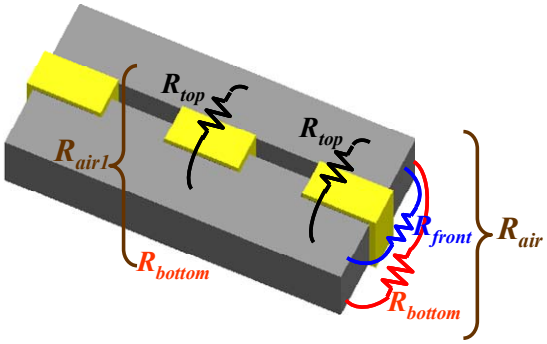

Figure 3.45 The air-around-the-winding reluctances R_{air} and R_{air1} and their reluctance components: the top reluctance R_{top}, the front reluctance R_{front} and the bottom reluctance R_{bottom}

Figure 3.46 shows the precision of the reluctance model when a_1=2.5mm, b_1=4mm, b_2=4mm, d=0.8mm, h=4.5mm, and σ=29μm. We can see that the precise reluctance model has around 80% precision for steady-state inductance L_{ss} and transient inductance L_{tr}. Therefore, the reluctance model can be used to design the three-phase ET-core coupled-inductor.

From Figure 3.46, it can also be seen that the three-phase ET-core coupled-inductor is nearly symmetric. According to the 3D simulation, it has only 3.6% difference for L_{ss}, and 0.24% difference for L_{tr}.

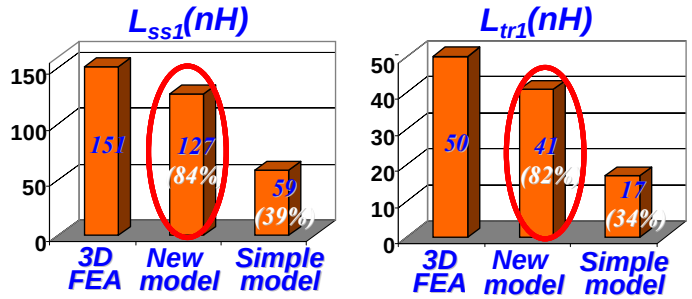

(a)

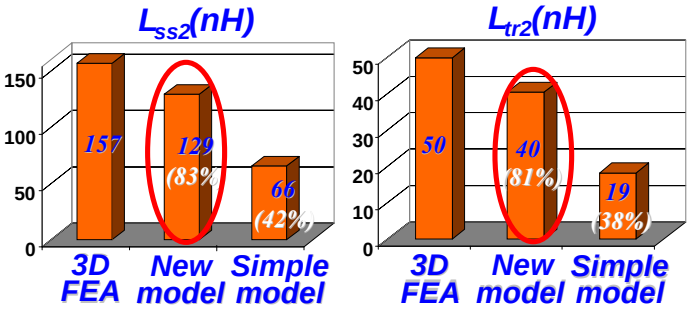

(b)

Figure 3.46 The precision of the reluctance model of the 3-phase ET core coupled-inductor structure (a_1=2.5mm, b_1=4mm, b_2=4mm, d=0.8mm, h=4.5mm, and σ=29μm) (a) The precision of the phase 1 inductances (b) The precision of the phase 2 inductances

3.4. Comparison of Different Coupled-inductor Structures

Table 3.2 lists the loss comparison of the low profile twisted-core coupled-inductor and the twisted-core coupled-inductor when the phase-current is 20A, f_s=1.2MHz, V_{in}=12V, V_o=1.2V. The total inductor loss can save 12 percent.

Table 3.2 The two-phase twisted-core coupled-inductor vs. two-phase low profile twisted-core coupled-inductor

	The twisted-core coupled-inductor	The low profile twisted-core coupled-inductor
The winding length	10mm (per phase)	17mm (per phase)
The winding loss	0.225W	0.38W
The core loss	0.7825W	0.51W
The total loss	1.01W	0.89W

Table 3.3 lists the loss comparison of the three-phase twisted winding coupled-inductor and the three-phase ET-core coupled-inductor when the phase-current is 20A, f_s=1.2MHz, V_{in}=12V, V_o=1.2V. It can be seen that the total inductor loss of the three-phase ET-core coupled-inductor can save 14 percent.

Table 3.3 The three-phase twisted winding coupled-inductor vs. the three-phase ET-core coupled-inductor

	The twisted winding coupled-inductor	The three-phase ET-core coupled-inductor
The winding length	32mm (per phase)	25mm (per phase)
The winding loss	1.08W	0.874W
The core loss	0.511W	0.517W
The total loss	1.591W	1.364W

From Table 3.2 and Table 3.3, we can see that the low-profile twisted-core coupled-inductors are better than the twisted-core coupled-inductor. This is because the low-profile twisted-core coupled-inductors trade off the winding loss and the core loss and a smaller inductor total loss can be achieved.

3.5. Summary

In this section, the twisted-core coupled-inductor and the low-profile twisted-core coupled-inductor are proposed to reduce the winding paths of the coupled-inductors.

To model the twisted-core coupled-inductor, a complex space cutting method is proposed to model the strong 3D fringing flux effect by extending C. Sullivan's space-cutting method. This modeling method can also be used for other complex magnetic structures with strong fringing effects. The resulting reluctance model can be used to get a sense of the inductance with respect to the structure dimensions, and to find a better coupled-inductor design.

The designs based on the reluctance models of the twisted-core coupled-inductors and the low-profile twisted-core coupled-inductors are illustrated and verified by experiment.

Chapter 4. LTCC Integrated Coupled-inductor Structures

Today, the trend in POL converters is integration. More and more POL converters are integrated to reduce the size and increase the power density. The present bottleneck to reaching higher power density is the large magnetic inductor size. In this chapter, different coupled inductor structures are proposed to reduce the magnetic inductor size and improve the whole POL converter power density based on the LTCC process. The proposed LTCC coupled-inductor structures are investigated, analyzed and designed. Based on the designs, LTCC coupled-inductor prototypes are customized. The experimental results with the customized LTCC coupled inductors verify the above theoretical analysis. With the proposed LTCC integrated coupled inductor, the integrated POL converter achieves a power density of 500W/in^3, which is about twice the power density of its LTCC non-coupled inductor buck POL converter counterpart.

4.1. CPES 3D LTCC Integrated POL Converter

The existing POL converers are either the low-current, high-power-density converters or the high-current, low-power-density converters [57-63]. There is no one with both the high-current and high power-density. A. Ball in CPES developed a 3D integrated POL converter which broke through the power-density-vs-current boundary of today's POL converters.

Figure 4.1 shows the 3D LTCC integrated POL converter concept. It is the layer-by-layer structure. The active stage is made by several layers and the passive stage, the inductor, is made by several LTCC layers and serves as the substrate of the whole converter. Based on the experimental testing, the B-H curve of the LTCC ferrite tape material after sintering is shown in Figure 4.2. The saturation flux density is around 0.18T.

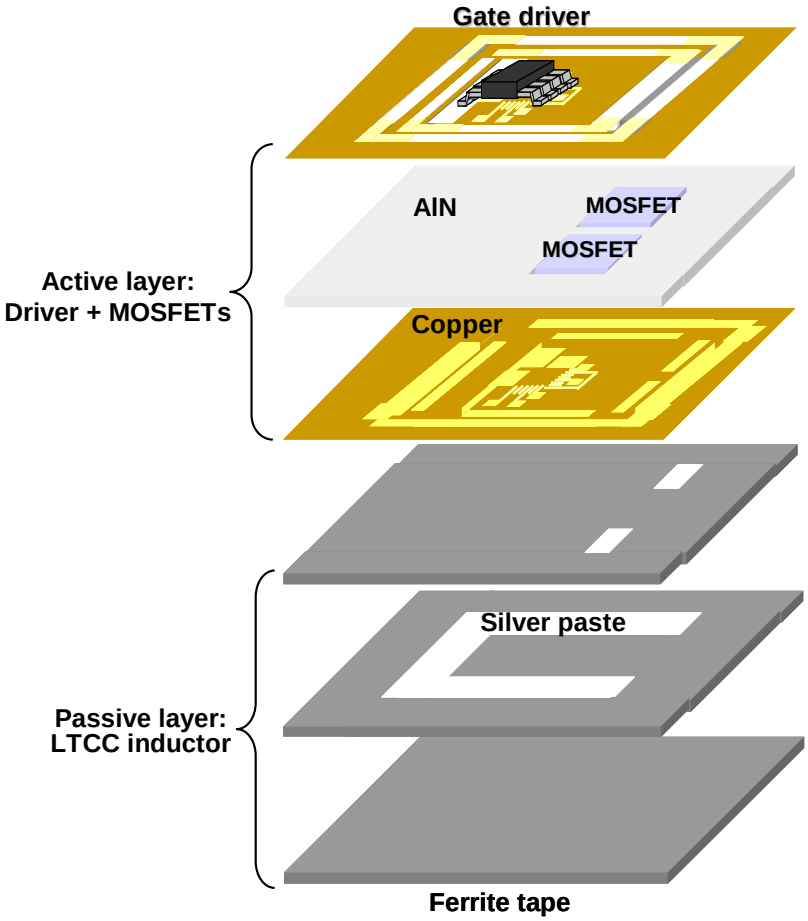

Figure 4.1 The CPES LTCC 3D integrated POL converter concept

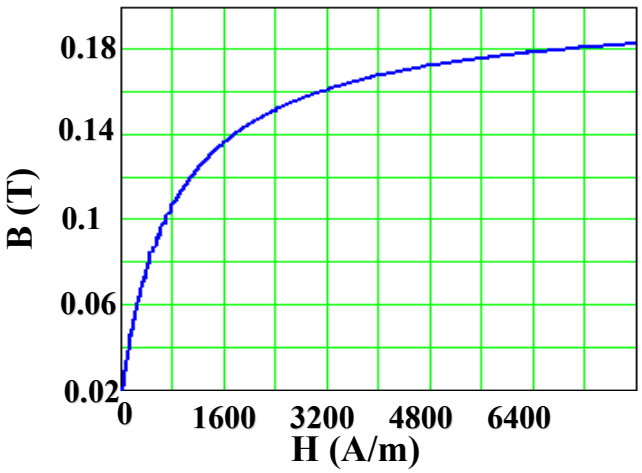

Figure 4.2 The B-H characeristic of the μ_{nom}=200 LTCC ferrite green tape material

In A. Ball's 3D integrated POL converter, both the high current limitation and the high power density limitation (thermal limitation) are addressed. Trench MOSFET switches are adopted to handle high current. The aluminum-nitride (AlN) double-bond copper (DBC) ceramics are used as the die holder to improve the active stage thermal conductivity and performance [64-73]. With the AlN DBC, double-side-cooling can be achieved, which further improves the thermal performance of the 3D integrated POL converter module.

An LTCC inductor with the special silver paste winding is adopted for the magnetic device. By controlling the size of the winding cross-section and its length, the inductor DCR can be designed to be very low and appropriate for high-current integrated POL converter module applications.

Figure 4.3 shows the CPES 20A 3D integrated stack power POL converter module prototype. Its specifications are V_{in}=5V, V_o=1.2V, f_s=1.3MHz and I_o=20A. Its footprint is 18x18 mm^2, and its power density is 260W/in^3. Figure 4.4 shows the LTCC integrated inductor for the 3D integrated POL converter.

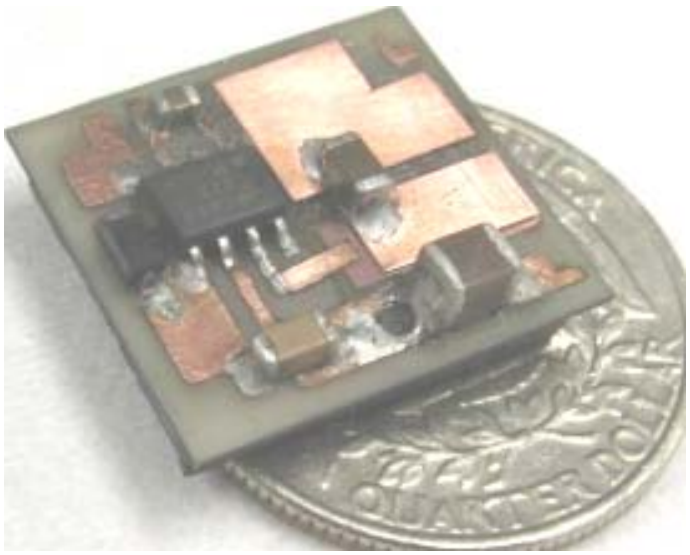

Figure 4.3 The CPES 3D integrated POL converter module prototype (V_{in}=5V, V_o=1.2V, f_s=1.3MHz, I_o=20A, footprint: 18mmx18mm) [73]. ***Used with permission of Arthur Ball, 2009***

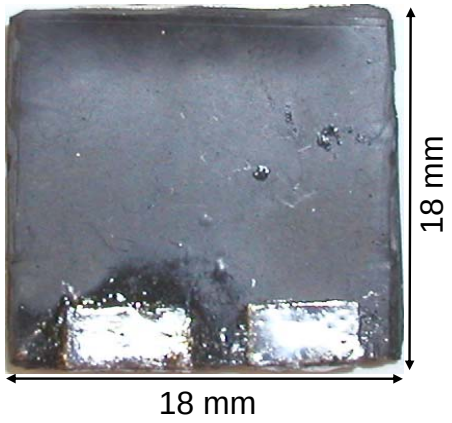

Figure 4.4 The LTCC integrated non-coupled inductor for the CPES LTCC 3D integrated POL converter module

To further increase the current level and the POL converter module power density, both the active stage and the passive inductor should be improved. By utilizing two AlN DBC layer to facilitate the trace layout and changing the driver package from SO-8 (5x6 mm^2) to the LLP (4x4 mm^2) to reduce the footprint, the new active stage can be built with the smaller footprint of 8x12 mm^2.

However, the LTCC inductor is 18x18mm^2 in footprint, much larger than the active stage. Therefore, the large LTCC inductor footprint has become the bottleneck for further improving the power density of the integrated POL converter (Figure 4.5).

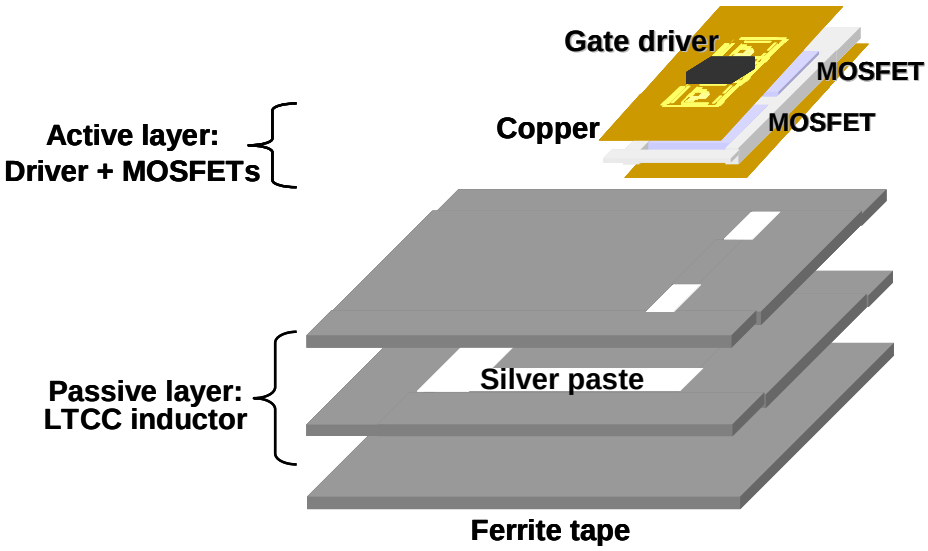

Figure 4.5 The large LTCC inductor footprint compared to the small active stage footprint (inductor footprint: 18x18mm^2; the active stage footprint: 8x12mm^2)

In Section 2 and 3 of this chapter, two LTCC integrated inverse-coupled inductor structures are proposed. Then, they are simulated, analyzed, designed, customized and compared. After that, the better LTCC integrated coupled-inductor structure is adopted to build the final 3D LTCC integrated coupled-inductor POL converter in Section 4. The electrical and thermal performances of the 3D integrated LTCC coupled-inductor POL converter are shown. Finaly, Section 5 summarizes the whole chapter.

4.2. LTCC Integrated Coupled-inductor Structure 1

Coupled-inductors are well-known for their capabilities to increase efficiency and improve the transient performance in multiphase buck converters. In this section, the coupled-inductor buck is proposed to significantly reduce the magnetic size and to improve the power density of the integrated POL converter.

Figure 4.6 shows a two-phase coupled-inductor buck converter. Figure 4.7 shows one LTCC inverse-coupled inductor structure (LTCC integrated coupled-inductor structure 1). The fluxes generated by the two phase-currents are also shown in Figure 4.7. It can be seen that the magnetic fluxes generated by the two-phase currents couple with each other. In the outer legs, the two magnetic fluxes cancel with each other. As defined in the chapter 1, the steady-state inductance and the transient inductance are

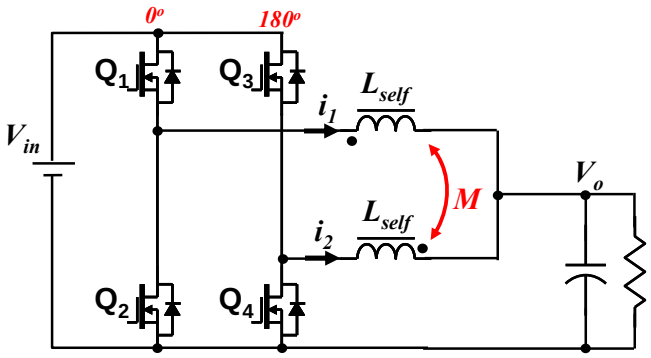

Figure 4.6 A two-phase coupled-inductor buck converter

$$L_{ss} = \frac{1-\alpha^2}{1+D\alpha/D'} L_{self} \tag{4.1}$$

$$L_{tr} = (1+\alpha)L_{self} \tag{4.2}$$

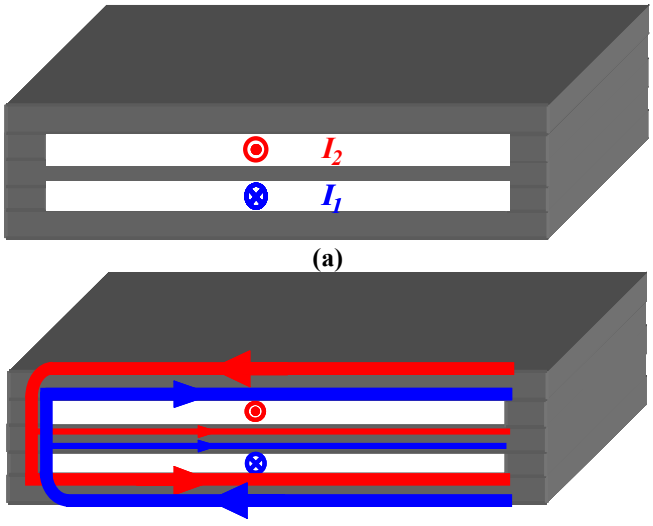

Figure 4.7 LTCC integrated coupled-inductor structure 1 (a) Structure 1 (b) The magnetic flux generated by the two-phase currents

The coupling coefficient α is

$$\alpha = \frac{M}{L_{self}} \tag{4.3}$$

In the next subsections, the LTCC coupled-inductor structure 1 will be analyzed and modeled. The design based on the reluctance model will be illustrated and the prototype will be customized and tested.

4.2.1. Controlling the coupling coefficient by the dimension t_2

Figure 4.8 shows the dimension definition of the LTCC integrated coupled-inductor structure 1. There are five dimensions: w_s, w_1, t_1, t_2 and t_s.

Maxwell 3D FEA simulation is adopted to evaluate the method to control the coupling coefficient. In the Maxwell 3D FEA simulation, the B-H curve of the LTCC ferrite material, the dimension information and the phase-current information I_1=I_2=20A are input into the Maxwell simulator.

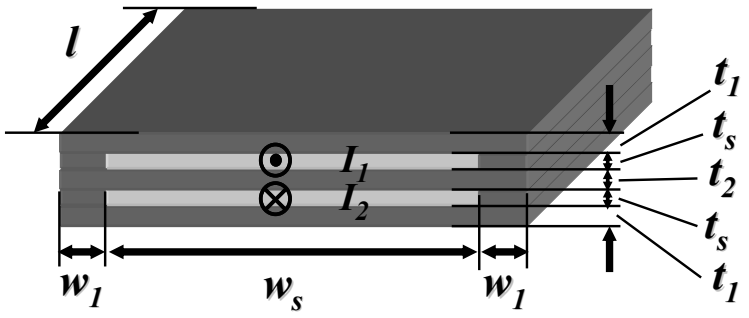

Figure 4.8 The dimension definition of the LTCC integrated coupled-inductor structure 1

In the three cases simulated with the Maxwell 3D FEA Tool (Figure 4.9), w_s=6mm, w_1=0.7mm, t_1=0.7mm, t_s=0.5mm, and l=24mm. In the case 1, t_2=0.6mm; in the case 2, t_2=1mm; in the case 3, t_2=1.4mm. When t_2 increases, the middle leg is less saturated. Therefore, the permeability of the middle leg is larger and the coupling coefficient is smaller. The couping coefficients for these three cases are shown in Figure 4.10.

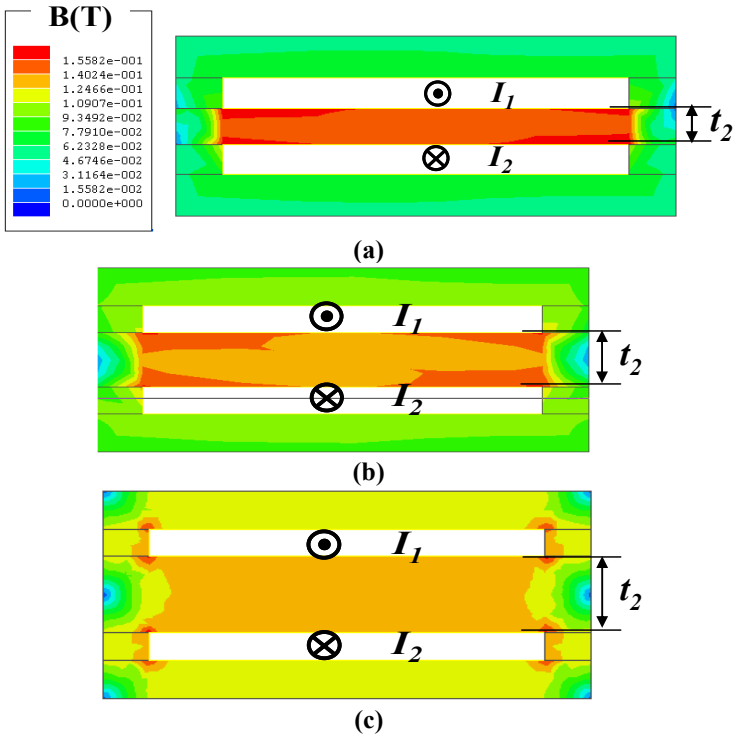

Figure 4.9 The DC flux density distribution of three LTCC coupled inductor structure 1 cases with different t_2 (w_s=6mm, w_1=0.7mm, t_1=0.7mm, t_s=0.5mm, and l=24mm) (a) t_2=0.6mm (b) t_2=1mm (c) t_2=1.4mm

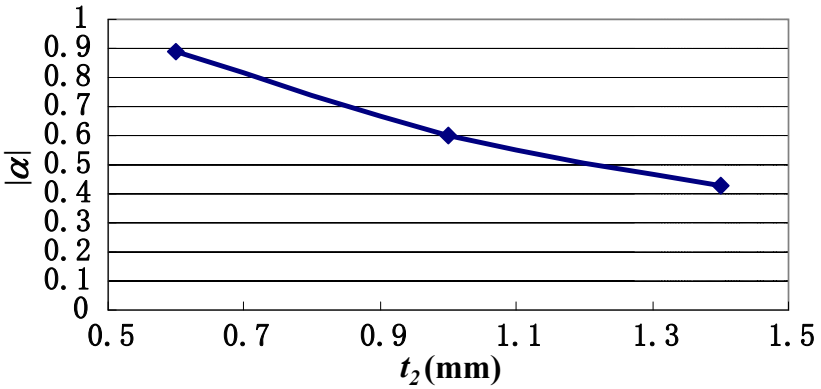

Figure 4.10 The effect of t_2 on the coupling coefficient (w_s=6mm, w_1=0.7mm, t_1=0.7mm, t_s=0.5mm, and l=24mm)

It can be seen from Figure 4.10 that when the t_2 increases, the coupling coefficient of the LTCC integrated coupled-inductor decreases. Therefore, t_2 can be used to control the coupling of the LTCC integrated coupled-inductor.

4.2.2. Reluctance Model

Figure 4.11 shows the DC flux density distribution when w_s=6mm, w_1=0.7mm, t_1=0.7mm, t_s=0.5mm, l=24mm, t_2=1mm and I_1=I_2=20A. It can be seen that although the different points in the core structure opereate at different B-H curve points, the points in the middle leg approximately operate in one area in the B-H curve and the points in the outer legs operate in another area in the B-H curve. If the permeabilities of the points in the middle leg are assumed to be the same and the permeabilities of the points in the outer legs are assumed to be the same, Figure 4.11 is simplified to Figure 4.12(a). There are two permeabilities for the whole magnetic structure. In another word, the B-H curve of the ferrite tape is approximated by the two-segment B-H curve shown in the Figure 4.12(b).

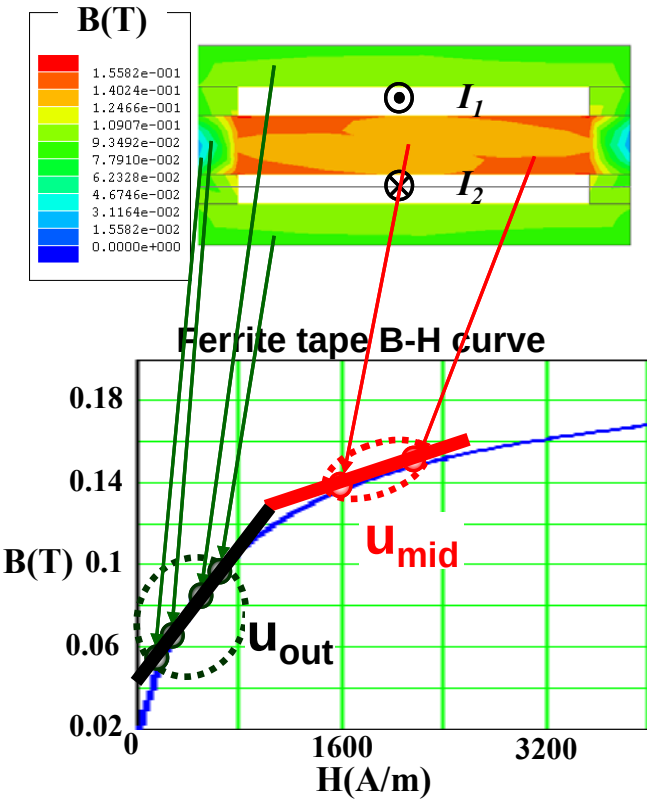

Figure 4.11 Mapping the DC flux density of different points in the LTCC integrated coupled-inductor structure 1 to the B-H curve of the ferrite tape (w_s=6mm, w_1=0.7mm, t_1=0.7mm, t_s=0.5mm, l=24mm, t_2=1mm)

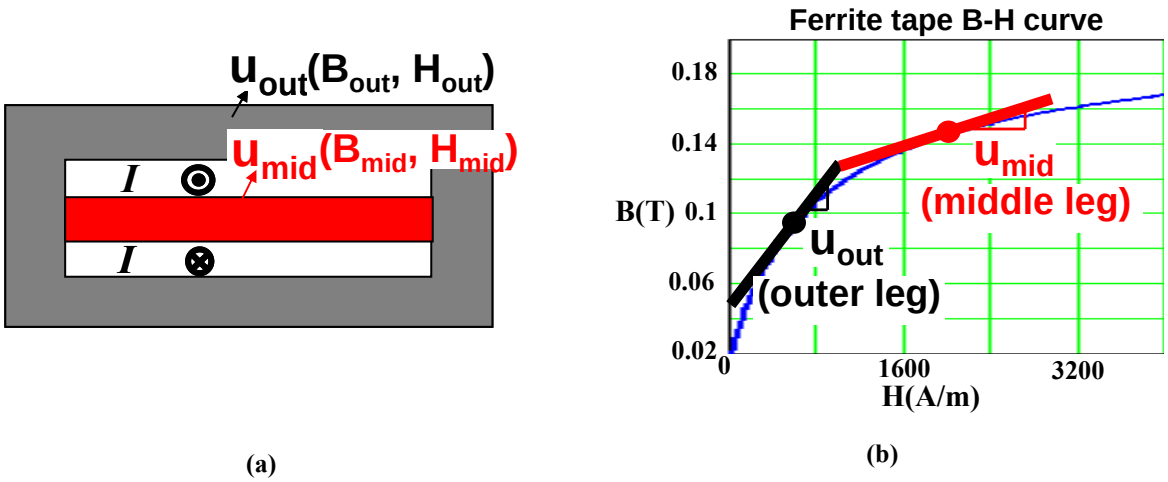

(a) **(b)**

Figure 4.12 The two-segment B-H curve approximation (a) The LTCC integrated coupled-inductor structure with two-segment approximation (b) The two-segment B-H curve approximation of the ferrite tape material

Under the two-segment B-H curve approximation, the relationship between the flux densities in the middle leg and the outer leg can be investigated. Figure 4.13 shows the DC fluxes generated by the two phase DC currents and the remaining fluxes after the DC flux cancellation. From Figure 4.13, it can be seen that

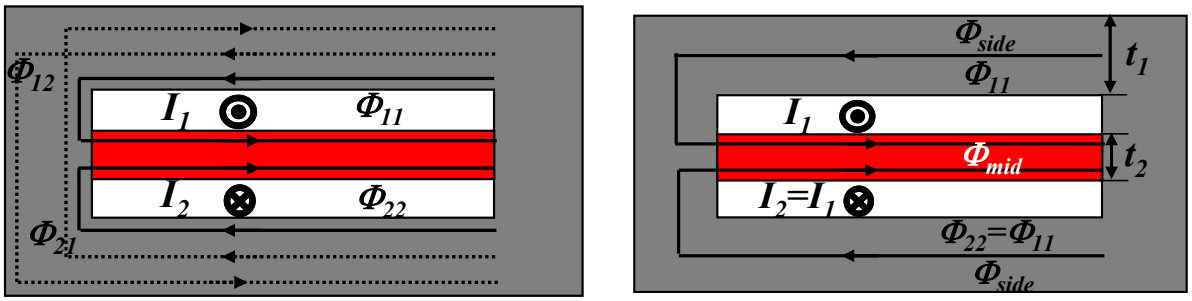

(a) (b)

Figure 4.13 The DC flux distribution in the LTCC integrated coupled-inductor structure 1 (b) The DC fluxes generated by the two phase DC currents (b) the remaining fluxes after the DC flux cancellation

$$\Phi_{mid} = 2\Phi_{11} = 2\Phi_{side} \tag{4.4}$$

Since

$$\Phi_{mid} = B_{mid} t_2 l \tag{4.5}$$

$$\Phi_{side} = B_{side} t_1 l \tag{4.6}$$

Therefore

$$B_{mid} / B_{side} = 2t_1 / t_2 \tag{4.7}$$

Combining the equation (4.7) and Figure 4.12(b), the relationship between the u_{out} and t_1/t_2 can be drawn with a certain B_{mid}. When B_{mid}=0.15T, Figure 4.14 shows this relationship.

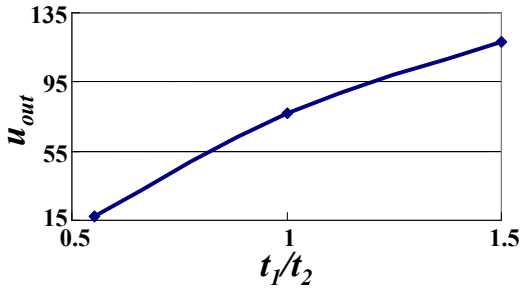

Figure 4.14 The relationship between the outer leg permeability u_{out} and the ratio t_1/t_2 when B_{mid}=0.15T

The reluactance model of the LTCC integrated coupled-inductor structure is very simple under the two-segment B-H curve approximation. Figure 4.15 shows the reluctance model of the LTCC integrated coupled-inductor structure.

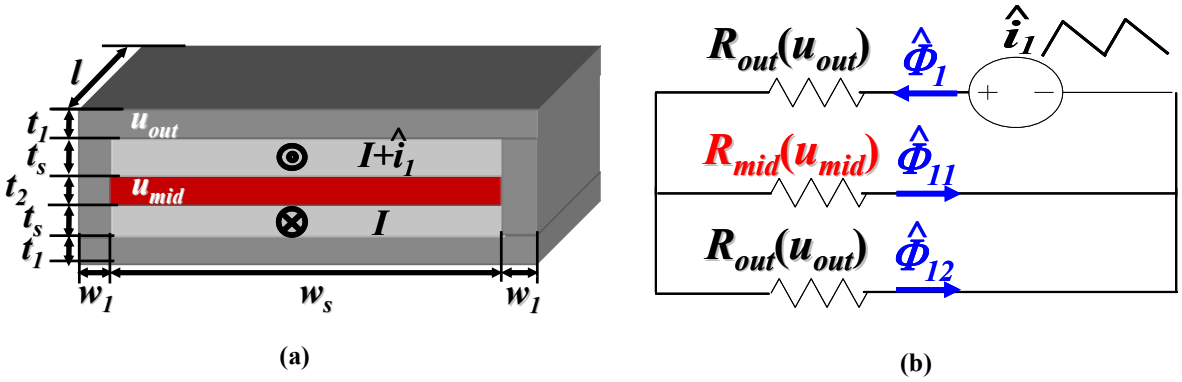

Figure 4.15 The reluctance model of the integrated coupled-inductor structure 1 (a) The LTCC coupled-inductor structure 1 with the dimension and the current excitation (b) The reluctance model

The reluctance of the outer leg is calculated based on the permeability in the outer leg, u_{out} and the reluctance of the middle leg is calculated based on the permeability in the middle leg, u_{mid}.

The R_{mid} and R_{side} equations are written as follows

$$R_{mid} = \frac{w_s}{u_0 u_{mid}\, t_2 l} \tag{4.8}$$

$$R_{out} = \frac{w_s}{u_0 u_{out}\, t_1 l} + \frac{2t_s}{u_0 u_{out}\, w_1 l} \tag{4.9}$$

Based on the reluctance model, the L_{self}, L_k and the coupling coefficient $|\alpha|$ can be calculated as follows

$$L_{self} = \frac{\hat{\Phi}_1}{\hat{i}_1} = \frac{R_{out} + R_{mid}}{R_{out}(R_{out} + 2R_{mid})} = K_1 \cdot l \tag{4.10}$$

where $\hat{\Phi}_1$ is the total flux generated by $\hat{i}_1$, and

$$K_1 = \frac{u_{out}u_0}{(\frac{w_s}{t_1}+\frac{2t_s}{w_1})[1+\frac{1}{1+\frac{(\frac{w_s}{t_1}+\frac{2t_s}{w_1})\frac{u_{mid}}{u_{out}}t_2}{w_s}}]} \tag{4.11}$$

$$L_k = \frac{\hat{\Phi}_{11}}{\hat{i}_1} = \frac{1}{R_{out}+2R_{mid}} \tag{4.12}$$

where $\hat{\Phi}_{11}$ is the flux generated by the $\hat{i}_1$, which flows through the middle leg and not through the outer legs.

$$|\alpha| = \frac{L_{self}-L_k}{L_{self}} = \frac{R_{mid}}{R_{out}+R_{mid}} \approx \frac{1}{1+\frac{t_2}{t_1}\cdot\frac{u_{mid}}{u_{out}}} \tag{4.13}$$

From the equation (4.13), it can be seen that $|\alpha|$ decreases as t_2 increases. It is the same as the conclusion drawn from the Maxwell 3D FEA simulation results. The equation (4.13) shows that the coupling coefficient α is the function of t_2 and t_1.

Substituting the equations (4.10) and (4.13) into the equation (1.13) and rearranging the terms,

$$L_{ss} = \frac{1-\alpha^2}{1+\frac{D}{D'}\alpha}\cdot K_1 \cdot l = K_3 \cdot l \tag{4.14}$$

where,

$$K_3 = \frac{1-\alpha^2}{1+\frac{D}{D'}\alpha}\frac{u_{out}u_0}{(\frac{w_s}{t_1}+\frac{2t_s}{w_1})[1+\frac{1}{1+\frac{(\frac{w_s}{t_1}+\frac{2t_s}{w_1})\frac{u_{mid}}{u_{out}}t_2}{w_s}}]} \tag{4.15}$$

Figure 4.16 shows the reluctance model's precision in case 2, when t_2=1mm. From Figure 4.16, it can be seen that the two-segment B-H curve approximation is acceptable. Although it is

not as precise as the 3D FEA simulation, it is much, much faster than the 3D FEA simulation. In the following, the reluctance model will be used to design the LTCC integrated coupled-inductor structure.

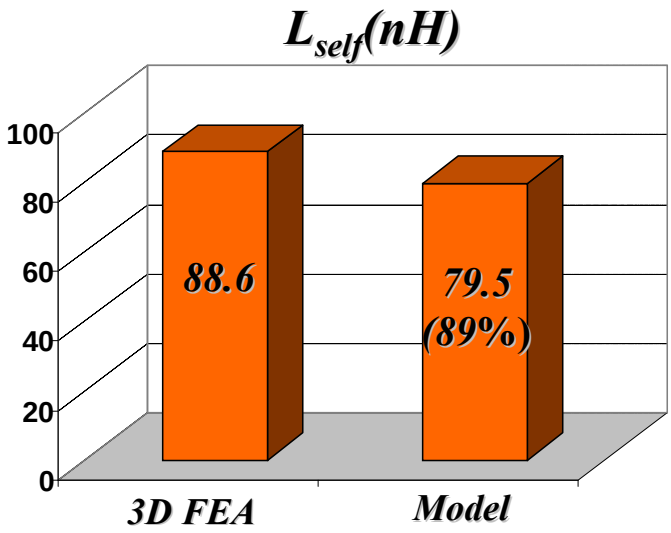

(a)

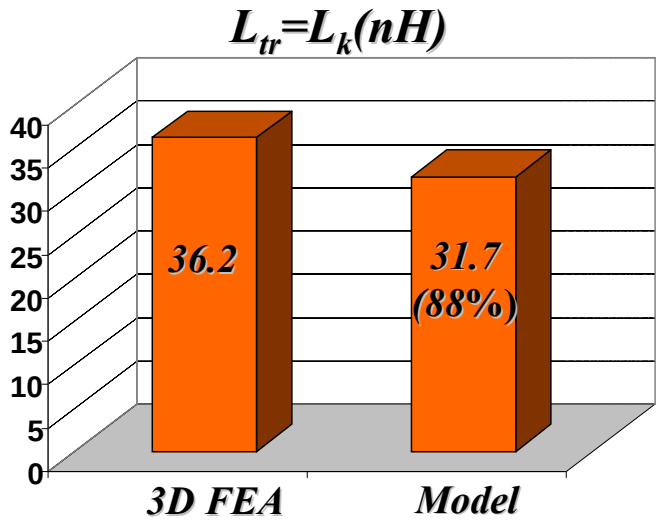

(b)

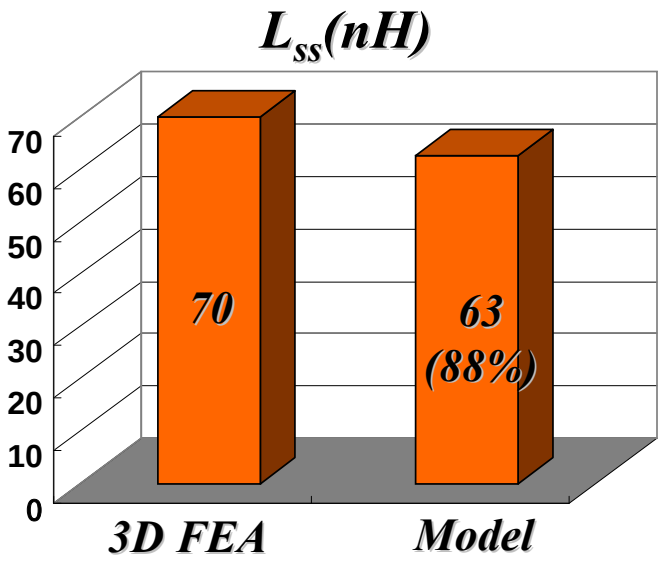

(c)

Figure 4.16 The precision of the reluctance model with the two-segment B-H curve approximation when w_s=6mm, w_1=0.7mm, t_1=0.7mm, t_s=0.5mm, *l*=24mm and t_2=1mm (a) The L_{self} precision (b) The L_{tr}=L_k precision (c) The L_{ss} precison

4.2.3. Design Example

Assuming that a LTCC integrated coupled-inductor needs to be designed for a two-phase integrated coupled inductor buck converter with the following design target:

V_{in}=5V,

V_o=1.2V,

f_s=1.3MHz,

I_{phase}=20A,

A smaller volume is preferred,

With a fixed steady state inductance L_{ss}, a smaller transient inductance L_{tr} is preferred.

The dimensions w_1, w_s, t_1, t_2, t_s and *l* (Figure 4.17) will be designed in the following design procedure step by step.

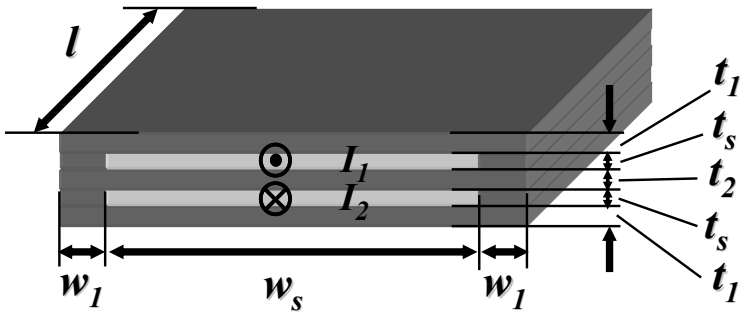

Figure 4.17 The dimensions of the LTCC integrated coupled-inductor structure 1

Step 1: Assume w=12mm and *l*=16mm

Figure 4.18 shows the active stage layout and the LTCC inductor footprint. The total footprint is 192mm^2. Keeping the total LTCC inductor footprint to be the same, there are many different combinations of width and length. Figure 4.19 shows one w and l dimension case of the LTCC inductor with the footprint of 192mm^2.

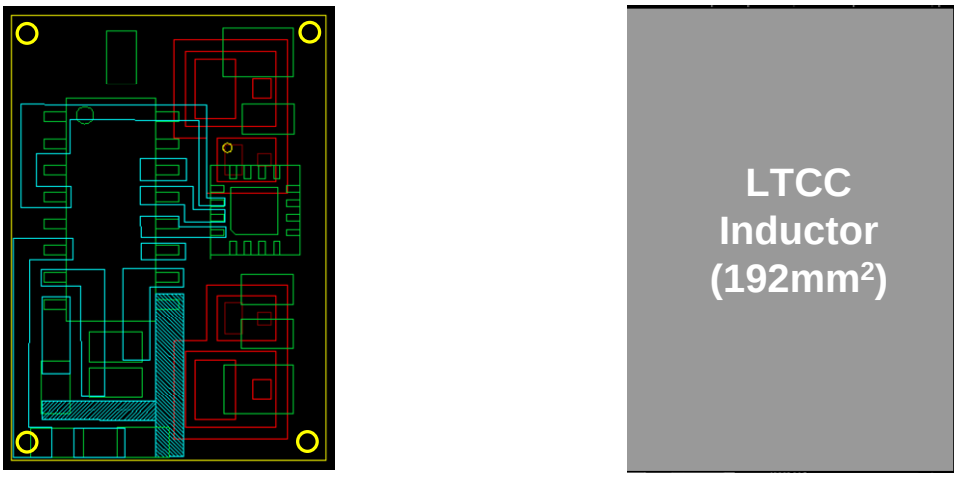

(a) **(b)**

Figure 4.18 Determining the LTCC coupled inductor footprint by the active stage of the LTCC coupled inductor buck converter (a) the active stage layout (b) the available footprint of the LTCC coupled inductor

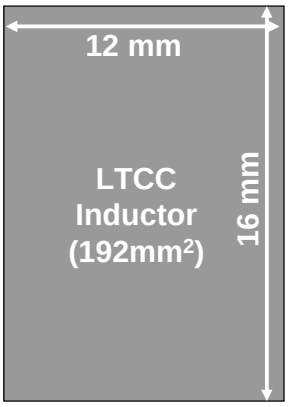

Figure 4.19 One w and *l* dimension case of the LTCC coupled inductor with the footprint of 192mm² (w=12mm, *l*=16mm)

Firstly, the design will be investigated for the w=12mm, and *l*=16mm. After this, the designs with w=8mm and w=4mm will be investigated. Figure 4.20 shows this LTCC coupled inductor with marked w and *l* dimensions.

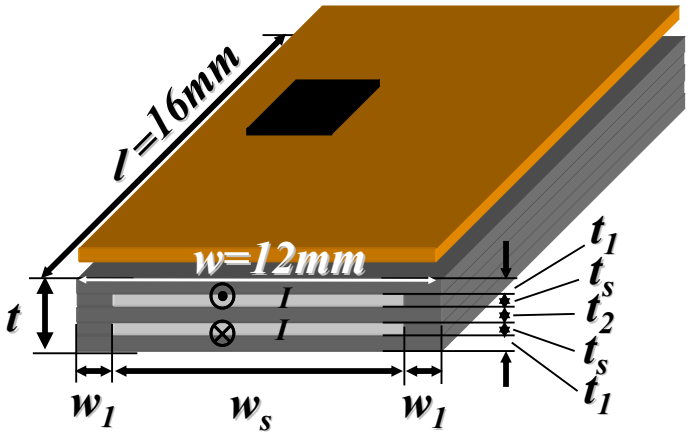

Figure 4.20 The LTCC integrated coupled-inductor with the marked w and *l* dimensions

Step 2: Calculate L_{ss}

We assume the phase-current ripple to be 50% of the phase current. Therefore, the steady-state inductance can be calculated.

$$L_{ss} = \frac{V_o(1-D)T_s}{0.5I_{phase}} = 68nH \tag{4.16}$$

Step 3: Select w_s

Figure 4.21 shows the dimension w_s. It can be seen that

$$w_s=w-2*w_1 \tag{4.17}$$

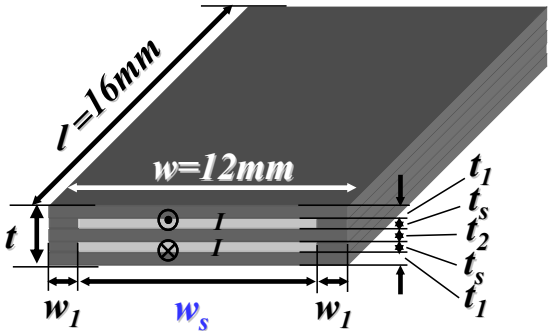

Figure 4.21 The w_s dimension of the LTCC coupled inductor with w=12mm and *l*=16mm

Theoretically, w_1 should be equal to t_1. However, because of the the LTCC process limitation, the w_1 is at least 1mm, which is normally larger than t_1. Therfore, w_1 is chosen to be 1mm.

$$w_s=w-2*w_1=10mm \tag{4.18}$$

Step 4: Select t_s

Figure 4.22 shows the dimension t_s. Here, t_s is determined by the winding loss. The relationship between the winding loss and the t_s is drawn in Figure 4.23. In Figure 4.23, δ is the skin depth, which is equal to 0.065mm at 1.3MHz. It can be seen that when t_s increases, there is a diminishing return in the winding loss. Therefore, t_s is chosen around the diminishing return area.

$$t_s=4.5\delta=0.3mm \tag{4.19}$$

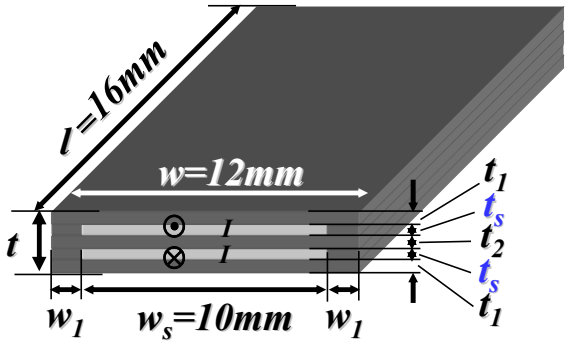

Figure 4.22 The t_s dimension of the LTCC coupled inductor with w=12mm, *l*=16mm and w_s=6mm

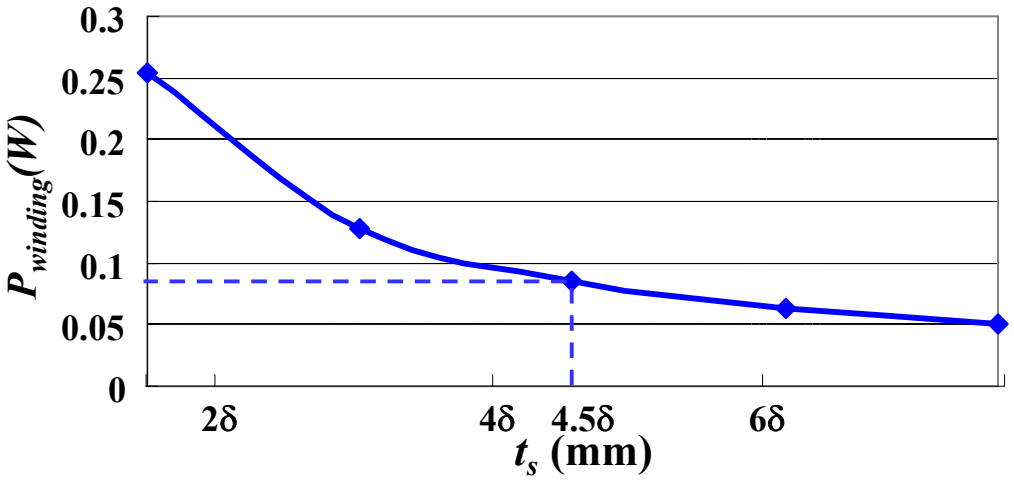

Figure 4.23 The winding loss vs. t_s graph of the LTCC coupled inductor structure 1 with w=12mm, *l*=16mm and w_s=10mm

Step 5: Select the coupling coefficient α

The selection of the coupling coefficient for the LTCC integrated coupled-inductor structure 1 is based on the volume and the transient inductance. Figure 4.24 shows the L_{tr} vs. α when the L_{ss} is fixed at 68nH. It can be seen that the stronger the coupling, the smaller the L_{tr} and the better the transient performance of the LTCC coupled-inductor buck converter.

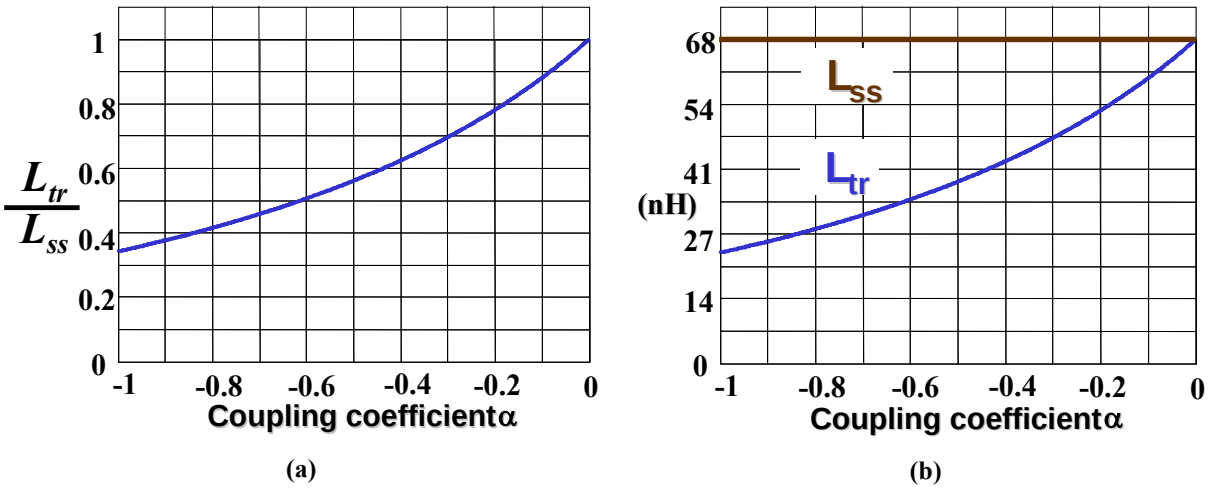

Figure 4.24 The L_{tr} of the LTCC coupled-inductor (a) The L_{tr}/L_{ss} vs. α of a two-phase coupled-inductor (b) the L_{tr} vs. α when the steady state inductance of the LTCC coupled-inductor structure 1 is L_{ss}=68nH

The relationship of the volume vs. the coupling coefficient of the LTCC coupled inductor is complex. In discrete coupled-inductors (Figure 4.25), the coupling coefficeint is determined mainly by the airgaps of the coupled inductor:

$$\alpha = \frac{\sigma_2}{2\sigma_1 + \sigma_2} \tag{4.20}$$

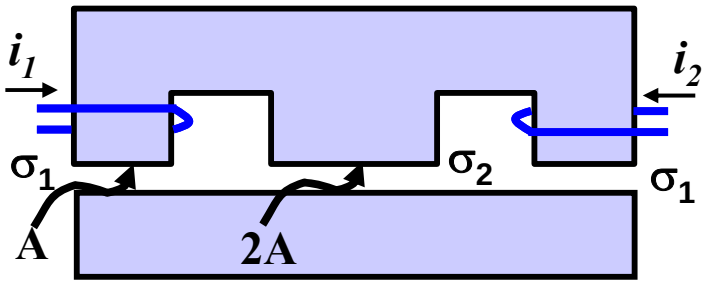

Figure 4.25 The discrete coupled-inductors with airgaps: the coupling coefficient α determined by airgaps σ_1 and σ_2 and not related to the volume of the coupled inductor

However, in LTCC integrated coupled inductors (Figure 4.26), there are no airgaps. Therefore, the coupling coefficient is determined by the dimensions of the LTCC integrated inductor. Accordingly, the coupling coefficient is related to the volume of the LTCC integrated coupled inductor. Since the relationship between the volume of the LTCC integrated coupled inductor and the coupling coefficient is quite complex, three designs will be made based on three coupling coefficents (α=-0.4, α=-0.6 α=-0.8, and α=-0.95). Then, the volumes of these three designs will be compared to find out the relationship between the volume of the LTCC integrated coupled inductor and the coupling coefficient. For the first try, choose

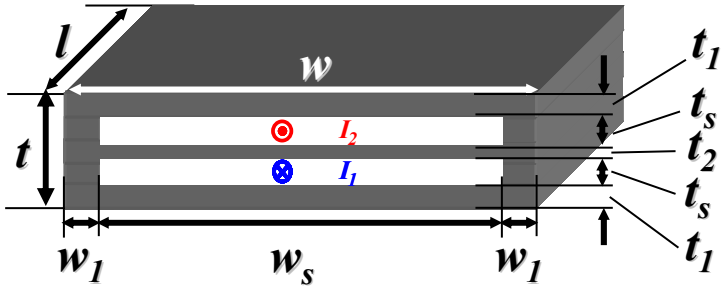

Figure 4.26 The LTCC integrated coupled-inductors without airgaps: the coupling coefficient α is determined by the dimensions and related to the volume of the LTCC integrated coupled inductor

$$\alpha = -0.4 \tag{4.21}$$

Assume α=-0.4, selecte t_1 and t_2

$$\begin{cases} \alpha = \alpha(t_1, t_2) \approx -1/(1 + \dfrac{t_2}{t_1} \cdot \dfrac{u_{mid}}{u_{out}}) = -0.4 \\ L_{ss} = L_{ss}(t_1, t_2) = \dfrac{(1-\alpha^2)l}{1 + \dfrac{D}{D'}\alpha} \dfrac{u_{out}\mu_0}{(\dfrac{w_s}{t_1} + \dfrac{2t_s}{w_1})\{1 + 1/[1 + \dfrac{(\dfrac{w_s}{t_1} + \dfrac{2t_s}{w_1})\dfrac{u_{mid}}{u_{out}} t_2}{w_s}]\}} = 68nH \\ u_{out} = u_{out}(\dfrac{t_1}{t_2}) \end{cases} \tag{4.22}$$

With numerical method, t_1 and t_2 can be calculated to be.

$$t_2=1.9\text{mm}, t_1=1\text{mm} \tag{4.23}$$

Now, all the dimensions are determined when the coupling coefficient α=-0.4. In the next step, the coupling coefficient will be changed and find out the relationship between the volume of the LTCC coupled inductor and the coupling coefficient.

Repeat with α=-0.6, α=-0.8and α=-0.95

When the coupling coefficient is chosen to be -0.6, the design steps 3-6 are repeated. The final design result is w_s=9.8mm, w_1=1.1mm, t_1=1.1mm, t_s=0.3mm, *l*=16mm and t_2=1.5mm.

When the coupling coefficient is chosen to be -0.8, the design steps 3-6 are repeated. The final design result is w_s=9.6mm, w_1=1.2mm, t_1=1.2mm, t_s=0.3mm, *l*=16mm and t_2=1.2mm.

When the coupling coefficient is chosen to be -0.95, the design steps 3-6 are repeated. The final design result is w_s=8.2mm, w_1=1.9mm, t_1=1.9mm, t_s=0.36mm, *l*=16mm and t_2=1.21mm.

Figure 4.27 shows the thickness comparison of the above three designs with different coupling coefficients when w=12mm and *l*=16mm. There is a sweet coupling coefficient point around α=-0.8 from the total thickness and volume point of view.

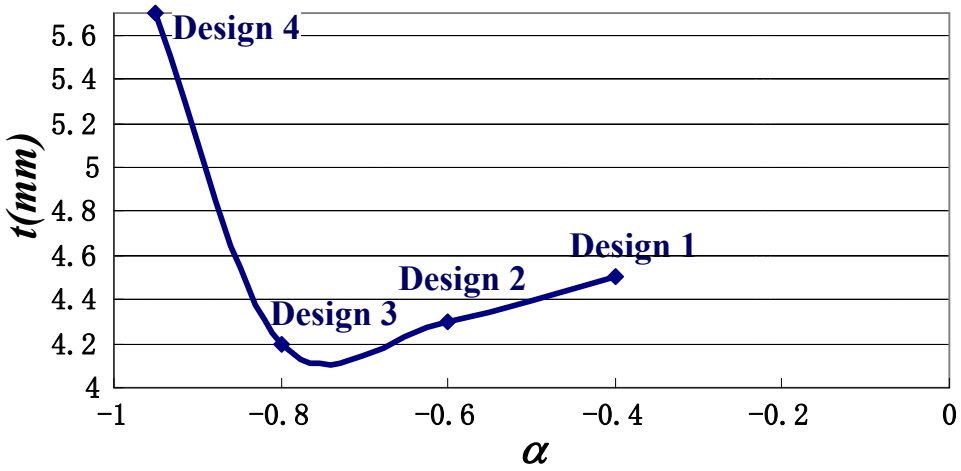

Figure 4.27 The comparison of the thickness for three LTCC integrated coupled-inductors with different coupling coefficients (w=12mm and *l*=16mm)

Figure 4.28 shows the transient inductance comparison of the above four designs with different coupling coefficients when w=12mm and *l*=16mm. When the coupling is stronger, the transient inductance is smaller and the transient performance of the converter is better.

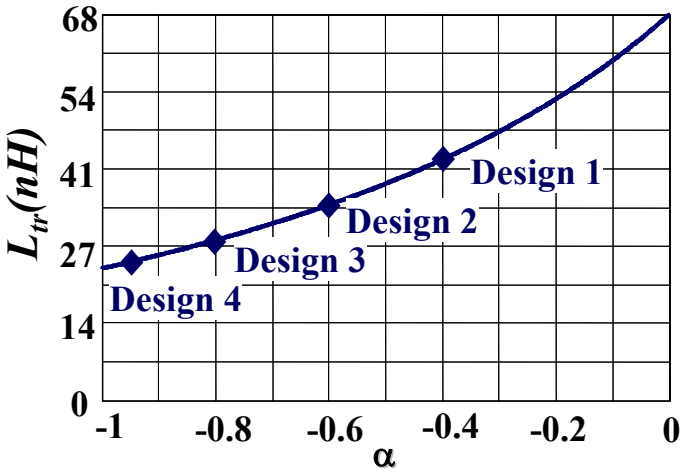

Figure 4.28 The comparison of the transient inductances for three LTCC integrated coupled-inductors with different coupling coefficients (w=12mm and *l*=16mm)

Figure 4.29 shows the graph of the thickness vs. the transient inductances for the above four designs with different coupling coefficients when w=12mm and *l*=16mm. The design 3(α=-0.8) and design 4(α=-0.95) are better designs. The design 3 has a smaller thickness but a larger transient inductance and the design 4 has a smaller transient inductance but a larger thickness.

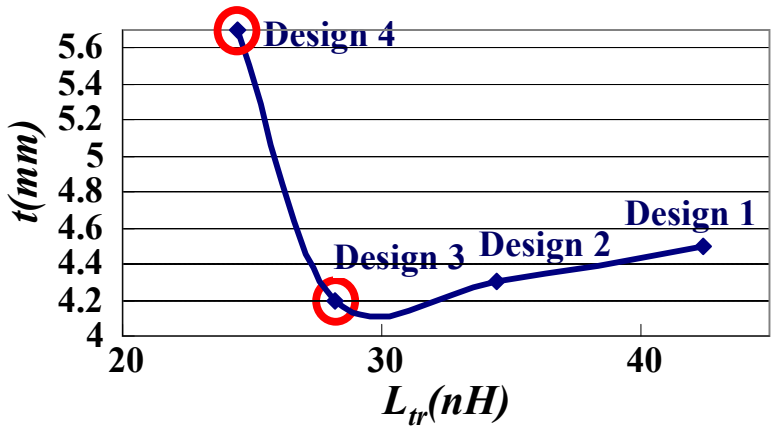

Figure 4.29 The graph of the thickness vs. the transient inductances for three LTCC integrated coupled-inductors with different coupling coefficients (w=12mm and *l*=16mm)

Step 6: Iterate the design process with the different width w

When the width w is chosen to be 8mm and *l* is chosen to be 24mm, the above design steps 3-7 are repeated. The final design results are α=-0.4, w_s=6mm, w_1=1mm, t_1=0.65mm, t_s=0.5mm, *l*=24mm, t_2=1.2mm; α=-0.6, w_s=6mm, w_1=1mm, t_1=0.7mm, t_s=0.5mm, *l*=24mm, t_2=1mm; α=-0.8, w_s=6mm, w_1=1mm, t_1=0.82mm, t_s=0.5mm, *l*=24mm, t_2=1mm.

Figure 4.30 shows the thickness comparison of the three designs with different coupling coefficients when w=8mm and *l*=24mm. There is a sweet coupling coefficient point around α=-0.6 from the total thickness and volume point of view.

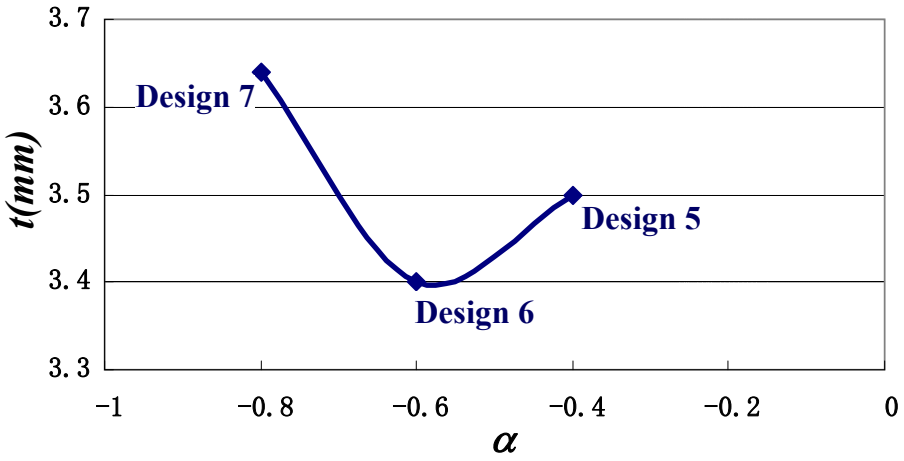

Figure 4.30 The comparison of the thickness for three LTCC integrated coupled-inductors with different coupling coefficients (w=8mm and *l*=24mm)

Figure 4.31 shows the transient inductance comparison of the above three designs with different coupling coefficients when w=8mm and *l*=24mm. When the coupling is stronger, the transient inductance is smaller and the transient performance of the converter is better.

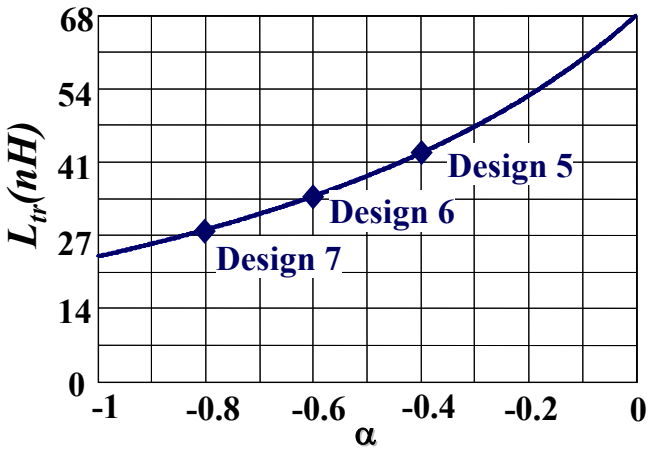

Figure 4.31 The comparison of the transient inductances for three LTCC integrated coupled-inductors with different coupling coefficients (w=8mm and *l*=24mm)

Figure 4.32 shows the graph of the thickness vs. the transient inductances for the above three designs with different coupling coefficients when w=8mm and *l*=24mm. The design 6 and design 7 are better designs. The design 6 has a smaller thickness but a larger transient inductance and the design 7 has a smaller transient inductance but a larger thickness.

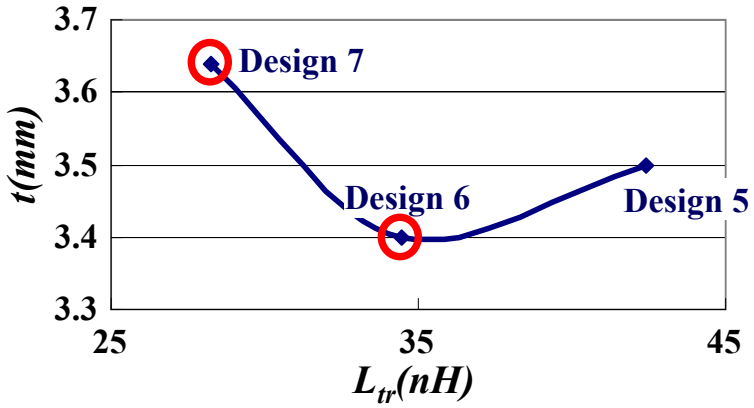

Figure 4.32 The graph of the thickness vs. the transient inductances for three LTCC integrated coupled-inductors with different coupling coefficients (w=8mm and *l*=24mm)

When the width w is chosen to be 4mm and *l* is chosen to be 48mm, the above design steps 3-7 are repeated. The final design results are α=-0.2, w_s=2mm, w_1=1mm, t_1=0.3mm, t_s=1.5mm,

l=48mm, t_2=0.63mm; α=-0.4, w_s=2mm, w_1=1mm, t_1=0.27mm, t_s=1.5mm, l=48mm, t_2=0.53mm; α=-0.6, w_s=2mm, w_1=1mm, t_1=0.32mm, t_s=1.5mm, l=48mm, t_2=0.61mm; α=-0.8, w_s=2mm, w_1=1mm, t_1=0.41mm, t_s=1.5mm, l=48mm, t_2=0.72mm.

Figure 4.33 shows the thickness comparison of the three designs with different coupling coefficients when w=4mm and l=48mm. There is a sweet coupling coefficient point around α=-0.4 from the total thickness and volume point of view.

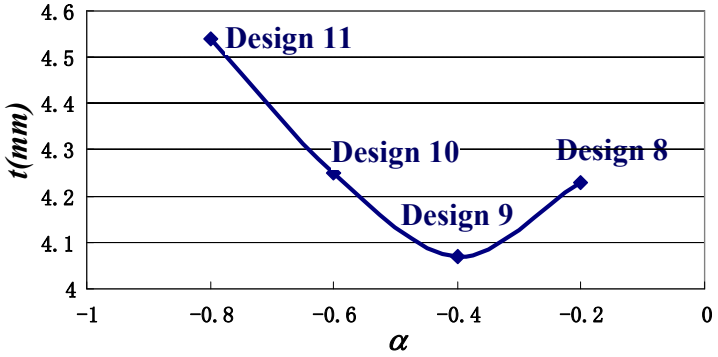

Figure 4.33 The comparison of the thickness for three LTCC integrated coupled-inductors with different coupling coefficients (w=4mm and *l*=48mm)

Figure 4.34 shows the transient inductance comparison of the above four designs with different coupling coefficients when w=4mm and l=48mm. When the coupling is stronger, the transient inductance is smaller and the transient performance of the converter is better.

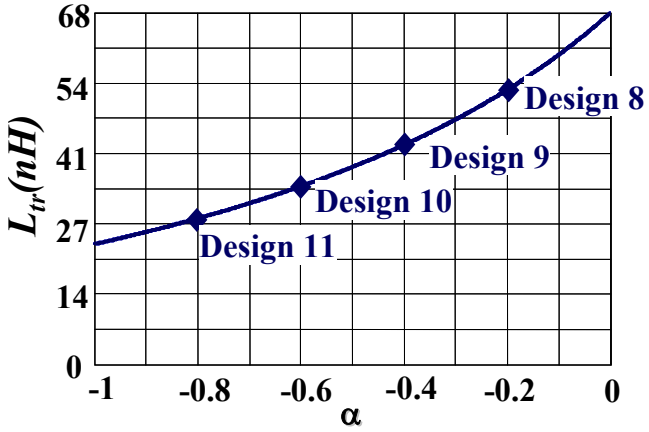

Figure 4.34 The comparison of the transient inductances for three LTCC integrated coupled-inductors with different coupling coefficients (w=4mm and *l*=48mm)

Figure 4.35 shows the graph of the thickness vs. the transient inductances for the above three designs with different coupling coefficients when w=4mm and l=48mm. There is a tradeoff

among design 9, 10 and 11. When the thickness is smaller and the volume is smaller, the transient inductance is larger and the transient performance is worse and vice versa. Therefore, all these three designs are the final design candidates.

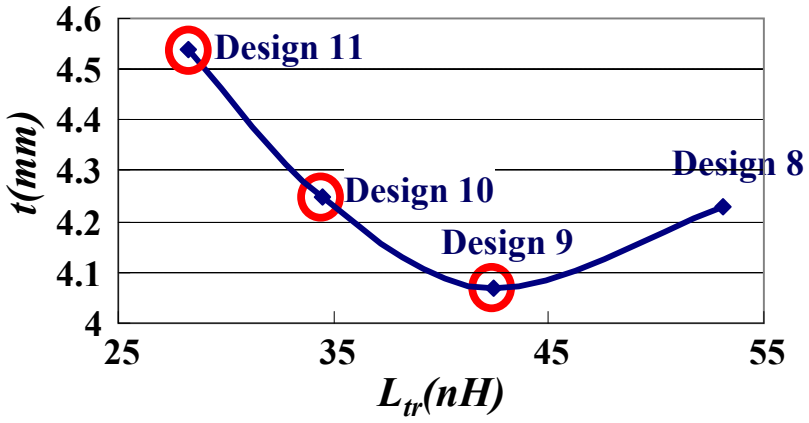

Figure 4.35 The graph of the thickness vs. the transient inductances for three LTCC integrated coupled-inductors with different coupling coefficients (w=4mm and *l*=48mm)

Figure 4.36 shows the previous designs with the same footprint 192mm^2 in the graph of the thickness vs. the transient inductance. The design 6 and design 7 are better design compared to other designs. The design 6 has a smaller thicknes and volume while the design 7 has a smaller transient inductance and a faster transient performance. However, based on our LTCC process experience, the thickness of the LTCC coupled inductor can't be more than 3.4mm. Therfore the design 6 is chosen as the final design.

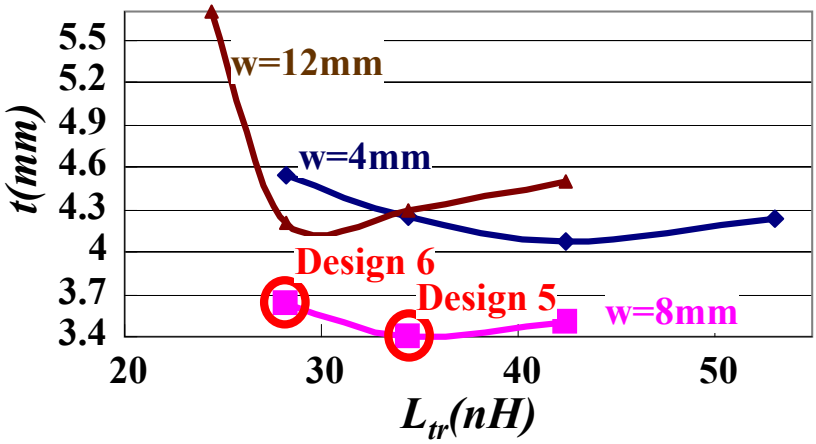

Figure 4.36 The graph of the thickness vs. the transient inductances for the LTCC integrated coupled-inductors with the same footprint 192mm^2

The Maxwell 3D FEA simulation is done to verify the design 6. From the simulation, L_{ss}=71nH and α=-0.62. Therefore, the design based on the two-segment reluctance model is acceptable.

4.2.4. Experimental Results

The designed coupled-inductor is 8x24mm^2. It is too long and the aspect ratio is not very good. Therefore, the U shape winding is adopted (Figure 4.37(a)) when the LTCC integrated coupled-inductor is customized. Figure 4.37(b) shows the prototype of the customized LTCC integrated coupled-inductor structure.

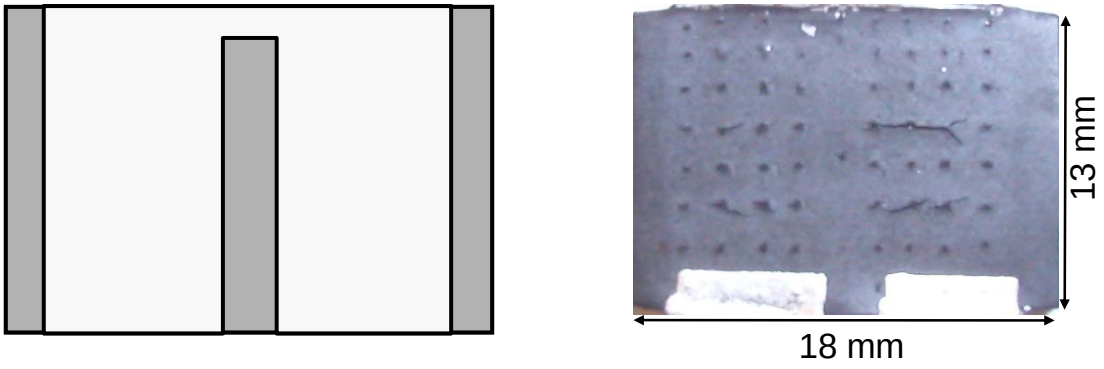

Figure 4.37 The customized LTCC integrated coupled-inductor prototype

The holes in Figure 4.37 are the off-gas holes. When the LTCC coupled-inductor is sintered in the LTCC process, air will be generated. With the off-gasing holes, air will find a way out, not breaking the whole prototype.

Figure 4.38 shows the testing result of the steady-state inductance. At the full load, I_{phase}=20A, L_{ss}=70nH. This verifies the reluctance model and the design process of the LTCC integrated coupled-inductor. It can also be seen that the steady-state inductance increases when the phase-current decreases. This characteristic can be used to improve the light-load efficiency of the POL converter.

Figure 4.39 shows the footprint reduction of the LTCC integrated coupled-inductor compared to the previous LTCC non-coupled-inductor. The footprint of the LTCC coupled-inductor reduces 28%.

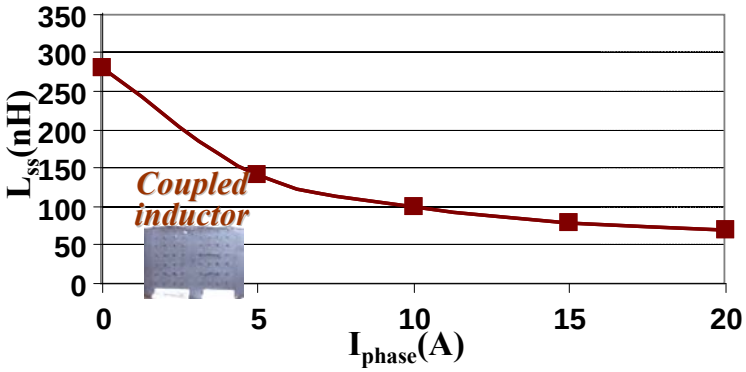

Figure 4.38 The steady-state inductance vs. the phase-current I_{phase}

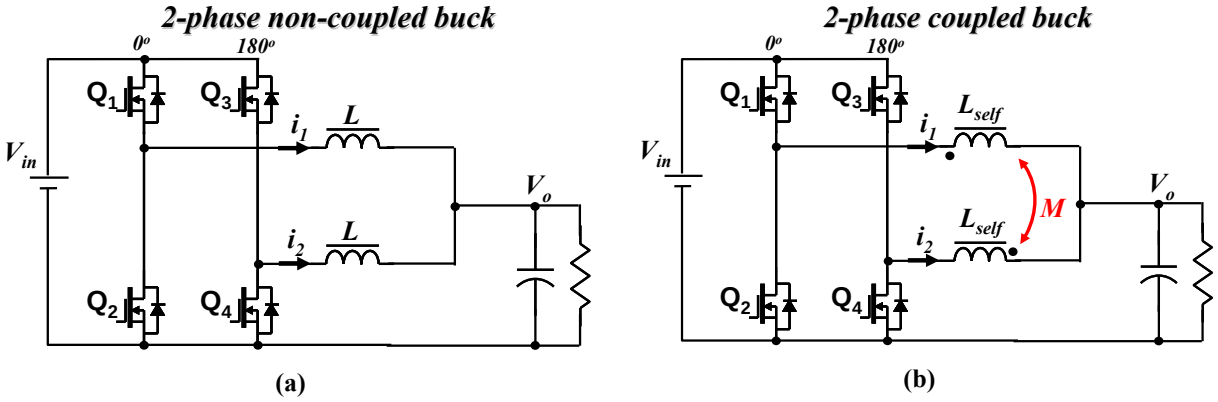

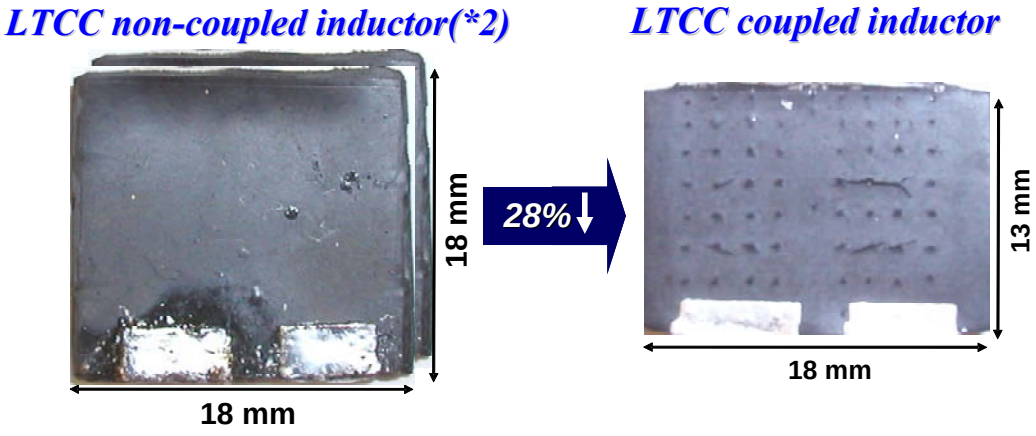

Figure 4.39 The footprint reduction of the LTCC integrated coupled-inductort (a) Two-phase non-coupled-inductor buck converter (b) Two-phase coupled-inductor buck converter (c) The footprint reduction of the LTCC coupled-inductor

With the better layout, the footprint of the active stage can be further reduced. Figure 4.40 shows the further improvement of the active stage. With the further improved active stage, the LTCC coupled-inductor is redesigned to be compatible with the reduced footprint.

The design result is w_s=4mm, w_1=1mm, t_1=0.71mm, t_2=1.0mm, t_s=0.75mm, l=20mm. The total thickness is t=3.92mm. Because of the thickness limitation of the LTCC process, this LTCC coupled-inductor can't be built. To build an LTCC integrated coupled-inductor which is compatible with the above active stage, another LTCC integrated coupled-inductor structure is investigated.

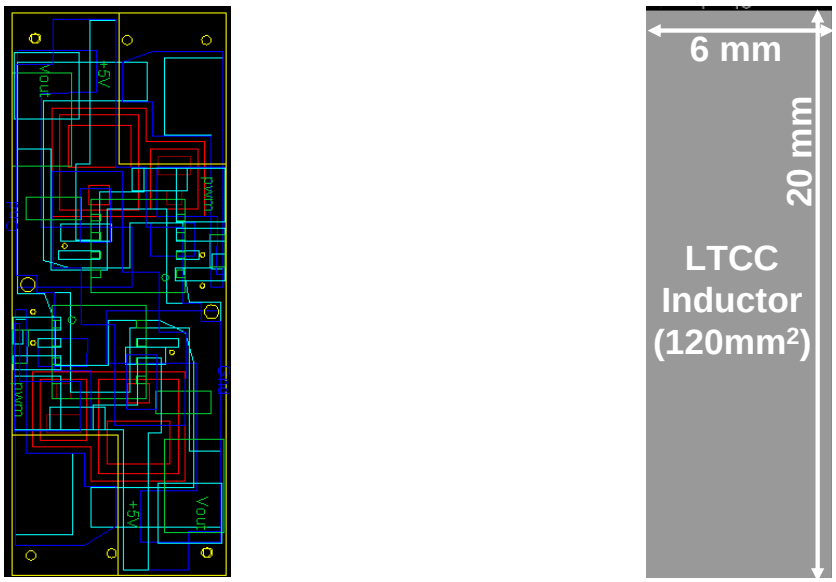

(a) **(b)**

Figure 4.40 The improved the active stage layout and the available LTCC coupled inductor footprint (a) the improved active stage layout (b) the LTCC coupled inductor footprint

4.3. LTCC Integrated Coupled-inductor Structure 2

The winding structure of the previous LTCC integrated coupled-inductor structure 1 is that one phase winding is on the top of the other phase winding. If one phase winding is on the side of the other phase winding, the LTCC coupled-inductor structure 2 is achieved (Figure 4.41).

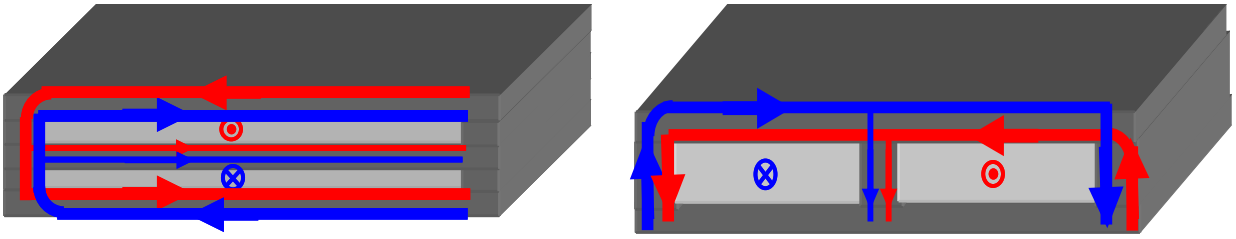

(a) (b)

Figure 4.41 Two LTCC integrated coupled-inductor structures (a) The LTCC integrated coupled-inductor structure 1 (b) The LTCC integrated coupled-inductor structure 2

Now we will compare these two LTC integrated coupled inductor structures qualitatively. In the comparison, we assume that the ferrite tape material is the same for the two structures (the u_r=200 ferrite tape material), and that the total width w, the thickness t and t_1 are the same, and that the inductances for the two LTCC integrated coupled-inductors are the same due to the same application. From the mean magnetic paths of the two LTCC integrated coupled-inductor structures shown in Figure 4.42, it can be clearly seen that

$$L_{mean\_1} > L_{mean\_2} \tag{4.24}$$

Here, 1 represents the structure 1. Since the inductance equation is

$$L = \frac{u_0 \cdot u_r \cdot t_1 \cdot l}{L_{mean}}, \tag{4.25}$$

the inductor length for the LTCC integrated coupled-inductor structure 1, l_1 is longer than the inductor length for the LTCC integrated coupled-inductor structure 2, l_2

$$l_1 > l_2 \tag{4.26}$$

Because the widths w for the two LTCC integrated coupled-inductor structures are the same,

$$\text{Footprint 1} > \text{Footprint 2} \tag{4.27}$$

The LTCC integrated coupled-inductor structure 2 potentially has a smaller footprint than the LTCC integrated coupled-inductor structure 1.

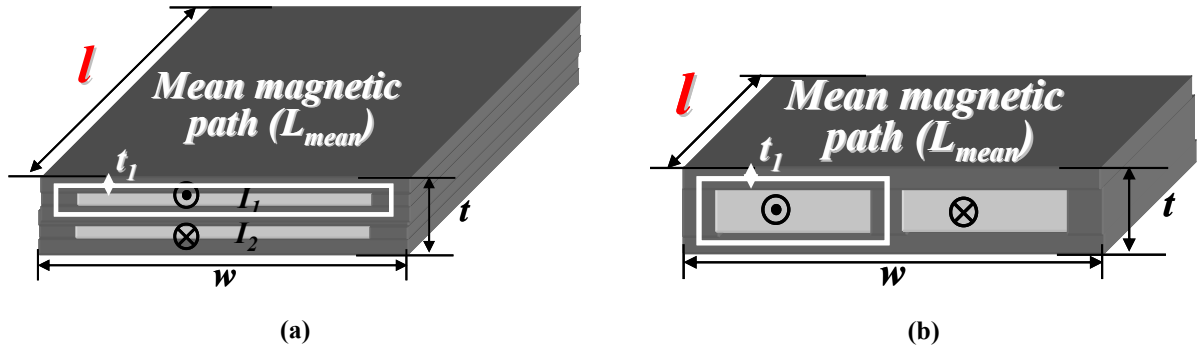

Figure 4.42 The mean magnetic paths for the two LTCC integrated coupled-inductor structures (a) The LTCC integrated coupled-inductor structure 1 (b) The LTCC integrated coupled-inductor structure 2

To model and design the LTCC integrated coupled-inductor structure 2, this structure is firstly analyzed with the Maxwell 3D FEA simulation to find out the method to control the coupling coefficient α.

4.3.1. Controlling the coupling coefficient by the dimension w_2

The dimension definition of the LTCC integrated coupled-inductor structure 2 is shown in Figure 4.43. There are six dimensions: t_1, t_s, w_s, w_1, w_2 and *l*. In the Maxwell 3D FEA simulation, the B-H curve of the LTCC ferrite material, the dimension information and the phase-current information (I_1=I_2=20A) are input into the Maxwell simulator. Three simulation cases are investigated. For the three cases, w_s=1.5mm, w_1=0.7mm, t_1=0.7mm, t_s=2mm, and *l*=20mm. In the case 1, w_2=0.6mm; in the case 2, w_2=1mm; in the case 3, w_2=1.4mm. The couping coefficients for these three cases are shown in Figure 4.44.

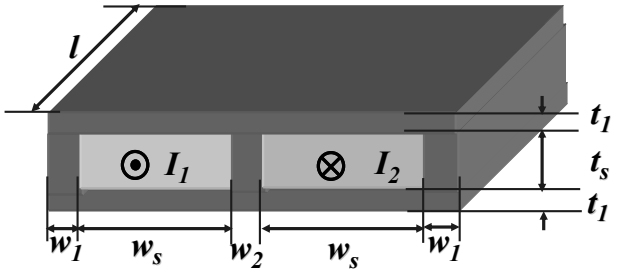

Figure 4.43 The dimension definition of the LTCC integrated coupled-inductor structure 2

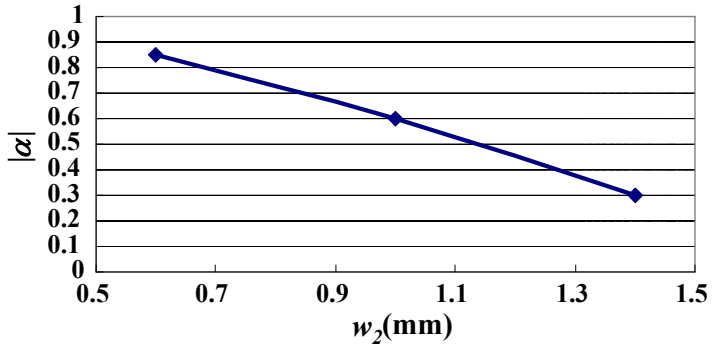

Figure 4.44 The coupling coefficient α vs. the dimension w_2 for the LTCC integrated coupled-inductor structure 2 with w_s=1.5mm, w_1=0.7mm, t_1=0.7mm, t_s=2mm, and *l*=20mm

It can be seen from Figure 4.44 that the coupling coefficient of the LTCC integrated coupled-inductor 2 decreases as w_2 increases. Therefore, w_2 can be used to control the coupling of the LTCC integrated coupled-inductor structure 2.

4.3.2. Reluctance Model

The DC magnetic flux density is also investigated for the case 2 when α=-0.6. Figure 4.45 shows the DC flux density distribution of the case 2 based on the Maxwell 3D FEA simulation. It can be seen that although the different points in the core structure operate at different B-H curve points, the points in the middle leg approximately operate in one area in the B-H curve and the points in the outer legs operate in another area in the B-H curve. If the permeabilities of the points in the middle leg are assumed to be the same and the permeabilities of the points in the outer legs are assumed to be the same, Figure 4.45 can be simplified to Figure 4.46(a). There are two permeabilities for the whole structure. In another word, the B-H curve of the ferrite tape is approximated by the two-segment B-H curve shown in the Figure 4.46(b).

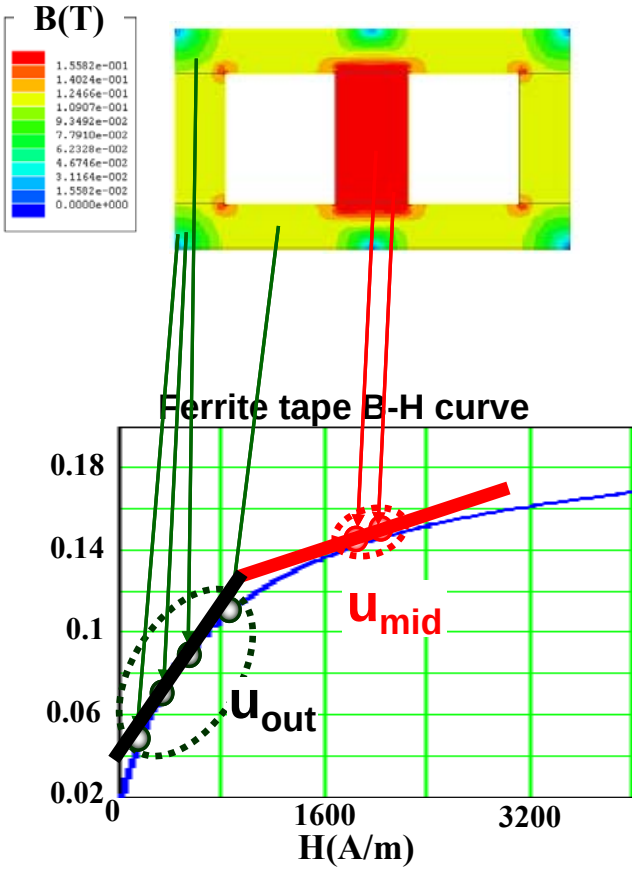

Figure 4.45 Mapping the DC flux density of different points in the LTCC integrated coupled-inductor structure 2 to the B-H curve of the ferrite tape (w_s=1.5mm, w_1=0.7mm, t_1=0.7mm, t_s=2mm, l=20mm, w_2=1mm)

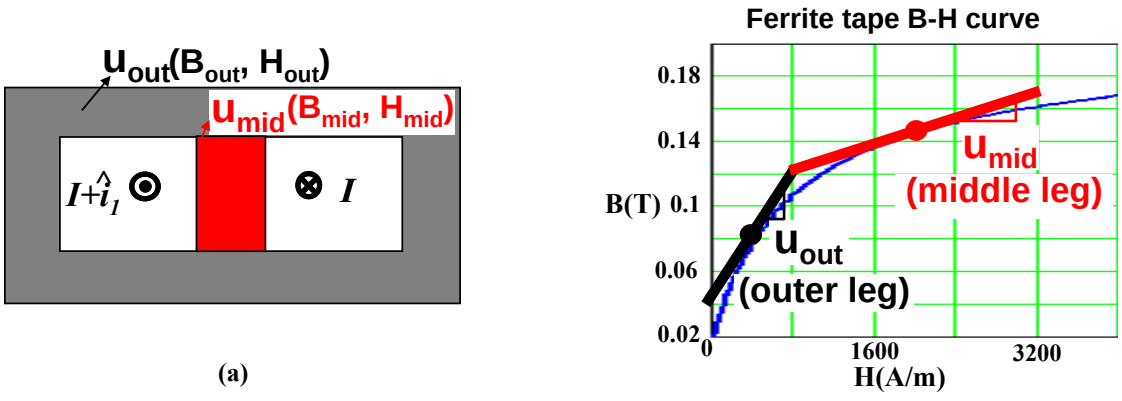

Figure 4.46 The two-segment B-H curve approximation (a) The LTCC integrated coupled-inductor structure with two-segment approximation (b) The two-segment B-H curve approximation of the ferrite tape material

Under the two-segment B-H curve approximation, the relationship between the flux densities in the middle leg and the outer leg can be investigated. Figure 4.47 shows the DC fluxes in the integrated coupled-inductor structure 2. From Figure 4.47, it can be seen that

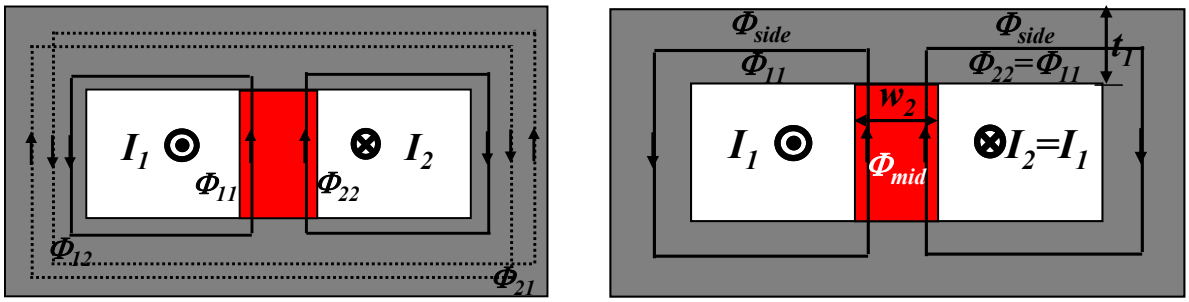

(a) (b)

Figure 4.47 The DC flux distribution in the LTCC integrated coupled-inductor structure 2 (b) The DC fluxes generated by the two phase DC currents (b) the remaining fluxes after the DC flux cancellation

$$\Phi_{mid} = 2\Phi_{11} = 2\Phi_{side} \tag{4.28}$$

Since

$$\Phi_{mid} = B_{mid} w_2 l \tag{4.29}$$

$$\Phi_{side} = B_{side} t_1 l \tag{4.30}$$

Therefore

$$B_{mid} / B_{side} = 2t_1 / w_2 \tag{4.31}$$

Combining the equation (4.31) and Figure 4.46(b), the relationship between the u_{out} and t_1/w_2 can be drawn with a certain B_{mid}. When B_{mid}=0.15T, Figure 4.48 shows this relationship.

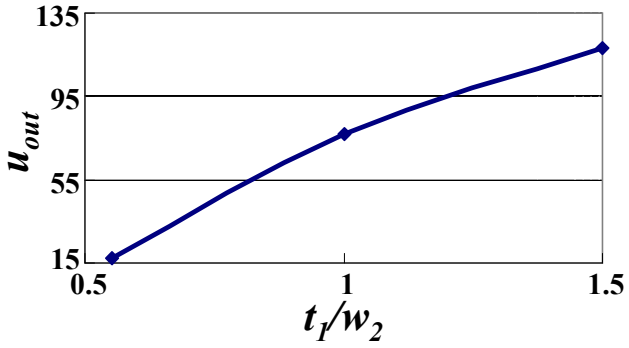

Figure 4.48 The relationship between the outer leg permeability u_{out} and the ratio t_1/w_2 when B_{mid}=0.15T

The reluctance model of the LTCC integrated coupled-inductor structure 2 is very simple under the two-segment B-H curve approximation. Figure 4.49 shows the reluctance model of the LTCC integrated coupled-inductor structure 2. The reluctance of the outer leg is calculated based on the permeability in the outer leg, u_{out} and the reluctance of the middle leg is calculated based on the lermeability in the middle leg, u_{mid}.

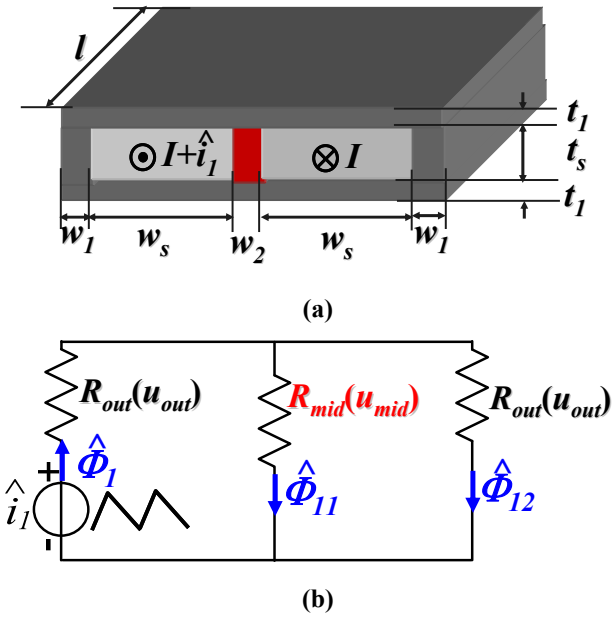

Figure 4.49 The reluctance model of the integrated coupled-inductor structure 2 (a) The LTCC coupled-inductor structure with the dimensions and the current excitation (b) The reluctance model

The R_{mid}, R_{out} equations are written as follows

$$R_{mid} = \frac{t_s}{u_0 u_{mid} w_2 l} \tag{4.32}$$

$$R_{out} = \frac{2w_s}{u_0 u_{out} t_1 l} + \frac{t_s}{u_0 u_{out} w_1 l} \tag{4.33}$$

Based on the reluctance model, the L_{self}, L_k and coupling coefficient $|\alpha|$ can be calculated as follows

$$L_{self} = \frac{\hat{\Phi}_1}{\hat{i}_1} = \frac{R_{out} + R_{mid}}{R_{out}(R_{out} + 2R_{mid})} = K_1 \cdot l \tag{4.34}$$

where $\hat{\Phi}_1$ is the total flux generated by the $\hat{i}_1$, and

$$K_1 = \frac{\mu_{out}\mu_0}{(\frac{2w_s}{t_1}+\frac{t_s}{w_1})[1+\frac{1}{1+\frac{(\frac{2w_s}{t_1}+\frac{t_s}{w_1})\frac{\mu_{mid}}{\mu_{out}}w_2}{t_s}}]} \tag{4.35}$$

$$L_k = \frac{\hat{\Phi}_{11}}{\hat{i}_1} = \frac{1}{R_{out}+2R_{mid}} \tag{4.36}$$

where $\hat{\Phi}_{11}$ is the flux generated by the $\hat{i}_1$, which flows through the middle leg and not through the outer leg.

$$|\alpha| = \frac{L_{self}-L_k}{L_{self}} = \frac{R_{mid}}{R_{out}+R_{mid}} = \frac{1}{1+f(t_1)\cdot w_2} \tag{4.37}$$

where

$$f(t_1) = \frac{(\frac{2w_s}{t_1}+\frac{t_s}{w_1})\frac{\mu_{mid}}{\mu_{out}}}{t_s} \tag{4.38}$$

From the equation (4.37), it can be seen that $|\alpha|$ decreases as w_2 increases. It is the same as the conclusion drawn from the Maxwell 3D FEA simulation results.

Substituting the equations (4.34) and (4.37) into the equation (1.13) and rearranging the terms,

$$L_{ss} = \frac{1-\alpha^2}{1+\frac{D}{D'}\alpha}\cdot K_1 \cdot l = K_3 \cdot l \tag{4.39}$$

where

$$K_3 = \frac{1-\alpha^2}{1+\frac{D}{D'}\alpha}\frac{\mu_{out}\mu_0}{(\frac{2w_s}{t_1}+\frac{t_s}{w_1})[1+\frac{1}{1+\frac{(\frac{2w_s}{t_1}+\frac{t_s}{w_1})\frac{\mu_{mid}}{\mu_{out}}w_2}{t_s}}]} \tag{4.40}$$

Figure 4.50 shows the reluctance model's precision in case 2, when t_2=1mm. From Figure 4.50, it can be seen that the two-segment B-H curve approximation is acceptable. Although it is

not as precise as the 3D FEA simulation, it is much faser than the 3D FEA simulation. In the following, the reluctance model will be used to design the LTCC coupled-inductor structure 2.

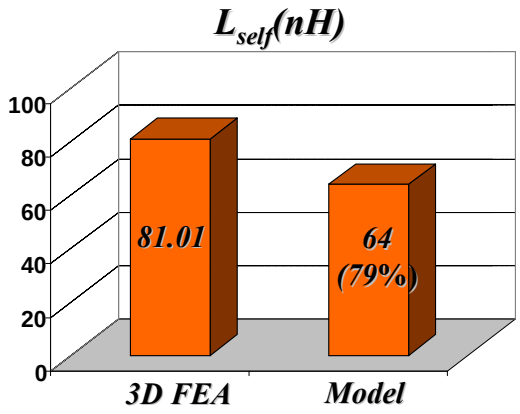

(a)

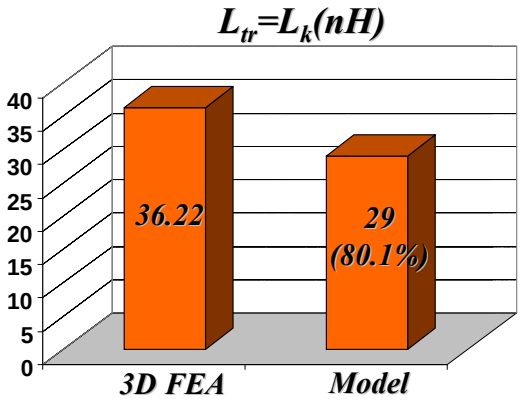

(b)

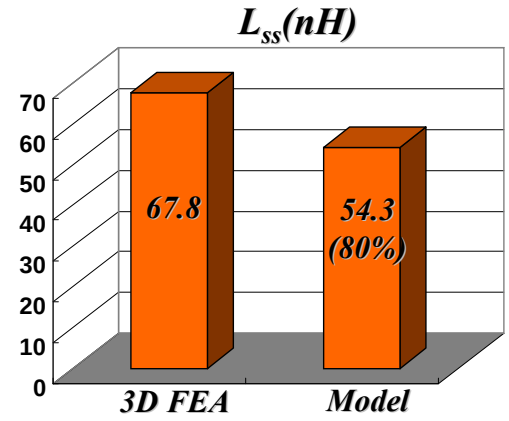

(c)

Figure 4.50 The precision of the reluctance model in case 2, when w_2=1mm
(a) L_{self} (b) L_{tr}=L_k (c) L_{ss}

4.3.3. Design Example

Assuming that a LTCC integrated coupled-inductor needs to be designed for a two-phase integrated coupled inductor buck converter with the following design target:

V_{in}=5V,

V_o=1.2V,

f_s=1.3MHz,

I_{phase}=20A,

A smaller volume is preferred,

With a fixed steady state inductance L_{ss}, a smaller transient inductance L_{tr} is preferred.

The dimensions w_1, w_2, w_s, t_1, t_s and *l* (Figure 4.51) will be designed in the following design procedure step by step.

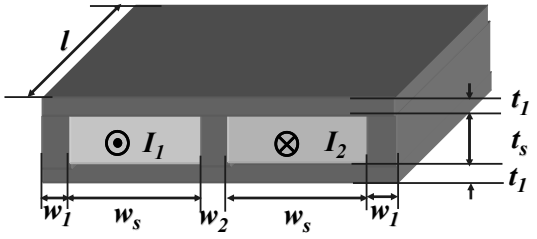

Figure 4.51 The dimensions of the LTCC integrated coupled-inductor structure 2

Step 1: Assume w=8mm and *l*=15mm

Keeping the total LTCC inductor footprint to be the same 120mm^2, there are many different combinations of width and length. Figure 4.52 shows one w and *l* dimension case of the LTCC inductor with the footprint of 120mm^2.

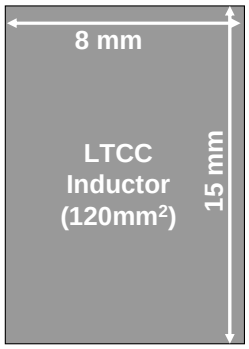

Figure 4.52 One w and *l* dimension case of the LTCC coupled inductor structure 2 for the footprint 120mm^2 (w=8mm, *l*=15mm)

Firstly, the design will be investigated for the w=8mm, and *l*=15mm. After this, the designs with w=6mm and w=4mm will be investigated. Figure 4.53 shows the LTCC coupled inductor with marked w and *l* dimensions.

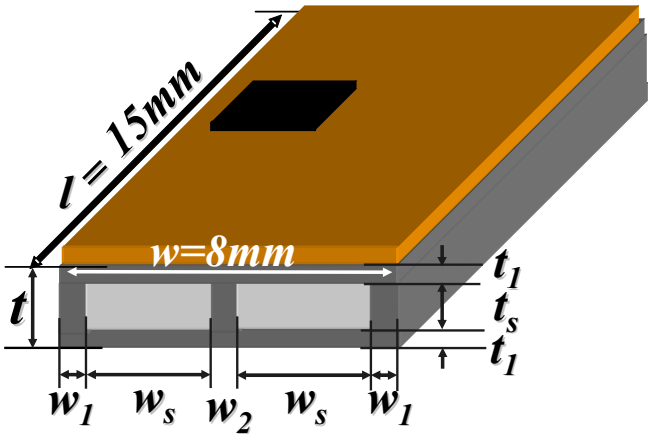

Figure 4.53 The LTCC integrated coupled-inductor with the marked w and *l* dimensions

Step 2: Calculate L_{ss}

We assume the phase-current ripple to be 50% of the phase current. Therefore, the steady-state inductance can be calculated.

$$L_{ss} = \frac{V_o(1-D)T_s}{0.5I_{phase}} = 68nH \tag{4.41}$$

Step 3: Select w_s

Figure 4.54 shows the dimension w_s. It can be seen that

$$w_s=(w-2*w_1-w_2)/2 \tag{4.42}$$

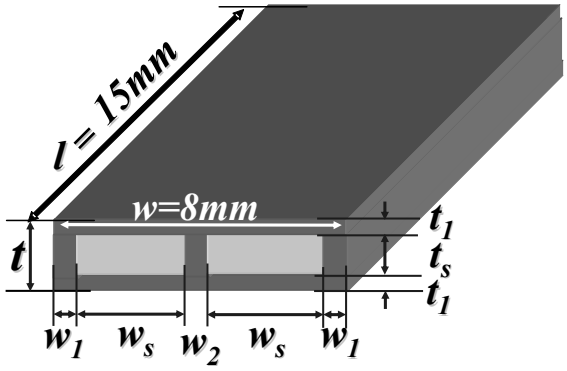

Figure 4.54 The w_s dimension of the LTCC coupled inductor with w=8mm and *l*=15mm

Theoretically, w_1 should be equal to t_1. However, because of the previous LTCC process experience, the w_1 is at least 1mm, which is normally larger than t_1. Therfore, w_1 is chosen to be 1mm. The w_2 is preselected to be the same as w_1, 1mm for the first try. It will be determined later with the coupling coefficient and the iteration process will be made for the final design.

$$w_s=(w-2*w_1-w_2)/2=2.5\text{mm} \tag{4.43}$$

Step 4: Select t_s

Figure 4.55 shows the dimension t_s. Here, t_s is determined by the winding loss. The relationship between the winding loss and the t_s is drawn in Figure 4.56. It can be seen that when t_s increases, there is a diminishing return in the winding loss. Therefore, t_s is chosen around the diminishing return area.

$$t_s=1.2\text{mm} \tag{4.44}$$

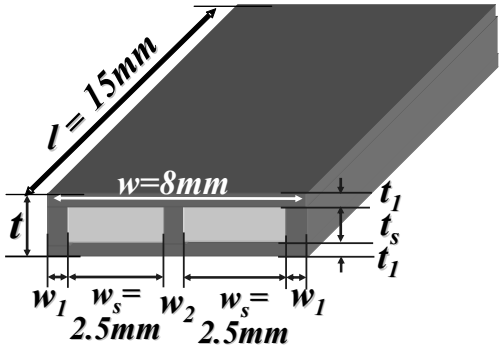

Figure 4.55 The t_s dimension of the LTCC coupled inductor with w=8mm, *l*=15mm and w_s=2.5mm

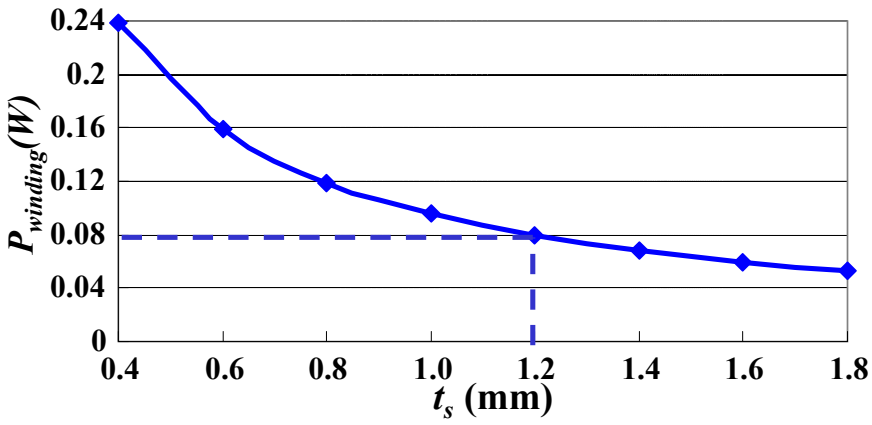

Figure 4.56 The winding loss vs. t_s graph of the LTCC coupled inductor structure 2 with w=8mm, *l*=15mm and w_s=2.5mm

Step 5: Select the coupling coefficient α

The selection of the coupling coefficient for the LTCC integrated coupled-inductor structure 2 is based on the volume and the transient inductance. For the transient performance with the same steady-state inductance, the stronger the coupling, the smaller the L_{tr} and the better the transient performance of the LTCC coupled-inductor buck converter. The relationship of the volume vs. the coupling coefficient of the LTCC coupled inductor is complex. Three designs will be made based on three coupling coefficents (α=-0.2, α=-0.4, α=-0.6 and α=-0.8) to find out the relationship between the volume of the LTCC integrated coupled inductor and the coupling coefficient. For the first try, choose

$$\alpha = -0.2 \tag{4.45}$$

Assume α=-0.2, select t_1 and w_2

The t_1 and w_2 are determined according to the reluctance model derived in the previous section. According to the reluctance model, the coupling coefficient α and the steady-state inductance L_{ss}

$$\begin{cases} \alpha = \alpha(t_1, w_2) = -\dfrac{1}{1+(\dfrac{2w_s}{t_1}+\dfrac{t_s}{w_1})\dfrac{u_{mid}}{u_{out}}\cdot\dfrac{w_2}{t_s}} = -0.2 \\ L_{ss} = L_{ss}(t_1, t_2) = \\ \dfrac{(1-\alpha^2)l}{1+\dfrac{D}{D'}\alpha}\dfrac{u_{out}u_0}{(\dfrac{w_s}{t_1}+\dfrac{2t_s}{w_1})\{1+1/[1+\dfrac{(\dfrac{w_s}{t_1}+\dfrac{2t_s}{w_1})\dfrac{u_{mid}}{u_{out}}t_2}{w_s}]\}} = 68nH \\ u_{out} = u_{out}(\dfrac{t_1}{w_2}) \end{cases} \quad (4.46)$$

Solving the equation (4.46), w_2 and t_1 are calculated to be

$$w_2=1.8\text{mm}, t_1=1.0\text{mm} \quad (4.47)$$

The w_2 value here, 1.7mm, is different from the presecting value of w_2 in the step 3, 1mm. Therefore, iteration needs to be done for step 3-6 until the two w_2 values are close enough. After iteration, the final design result is w_1=1.05mm, w_2=1.9mm, w_s=2.0mm, t_1=1.05mm, t_s=1.46mm and *l*=15mm.

Now, all the dimensions are determined when the coupling coefficient α=-0.2. In the next step, the coupling coefficient will be changed and find out the relationship between the volume of the LTCC coupled inductor and the coupling coefficient.

Assume α=-0.4, α=-0.6 and α=-0.8, select t_1 and w_2

When the coupling coefficient is chosen to be -0.4, the design steps 3-6 are repeated. The final design result is w_1=1.05mm, w_2=1.6mm, w_s=2.2mm, t_1=1.05mm, t_s=1.4mm and *l*=15mm.

When the coupling coefficient is chosen to be -0.6, the design steps 3-6 are repeated. The final design result is w_1=1.15mm, w_2=1.5mm, w_s=2.1mm, t_1=1.15mm, t_s=1.4mm and *l*=15mm.

When the coupling coefficient is chosen to be -0.8, the design steps 3-6 are repeated. The final design result is w_1=1.3mm, w_2=1.7mm, w_s=1.85mm, t_1=1.3mm, t_s=1.6mm and *l*=15mm.

Figure 4.57 shows the thickness comparison of the above three designs with different coupling coefficients when w=8mm and *l*=15mm. There is a tradeoff between the total thickness and the coupling coefficient for design 2, 3 and 4.

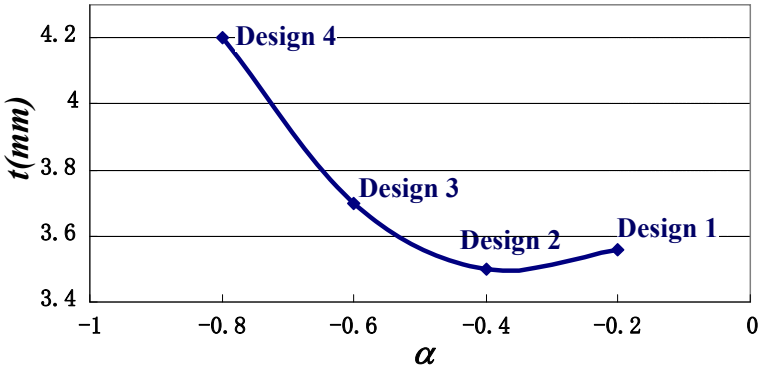

Figure 4.57 The comparison of the thickness for three LTCC integrated coupled-inductors with different coupling coefficients (w=8mm and *l*=15mm)

Figure 4.58 shows the transient inductance comparison of the above four designs with different coupling coefficients when w=8mm and *l*=15mm. When the coupling is stronger, the transient inductance is smaller and the transient performance of the converter is better.

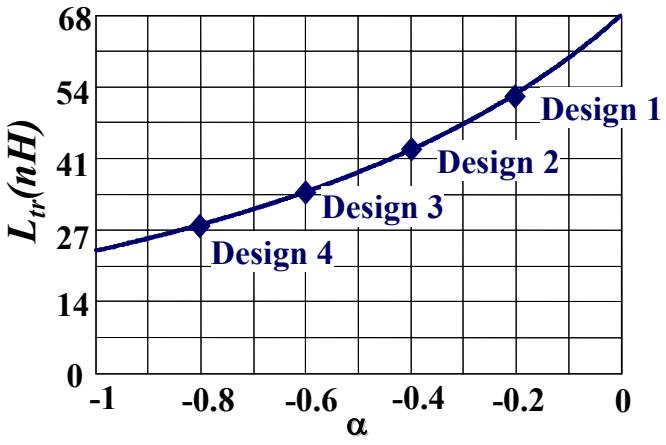

Figure 4.58 The comparison of the transient inductances for three LTCC integrated coupled-inductors with different coupling coefficients (w=8mm and *l*=15mm)

Figure 4.59 shows the graph of the thickness vs. the transient inductances for the above four designs with different coupling coefficients when w=8mm and *l*=15mm. There is a trade off between the transient performance and the thickness of the LTCC integrated coupled inductor.

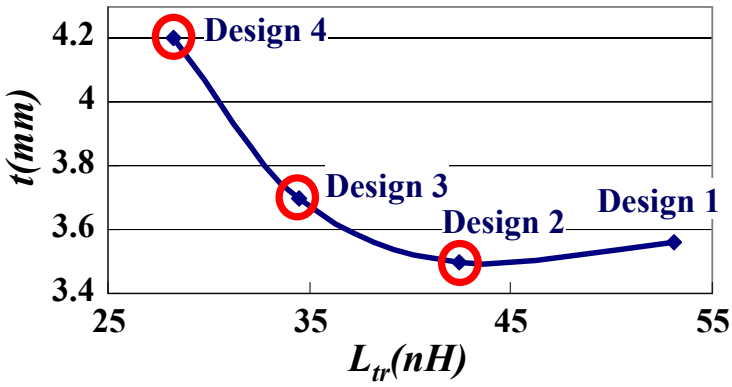

Figure 4.59 The graph of the thickness vs. the transient inductances for three LTCC integrated coupled-inductors with different coupling coefficients (w=8mm and *l*=15mm)

Step 6: Iterate the design process with the different width w

When the width w is chosen to be 6mm and *l* is chosen to be 20mm, the above design steps 3-7 are repeated. The final design results are α=-0.4, w_1=1mm, w_2=1.3mm, w_s=1.35mm, t_1=0.7mm, t_s=2.2mm and *l*=20mm; α=-0.6, w_1=1mm, w_2=1mm, w_s=1.5mm, t_1=0.7mm, t_s=2mm and *l*=20mm; α=-0.8, w_1=1mm, w_2=1.2mm, w_s=1.4mm, t_1=1mm, t_s=2.14mm and *l*=20mm.

Figure 4.60 shows the thickness comparison of the three designs with different coupling coefficients when w=6mm and *l*=20mm. There is a sweet coupling coefficient point around α=-0.6 from the total thickness and volume point of view.

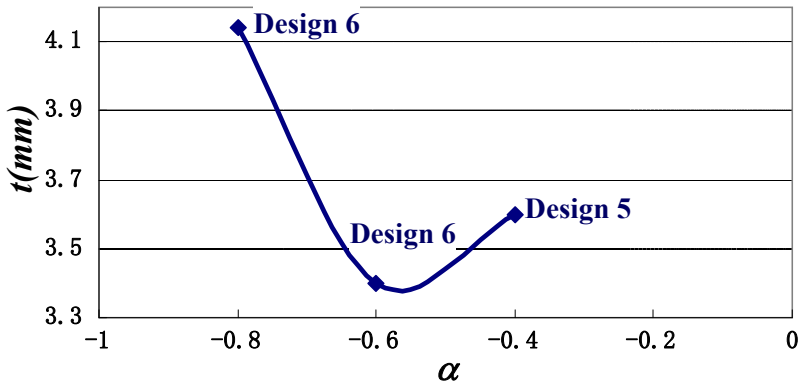

Figure 4.60 The comparison of the thickness for three LTCC integrated coupled-inductors with different coupling coefficients (w=6mm and *l*=20mm)

Figure 4.61 shows the transient inductance comparison of the above three designs with different coupling coefficients when w=6mm and *l*=20mm. When the coupling is stronger, the transient inductance is smaller and the transient performance of the converter is better.

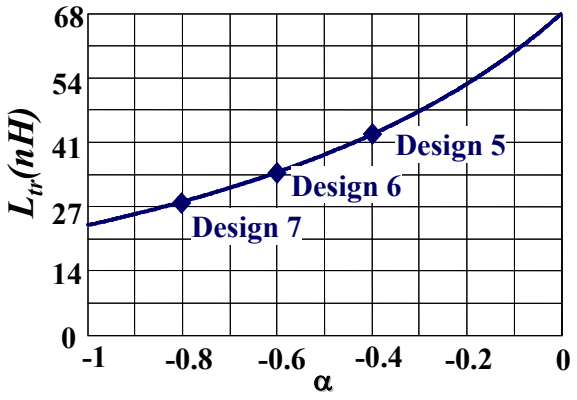

Figure 4.61 The comparison of the transient inductances for three LTCC integrated coupled-inductors with different coupling coefficients (w=6mm and *l*=20mm)

Figure 4.62 shows the graph of the thickness vs. the transient inductances for the above three designs with different coupling coefficients when w=6mm and *l*=20mm. The design 6 and design 7 are better designs. The design 6 has a smaller thickness but a larger transient inductance and the design 7 has a smaller transient inductance but a larger thickness.

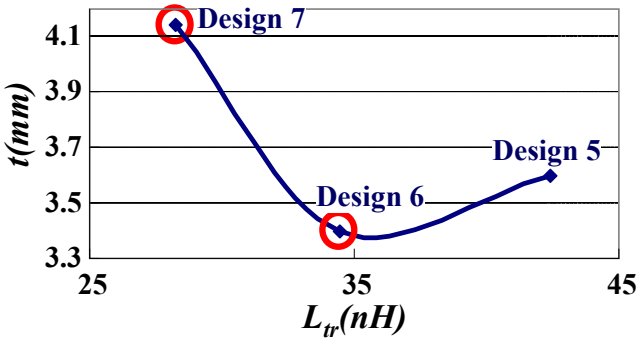

Figure 4.62 The graph of the thickness vs. the transient inductances for three LTCC integrated coupled-inductors with different coupling coefficients (w=6mm and *l*=20mm)

When the width w is chosen to be 4mm and *l* is chosen to be 30mm, the above design steps 3-7 are repeated. The final design results are α=-0.4, w_1=1mm, w_2=0.7mm, w_s=0.65mm, t_1=0.3mm, t_s=4.6mm and *l*=30mm; α=-0.6, w_1=1mm, w_2=0.55mm, w_s=0.7mm, t_1=0.3mm, t_s=4.14mm and *l*=30mm; α=-0.8, w_1=1mm, w_2=0.6mm, w_s=0.7mm, t_1=0.4mm, t_s=4.2mm and *l*=30mm.

Figure 4.63 shows the thickness comparison of the three designs with different coupling coefficients when w=4mm and *l*=30mm. There is a sweet coupling coefficent point from the total thickness of the LTCC integrated coupled inductor point of view.

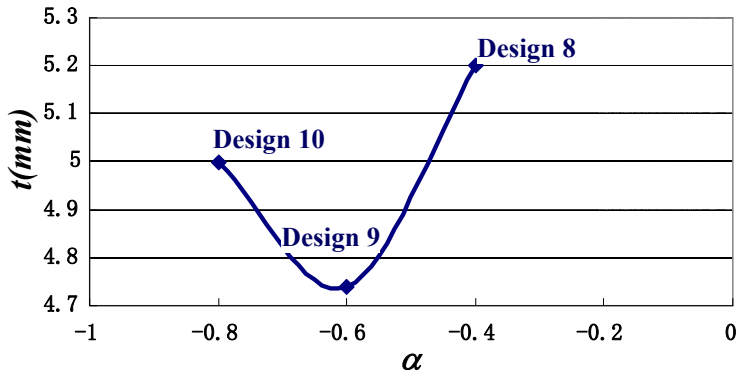

Figure 4.63 The comparison of the thickness for three LTCC integrated coupled-inductors with different coupling coefficients (w=4mm and *l*=30mm)

Figure 4.64 shows the transient inductance comparison of the above three designs with different coupling coefficients when w=4mm and *l*=30mm. When the coupling is stronger, the transient inductance is smaller and the transient performance of the converter is better.

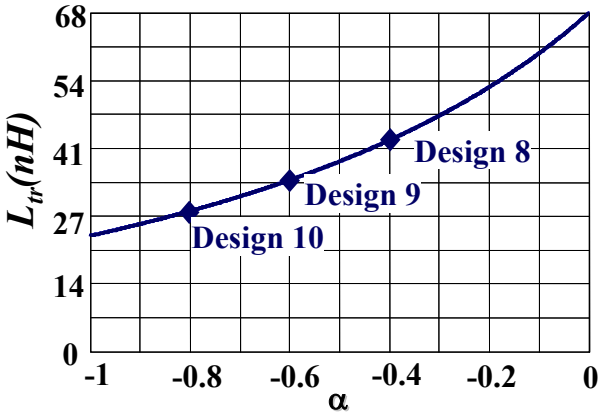

Figure 4.64 The comparison of the transient inductances for three LTCC integrated coupled-inductors with different coupling coefficients (w=4mm and *l*=30mm)

Figure 4.65 shows the graph of the thickness vs. the transient inductances for the above three designs with different coupling coefficients when w=4mm and *l*=30mm. The design 9 has a smaller thickness but a larger transient inductance and the design 10 has a smaller transient inductance but a larger thickness. Therefore, these two designs are the final design candidates.

Figure 4.66 shows the previous designs with the same footprint 120mm^2 in the graph of the thickness vs. the transient inductance. The design 6 and design 7 are better design compared to other designs. The design 6 has a smaller thicknes and volume while the design 7 has a smaller transient inductance and a faster transient performance. However, based on our LTCC process

experience, the thickness of the LTCC coupled inductor can't be more than 3.4mm. Therfore the design 6 is chosen as the final design.

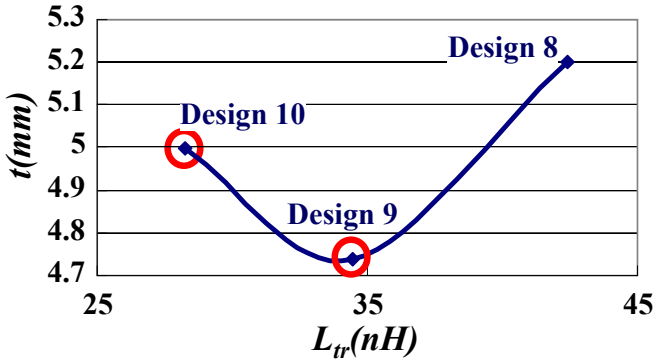

Figure 4.65 The graph of the thickness vs. the transient inductances for three LTCC integrated coupled-inductors with different coupling coefficients (w=4mm and *l*=30mm)

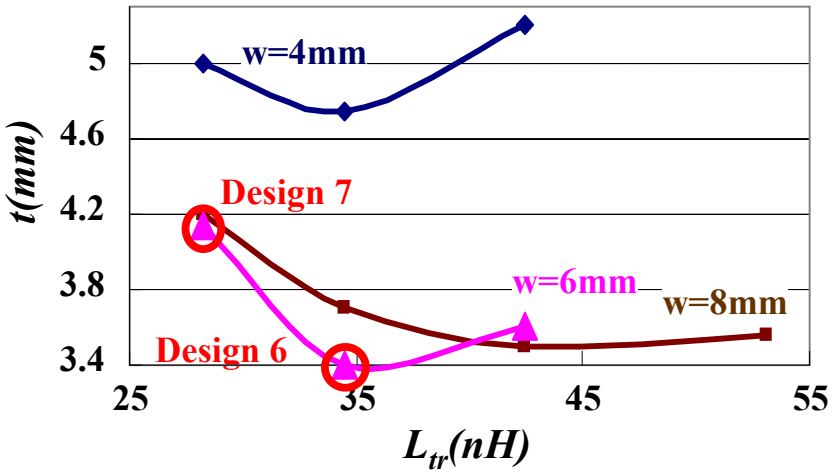

Figure 4.66 The graph of the thickness vs. the transient inductances for the LTCC integrated coupled-inductors with the same footprint 120mm^2

Figure 4.67 shows the customized prototype according to the design 6. It can be seen that there is a big crack on the side of the LTCC integrated coupled-inductor 2 prototype, which is caused by the strong air pressure in the sintering process. For this LTCC integrated coupled-inductor structure 2, all the air generated in the sintering process has to come off the prototype from one single out leg. Moreover, the off-gasing surface area of the LTCC integrated coupled-inductor structure 2 is smaller than that of the LTCC integrated coupled-inductor structure 1. As a result, the w_1 of the LTCC integrated coupled-inductor structure 2 needs to be larger than 1mm. The w_1 is increased little by little to find the necessary w_1 for the LTCC integrated coupled-

inductor structure 2. Based on the experiments, there is almost no crack when w_1=2mm (Figure 4.68). Therefore, w_1 is selected to be 2mm.

(a) (b)

Figure 4.67 The LTCC integrated coupled-inductor 2 prototype when w_1=1mm (w_2=1mm, w_s=1.5mm, t_1=0.7mm, t_s=2mm and *l*=20mm) (a) the top view (b) the side view

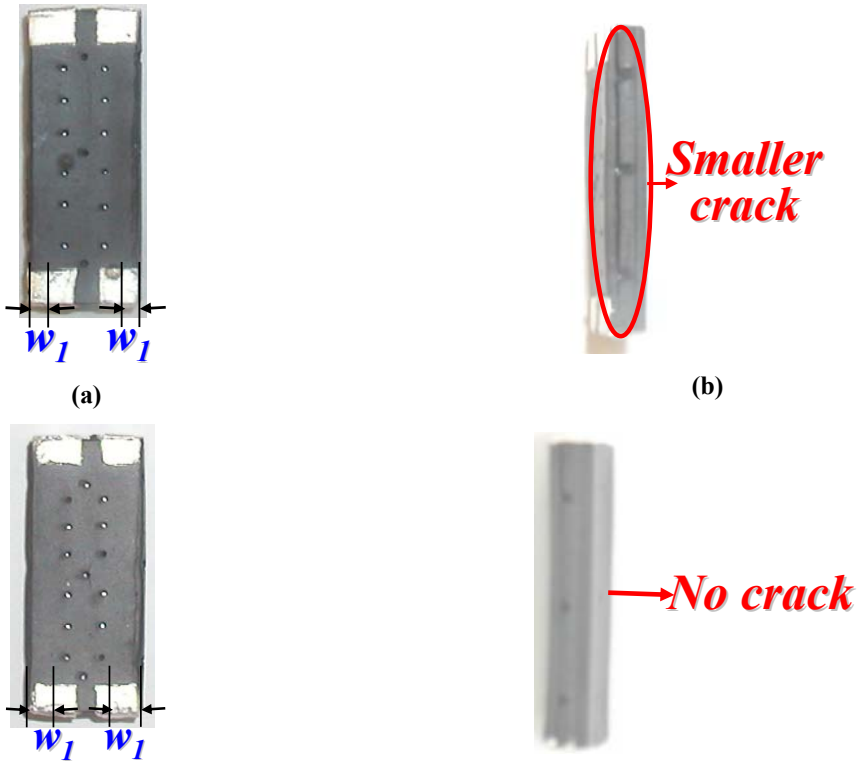

(a) (b) (c) (d)

Figure 4.68 The LTCC integrated coupled-inductor 2 prototype (w_2=1mm, w_s=1.5mm, t_1=0.7mm, t_s=2mm and *l*=20mm) (a) the top view, w_1=1.5mm (b) the side view, w_1=1.5mm (c) the top view, w_1=2mm (d) the side view, w_1=2mm

The final design result is w_1=2mm, w_2=1mm, w_s=1.5mm, t_1=0.7mm, t_s=2mm and l=20mm. The Maxwell FEA simulation is done for this design. According to the simulation, L_{ss}=72nH and α=-0.63. The design based on the reluctance model is acceptable.

4.3.4. Experimental Results

Figure 4.69 shows the final integrated coupled-inductor structure 2 prototype. Figure 4.70 shows the steady-state inductance testing result. At the full load, when I_{phase}=20A, L_{ss}=71nH. This verifies the reluctance model and the design process of the LTCC integrated coupled-inductor structure 2. It can also be seen that the steady-state inductance increases when the phase-current decreases. This characteristic can be used to improve the light-load efficiency of the POL converter.

Figure 4.69 The final two-phase LTCC integrated coupled-inductor structure 2 prototype (w_1=2mm, w_2=1mm, w_s=1.5mm, t_1=0.7mm, t_s=2mm and l=20mm)

Figure 4.71 shows the footprint comparison of the LTCC integrated non-coupled-inductor, the LTCC integrated coupled-inductor 1 and the LTCC integrated coupled-inductor 2. The footprint of the LTCC coupled-inductor 2 can reduce 51 percent footprint totally.

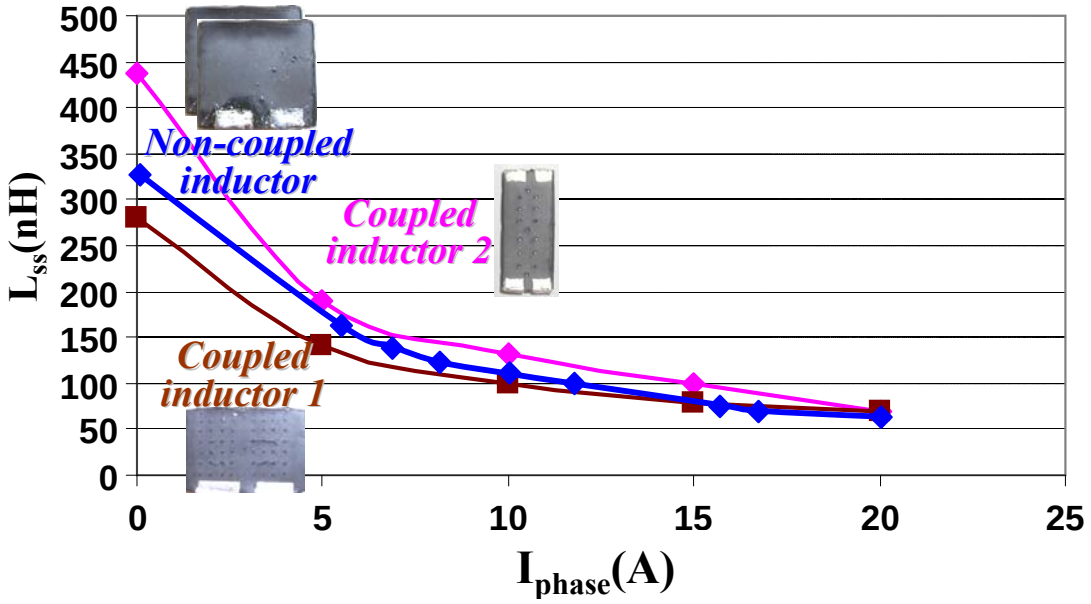

Figure 4.70 The steady-state inductance vs. the phase-current graph of two non-coupled-inductors, the two-phase coupled-inductor structure 1 and the two-phase coupled-inductor structure 2

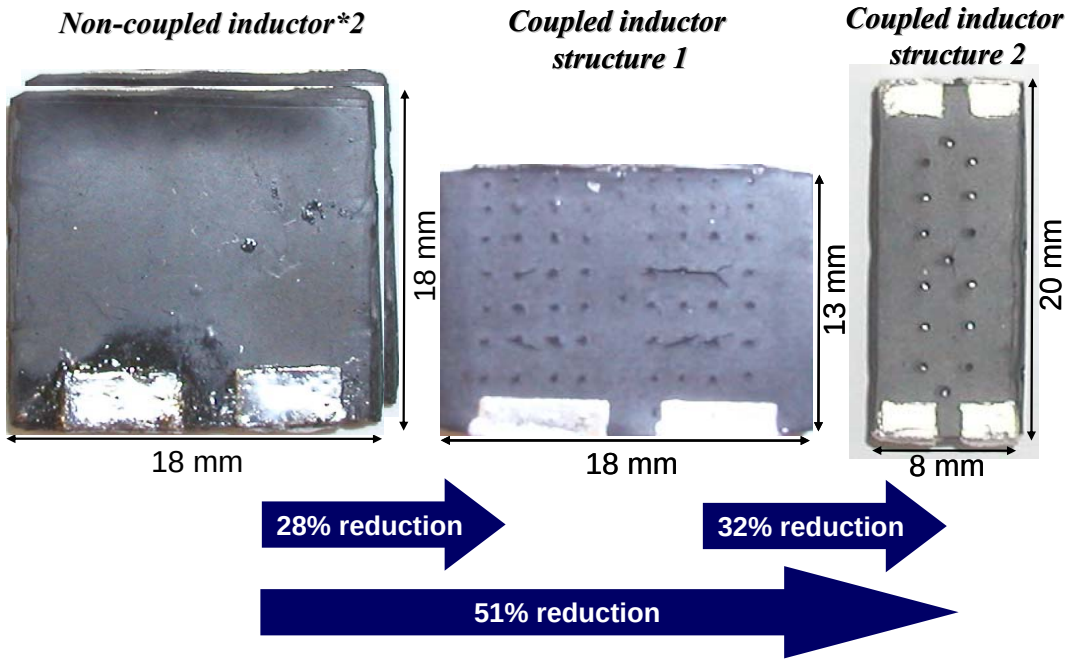

Figure 4.71 The footprint comparison of two LTCC non-coupled-inductors, the two-phase LTCC coupled-inductor structure 1 and the two-phase LTCC coupled-inductor structure 2

Figure 4.72 shows the efficiency comparison of the POL converters with two LTCC integrated non-coupled-inductors, the LTCC integrated coupled-inductor structure 1 and the

LTCC integrated coupled-inductor structure 2. The testing conditions are V_{in}=5V, V_o=1.2V, f_s=1.3MHz, based on the PCB active stage. It can be seen that the efficiencies are similar, which is expected because the L_{ss} of the three POL converters are designed to be the same.

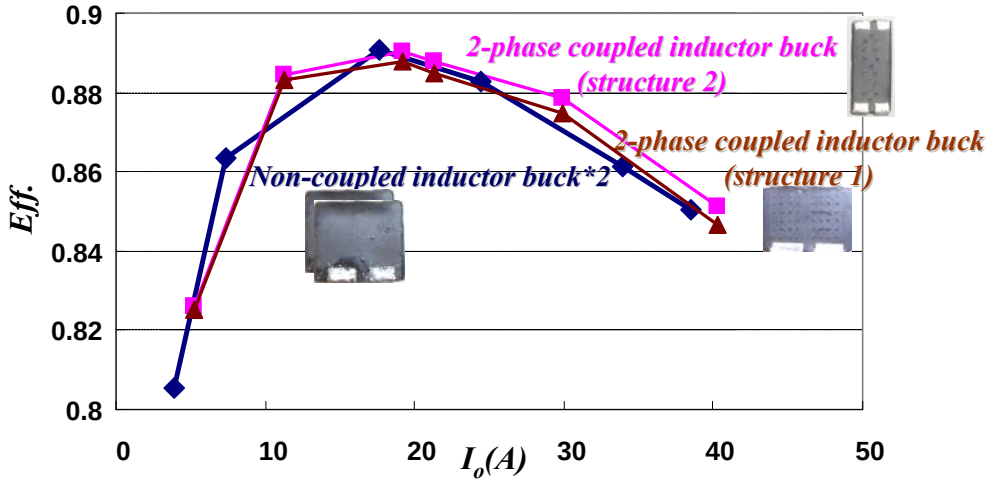

Figure 4.72 The efficiency comparison of the POL converters with two LTCC non-coupled-inductors, the two-phase LTCC coupled-inductor structure 1 and the two-phase LTCC coupled-inductor structure 2

4.4. CPES 3D LTCC Integrated Coupled-inductor POL Converter

The two-phase LTCC integrated coupled-inductor structure 2 prototype is connected with the improved active stage to build the integrated LTCC coupled inductor POL converter. Figure 4.73 shows the final two-phase LTCC integrated coupled-inductor POL converter module. The specifications are: V_{in}=5V, V_o=1.2V, f_s=1.3MHz, and I_o=40A. Its footprint is about 8x20mm^2 and its power density is amazingly 500W/in^3, twice that of the previous LTCC integrated non-coupled-inductor POL converter module.

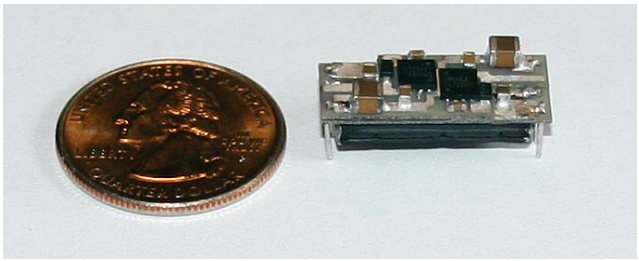

Figure 4.73 The two-phase LTCC integrated coupled-inductor buck (Picture by Author and A. Ball, 2008)

Since the LTCC integrated coupled-inductor POL converter doubles the POL converter power density, the thermal condition of this POL converter is worse than the previous LTCC

integrated non-coupled inductor POL converter. Although the AlN DBC active stage greatly improves the thermal performance compared to the normal PCB active stage, the thermal condition of the LTCC integrated coupled-inductor POL converter is still a convern. In the experiments, the fan with 100LFM is needed to avoid the circuit to burn out. Further investigation on whether there are hot spots in the LTCC integrated coupled-inductor POL converter and how to improve the thermal performance of the LTCC integrated coupled-inductor POL converter is needed.

4.5. Summary

Today, the converters are more and more integrated to increase the power-density. In this chapter, the bottleneck of the high power density is identified to be the large inductor size. Different integrated coupled-inductor structures are proposed to reduce the inductor size and improve the power density of the converter. The hardware based on the LTCC inductor shows that the inductor size can be reduced by half by coupling the inductors. The built integrated two-phase coupled inductor converter achieves an amazing 500W/in^3 power density, twice that of its integrated non-coupled inductor converter counterpart.

Chapter 5. Evaluation of the Benefits of Coupling in Multiphase Coupled-inductor Buck Converters

The multiphase interleaving buck converter normally has more than two phases. For example, Figure 5.1 is an industrial six-phase interleaving buck converter for a server buck VR (Intersil ISL 6327). The specifications of the converter are L_{phase}=100nH, V_{in}=12V, V_o=1.2V, f_s=600kHz, six 100μF output bulk capacitors, and thirty-three 10μF ceramic capacitors.

Therefore, there are several different coupled-inductor buck converter setups for the multiphase interleaving buck converter. For this six-phase server buck VR, there are three different coupled-inductor buck converter setups to improve the original non-coupled-inductor buck converter performance: three two-phase coupled-inductor buck converter, two three-phase coupled-inductor buck converter, and one six-phase coupled-inductor buck converter. It is unclear which coupled-inductor buck converter setup is the best.

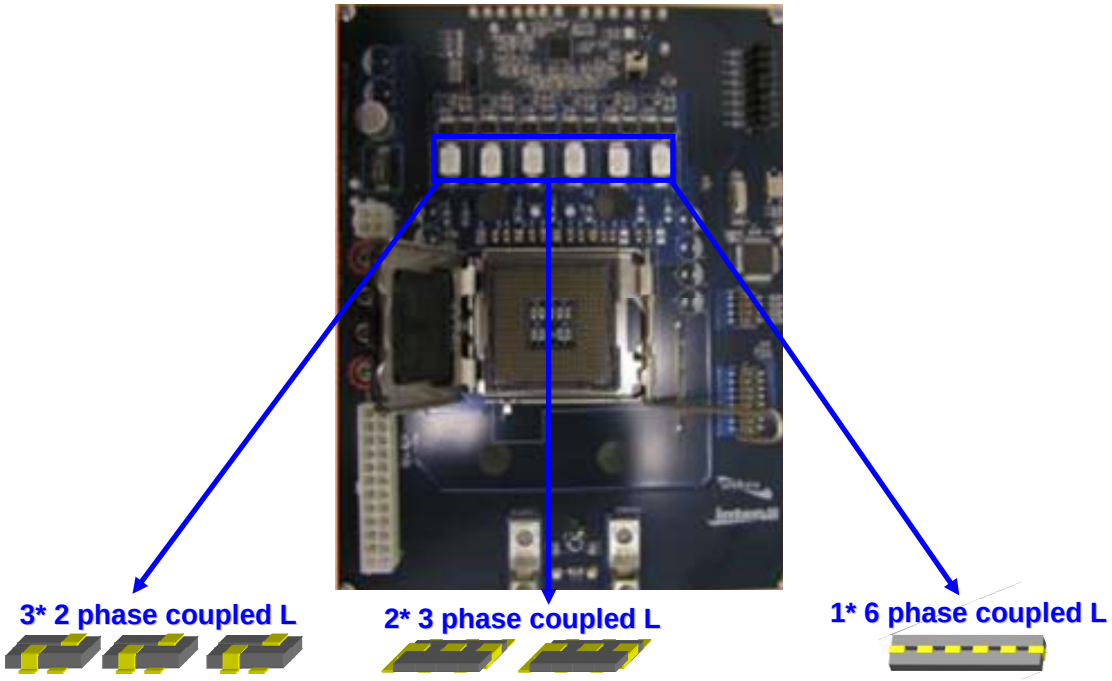

Figure 5.1 Intersil's ISL6327 six-phase server buck converter demo board and its different coupled-inductor buck converter setups (Picture by author, 2006)

In this section, the above question will be answered based on this multiphase buck demo board step by step. Firstly, the benefits of 3*2-phase coupled inductor bucks are analyzed and verified by experimental results. Then, the benefits of 2*3-phase coupled inductor bucks are analyzed and verified by experimental results. Finally, the benefits of 1*6-phase coupled inductor bucks are analyzed, and the benefit comparison of the three different setups is shown. The suggested coupled inductor buck setup is given.

5.1. Three Two-phase Coupled-inductor Buck Converter

For the three two-phase coupled-inductor buck converter, we can demonstrate the buck converter transient performance improvement (the output bulk capacitor reduction) or the buck converter steady-state performance improvement (efficiency improvement) by using two-phase coupled inductors.

A. Keeping the same efficiency

Firstly, we use three two-phase coupled-inductor buck converters to reduce the output bulk capacitors while keeping the coupled-inductor buck converter efficiency the same as the original non-coupled inductor buck converter. The steady-state inductance is kept the same as the non-coupled inductor: L_{ss}=L=100nH.

According to the equation (1.17),

$$\frac{L_{tr}}{L_{ss}} = \frac{1 + \frac{D}{D'} \cdot \alpha}{1 - \alpha} \tag{5.1}$$

which is shown in Figure 5.2 for the multiphase buck VR case D=0.1.

We can see that the stronger coupling results in a smaller L_{tr} (a potential faster VR transient performance), but we can't choose $|\alpha|$ to be too close to one, or it will cause core saturation. The practical $|\alpha|$ value is around 0.8-0.9, and the L_{tr} is about half of the steady-state inductance. In this evaluation, we choose $L_{tr}=0.5L_{ss}$=50nH. The design point is shown in Figure 5.2.

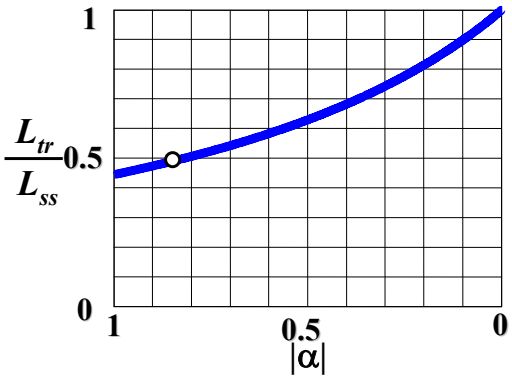

Figure 5.2 The ratio of the transient inductance to the steady-state inductance L_{tr}/L_{ss} vs. the coupling coefficient |α| (the duty cycle D=0.1)

The two-phase low-profile twisted-core coupled inductor is used in this two-phase coupled-inductor buck converter. Based on the new reluctance model and design procedure developed in the last chapter, we design three two-phase low-profile twisted-core coupled inductors.

Figure 5.3 shows the output capacitor reduction mechanism of the two-phase coupled-inductor buck converter. Figure 5.4 shows the experimental output capacitor reduction with the three two-phase coupled-inductor buck converter. Figure 5.5 shows an efficiency comparison of the buck converter with three two-phase coupled inductors and the original non-coupled buck converter. We can see that with the similar efficiency, the buck converter with three two-phase coupled inductors can reduce five 100μF ceramic capacitors.

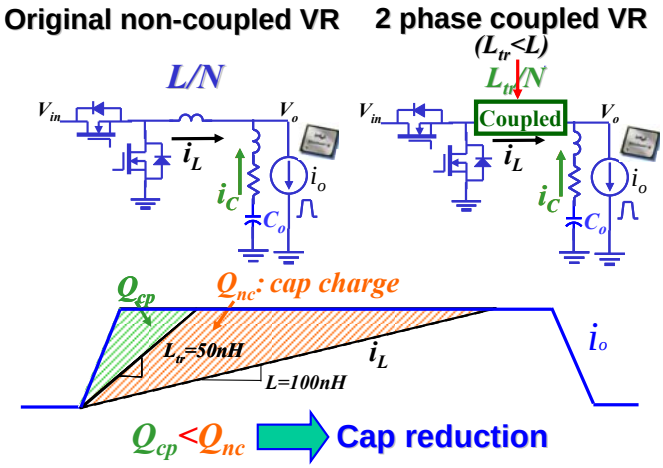

Figure 5.3 The output capacitor reduction mechanism of the two-phase coupled-inductor buck converter

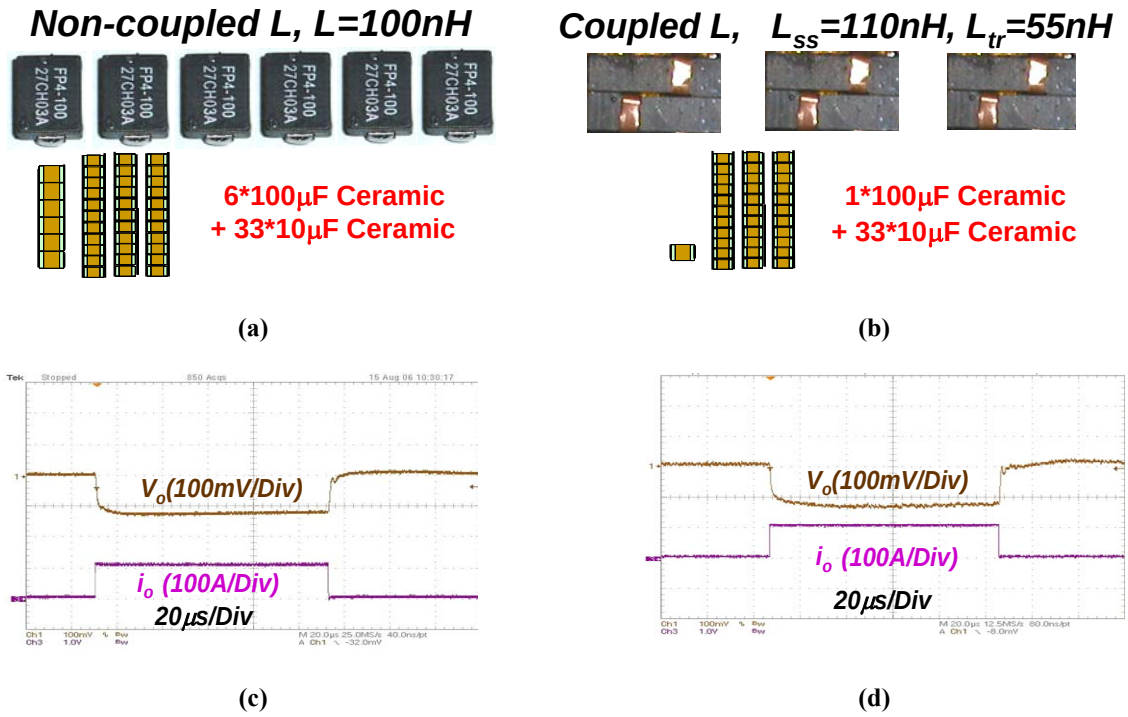

Figure 5.4 Output bulk capacitor reduction of the three two-phase coupled buck converter (a) Output bulk caps of the original board (b) Output bulk caps of the three-two-phase coupled buck (c) Transient waveform of the original board (d) Transient waveform of the three two-phase coupled buck

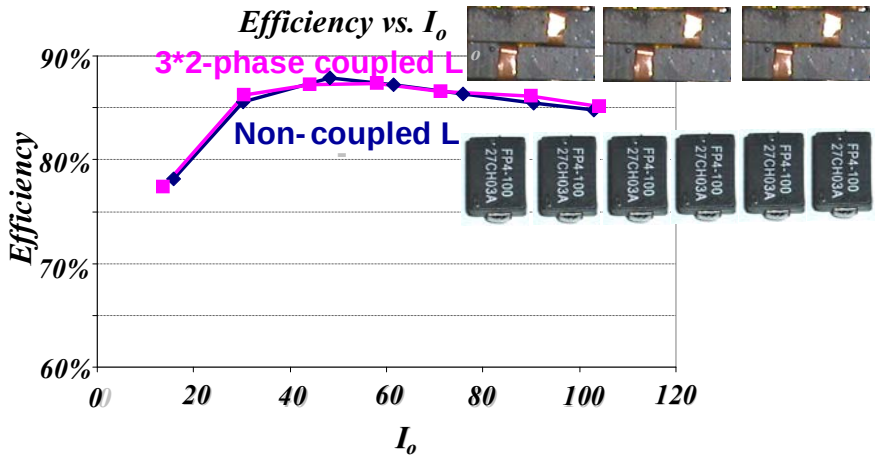

Figure 5.5 The efficiency comparison of the original non-coupled-inductor demo board and three two-phase coupled-inductor VR

Figure 5.6 shows the output voltage ripple comparison. We can see that the output voltage ripple is increased for the buck converter with three two-phase coupled inductors. This is because L_{tr} is less than L, and the output voltage ripple is determined by the transient inductance.

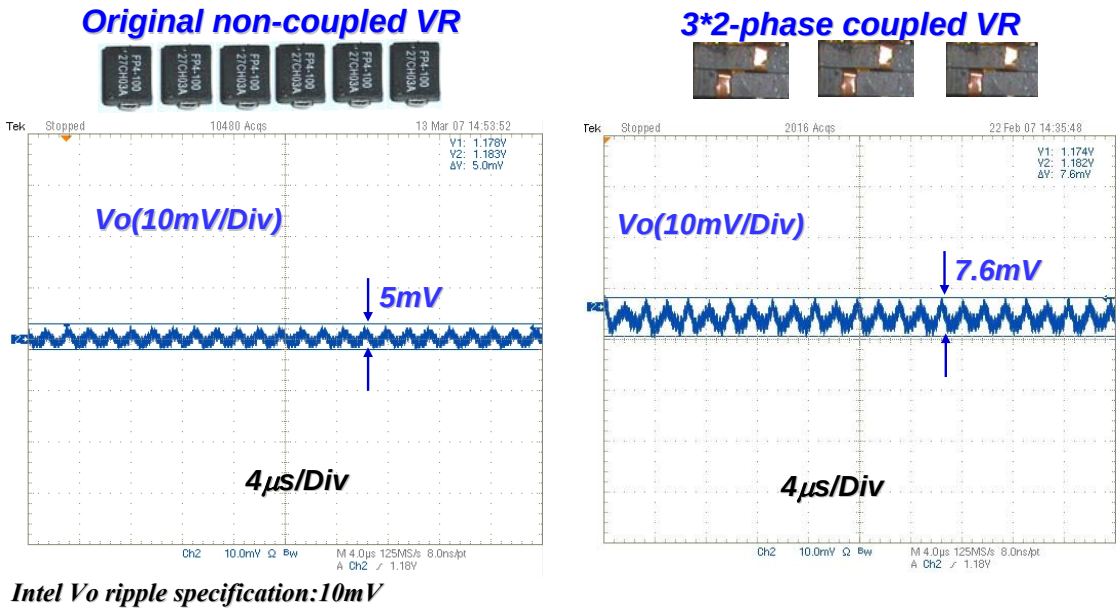

Figure 5.6 The output voltage ripple comparison of the original non-coupled-inductor buck converter and the three two-phase coupled-inductor buck converter

B. Keeping the same output capacitors

Secondly, we use a buck converter with three two-phase coupled inductors to increase the buck converter efficiency while keeping the coupled-inductor buck converter transient performance the same as the original non-coupled inductor buck converter while using the same number of output capacitors. The transient inductance is kept the same as the non-coupled inductor: L_{tr}=L=100nH.

Figure 5.7 shows the L_{ss}/L_{tr} vs. $|\alpha|$ curve. We can see that the maximum steady-state inductance L_{ss} is around twice of the L_{tr}. We choose L_{ss}=2 L_{tr}=200nH.

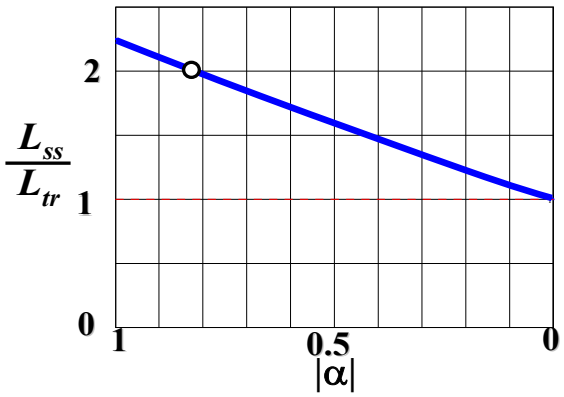

Figure 5.7 The ratio of the steady-state inductance to the transient inductance L_{ss}/L_{tr} vs. the coupling coefficient $|\alpha|$ (the duty cycle D=0.1)

Following the two-phase semi-twisted core coupled inductor design procedure, we can design the coupled inductor, customize it and build the three two-phase coupled-inductor buck converter.

Figure 5.8 shows the multiphase buck converter loss breakdown based on the precise analytical loss model proposed in [22]. We can see that the three two-phase coupled-inductor buck converter efficiency improvement is mainly due to the reduction in the turn-off loss of the top switch.

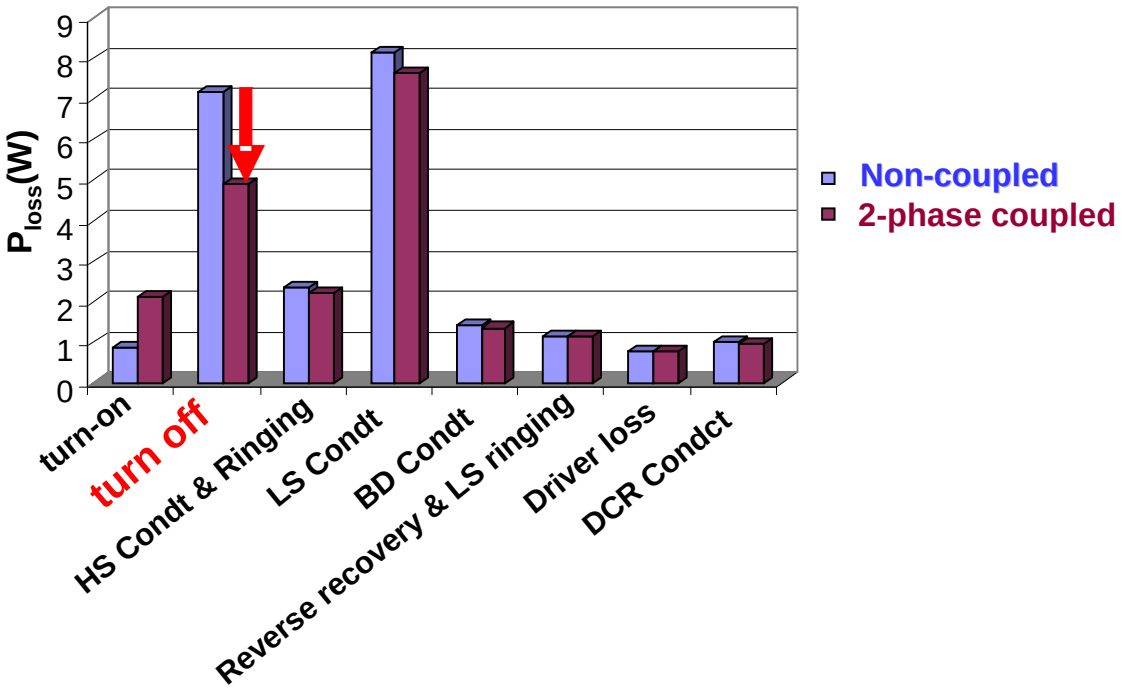

Figure 5.8 The loss breakdown of the original six-phase non-coupled-inductor buck converter with L=100nH and the three two-phase coupled-inductor buck converter with L_{tr}=100nH and L_{ss}=200nH (V_{in}=12V, V_o=1.2V, I_o=100A, f_s=600kHz; Top switch: HAT2168; bottom switch: HAT2165)

The experimental efficiency improvement is shown in Figure 5.9. The transient AVP waveforms of the original non-coupled inductor buck converter and the three two-phase coupled-inductor buck converter are shown in Figure 5.10. We can see that with the same multiphase buck VR transient AVP performance, the three two-phase coupled-inductor buck converter can improve efficiency by 1%.

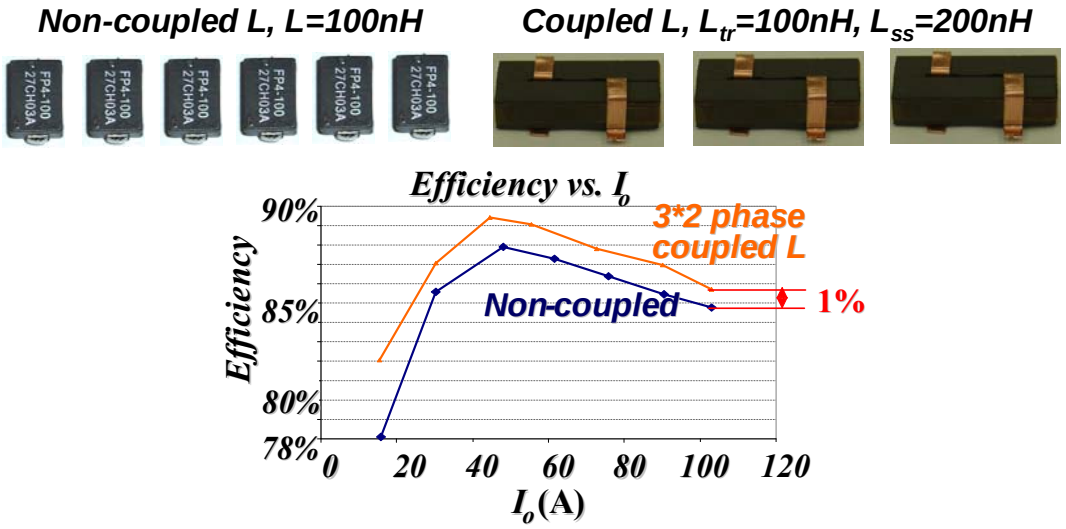

Figure 5.9 The efficiency improvement of the three two-phase coupled-inductor buck converter compared to the original non-coupled-inductor buck converter

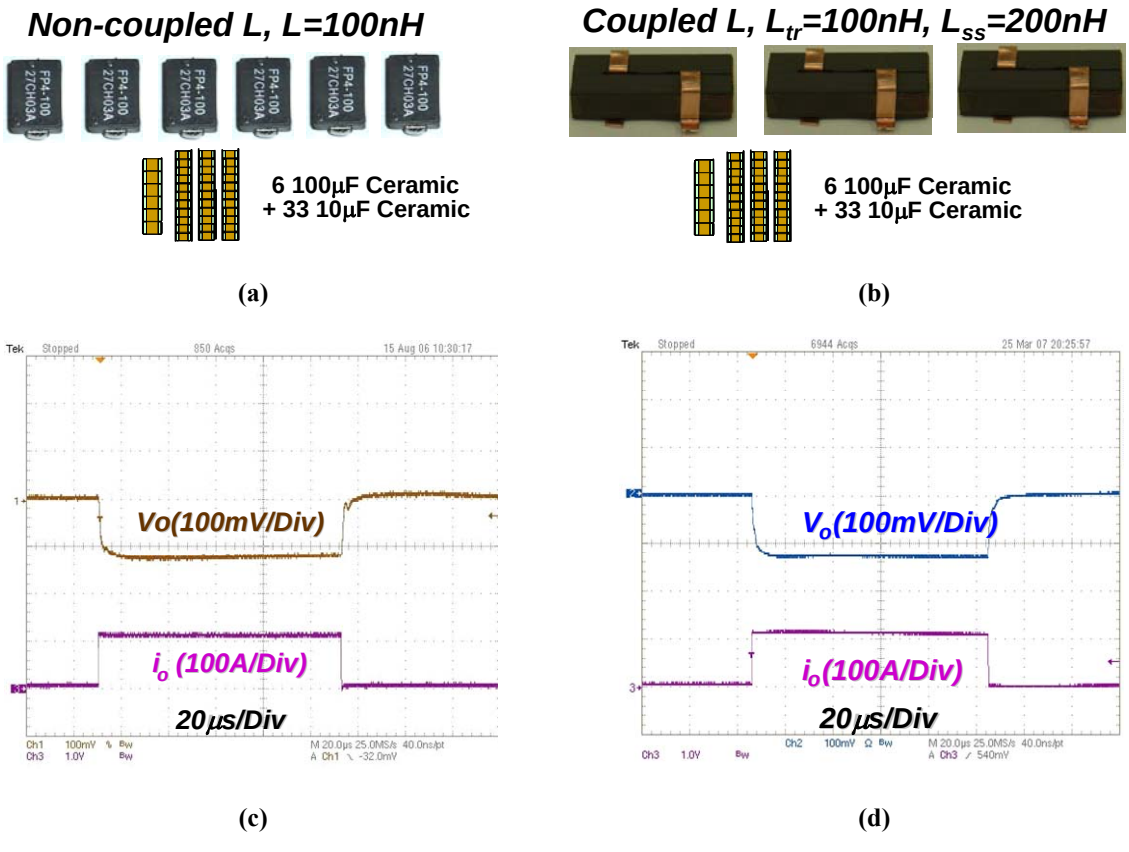

Figure 5.10 The output capacitor reduction of the three two-phase coupled inductor buck converter compared to the original non-coupled-inductor buck converter (a) Output bulk caps of the original board (b) Output bulk caps of the three-two-phase coupled buck (c) Transient waveform of the original board (d) Transient waveform of the three two-phase coupled buck

The output voltage ripple comparison is shown in Figure 5.11. We can see that the converters have a similar output voltage ripple because they have a similar L_{tr}.

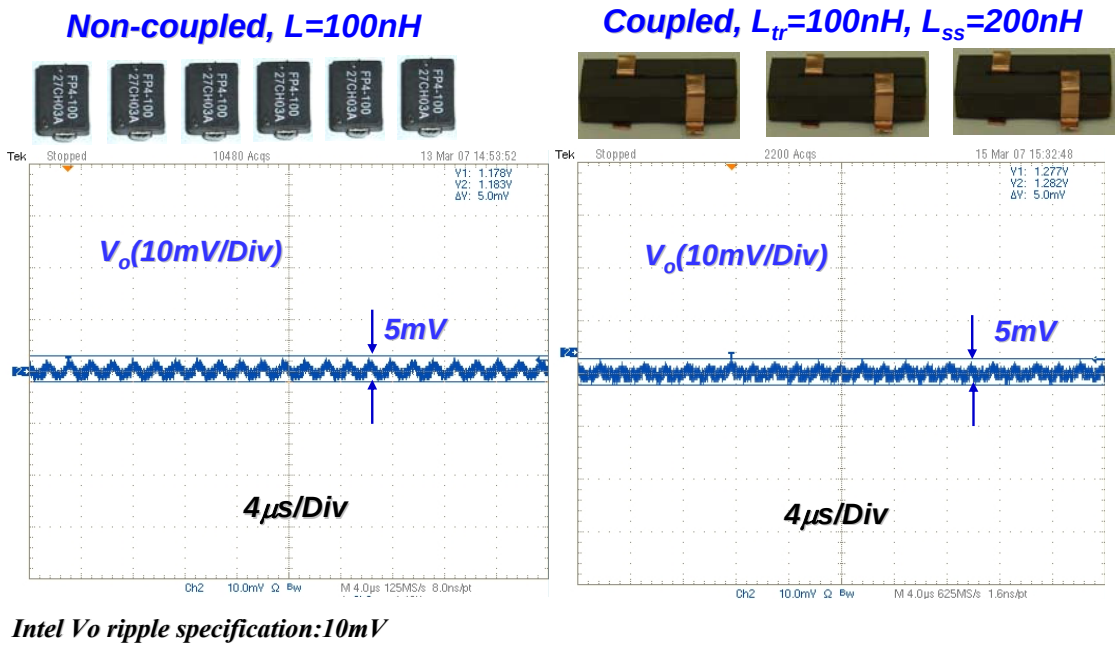

Figure 5.11 The output voltage ripple comparison of the original non-coupled-inductor buck converter and the three two-phase coupled-inductor buck converter

In summary, using a three two-phase coupled-inductor buck converter can reduce five 100μF ceramic output capacitors, or increase efficiency by 1%.

5.2. Two Three-phase Coupled-inductor Buck Converter

Three-phase coupled inductors can further increase the L_{ss}/L_{tr} ratio; thus they have the potential to achieve more benefits than two-phase coupled inductors. Like using two-phase coupled inductors, we can use two three-phase coupled-inductor buck converters to reduce the number of output bulk capacitors or to increase the multiphase buck converter efficiency.

A. Keeping the same efficiency

Firstly, we try to keep the steady-state inductance the same as the original multiphase non-coupled inductor buck converter, where L_{ss}=L=100nH, and reduce the L_{tr} to reduce the number of output capacitors.

The L_{tr}/L_{ss} equation for the three-phase coupled-inductor buck converter is shown below.

$$\frac{L_{tr}}{L_{ss}} = \frac{1+(\frac{1}{2}+\frac{D}{D'})\cdot\alpha}{1-\frac{\alpha}{2}} \tag{5.2}$$

Figure 5.12 shows the L_{tr}/L_{ss} vs. $|\alpha|$ for the three-phase coupled-inductor buck converter when D=0.1. The corresponding curve for the two-phase coupled-inductor buck converter is also shown here for reference.

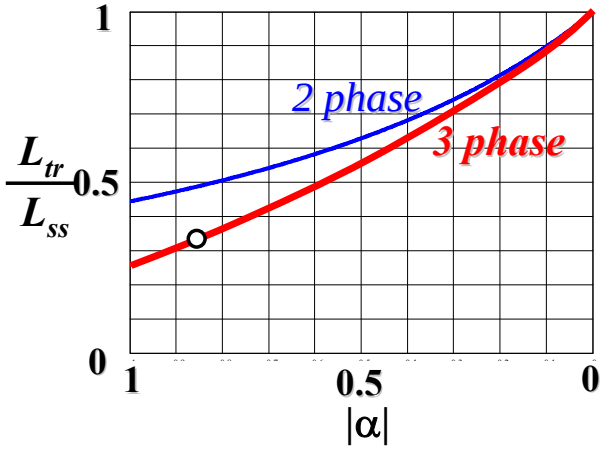

Figure 5.12 The ratio of the transient inductance to the steady-state inductance L_{tr}/L_{ss} vs. the coupling coefficient $|\alpha|$ for the two-phase and three-phase coupled-inductor buck converters (the duty cycle D=0.1)

We can see that practically the minimum L_{tr} is around one third of the L_{ss}. We choose $L_{tr}=1/3L_{ss}=33nH$. The design point is shown in Figure 5.12.

The necessary number of output bulk capacitors can be estimated by simulation. With the multiphase buck circuit model with the Intersil ISL6327 controller, the driver and the device models on the website. Figure 5.13 shows the output bulk capacitance C_o vs. the phase transient inductance L_{tr} curve, satisfying the transient AVP requirement.

With the capacitors shown in Figure 5.13, the simulation circuit is run with $L_{tr}=33nH$, and it is found that the $V_{oripple}$ is already 12.5mV (Figure 5.14), which is larger than the Intel VR11 specification 10mV. Therefore, it can be seen that the $V_{oripple}$ requirement (10mV), not the VR transient requirement, is the bottleneck for reducing the output capacitors in this case.

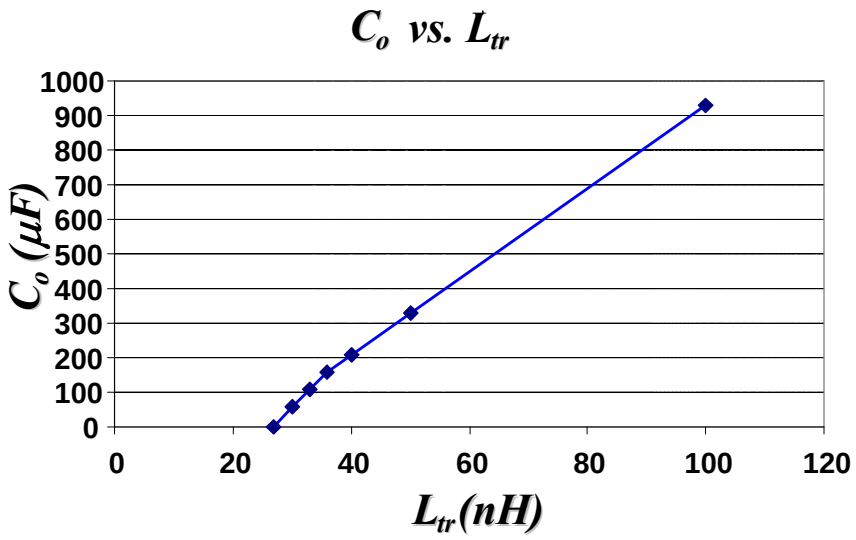

Figure 5.13 The output capacitance C_o vs. the transient inductance L_{tr} of the Intersil ISL6327 six-phase buck converter fulfilling the transient AVP requirement

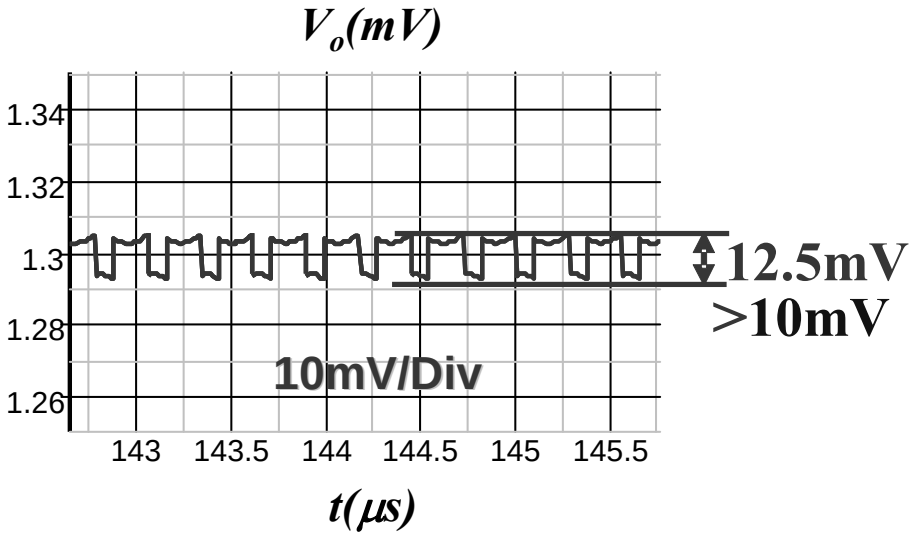

Figure 5.14 The simulated output voltage ripple when the transient inductance of the symmetric six-phase buck converter with L_{tr}=33nH (V_{in}=12V, V_o=1.2V, f_s=600kHz)

Therefore, L_{tr} must be increased to satisfy the 10mV $V_{oripple}$ requirement. In the real circuit, the phase shift is normally not perfect (180°). Figure 5.15 shows the $V_{oripple}$ vs. the non-perfect phase shift. It can be seen that the $V_{oripple}$ increases when the phase shift deviates from 180°. Considering this non-perfect phase shift and the noise in the real circuit, which increase the $V_{oripple}$, experiments are done to find the boundary L_{tr} corresponding to the 10mV $V_{oripple}$. Based

on the experimental results, it is found that when L_{tr}=43nH, the V_o ripple is about 10mV (Figure 5.16).

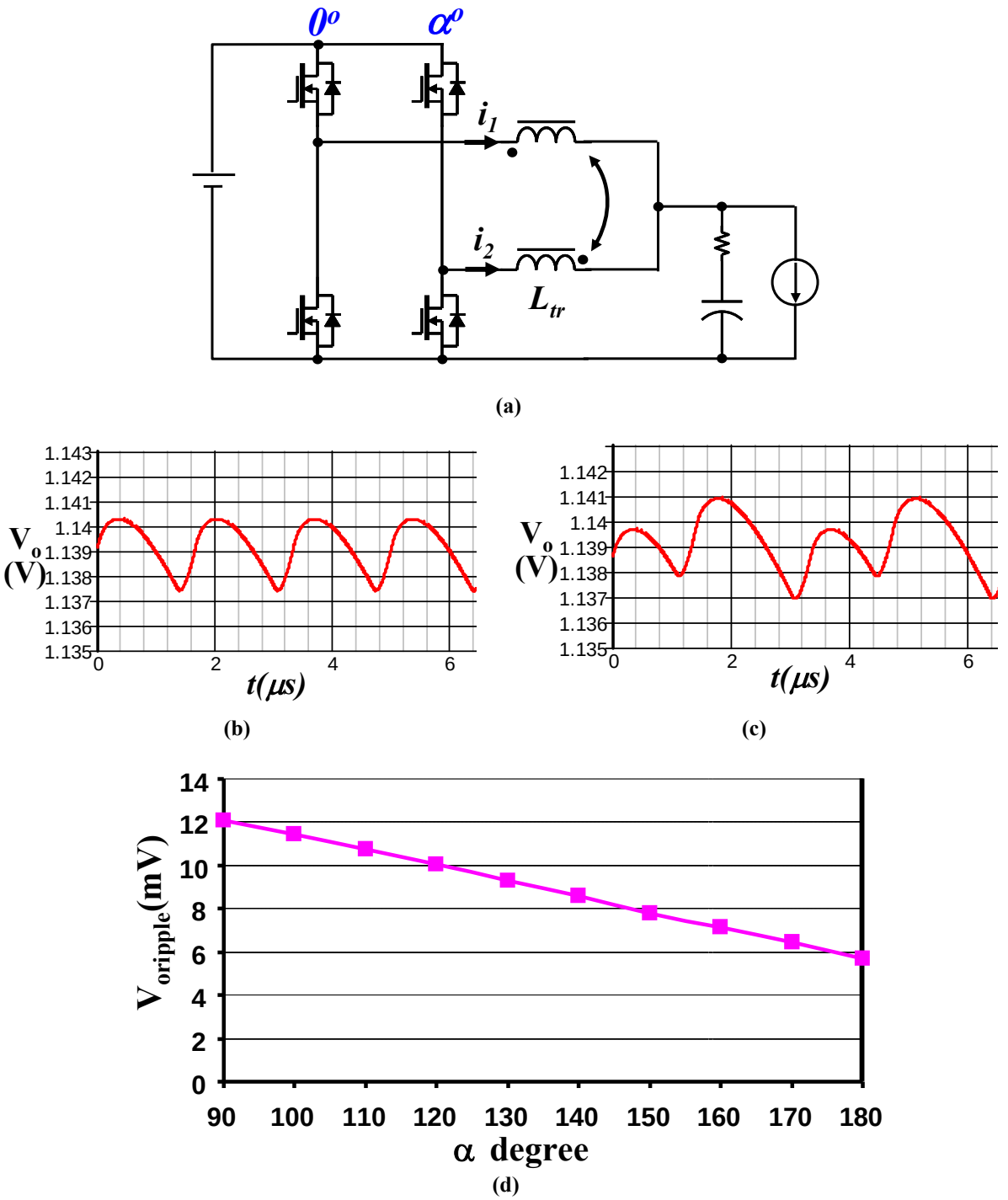

Figure 5.15 The simulated output voltage ripple $V_{oripple}$ vs. the phase shift angle α in a coupled-inductor buck converter (a) The 2-phase coupled inductor buck with the α degree phase shift (b) The $V_{oripple}$ @ 180 phase shift (c) The $V_{oripple}$ @ non-180 phase shift (d) The $V_{oripple}$ vs. the non-perfect phase shift α

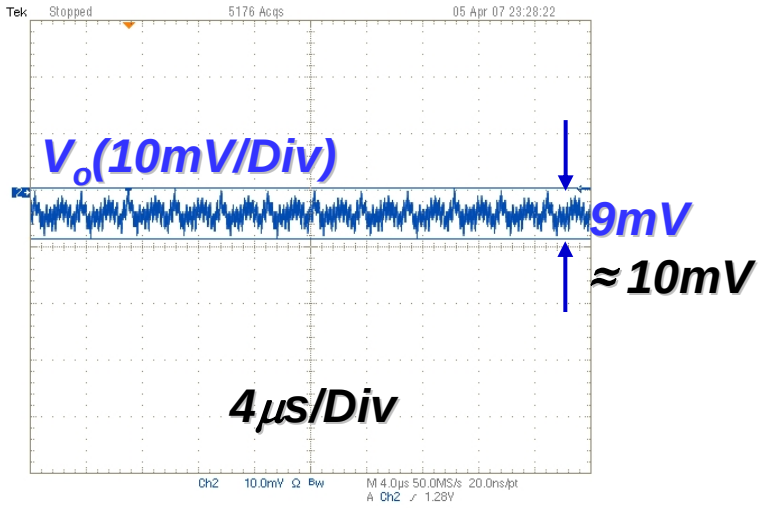

Figure 5.16 The tested output voltage ripple in the three two-phase coupled-inductor ISL6327 buck converter with L_{tr}=43nH

Therefore, L_{tr} can be set at 43nH, and the three-phase coupled inductor's remaining L_{ss}/L_{tr} capability can be used to increase the steady-state inductance. Considering the three-fold difference between L_{ss} and L_{tr}, $L_{ss}=3L_{tr}=129$nH.

Following the design process, we can design the three-phase coupled inductor, customize it and build the three-phase coupled-inductor VR. Figure 5.17 shows the output capacitor reduction with the three-phase coupled-inductor buck converter, and Figure 5.18 shows the efficiency improvement of the three-phase coupled-inductor buck converter.

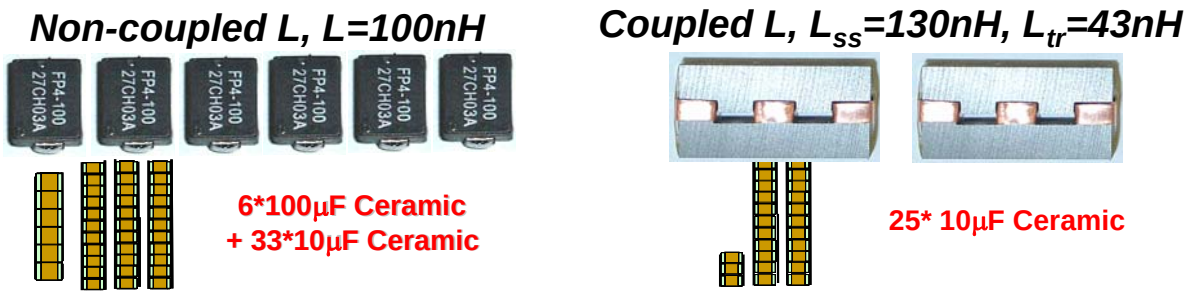

(a) **(b)**

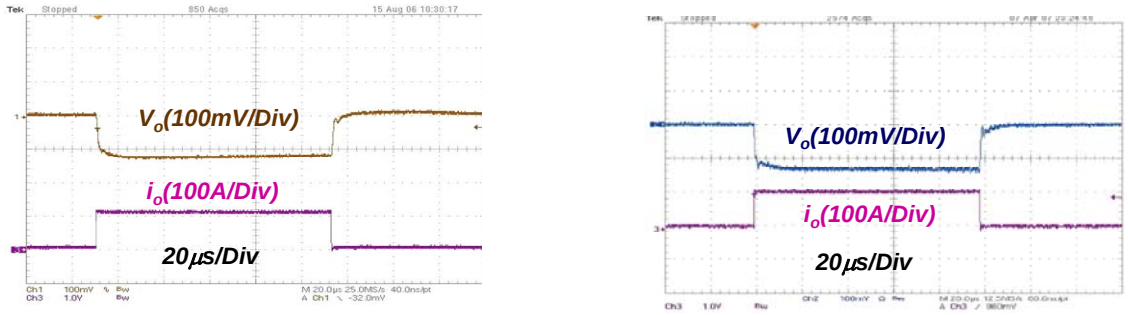

(c) (d)

Figure 5.17 Output capacitor reduction of the two three-phase coupled-inductor buck converter compared to the original non-coupled-inductor buck converter (a) Output bulk caps of the original board (b) Output bulk caps of the two three-phase coupled buck converter (c) The transient waveform of the original board (d) The transient waveform of the two three-phase coupled buck

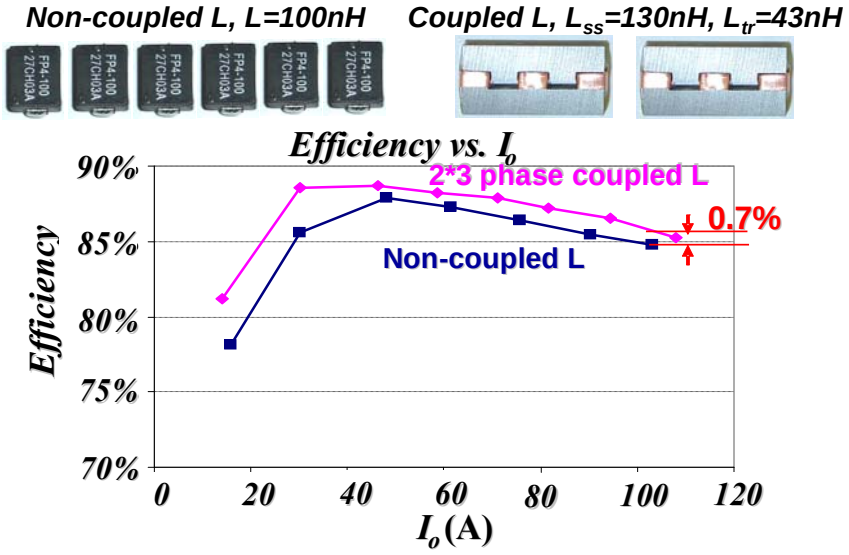

Figure 5.18 The efficiency improvement of the two three-phase coupled-inductor buck converter compared to the original non-coupled-inductor buck converter

B. Keeping the same output capacitors

Secondly, we keep the transient inductance L_{tr} to be the same as the original multiphase non-coupled inductor buck converter and improve the efficiency of the three-phase coupled-inductor buck converter as much as possible. L_{tr} is set to be 100nH. Since practically L_{ss} is at most around three times larger than L_{tr}, we choose L_{ss}=3 L_{tr}=300nH.

Based on the precise multiphase buck converter analytical loss model [22], the efficiency comparison of the non-coupled inductor buck converter, the three two-phase coupled-inductor

buck converter and the two three-phase coupled-inductor buck converter can be found in Figure 5.19. It can be seen that the two three-phase coupled-inductor buck converter can only improve the efficiency 0.1% beyond the three two-phase coupled-inductor buck converter . This can be explained by the loss breakdowns of these three multiphase buck converters, as shown in Figure 5.20. It can be seen that the additional turn-off loss reduction of the two three phase coupled-inductor buck converter compared to the three two-phase coupled-inductor buck converter is very small, since the current ripple in the three two-phase coupled-inductor buck converter is already very small. Therefore, two three-phase coupled-inductor buck converter can only increase the efficiency a negligible amount beyond that of the two-phase coupled-inductor buck converter. Practically, it is not wise to use the two three-phase coupled-inductor buck converter only to improve the efficiency.

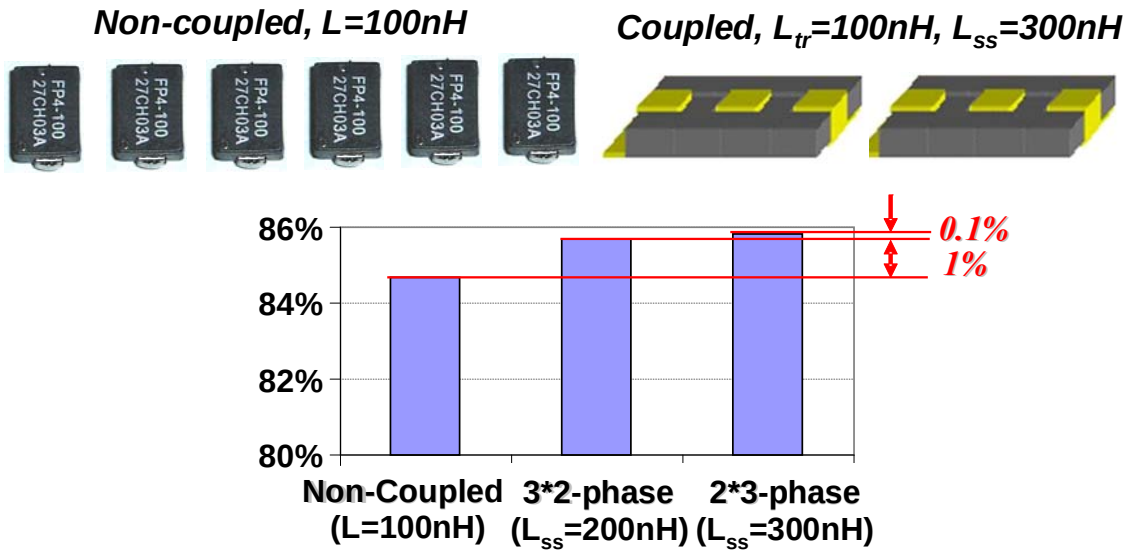

Figure 5.19 The calculated efficiency of the two three-phase coupled-inductor buck converter (L_{tr}=100nH, L_{ss}=300nH) compared to the three two-phase coupled-inductor buck converter (L_{tr}=100nH, L_{ss}=200nH) and the original non-coupled-inductor buck converter (L=100nH)

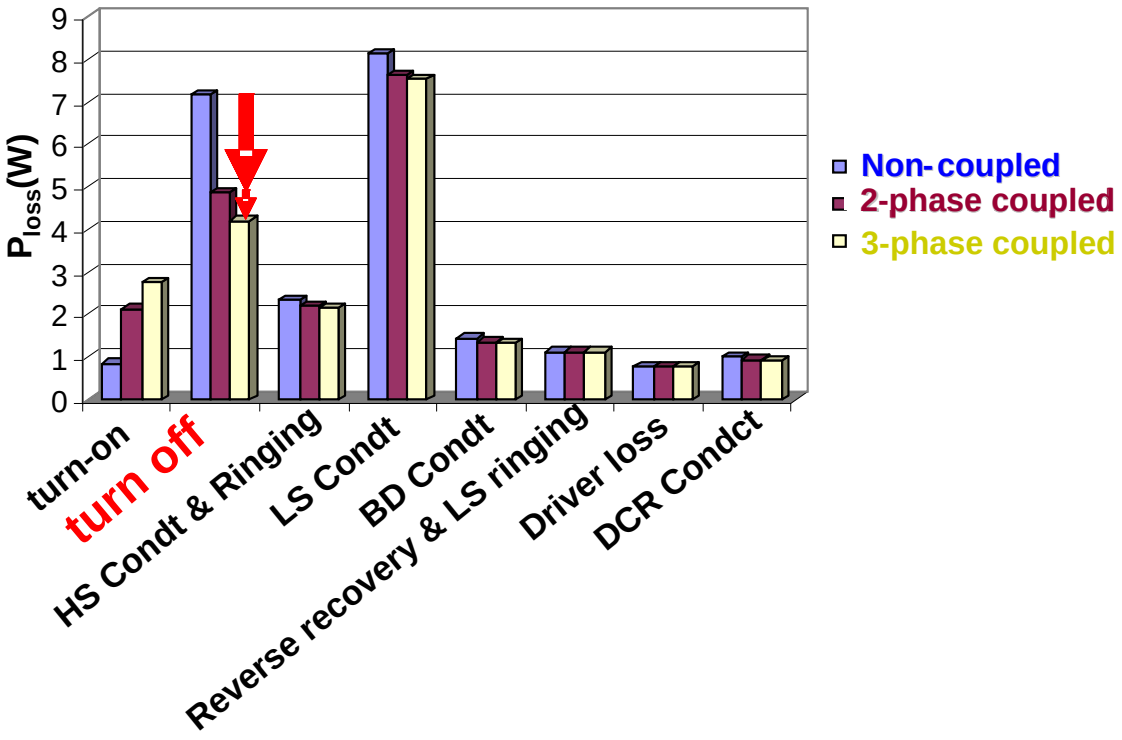

Figure 5.20 The loss breakdown of the original six-phase non-coupled-inductor buck converter with L=100nH and the three two-phase coupled-inductor buck converter with L_{tr}=100nH and L_{ss}=300nH (V_{in}=12V, V_o=1.2V, I_o=100A, f_s=600kHz; Top switch: HAT2168; bottom switch: HAT2165)

In summary, the two three-phase coupled-inductor VR can reduce six 100µF and eight 10µF ceramic capacitors and improve the VR efficiency 0.7%. In terms of increasing the multiphase buck converter efficiency, more-phase coupling has a diminishing return. For this ISL6327 multiphase buck VR, the diminishing return phase number point is the (three) two-phase coupling. More-than-two-phase coupling is not suggested to merely increase the multiphase buck converter efficiency.

5.3. One Six-phase Coupled-inductor Buck Converter

One six-phase coupled-inductor can further enlarge the difference between the steady-state inductance L_{ss} and the transient inductance L_{tr}. Therefore, one six-phase coupled-inductor buck converter theoretically has the potential to further increase the multiphase buck converter performance. In the previous section, it is found that using one six-phase coupled-inductor to increase the multiphase buck converter efficiency (keeping L_{tr}=L=100nH and increasing

L_{ss}=600nH) meets the diminishing benefit return. Here, only the one six-phase coupled-inductor buck converter setup with the reduced output capacitors is considered.

However, the asymmetry issue is met in one six-phase coupled-inductor buck. In fact, the practical n-phase (n>=3) line-structure coupled-inductor is asymmetric theoretically. Figure 5.21 shows the asymmetry of three-phase ET core coupled-inductor and six-phase ET core coupled-inductor. It can be seen that the more phase are coupled, the more asymmetric the coupled-inductor structure is. The three-phase coupled-inductor is nearly symmetric. The bad effects of its little L_{ss} and L_{tr} differences are negligible. Therefore, the output bulk caps will not increase because of the asymmetry. On the contrary, the six-phase ET core coupled-inductor is very asymmetric. The output voltage ripple will increase, which prohibits the output bulk cap reduction. The inductor phase current ripple will be different, which leaves burden to the converter control system.

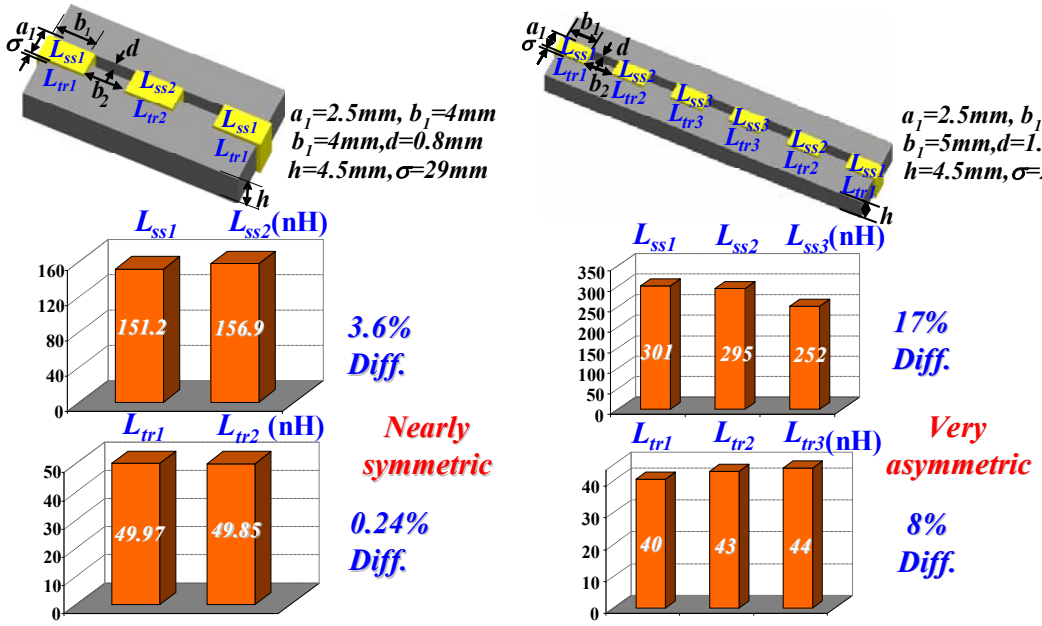

Figure 5.21 Asymmetry of three-phase and six-phase coupled-inductors

One method to reduce the asymmetry of six-phase ET core coupled-inductor is to add the wings at the side of the six-phase coupled-inductor (Figure 5.22). Figure 5.23 shows the curve of the transient inductance difference vs. the wing length c_1. The L_{tr} difference is related to the output voltage ripple and accordingly the output bulk cap reduction. It can be seen that the L_{tr} difference is smallest at c_1=1mm.

At c_1=1mm point, the differences of the phase steady state inductances and the transient inductances in the six-phase ET core coupled-inductor are shown in Figure 5.23. The steady state inductance difference will cause the 26% phase current ripple difference (Figure 5.24). The transient inductance difference will cause the 10% larger output voltage ripple (Figure 5.25). Therefore, although the asymmetry is attenuated by adding the wings, the remaining asymmetry still causes some issues.

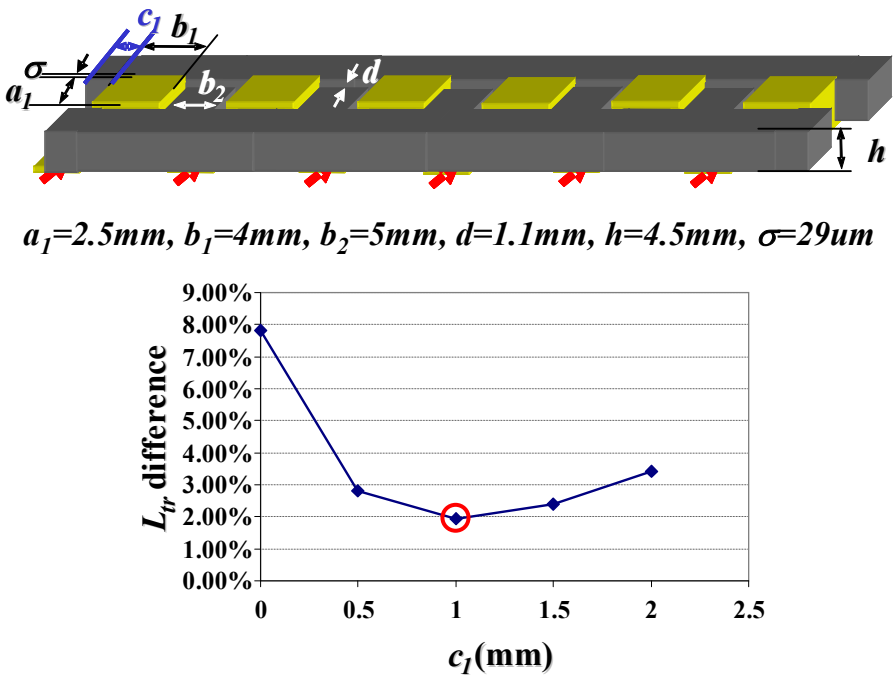

Figure 5.22 The asymmetry of the six-phase coupled-inductor with wings

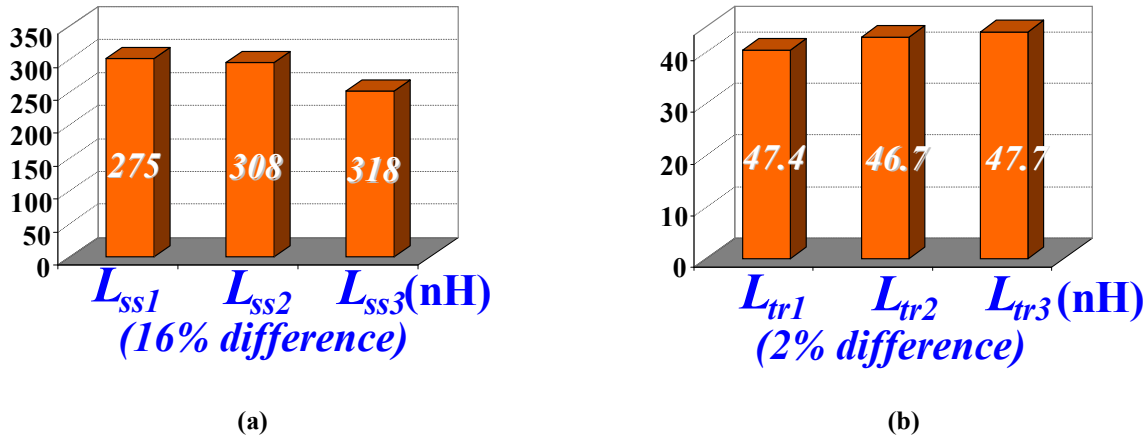

(a) **(b)**

Figure 5.23 Asymmetry of the 6-phase ET core coupled-inductor @ c_1=1mm

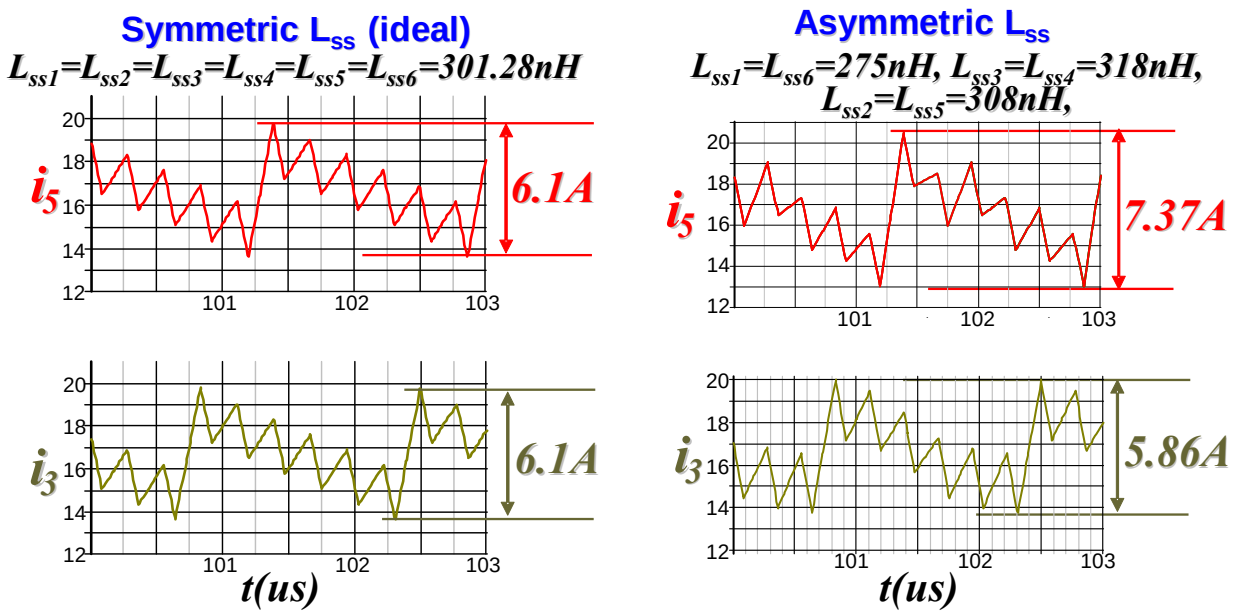

(a) (b)

Figure 5.24 The phase current ripple unbalance (a) the phase current of the six-phase symmetric coupled-inductor (b) the phase current difference of the six-phase asymmetric ET core coupled-inductor @c_1=1mm

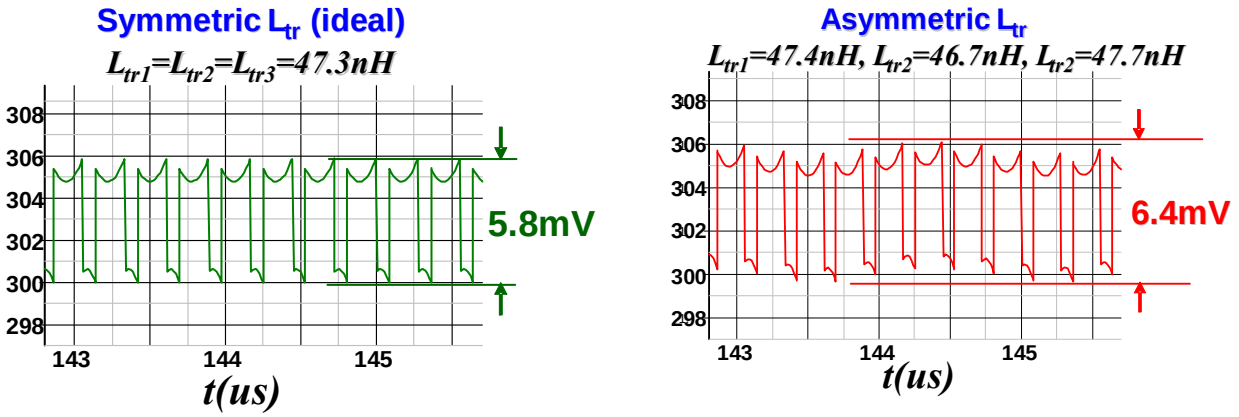

(a) (b)

Figure 5.25 The output voltage ripple increase (a) the V_o ripple in the six-phase symmetric coupled-inductor (b) the V_o ripple in the six-phase asymmetric ET core coupled-inductor @c_1=1mm

According to Figure 5.25, the $V_{oripple}$ of the one six-phase asymmetric ET-core coupled-inductor buck converter is 10% higher than that of the symmetric six-phase buck converter when the average transient inductance for both cases are the same. Figure 5.26 shows the estimated

$V_{oripple}$ for the six-phase ET-core coupled-inductor buck converter assuming the $V_{oripple}$ of the one six-phase ET-core coupled-inductor buck converter is 10% higher than the symmetric buck converter with the same average transient inductance. In Figure 5.26, the solid line is the tested $V_{oripple}$ of the symmetric six-phase buck converter; the dotted line is the estimated $V_{oripple}$ of the six-phase ET-core coupled-inductor buck converter based on that. It is found that the minimum average transient inductance of the six-phase ET-core coupled-inductor is 48nH.

According to Figure 5.26, thirty-one 10μF ceramic capacitors are needed to achieve the required AVP transient function. Figure 5.27 shows the estimated output bulk capacitor comparison of the two three-phase coupled buck converter and the one six-phase coupled-inductor buck converter. Six additional 10μF ceramic capacitors are needed. With a transient inductance of 48nH, the average steady-state inductance of the one six-phase coupled-inductor buck converter can be estimated to be six times that; 288nH. Figure 5.28 shows the efficiency comparison of the non-coupled-inductor buck converter, the two three-phase coupled-inductor buck converter and the one six-phase coupled-inductor buck converter. For the one six-phase coupled-inductor buck converter, the efficiency is estimated based on the precise analytical loss model of the multiphase buck converter. It can be that the one six-phase coupled-inductor buck converter only increases the efficiency by 0.4% over the two three-phase coupled-inductor buck converter. Moreover, the different-phase steady-state inductances in the one six-phase coupled-inductor buck converter will cause the issue in some control methods. For example, in the peak current mode control, this difference will cause a phase average current unbalance and unbalanced heat distribution among different phases. For these reasons, the two three-phase coupled-inductor buck converter is more practical than the one six-phase coupled-inductor buck converter.

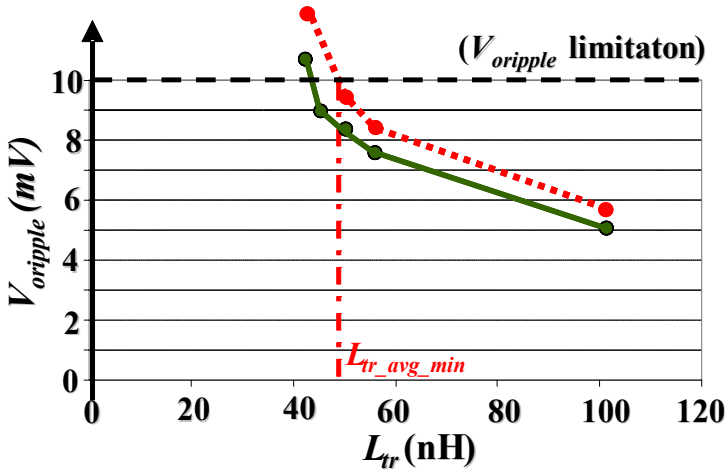

Figure 5.26 The output voltage ripple $V_{oripple}$ vs. the transient inductance L_{tr} for the six-phase ET-core coupled-inductor buck converter

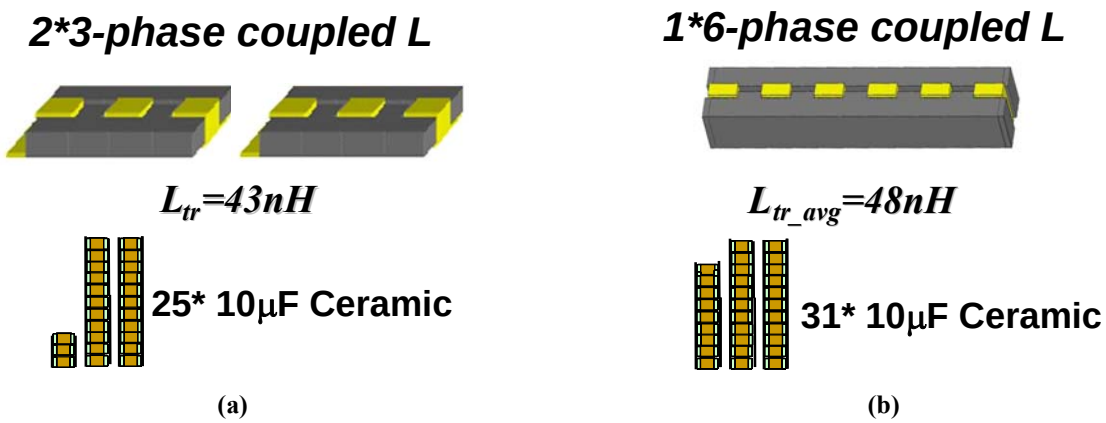

Figure 5.27 The output bulk capacitor comparison between the two three-phase coupled-inductor buck converter and the six-phase coupled-indutor buck converter (a) The two three-phase coupled-inductor buck converter case (b) The six-phase coupled-inductor buck converter case

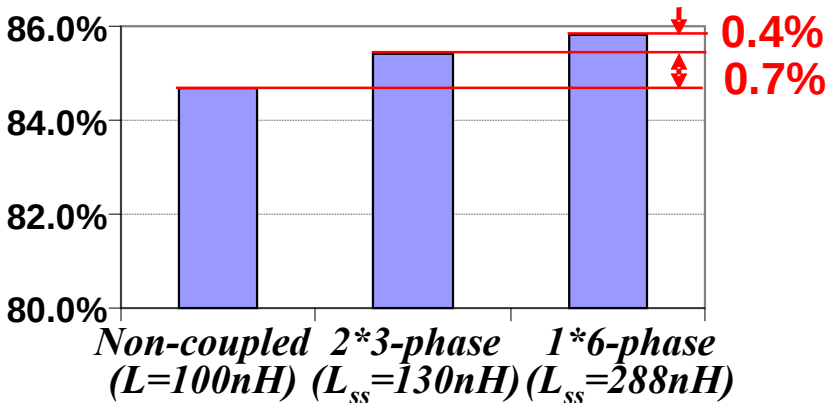

Figure 5.28 The efficiency comparison of the original non-coupled buck converter (L=100nH), the two three-phase coupled buck converter (L_{ss}=130nH) and the one six-phase coupled buck converter (L_{ss}=288nH)

In conclusion, to increase the multiphase buck converter efficiency, the three two-phase coupled-inductor buck converter is the most practical design. To reduce the number of output capacitors, the two three-phase coupled-inductor buck converter is the best design.

In the chapter 4, the size of the LTCC coupled-inductors is greatly reduced compared to that of the LTCC non-coupled-inductors. The material of the LTCC inductor is the NiZn ferrite tape. The core loss of this material is relative low and is not the limitation for the LTCC inductor size.

In this chapter, the sizes of the coupled-inductors (three two-phase coupled-inductors, two three-phase coupled-inductors and one six-phase coupled-inductor) are not dramatically reduced compared to the size of the original six non-coupled inductors. The core material of this chapter's coupled-inductors is MnZn ferrite. The size of these coupled-inductors is limited by the core loss density. Therefore, the cross-section is fixed. Accordingly, the size of the coupled-inductors will not dramatically decrease compared to the non-coupled-inductors. If the core saturation is the limitation for the coupled-inductors, the size of the coupled-inductors will decrease significantly compared to that of the non-coupled-inductors.

5.4. Summary

In this chapter, it is found that there is a diminishing return when the phase number of the multiphase coupled-inductor buck converter is increased to improve the efficiency, and that there is also a diminishing return when the phase number of the multiphase coupled-inductor buck converter is increased to reduce the outpur capacitance. For the ISL6327 six-phase coupled-inductor buck converter, the two three-phase coupled-inductor buck converter (L_{tr}=43nH, L_{ss}=130nH) is the most favorable design setup.

Chapter 6. Current Sensing of Multiphase Coupled-inductor Buck Converters

Current sensing is necessary for phase-current sharing and current protection in every multiphase buck converter. In the multiphase interleaving buck converters for CPU VR applications and some graphic card applications, current sensing is also needed for the AVP function.

In today's industrial multiphase interleaving buck converters, the DCR current sensing method [74-82] is adopted for achieving the above three functions. The DCR current sensing method originally came from the Maxwell-Wien bridge circuit. Recently, it has become widely used in the multiphase buck converter because of its many merits. It utilizes the parasitic resistance of the inductor, the DCR, to sense the inductor current, achieving a low-cost current-sensing solution. It is also relatively precise compared to some other current-sensing methods, such as the MOSFET R_{ds_on} current-sensing method. Moreover, it consumes hardly any additional power, and is an intrinsically lossless current-sensing method. Because of all these advantages, almost every multiphase interleaving buck converter for desktop and server CPUs uses the DCR current-sensing method.

Figure 6.1 shows the conventional DCR current-sensing method. The sensing network is an Resistor-capacitor (RC) network in parallel with the inductor. When the RC sensing network time constant matches the inductance-DCR time constant,

$$R_{cs}C_{cs} = L / DCR \tag{6.1}$$

the sensing signal v_{cs} is proportional to the sensed current signal i_L

$$v_{cs} = DCR \cdot i_L \tag{6.2}$$

where R_{cs} and C_{cs} are the resistance and capacitance of the current sensing network, respectively; L is the self-inductance of the inductor, and DCR is the parasitic equivalent series DC resistance of the inductor.

Although the conventional DCR current sensing method is very popular for today's multiphase non-coupled inductor buck converter, it doesn't work in the multiphase coupled-inductor buck converter.

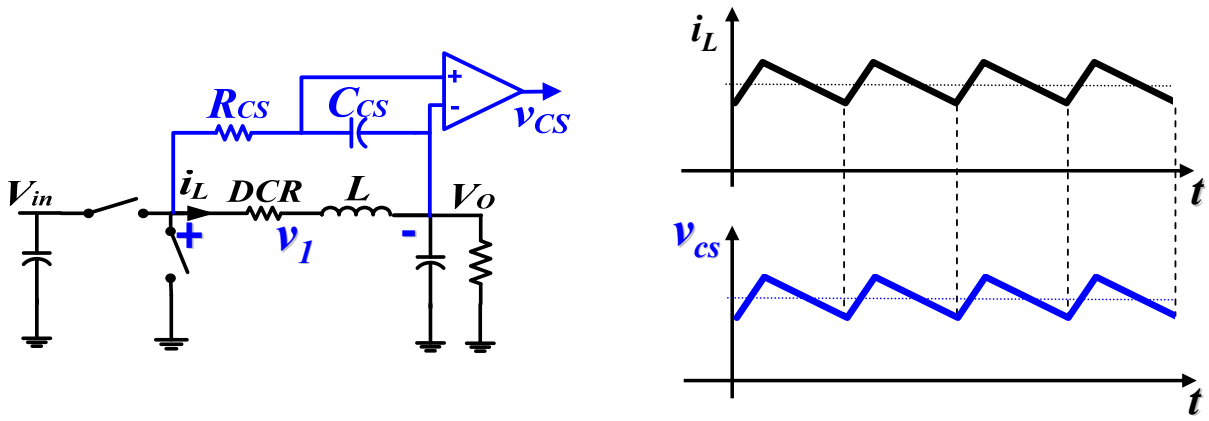

(a) (b)

Figure 6.1 The conventional DCR current sensing method in a simple buck converter (a) The buck converter with a conventional DCR current sensing network (b) The inductor current waveform and the current sensing signal waveform

6.1. Issues of the Conventional DCR Current Sensing Method

The literature does not mention using the DCR current-sensing method in the multiphase coupled-inductor buck converter, and whether it is still valid in the multiphase coupled-inductor buck converter needs investigating. Figure 6.2 shows a circuit diagram where the conventional DCR current-sensing method is directly used in a two-phase coupled-inductor buck converter. In the RC sensing network,

$$R_{cs}C_{cs} = L_{self} / DCR \tag{6.3}$$

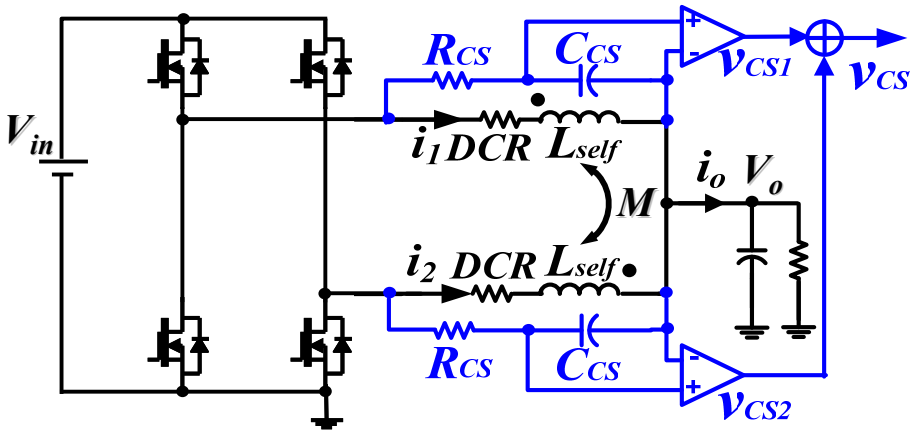

Figure 6.2 The conventional DCR current sensing method directly used in the multiphase coupled-inductor buck converter

The phase-current-sensing result of the conventional DCR current-sensing method in the multiphase coupled-inductor buck converter is shown in Figure 6.3. Here, $<i_1>_{avg}$ represents the average value of i_1 during one switching period, and $<v_{cs1}>_{avg}$ represents the average value of v_{cs1} during one switching period. It can be seen that even the waveform of i_1 and the waveform of v_{cs1} are different.

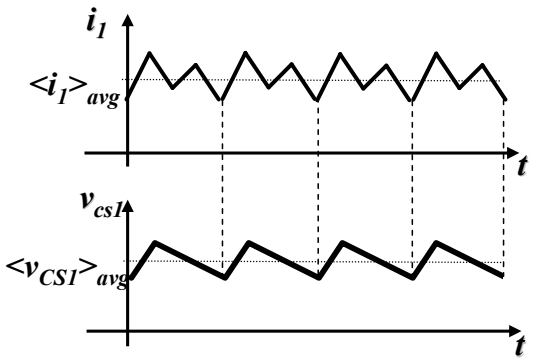

Figure 6.3 The phase current waveform and the current sensing signal waveform in the multiphase coupled-inductor buck converter with the conventional DCR current sensing method

The total current-sensing result of the conventional DCR current-sensing method in the multiphase coupled-inductor buck converters is shown in Figure 6.4. Here, $<i_o>_{avg}$ represents the average current of i_o during one switching period, and $<v_{cs}>_{avg}$ represents the average voltage of v_{cs} during one switching period. It can be seen that although the sensing signal v_{cs} has the same

shape as the total current waveform i_o, the amplitude of the v_{cs} is not right, and v_{cs} is not proportional to i_o.

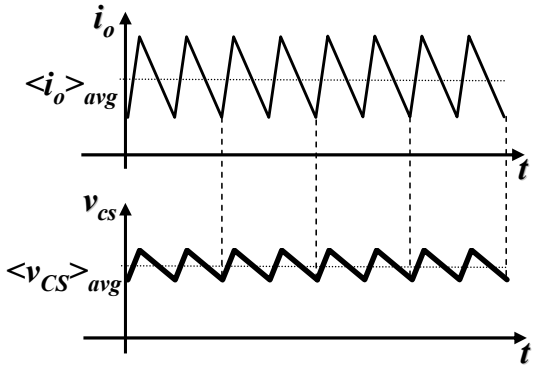

Figure 6.4 The total inductor current waveform and the total current sensing waveform of the multiphase coupled-inductor buck converter with the conventional DCR current sensing method

When the peak current mode control is used, the phase-current needs to be sensed precisely to achieve the phase-current protection, the AVP function. When the average current mode control is used, the total current needs to be sensed precisely to achieve the total current protection and the AVP function.

This chapter first proposes a precise total current sensing method for the multiphase coupled-inductor buck converter. Then, a precise phase-current sensing method for the multiphase coupled-inductor buck converter is proposed. Both of the two current-sensing methods are verified by the experimental results.

6.2. The DCR Total Current Sensing Method

6.2.1. The Two-phase Coupled-inductor Buck Converter

Figure 6.5 shows the proposed DCR total current sensing method in the two-phase coupled-inductor buck converter [83]. The two-phase coupled-inductor buck converter can also be viewed from another angle with the ideal transformer as the controlled voltage source (Figure 6.6). In Figure 6.6, through the sensing network, the two controlled voltage sources with opposite directions are sensed by v_{cs1} and v_{cs2} respectively. When v_{cs1} and v_{cs2} are added together to obtain the v_{cs} signal, the effects of the two controlled voltage sources cancel each other out. Therefore, the only effective inductance in the coupled-inductor is the leakage inductance. With

this knowledge, we can guess that an RC sensing network with time-constant matching with the L_k/DCR should give the desired v_{cs}.

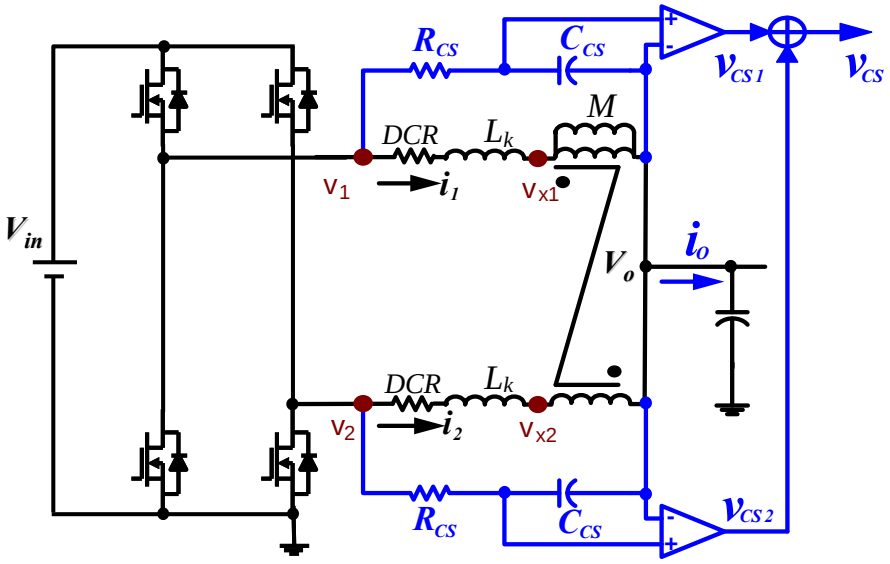

Figure 6.5 The proposed DCR total current sensing method in a two-phase coupled-inductor buck converter

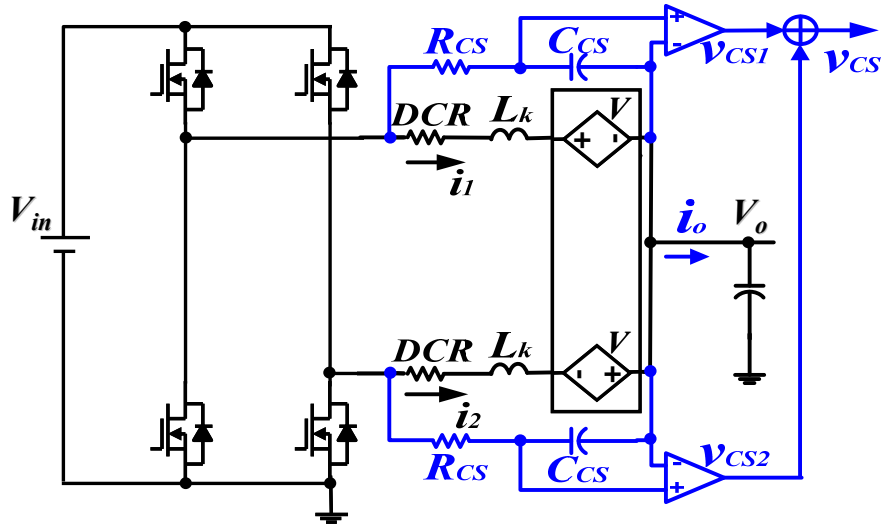

Figure 6.6 Another circuit representation of the two-phase coupled-inductor buck converter with the proposed current sensing network

This guess can be verified by the detail derivation. The v_{cs} is the summation of the sensing signals v_{cs1} and v_{cs2}:

$$v_{cs} = v_{cs1} + v_{cs2} \tag{6.4}$$

After a simple derivation, v_{cs1} and v_{cs2} can be expressed as (Figure 6.5)

$$v_{cs1} = (v_1 - V_o)\frac{1}{1 + R_{CS}C_{CS}s} \tag{6.5}$$

$$v_{cs2} = (v_2 - V_o)\frac{1}{1 + R_{CS}C_{CS}s} \tag{6.6}$$

Substituting the equations (6.5) and (6.6) into the equation (6.4), we get

$$v_{cs} = \frac{v_1 + v_2 - 2V_o}{1 + R_{CS}C_{CS}s} \tag{6.7}$$

The phase inductor currents can be expressed as

$$i_1 = \frac{v_1 - v_{x1}}{DCR + L_k s} \tag{6.8}$$

$$i_2 = \frac{v_2 - v_{x2}}{DCR + L_k s} \tag{6.9}$$

Adding the equations (6.8) and (6.9) together, the total current i_o is

$$i_o = i_1 + i_2 = \frac{v_1 + v_2 - (v_{x1} + v_{x2})}{DCR + L_k s} \tag{6.10}$$

Since the transformer M is an ideal 1:1 transformer,

$$v_{x1} - V_o = V_o - v_{x2} \tag{6.11}$$

Substituting the equation (6.11) into the equation (6.10),

$$i_o = \frac{v_1 + v_2 - 2V_o}{DCR(1 + L_k s / DCR)} \tag{6.12}$$

Comparing the equations (6.7) and (6.12), it can be found that

$$v_{cs} = DCR \cdot i_o \tag{6.13}$$

if and only if

$$R_{CS}C_{CS} = L_k / DCR \tag{6.14}$$

This result means that when $R_{CS}C_{CS} = L_k / DCR$, the sensing signal v_{cs} is proportional to the total output current i_o, and the coefficient between them is DCR.

Figure 6.7 and Figure 6.8 show the steady-state and dynamic simulation results for v_{cs} and i_o with the two-phase coupled-inductor buck converter. In the simulation, f_s=300kHz, L_k=300nH, |M|=1.2μH, DCR=1mΩ, R_{cs}=10kΩ, and C_{cs}=30nF. From Figure 6.7 and Figure 6.8, it can be seen that the v_{cs} signal can exactly represent the total output current i_o in both the steady-state and dynamic conditions, and the coefficient between them is DCR.

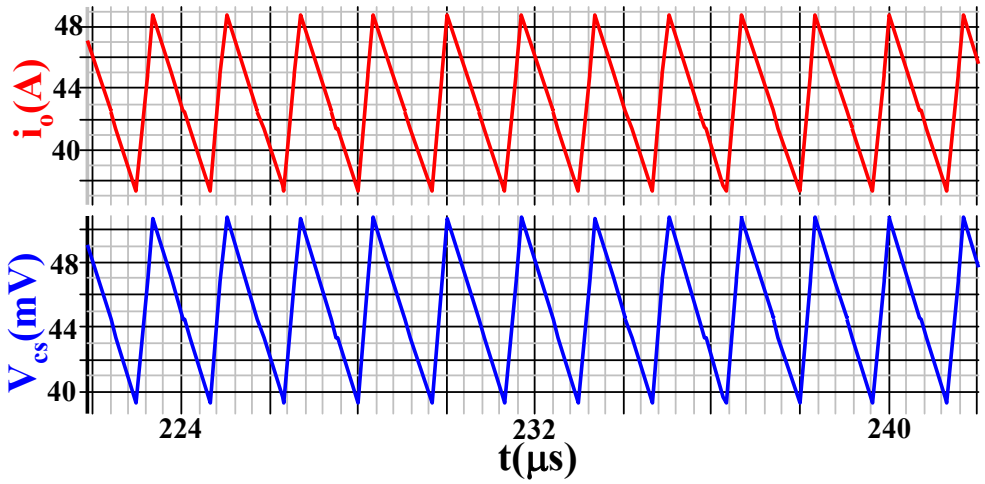

Figure 6.7 The steady-state total current i_o and the total current sensing signal v_{cs} simulation results in a two-phase coupled-inductor buck converter (f_s=300kHz, L_k=300nH, |M|=1.2μH, DCR=1mΩ, R_{cs}=10kΩ, and C_{cs}=30nF)

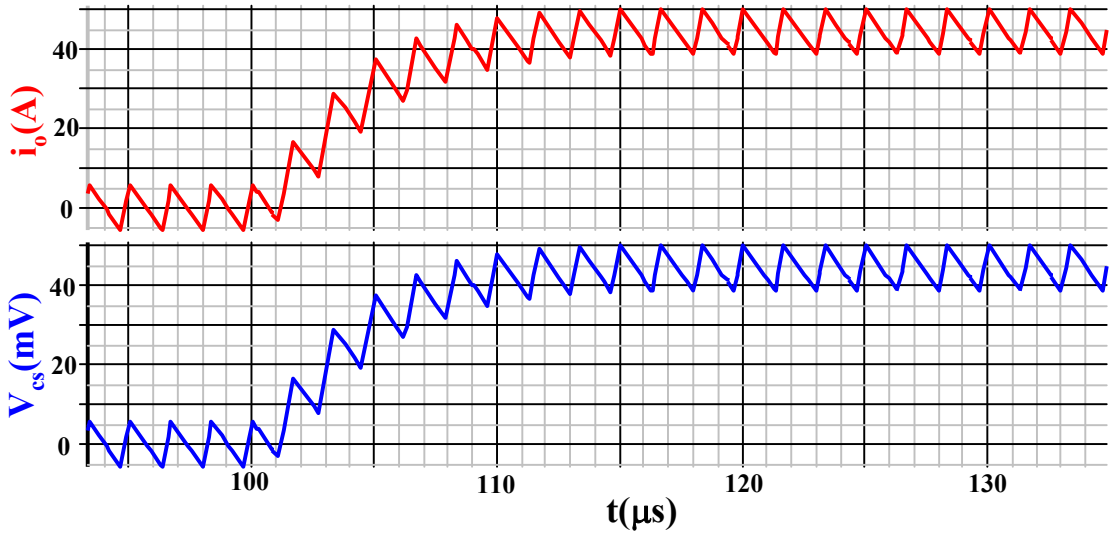

Figure 6.8 The transient total current i_o and the total current sensing signal v_{cs} simulation results in a two-phase coupled-inductor buck converter (f_s=300kHz, L_k=300nH, |M|=1.2μH, DCR=1mΩ, R_{cs}=10kΩ, and C_{cs}=30nF)

The proposed DCR current sensing method for buck converters with two-phase coupled-inductors can also be extended to buck converters with n-phase coupled-inductors.

6.2.2. The N-phase Coupled-inductor Buck Converter

Figure 6.9 shows the proposed DCR total current sensing method with an n-phase coupled-inductor buck converter. In the n-phase coupled-inductor buck converter, there is a mutual inductance M_{ij} between the phase i and phase j ($1 \le i < j \le n$). Similar to the two-phase coupled-inductor buck converter,

$$v_{cs} = \sum_{i=1}^{n} v_{csi} = \sum_{i=1}^{n} \frac{v_i - V_o}{1 + R_{CS} C_{CS} s} \tag{6.15}$$

$$i_o = \sum_{j=1}^{n} i_j = \sum_{j=1}^{n} \frac{v_j - v_{xj1}}{DCR + L_k s} \tag{6.16}$$

Because of the 1:1 ideal transformer M_{ij} ($1 \le i < j \le n$),

$$\begin{aligned} &\sum_{j=1}^{n} v_{xj1} = v_{x11} + v_{x21} + \sum_{j=3}^{n} v_{xj1} = v_{x12} + v_{x22} + \sum_{j=3}^{n} v_{xj1} = \ldots \\ &= (n-2)V_o + v_{x(n-1)(n-1)} + v_{xn(n-1)} = nV_o \end{aligned} \tag{6.17}$$

Substituting the equation (6.17) to the equation (6.16), we get

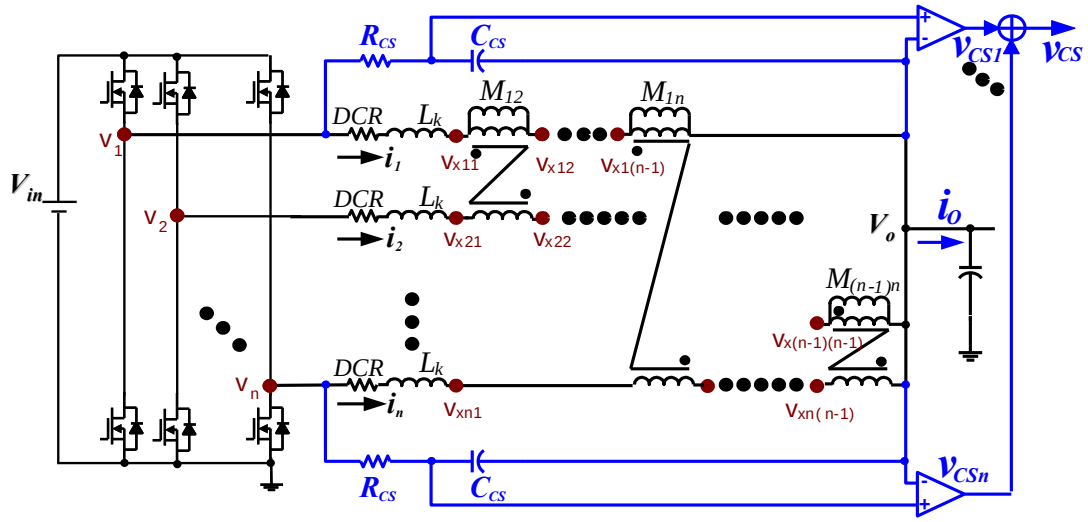

Figure 6.9 The proposed DCR total current sensing method in the n-phase coupled-inductor buck converter

$$i_o = \frac{\sum_{j=1}^{n} v_j - nV_o}{DCR(1 + L_k s / DCR)} \tag{6.18}$$

Comparing the equations (6.15) and (6.18), it can be found that

$$v_{cs} = DCR \cdot i_o \tag{6.19}$$

if and only if

$$R_{CS}C_{CS} = L_k / DCR \tag{6.20}$$

This result means that when $R_{CS}C_{CS} = L_k / DCR$, the sensing signal v_{cs} is proportional to the total output current i_o, and the coefficient between them is DCR. Since the relationship among the mutual inductance M_{ij} ($1 \le i < j \le n$) isn't defined in the derivation, the above conclusion is valid for both the case when the values $M_{ij}(1 \le i < j \le n)$ are the same and the case when the values $M_{ij}(1 \le i < j \le n)$ are not the same.

Figure 6.10 shows the steady-state and dynamic simulation results for v_{cs} and i_o in the 4-phase coupled-inductor buck case. In the simulation, there are four phases, f_s=300kHz,

L_k=300nH, $|M_{12}|$=1.2μH, $|M_{13}|$=0.5μH, $|M_{14}|$=40.1μH, $|M_{23}|$=2μH, $|M_{24}|$=0.5μH, $|M_{34}|$=1.2μH, DCR=1mΩ, R_{cs}=10kΩ, and C_{cs}=30nF.

From Figure 6.10, it can be seen that the v_{cs} signal can exactly represent the total output current i_o in both steady-state and dynamic conditions, and the coefficient is DCR.

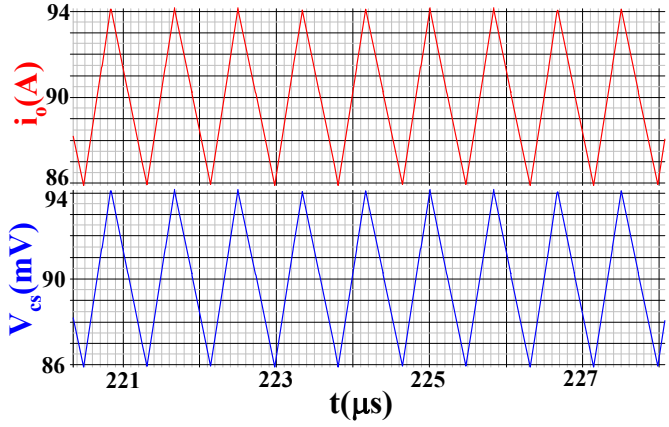

(a)

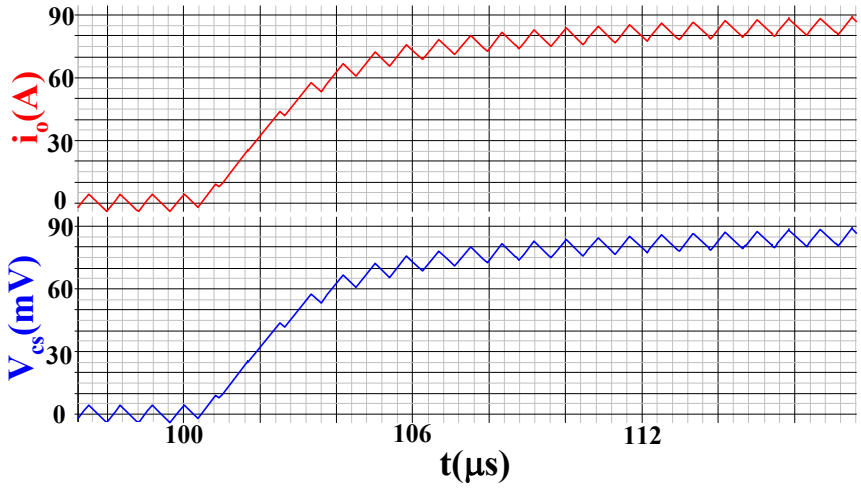

(b)

Figure 6.10 The total current i_o and the total current sensing signal v_{cs} simulation results in a four-phase coupled-inductor buck converter (f_s=300kHz, L_k=300nH, $|M_{12}|$=1.2μH, $|M_{13}|$=0.5μH, $|M_{14}|$=40.1μH, $|M_{23}|$=2μH, $|M_{24}|$=0.5μH, $|M_{34}|$=1.2μH, DCR=1mΩ, R_{cs}=10kΩ, and C_{cs}=30nF) (a) the steady-state simulation results (b) the transient simulation results

6.2.3. Experimental Verification

The proposed DCR current sensing method is also verified by experiments. Figure 6.11 shows the experimental v_{cs} and i_o waveforms in a two-phase coupled-inductor buck converter using the proposed DCR total current sensing method. The experimental results are based on a

2MHz coupled-inductor buck converter when DCR=11.3mΩ, L_k=102nH, R_{cs}=9.03kΩ, and C_{cs}=100pF. Figure 6.12 shows the experimental v_{cs}, v_{cs1} , v_{cs2} and i_o waveforms in the two-phase buck converter with the center-tap coupled-inductors (Figure 1.36) using the proposed DCR total current sensing method. The experimental results are based on a 2MHz coupled-inductor buck converter with R=3.5mΩ, R_o=10.5mΩ, ($2R_o$+R=24.5mΩ), L=26.3nH, R_{cs}=23kΩ, and C_{cs}=100pF. From Figure 6.11 and Figure 6.12, it can be seen that the analysis of the proposed DCR total current sensing method is valid.

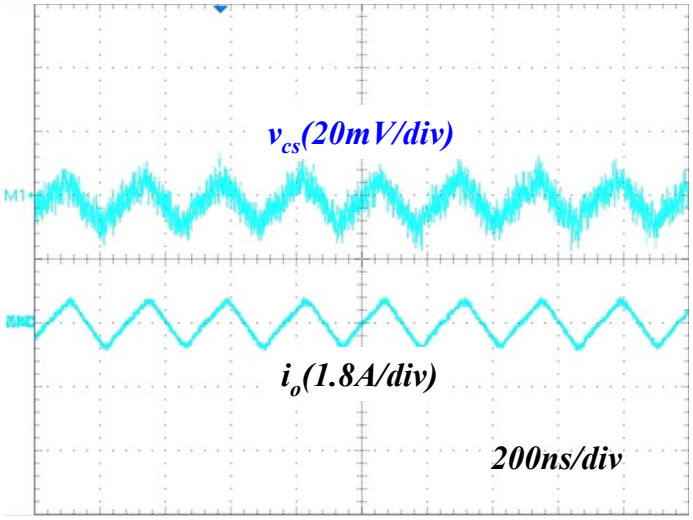

Figure 6.11 The total current sensing signal v_{cs} and the total inductor current i_o waveforms in the integrated two-phase coupled-inductor buck converter using the proposed DCR total current sensing method (DCR=11.3mΩ, L_k=102nH, R_{cs}=9.03kΩ, and C_{cs}=100pF)

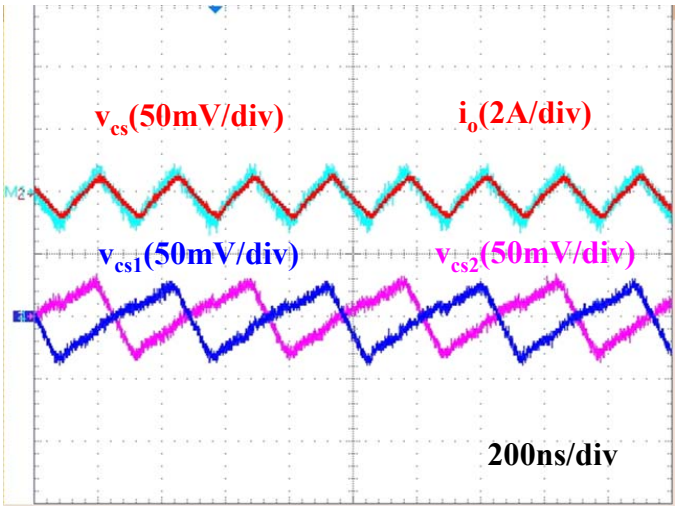

Figure 6.12 The total current sensing signal v_{cs}, the phase 1 current sensing signal v_{cs1}, the phase 2 current sensing signal v_{cs2} and the total inductor current i_o waveforms in the center-tap coupled-inductor buck converter using the proposed DCR total current sensing method (R=3.5mΩ, R_o=10.5mΩ, L=26.3nH, R_{cs}=23kΩ, and C_{cs}=100pF)

In this section, a DCR total current sensing method is proposed in multiphase coupled-inductor buck converters. The experimental results verify the validity of the proposed DCR total current sensing method.

6.3. The DCR Phase Current Sensing Method

6.3.1. The Two-phase Coupled-inductor Buck Converter

Although the above DCR current sensing method can sense the total current precisely, it can't sense the phase-current precisely (Figure 6.13). To achieve phase-current protection in the peak current model control buck converter, a precise phase-current sensing method needs to be developed.

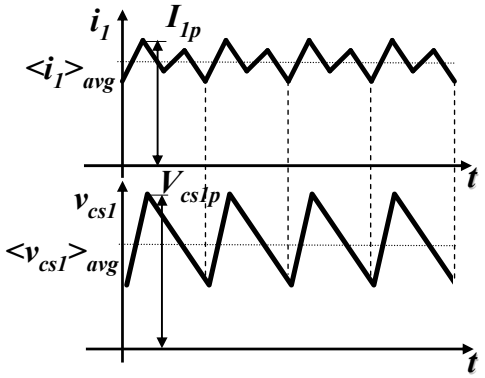

Figure 6.13 The drawback of the previous DCR total current sensing method in the coupled-inductor buck converter (i_1: the phase 1 current; v_{cs1}: the phase 1 current sensing signal)

To develop a DCR current sensing method to sense the phase-current precisely, the phase-current of the coupled-inductor buck converter needs to be investigated in detail. The basic coupled-inductor equation is

$$v_1 = (DCR + L_{self} \cdot s)i_1 + M \cdot s \cdot i_2 \tag{6.21}$$

$$v_2 = M \cdot s \cdot i_1 + (DCR + L_{self} \cdot s)i_2 \tag{6.22}$$

From the equations (6.21) and (6.22), it can be derived that

$$i_1 = i_{1p1} + i_{1p2} \tag{6.23}$$

where

$$i_{1p1} = \frac{DCR + L_{self}\, s}{DCR^2 + 2DCR \cdot L_{self}\, s + (L_{self}^2 - M^2)s^2} v_1 \tag{6.24}$$

$$i_{1p2} = \frac{-M \cdot s}{DCR^2 + 2DCR \cdot L_{self}\, s + (L_{self}^2 - M^2)s^2} v_2 \tag{6.25}$$

i_{1p1} is the current component of the Phase 1 current i_1 which is excited by the voltage across the first phase inductor voltage v_1; i_{1p2} is the current component of the Phase 1 current i_1 which is excited by the voltage across the second phase inductor voltage v_2.

To simplify the implementation, i_{1p1} and i_{1p2} are further decomposed into two terms.

$$i_{1p1} = i_{11} + i_{12} \tag{6.26}$$

$$i_{1p2} = i_{13} - i_{14} \tag{6.27}$$

$$i_{11} = \frac{0.5 v_1}{DCR + (L_{self} + M) \cdot s} \tag{6.28}$$

$$i_{12} = \frac{0.5 v_1}{DCR + (L_{self} - M) \cdot s} \tag{6.29}$$

$$i_{13} = \frac{0.5 v_2}{DCR + (L_{self} + M) \cdot s} \tag{6.30}$$

$$i_{14} = \frac{0.5 v_2}{DCR + (L_{self} - M) \cdot s} \tag{6.31}$$

These four components in current i_1 will be sensed respectively and then the sensed signal for i_1 will be built.

To sense the i_{11}, an RC sensing network is added (Figure 6.14). After derivation, when the sensing network parameters satisfy

$$R_{CS} C_{cs} = (L_{self} + M) / DCR \tag{6.32}$$

then

$$v_{cs11} = DCR \cdot i_{11} \tag{6.33}$$

Similarly, the phase-current components i_{12}, i_{13} and i_{14} can be sensed with an RC sensing network. Then the phase-current i_1 sensing network can be built (Figure 6.15). In Figure 6.15,

$$R_{csp}C_{cs} = (L_{self} - M)/DCR \tag{6.34}$$

The relationship between v_{cs1} and i_1 is

$$v_{cs1} = DCR \cdot i_1 \tag{6.35}$$

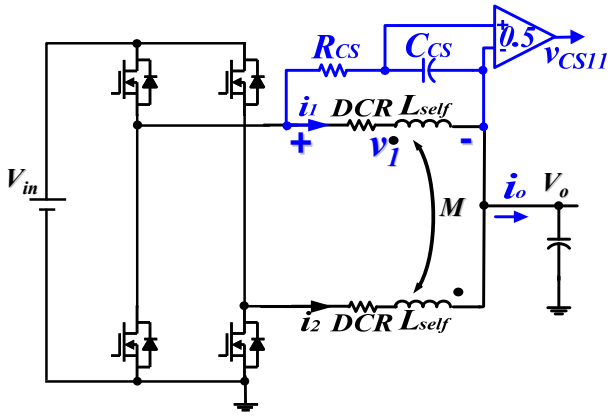

Figure 6.14 The RC current sensing network to sense the current component i_{11} in the two-phase coupled-inductor buck converter

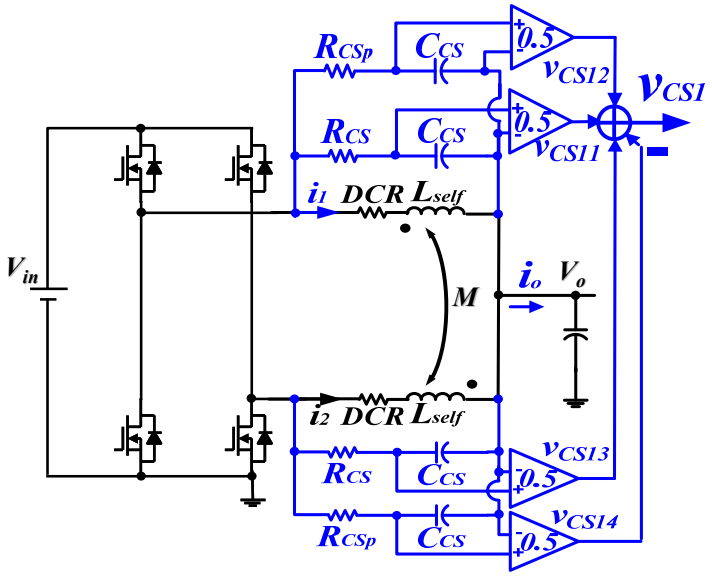

Figure 6.15 The DCR phase-current sensing network to sense the phase-current i_1 in the two-phase coupled-inductor buck converter

From the equations (6.21) and (6.22), the phase-current i_2 can be expressed as

$$i_2 = i_{2p1} + i_{2p2} \tag{6.36}$$

$$i_{2p1} = i_{11} - i_{12} \tag{6.37}$$

$$i_{2p2} = i_{13} + i_{14} \tag{6.38}$$

The above four RC current sensing networks can still be used (Figure 6.16).

$$v_{cs2} = DCR \cdot i_2 \tag{6.39}$$

In Figure 6.16, the sensed signals v_{cs1} and v_{cs2} are added to build v_{cs}, which represents the total current signal i_o.

$$v_{cs} = DCR \cdot i_o \tag{6.40}$$

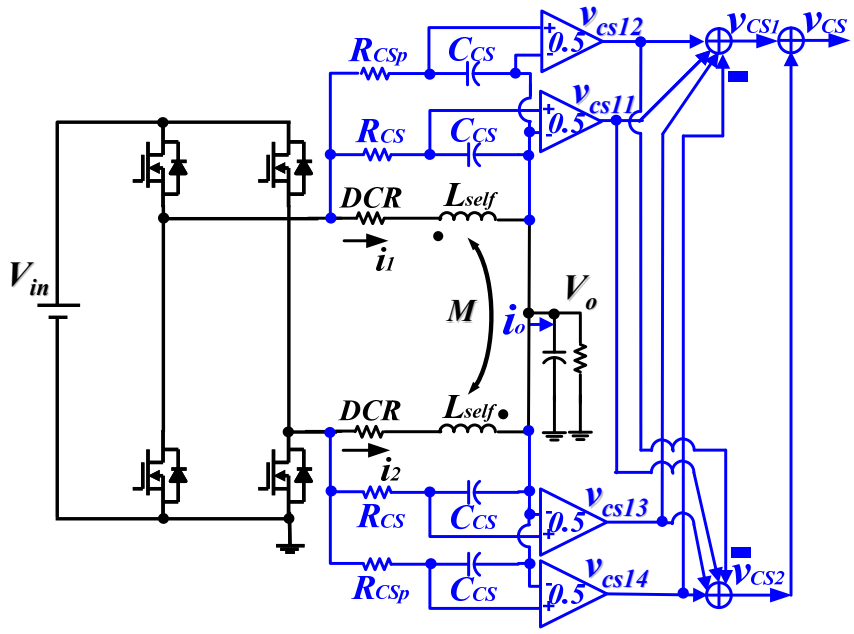

Figure 6.16 The complete DCR phase-current sensing network to sense both the phase-currents i_1 and i_2 in the two-phase coupled-indcutor buck converter

The RC sensing network in Figure 6.16 can be further simplified. Figure 6.17 shows the simplified DCR current sensing network. In Figure 6.17

$$R_{csa}C_{cs} = 2(L_{self} + M)/DCR \tag{6.41}$$

and

$$R_{csb}C_{cs} = (L_{self} - M)/DCR \tag{6.42}$$

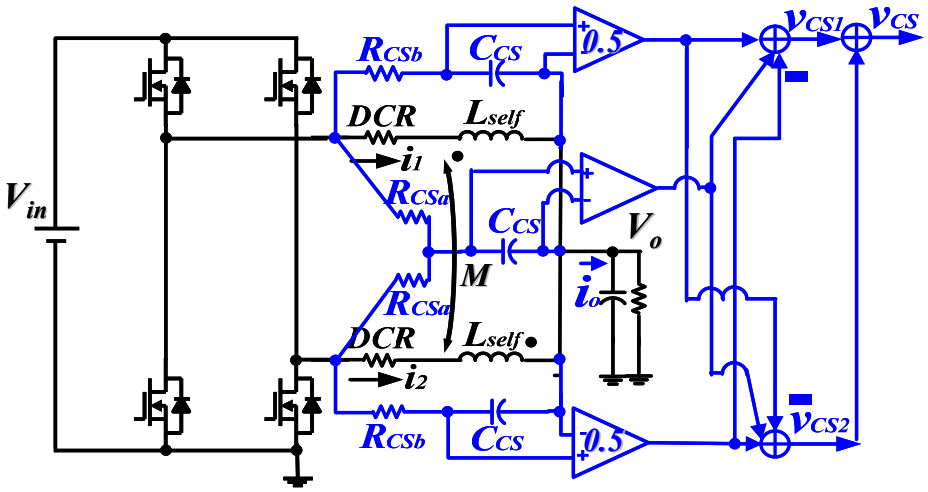

Figure 6.17 The simplified DCR phase-current sensing network for the two-phase coupled-inductor buck converter

6.3.2. The N-phase Coupled-inductor Buck Converter

The proposed DCR phase-current sensing method can also be extended to the n-phase coupled-inductor buck converter (Figure 6.18). In Figure 6.18, the RC parameters should satisfy

$$R_{csx}C_{cs} = n[L_{self} - (n-1)|M|]/DCR \tag{6.43}$$

$$R_{csy}C_{cs} = n(L_{self} + |M|)/DCR \tag{6.44}$$

and

$$R_{csb}C_{cs} = (L_{self} + |M|)/DCR \tag{6.45}$$

Then the relationships between the sensing signals and the phase-currents are

$$v_{cs1} = DCR \cdot i_1, v_{cs2} = DCR \cdot i_2, \ldots, v_{csn} = DCR \cdot i_n \tag{6.46}$$

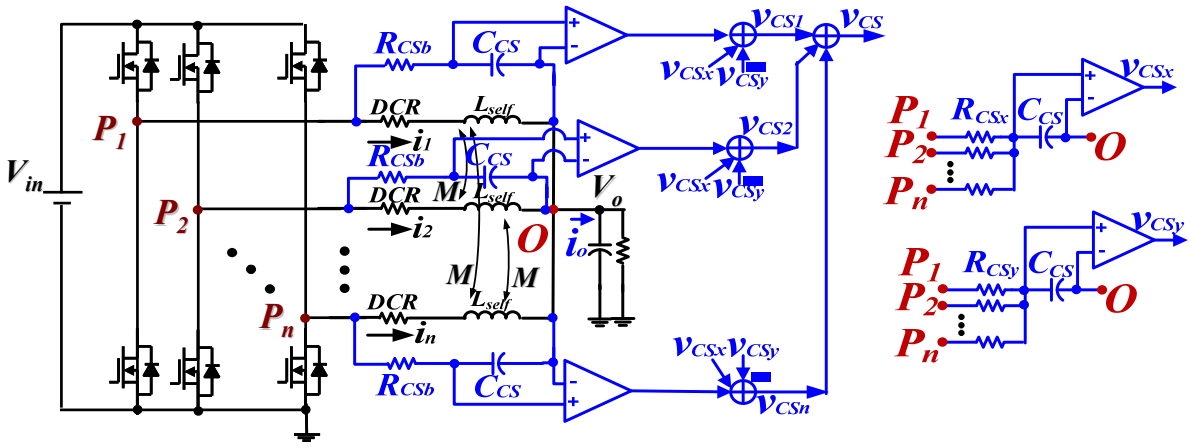

Figure 6.18 The DCR phase-current sensing network for all the phase currents i_1, i_2 … i_n in the n-phase coupled-inductor buck converter

6.3.3. Experimental Verification

Figure 6.19 shows the experimental results for the DCR phase-current sensing method in a two-phase coupled-inductor buck converter (Figure 6.17). In the experiment, the the setup is f_s=300kHz, L_k=302nH, M=-492nH, DCR=25mΩ, R_{csa}=1.2kΩ, R_{csb}=5.14kΩ, and C_{cs}=10nF.

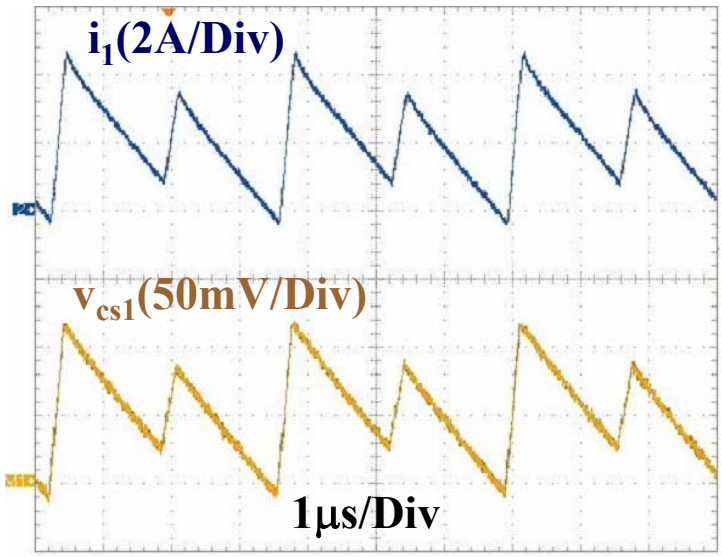

Figure 6.19 The phase-current i_1 waveform and the phase current sensing signal vcs1 waveform in a two-phase coupled-inductor buck converter with the proposed DCR phase-current sensing method (f_s=300kHz, L_k=302nH, M=-492nH, DCR=25mΩ, R_{csa}=1.2kΩ, R_{csb}=5.14kΩ, and C_{cs}=10nF)

6.4. Summary

In this section, the issues of using the conventional DCR current sensing method directly in the multiphase coupled-inductor buck converter are identified. Then, the DCR total current sensing method and the DCR phase-current sensing method are proposed to solve the problems with current sensing. The experimental results verify the proposed DCR current sensing methods. The proposed DCR current sensing methods are also generalized to n-phase coupled-inductor buck converters.

Chapter 7. The Light Load Efficiency Improvement of Multiphase Coupled-inductor Buck Converters (The DCM Operations)

All the previous research has focused on the continuous current mode (CCM) operation of the multiphase coupled-inductor buck converter. Nobody has published an investigation of the discontinuous current mode (DCM) operation of the multiphase coupled-inductor buck converter. However, DCM is widely used in multiphase interleaving buck converters, such as laptop CPU VRs.

In the laptop application, the CPU goes into the sleep mode frequently to save energy and extend the battery life. Accordingly, the dedicated CPU VR is under light-load conditions 80% of the time (Figure 7.1). To improve the efficiency of the multiphase buck converter and extend the battery life [84-87], most laptop CPU VRs enter DCM to reduce the switching frequency of the multiphase buck converter. The constant on-time control is a popular control method for achieving the desired DCM to reduce the switching frequency of the multiphase buck converter. Figure 7.2 shows the phase-current waveform of the constant on-time control multiphase buck converter in DCM. With constant on-time control, the switching frequency of the multiphase buck converter changes smoothly from CCM to DCM and vice versa.

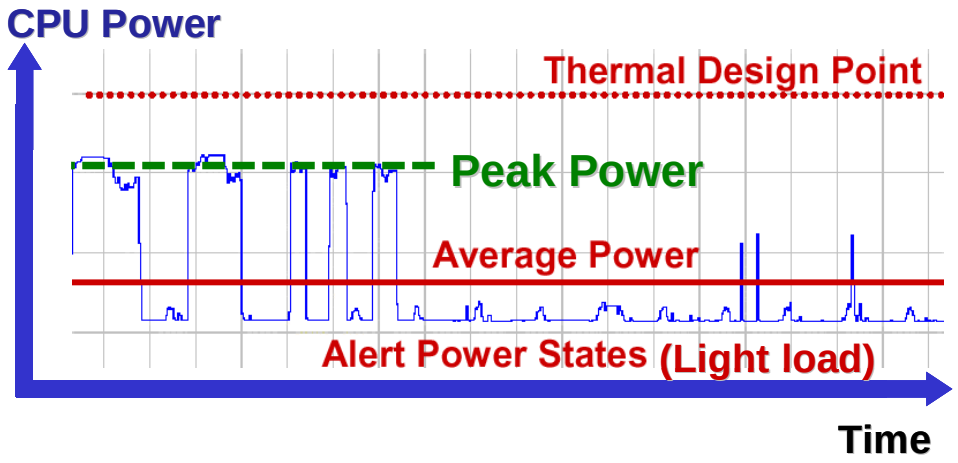

Figure 7.1 The graph of a typical CPU power vs. time for a laptop CPU with the peak power, the average power and the thermal design power marked

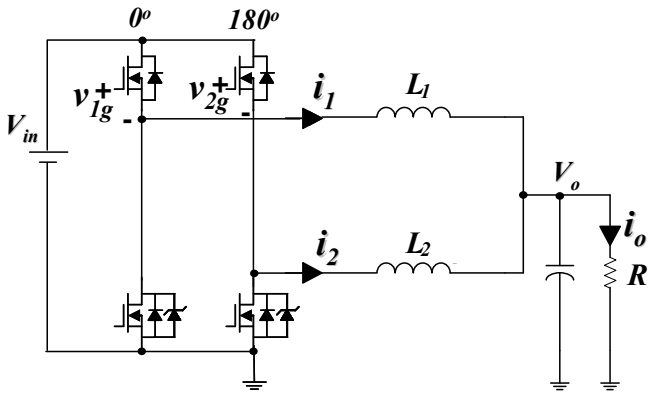

(a)

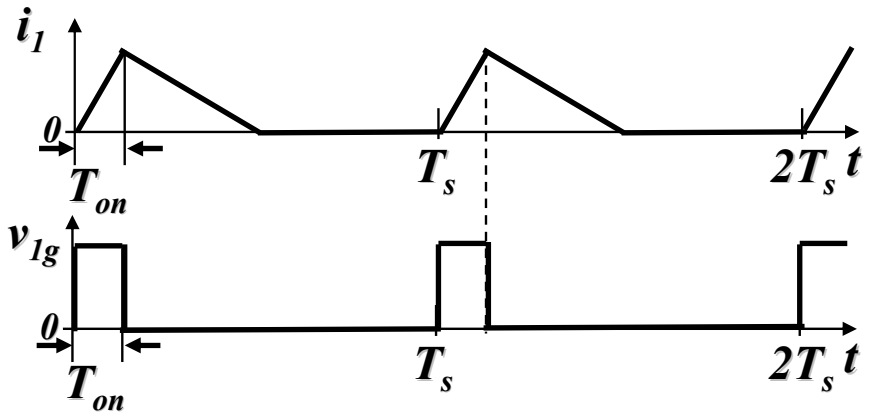

(b)

Figure 7.2 The phase-current waveforms of a multiphase buck converter with the constant on-time control in DCM (a) the multiphase buck converter (b) the phase 1 current waveform and the top-switch gate driving signal waveform of the phase 1

When the multiphase coupled-inductor buck converter goes into DCM under light-load condition to reduce the switching frequency and improve the converter efficiency, the circuit scenario is unknown. Therefore, the DCM of the multiphase coupled-inductor buck converter needs extensive research, especially since laptop computers are gaining more of the computer market share and will outsell desktop computers in the next several years.

In this chapter, for the first time, the low efficiency issue of the multiphase coupled-inductor buck converter in DCM operation is identified. Then, the DCM operation of the multiphase coupled-inductor buck converter is analyzed in detail. After that, the reason for the low efficiency is shown. Finally, the solution to the low light-load efficiency issue of the

multiphase coupled-inductor buck converter in DCM is proposed and verified by experimental results.

7.1. Low Efficiency Issue of Coupled-inductor Buck Converters Under Light-load

Although the multiphase coupled-inductor buck converter has a lot of benefits during CCM operation, it has low efficiency in DCM operation under light-load conditions. Based on an industrial laptop buck VR demo board using the constant-on time control method, we tested the light-load efficiencies of both non-coupled laptop buck VRs and coupled laptop buck VRs. In the testing, the steady-state inductances in the heavy load are kept the same to maintain the same heavy-load efficiency. Figure 7.3 shows the testing results under light-load conditions by applying the coupled-inductor directly into an industrial laptop buck VR demo board [88]. Figure 7.3 shows that simply replacing the non-coupled-inductor with a coupled inductor will cause the low light-load efficiency issue.

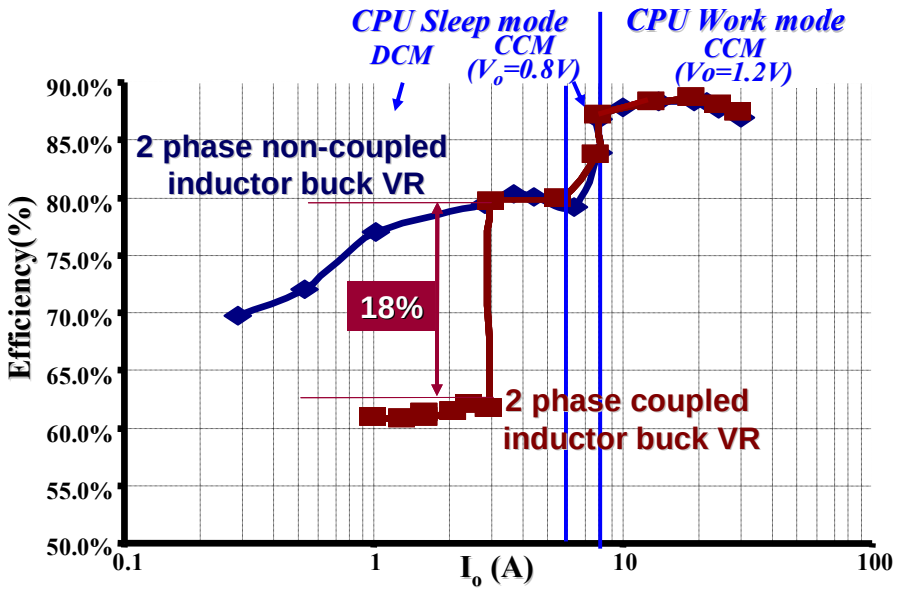

Figure 7.3 The light-load efficiency comparision of the two-phase non-coupled-inductor laptop buck converter and coupled-inductor laptop buck converter based on Max1545 demo board (V_{in}=12V, T_{on}=330ns)

To solve the low light-load efficiency issue, the DCM operation of the multiphase coupled-inductor buck converter is analyzed in detail in the next section [89].

7.2. DCM Operations of Multiphase Coupled-inductor Buck Converters Under Light-load

When the output load current of a couled inductor buck is heavy, the coupled-inductor buck converter works in the CCM mode. When the output load current of a coupled-inductor buck converter is lighter and lighter, the coupled-inductor buck converter will go into the DCM mode. In this section, the DCM operation of the two-phase coupled-inductor buck converter will be analyzed firstly. Then the DCM operation analysis will be extended to the n-phase coupled-inductor buck case. For simplicity, an assumption is made that all the phase inductor currents go through the SR when the top switch is off and there is no voltage drop across the SR when the SR is on.

Figure 7.4 shows the phase-current waveforms of a two-phase strong coupled-inductor buck converter in the CCM and DCM when the output load current reduces. For the simplicity of further analysis, the waveforms are shown with the constant-on time control method implemented in the coupled-inductor buck converter.

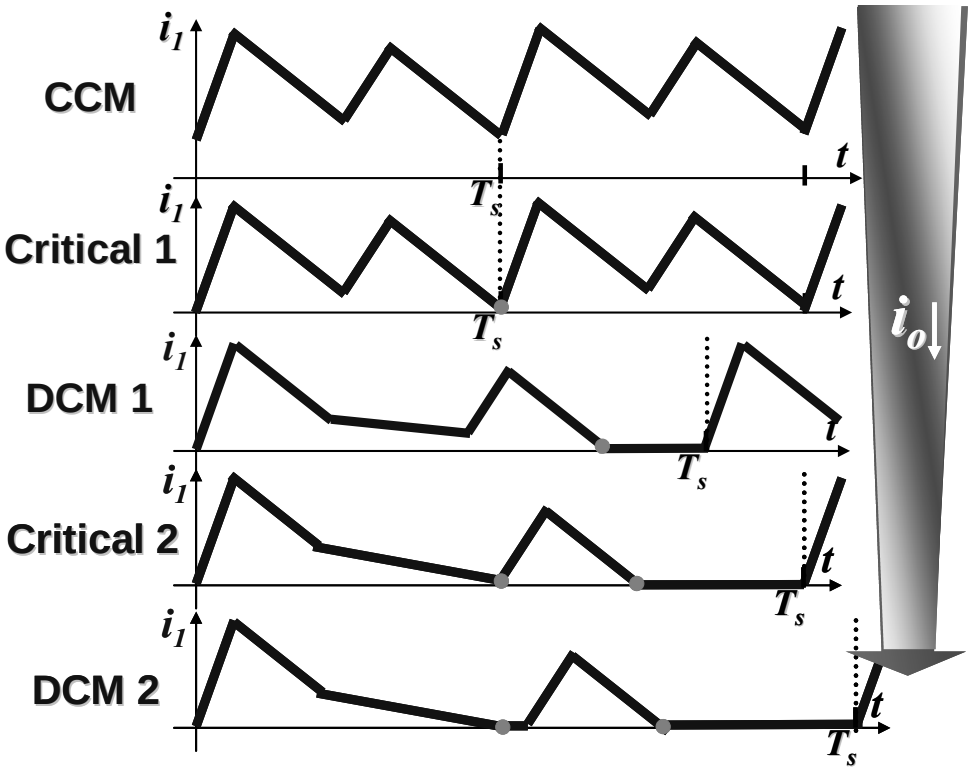

Figure 7.4 The phase-current waveforms of a two-phase coupled-inductor buck converter under different load conditions

It can be seen that, unlike the single DCM mode of a non-coupled-inductor buck converter, there are two different DCM modes (DCM1 mode and DCM2 mode) for a two-phase coupled-inductor buck converter. Although the phase inductor current shapes are different in the two DCM modes, both the phase inductor currents in the two DCM modes couple in one part of the switching period, and decouple in the other part of the switching period. In the following subsections, the two DCM modes are investigated in detail.

7.2.1.1. The DCM1 mode

When a coupled-inductor buck converter is in the DCM1 mode, the phase-current reaches zero only once during one switching period. The key waveforms of the coupled-inductor buck converter in the DCM1 mode are shown in Figure 7.5.

At time 0, the Phase 1 inductor current i_1 is zero, and the Phase 2 inductor current i_2 is an intermediate value i_m. During the time range from 0 to t_0, the Phase 1 top switch is turned on and the Phase 2 top switch is turned off. During this time range, i_1 increases from 0 to the maximum value. For the coupling effect, i_2 also increases. During the time range from t_0 to t_1, both the Phase 1 top switch and the Phase 2 top switch are turned off, and the two-phase currents i_1 and i_2 decrease until i_2 reaches zero at t_1. From 0 to t_1, the two phase inductor currents are coupled. During the time range t_1, $T_s/2$, the Phase 1 inductor works like a non-coupled inductor with its self-inductance L_1. The phase-current i_1 decreases until it reaches an inter-mediate value i_m at time $T_s/2$. The Phase 2 synchronous rectifier is turned off at time t_1 to avoid the Phase 2 current i_2 becoming a negative value. The Phase 2 current i_2 stays at zero during the time range t_1 to $T_s/2$. From t_1 to $T_s/2$, the two phase inductor currents are decoupled.

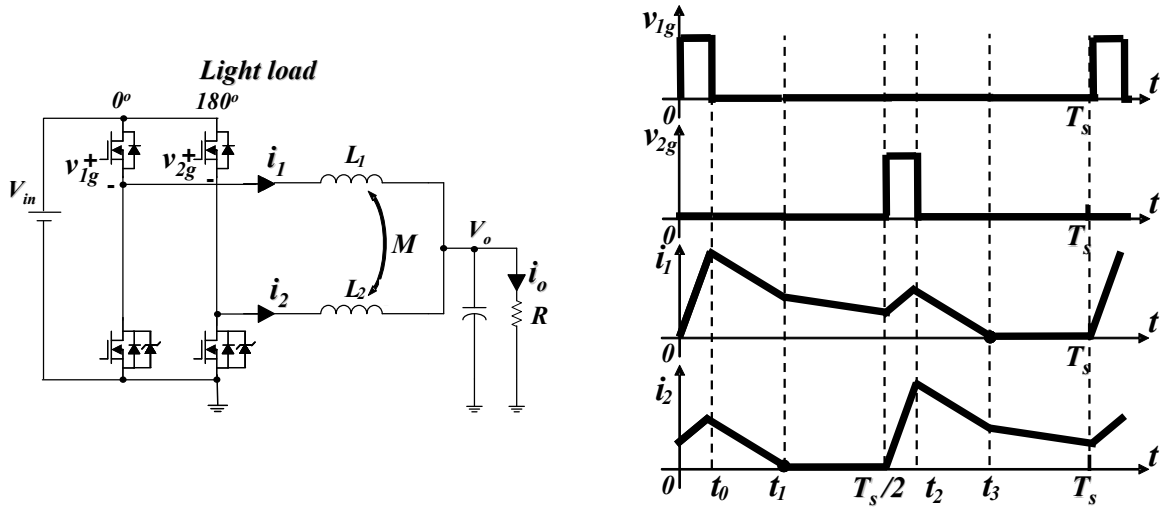

(a) **(b)**

Figure 7.5 The gate driving voltage waveforms and the phase current wavefors of the two-phase coupled-inductor buck converter in DCM1 (a) The two-phase coupled-inductor buck converter (b) The gate driving voltage and phase current waveforms

From $T_s/2$ to T_s, the coupled-inductor buck converter follows the first half-switching period working principle, except that Phase 1 and Phase 2 are exchanged. In summary, the two phase inductor currents i_1, i_2 couple and decouple alternatively during one switching period in the DCM1 mode of coupled-inductor buck converters.

To verify the above analysis, the simulation and the experiment are performed. Figure 7.6 shows the phase-current waveforms of the two-phase coupled-inductor buck converter in DCM1. The phase-currents couple and decouple alternatively. Figure 7.7 shows the experimental phase inductor current i_1 waveform in the DCM1 mode of a two-phase coupled-inductor laptop buck VR. The experimental setup is that V_{in}=12V, V_o=1.37V, M=-1.56μH, and L=L_1=L_2=1.72μH. From Figure 7.7, it can be seen that the phase-currents couple and decouple alternatively during one switching period, as was discussed previously. The oscillation in the i_1 waveform is due to the resonance between the equivalent capacitance between the SR drain and source and the total leakage inductance of the coupled-inductors.

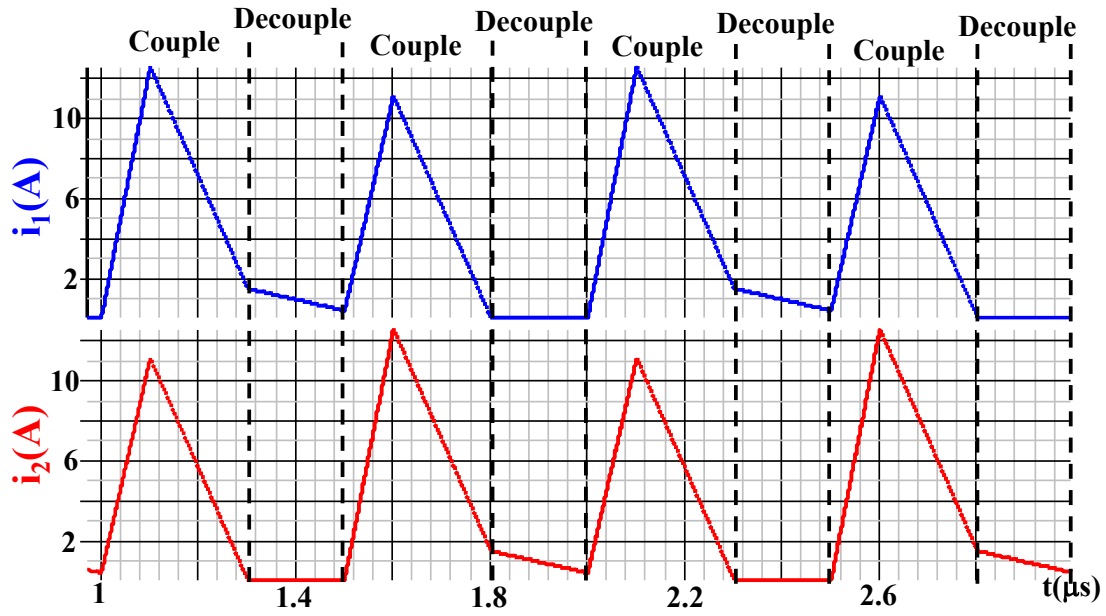

Figure 7.6 The simulated phase-current waveforms of the two-phase coupled-inductor buck converter in DCM1

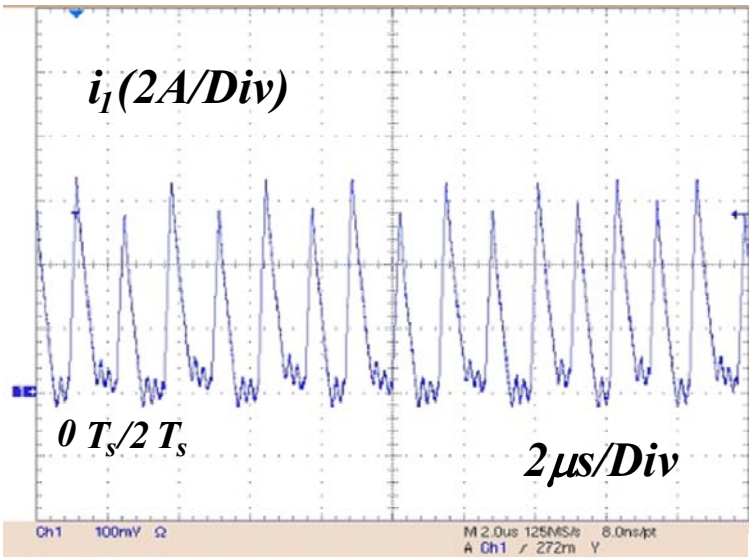

Figure 7.7 The phase-current i_1 waveform of the two-phase coupled-inductor buck converter in the DCM1 mode (V_{in}=12V, V_o=1.37V, M=-1.56μH, and L=L_1=L_2=1.72μH)

The V_o/V_{in} and f_s relationship of the coupled-inductor buck converter is necessary for the control of the two-phase coupled-inductor buck converter in DCM1. After derivation (Appendix 2), it is found that

$$r \triangleq \frac{V_o}{V_{in}} = \frac{2}{1+\sqrt{1+4\frac{L_{ss}}{D^2 R T_s}}} \tag{7.1}$$

and

$$f_s = \frac{1}{T_s} = \frac{r^2 L_{ss}}{(1-r){T_{on}}^2 R} \tag{7.2}$$

where L_{ss} is redefined to be

$$L_{ss} = \frac{L^2 - M^2}{L + \frac{r}{1-r} M} \tag{7.3}$$

Recalling that, for the non-coupled-inductor buck converter, the V_o/V_{in} and f_s relationship is

$$\frac{V_o}{V_{in}} = \frac{2}{1+\sqrt{1+4\frac{K}{D^2}}}, \qquad K = \frac{L_{nc}}{R T_{s\_nc}} \tag{7.4}$$

and

$$f_{s\_nc} = \frac{r^2 L_{nc}}{(1-r){T_{on}}^2 R} \tag{7.5}$$

Comparing the equations (7.1), (7.2), (7.4) and (7.5), it can be found that the V_o/V_{in} and f_s relationship of the two-phase coupled-inductor buck in DCM1 is the same as that of the non-coupled-inductor buck if L_{ss} replaces L_{nc} in the equation.

7.2.1.2. The DCM2 mode

In the DCM2 mode of coupled-inductor buck converters, the phase-current reaches a zero-current twice during one switching period. The key waveforms of coupled-inductor buck converters in DCM2 mode are shown in Figure 7.8.

At time 0, both the Phase 1 inductor current i_1 and the Phase 2 inductor current i_2 are zero. During the time range from 0 to t_0, the Phase 1 top switch is on, the Phase 2 top switch is off, and

i_1 increases from 0 to the peak current I_p. For the coupling effect, i_2 also increases from 0 to a smaller peak value, i_p'. During the time range t_0 to t_1, both the Phase 1 top switch and the Phase 2 top switch are off, and the two-phase currents i_1 and i_2 decrease until i_2 reaches 0 at time t_1. From 0 to t_1, the two phase inductor currents are coupled together. During the time range t_1 to t_2, both the Phase 1 top switch and the Phase 2 top switch are off, and the Phase 1 inductor works like a non-coupled inductor with self-inductance L_1. The Phase 1 current i_1 decreases until it reaches 0 at t_2. At t_2, the Phase 1 bottom synchronous rectifier is turned off to avoid i_1 becoming a negative value. During the time range t_1 to t_2, the two phase inductor currents are decoupled. During the time range t_2 to $T_s/2$, both phase-currents i_1 and i_2 are kept at zero. The whole circuit seems to stop except that the output capacitors provide current to the load.

From $T_s/2$ to T_s, the coupled-inductor buck converter follows the working principle of the first half of the switching period, except that Phase 1 and Phase 2 are exchanged. In summary, the two phase inductor currents i_1 and i_2 couple, decouple and stop alternatively during one switching period.

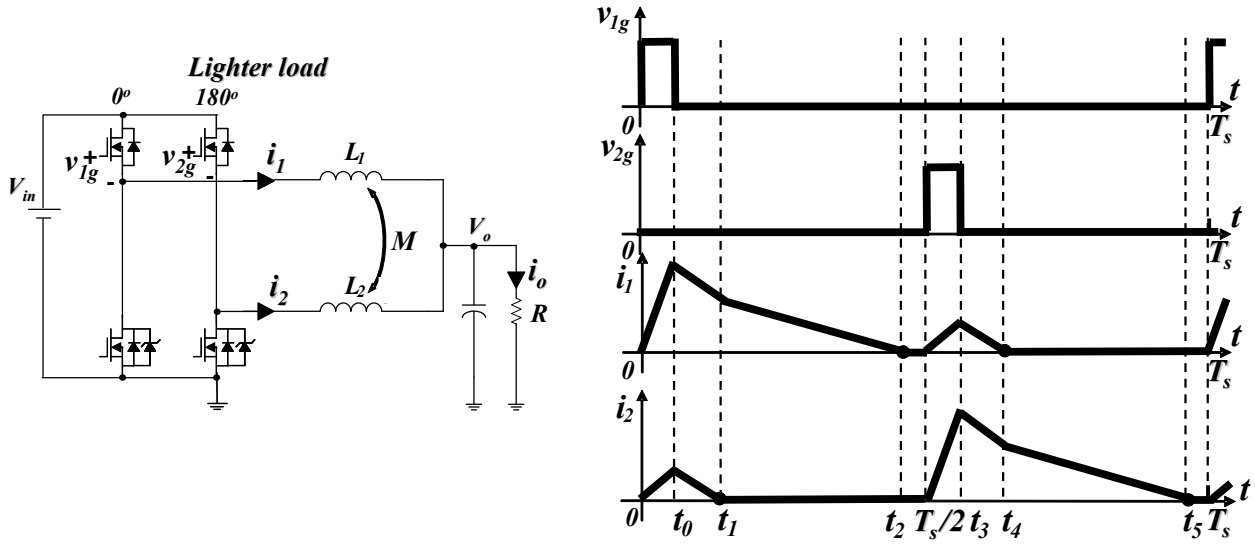

(a) **(b)**

Figure 7.8 The gate driving voltage and the phase current waveforms of the two-phase coupled-inductor buck converter in DCM2 (a) The two-phase coupled-inductor buck converter (b) The gate driving voltage and phase current waveforms

To verify the above analysis, experiments are performed. Figure 7.9 shows the experimental phase inductor current i_1 waveform in the DCM1 mode of a coupled-inductor laptop VR. The experiment setup has the values: V_{in}=12V, V_o=1.37V, M=-1.56μH, and

L=1.72μH. From Figure 7.10, we can see that the phase-currents couple and decouple alternatively during one switching period, as was discussed previously. The oscillation in the i_1 waveform is due to the resonance between the capacitance in the SR drain and source and the leakage inductance of the coupled inductors.

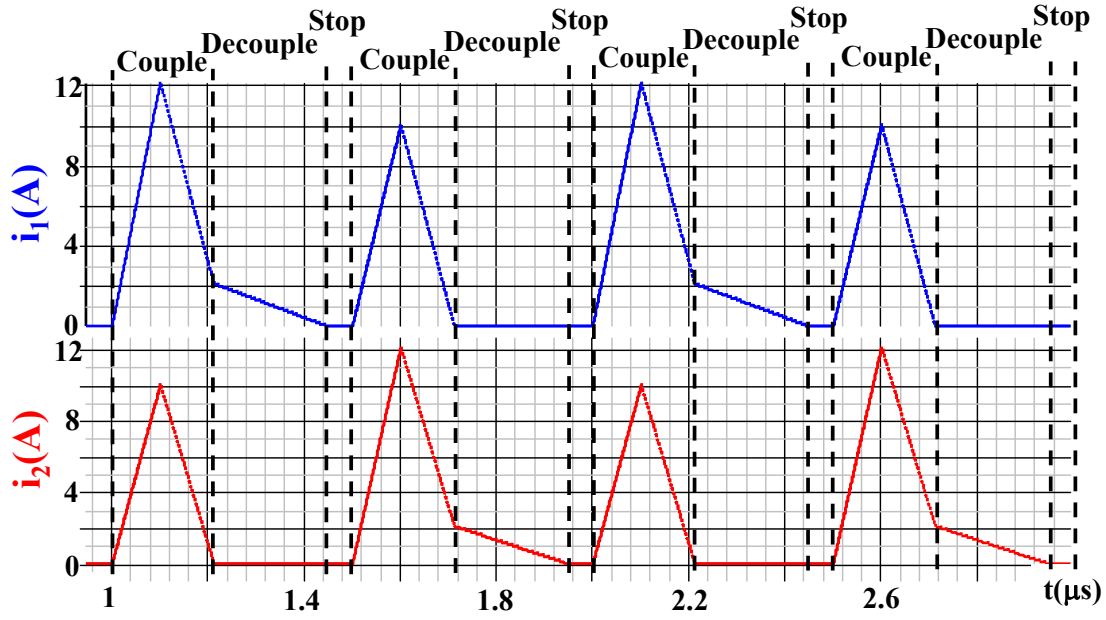

Figure 7.9 The simulated phase-current waveforms of the two-phase coupled-inductor buck converter in DCM2

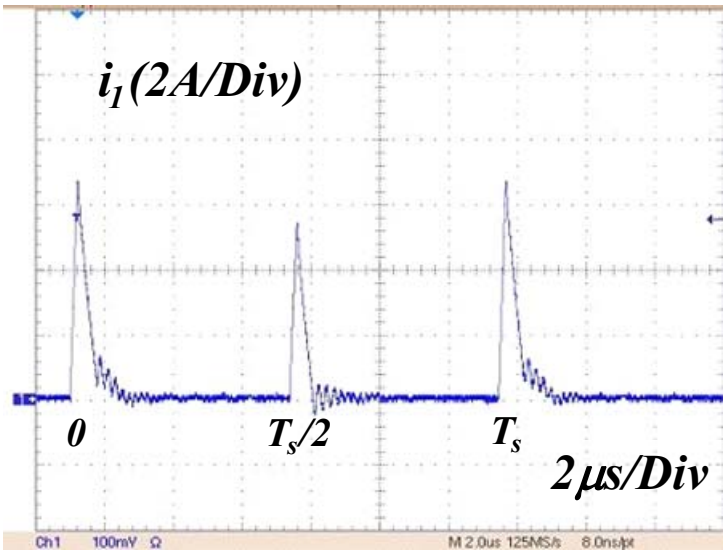

Figure 7.10 The phase-current i_1 waveform of the two-phase coupled-inductor buck converter in the DCM2 mode (V_{in}=12V, V_o=1.37V, M=-1.56μH, and L=1.72μH)

The V_o/V_{in} and f_s relationship of the coupled-inductor buck converter is necessary for the control of the two-phase coupled-inductor buck converter in DCM2. After derivation (Appendix 2), it is found that

$$r = \frac{V_o}{V_{in}} = \frac{2}{1+\sqrt{1+4\frac{L_{ss}}{D^2 R T_s}}} \tag{7.6}$$

and

$$f_s = \frac{1}{T_s} = \frac{r^2 L_{ss}}{(1-r){T_{on}}^2 R} \tag{7.7}$$

Comparing the equations (7.1), (7.2), (7.6) and (7.7), it can be found that the V_o/V_{in} and f_s relationship of the two-phase coupled-inductor buck converter in DCM1 is the same as that of the two-phase coupled-inductor buck converter in DCM2.

Comparing the equations (7.4), (7.5), (7.6) and (7.7), it can be found that the V_o/V_{in} and f_s relationship of the two-phase coupled-inductor buck converter in DCM2 is the same as that of the non-coupled-inductor buck converter if L_{ss} replaces L_{nc} in the equation.

7.3. Reason for the Low Light-Load Efficiency

In this section, the reason for the low light-load efficiency issue of the coupled-inductor buck converter in DCM will be explained. Since the efficiency testing result is based on the two-phase coupled-inductor buck converter, the low efficiency issue will be explained based on the two-phase coupled-inductor buck converter in the following. For the n-phase coupled-inductor buck converter (Appendix 3), the concept still holds.

In the previous section, it can be seen that the two-phase coupled-inductor buck converter goes into two DCM modes (the DCM1 mode and the DCM2 mode) as the load becomes lighter. In DCM1 mode, the phase inductor currents i_1 and i_2 reach zero only once during one switching period, and in the DCM2 mode, the phase inductor currents i_1 and i_2 reach zero twice during one switching period (Figure 7.11). Reaching zero-current twice in DCM2 mode of coupled-inductor buck converters, caused by the coupling effects between phase inductors, is the reason for the low light-load efficiency of coupled-inductor buck converters.

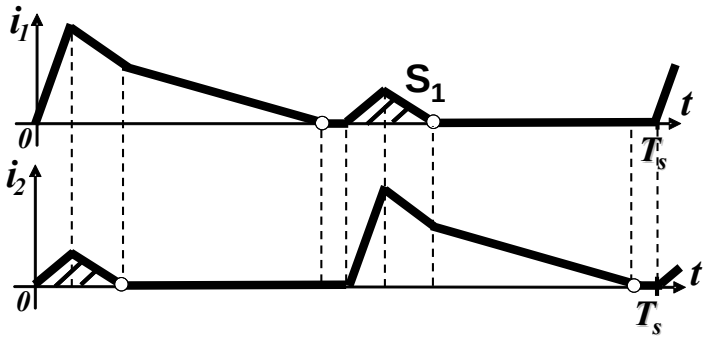

Figure 7.11 The phase current waveforms of the two-phase coupled-inductor buck converter in DCM2 mode: the phase current reaches zero twice in one switching period

To achieve the DCM modes, the synchronous rectifiers (SRs) need to be turned off when the phase-currents are reduced to zero. Therefore, there are two possible methods for conducting the currents induced by the coupling effects in the second half of the switching period. We can turn on the SR to conduct the currents, the twice-SR-gate-driving method; we can also keep the SR off and use a Schottky diode paralleling with the SR to conduct the currents, the paralleled-diode-conduction method. These two methods and their consequences are illustrated below.

In the twice-SR-gate-driving method, the SR is turned on twice in one switching period. The control law of the twice-SR-gate-driving method is

$$\begin{cases} v_{bg} = \text{"1"} & when \quad i_{SR} > 0 \\ v_{bg} = \text{"0"} & other \end{cases} \tag{7.8}$$

where the v_{bg} is the SR's gate driving voltage. The i_1 and the corresponding v_{bg} waveform are shown in Figure 7.12.

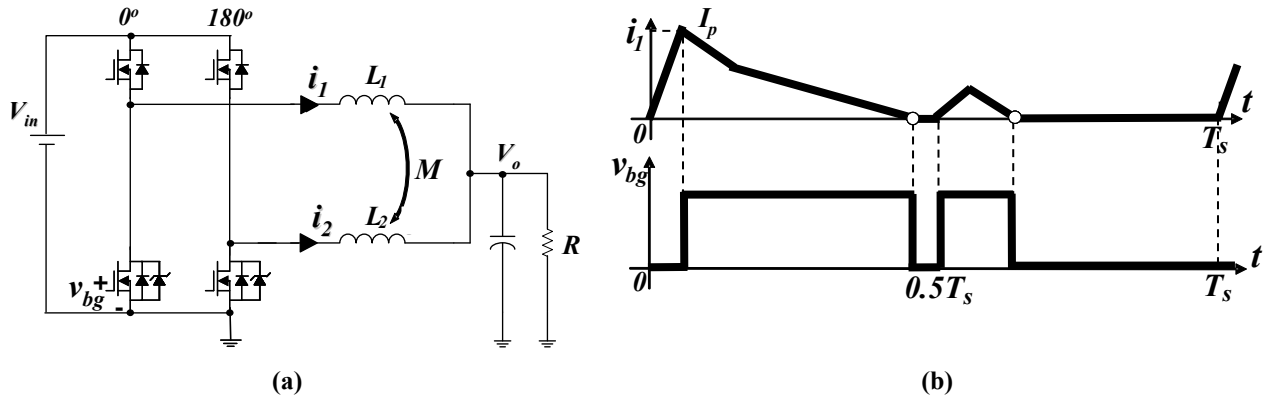

(a) **(b)**

Figure 7.12 The phase current i_1 and the gate driving voltage v_{bg} waveforms of the coupled-inductor buck converter in DCM2 with the twice-SR-gate-driving method (a) the two-phase coupled buck converter (b) the i_1 and v_{bg} waveforms

The total loss of the coupled-inductor buck converter in this control method can be approximated as

$$P_{loss\_tot} = V_{in} \cdot I_P \cdot \Delta t \cdot f_s + 4 \cdot Q_{g\_SR} \cdot V_{g\_SR} \cdot f_s + 2 \cdot Q_{g\_top} \cdot V_{g\_top} \cdot f_s + P_{cond} \tag{7.9}$$

where Δt is the top switch switching time; Q_{g_SR} and V_{g_SR} are the SR's gate charge and gate driving voltage; Q_{g_top} and V_{g_top} are the top switch's gate charge and gate driving voltage; and P_{cond} is the total conduction loss of both the top switch and the SR. Since the SRs switch twice during one switching period, the SRs' gate driving losses are doubled.

Because the conduction loss under light-load is not dominant, we assume the conduction loss in the non-coupled inductor buck converter is similar to that in the coupled-inductor buck converter; thus the total loss of non-coupled inductor buck converters can be approximated as

$$P_{loss\_tot\_nc} = V_{in} \cdot I_P \cdot \Delta t \cdot f_{s\_nc} + 2 \cdot Q_{g\_SR} \cdot V_{g\_SR} \cdot f_{s\_nc} + 2 \cdot Q_{g\_top} \cdot V_{g\_top} \cdot f_{s\_nc} + P_{cond} \tag{7.10}$$

In the above equation, it is assumed that the coupled-inductor buck converters and the non-coupled-inductor buck converters have the same steady-state inductances.

Comparing the equations (7.9) and (7.10), it can be seen that the relationship between f_s and f_{s_nc} determines the relationship between P_{loss_tot} and $P_{loss\_tot\_nc}$. Since the steady-state inductances of the coupled-inductor buck converter and the non-coupled-inductor buck converter are the same (L_{eq1}=L_{nc}), and V_o, V_{in}, R, and T_{on} are fixed in the constant-on time control laptop VRs, substituting the equation (7.7) into the equation (7.5)

$$f_s = f_{s\_nc} \tag{7.11}$$

Combining the equations (7.9), (7.10) and (7.11),

$$P_{loss\_tot} = P_{loss\_tot\_nc} + 2 \cdot Q_{g\_SR} \cdot V_{g\_SR} \cdot f_s \tag{7.12}$$

It can be seen that the total loss of the coupled-inductor buck converter in DCM2 mode is $2 \cdot Q_{g\_SR} \cdot V_{g\_SR} \cdot f_s$ larger than that of the non-coupled-inductor buck converters. Since Q_{g_SR} is

quite large in the case of the small duty cycle buck, the efficiency of the coupled-inductor buck converter in the DCM2 mode will drop a great deal.

In the paralleled-diode-conduction method, the SR is turned on only once during one switching period. The control law of the paralleled-diode-conduction method is

$$\begin{cases} v_{bg} = \text{"1"} & when \quad i_{SR} > 0 \ and \ nT_s \le t \le (n+0.5)T_s \\ v_{bg} = \text{"0"} & other \end{cases} \tag{7.13}$$

where v_{bg} is the SR's gate driving voltage. The phase inductor current i_1, the corresponding v_{bg} and the phase inductor voltage v_1 waveforms are shown in Figure 7.13.

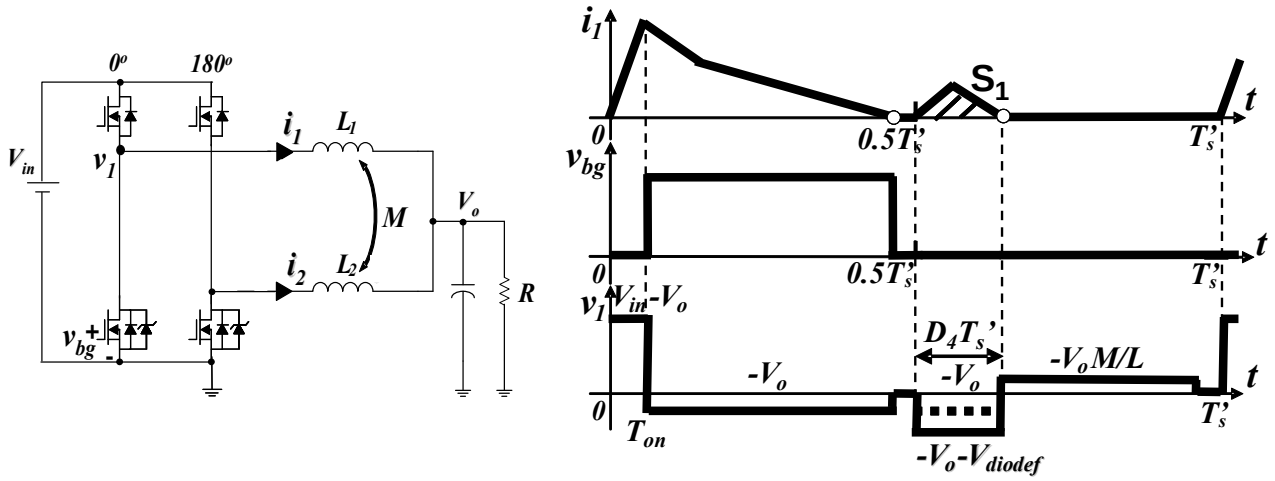

(a) **(b)**

Figure 7.13 The phase current i_1, the bottom switch gate driving voltage v_{bg} and the switching point voltage v_1 waveforms of the two-phase coupled-inductor buck converter in DCM2 with the paralleled-diode-conduction method (a) the two-phase coupled buck converter (b) the i_1, v_{bg} and v_1 waveforms

The total loss of the coupled-inductor buck converter in this control method can be approximated as

$$\begin{aligned} P'_{loss\_tot} &= V_{in} \cdot I_P \cdot \Delta t \cdot f'_s + 2 \cdot Q_{g\_SR} \cdot V_{g\_SR} \cdot f'_s \\ &+ 2 \cdot Q_{g\_top} \cdot V_{g\_top} \cdot f'_s + P'_{cond} \end{aligned} \tag{7.14}$$

where P'_{cond} is the total conduction loss of the top switch, the SR and the SR paralleled diode; and f_s' is the switching frequency.

In this paralleled-diode-conduction method, the phase inductor current (S_1 area) in the second half of the switching period is conducted by the SR paralleled diode. Therefore, there is a V_{diodef} (0.3V-0.6V) voltage drop at the phase inductor voltage v_1 during the S_1 time range. If the constant on-time control is used and V_{in}, V_o, L, M and R are kept the same, T_s' will decrease to keep the output voltage V_o, and f_s' will increase.

$$f'_s > f_s = f_{s\_nc} \tag{7.15}$$

Moreover, since the S_1 area current is conducted by the SR paralleled diode, the voltage drop across the SR source and drain, V_{diodef} is much larger than the voltage drop with the SR conduction, V_{SRf} (<30mV). Therefore, the bottom switch conduction loss P'_{cond_bot} is much larger than P_{cond_bot} in the twice-SR-gate-driving method. Accordingly,

$$P'_{cond} > P_{cond} \tag{7.16}$$

Substituting the equations (7.15) and (7.16) into the equations (7.10) and (7.14),

$$P'_{loss\_tot} > P_{loss\_tot\_nc} \tag{7.17}$$

Since the total loss of the coupled-inductor buck converter in DCM2 with the paralleled-diode-conduction method is larger than that of the non-coupled-inductor buck converter, the efficiency of the coupled-inductor buck converter in DCM2 will drop.

Figure 7.14 shows the testing efficiency results based on the industrial constant-on time control laptop buck VR demo board.

Although the above analysis and testing results are based on the constant-on time control method, the same conclusion holds even if the constant switching frequency control method is used: the light-load efficiency of the coupled-inductor buck converter in DCM is lower than that of the non-coupled-inductor buck converter in DCM when the steady-state inductances are the same.

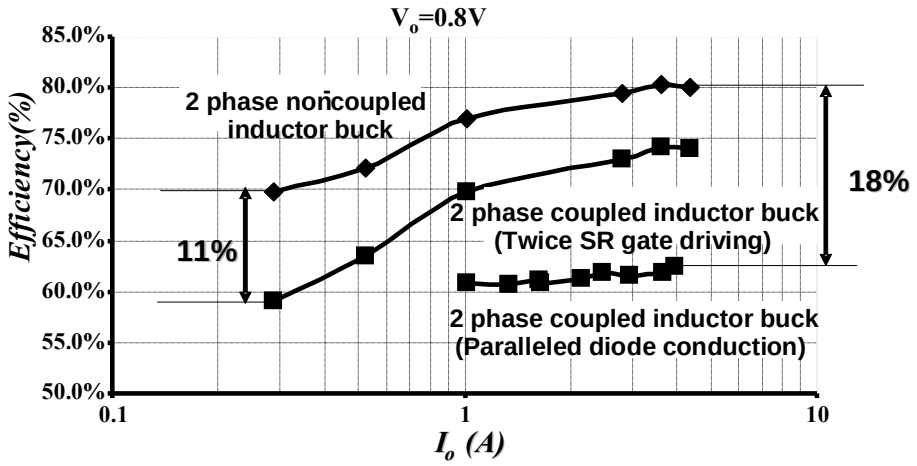

Figure 7.14 The light-load efficiency comparison of the two-phase coupled-inductor laptop buck converter and the non-coupled-inductor laptop buck converter (V_{in}=12V and T_{on}=330ns)

7.4. Improvement of the Light-load Efficiency

In this section, a solution to improve the light-load efficiency of the coupled-inductor buck converter in DCM will be illustrated. The solution is explained based on the two-phase coupled-inductor buck converter, while the concept can be extended to the n-phase coupled-inductor buck converter.

Since the two-phase coupled-inductor buck converter has a similar efficiency as the non-coupled-inductor buck converter in DCM1 and has a lower efficiency than the two-phase non-coupled-inductor buck converter in DCM2, the low efficiency issue can be solved by avoiding the coupled-inductor buck converter working in the DCM2 mode. The burst-in-DCM1-mode solution is proposed to achieve this concept. Figure 7.15 shows the burst-in-DCM1-mode solution. When the load current is quite low, the coupled-inductor buck converter converter is controlled to work in DCM1 for a short time and then the two-phase coupled-inductor buck converter shuts down for a long time.

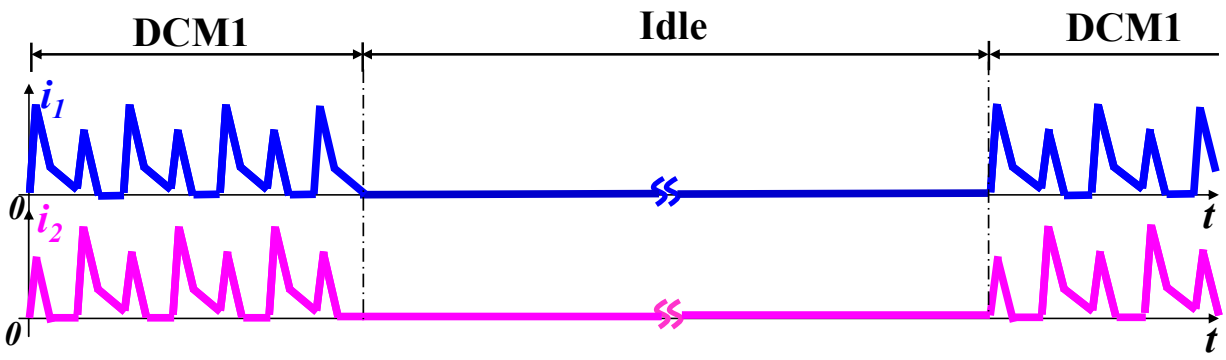

Figure 7.15 The phase current waveforms of the two-phase coupled-inductor buck converter under the light load with the burst-in-DCM1-mode solution

The switching frequency f_s vs. the output current i_o graph is shown in Figure 7.16. From Figure 7.16, it can be seen that one control strategy for the solution is

$$\begin{cases} Constant\ on-time\ control & f > f_{crit2} \\ Burst-in-DCM1\ control & f \le f_{crit2} \end{cases} \tag{7.18}$$

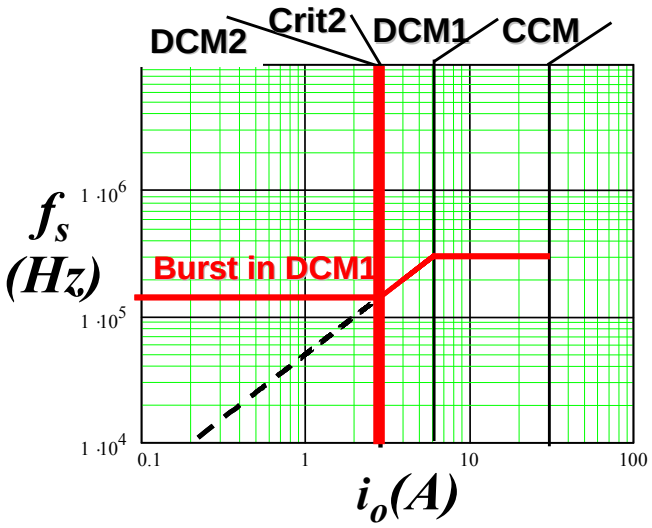

Figure 7.16 The switching frequency f_s vs. the output current i_o of the coupled-inductor buck converter with the burst-in-DCM1-mode control

Figure 7.17 shows the $v_{1g}+v_{2g}$ signal in DCM1 and DCM2 modes. The $v_{1g}+v_{2g}$ signal keeps "high" in DCM1 and doesn't keep "high" in DCM 2. Therefore, another control strategy is

$$\begin{cases} Constant\ on-time\ control & v_{1g}+v_{2g}\ is\ continuously\ "high" \\ Burst-in-DCM1\ control & v_{1g}+v_{2g}\ isn't\ continuously\ "high" \end{cases} \tag{7.19}$$

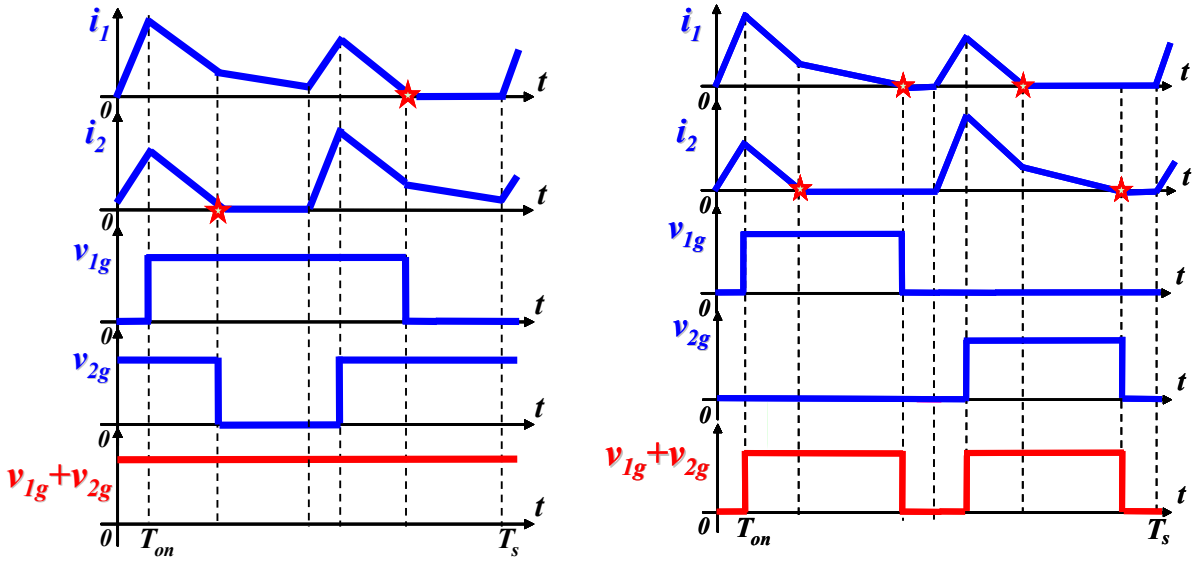

Figure 7.17 The phase current i_1 and i_2, the gate driving voltage v_{1g} and v_{2g} and $v_{1g}+v_{2g}$ waveforms of the two-phase coupled-inductor buck converter in DCM1 and DCM2 modes (a) The i_1, i_2, v_{1g}, v_{2g} and $v_{1g}+v_{2g}$ waveforms in DCM1 (b) the i_1, i_2, v_{1g}, v_{2g} and $v_{1g}+v_{2g}$ waveforms in DCM2

The burst-in-DCM1-mode solution can be realized with the hysteretic control (Figure 7.18). The signal V_x

$$V_x = V_o + H_v \cdot \Delta V_i \tag{7.20}$$

is controlled to be within the band of the V_{ref} and $V_{ref}+V_{band}$.

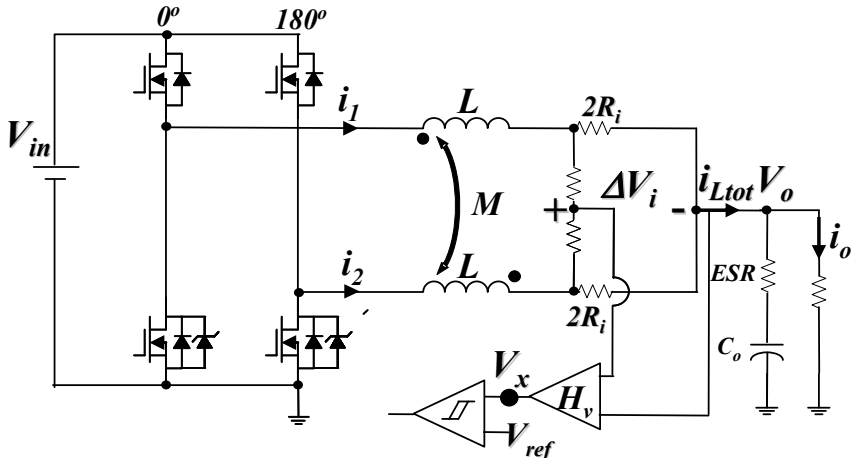

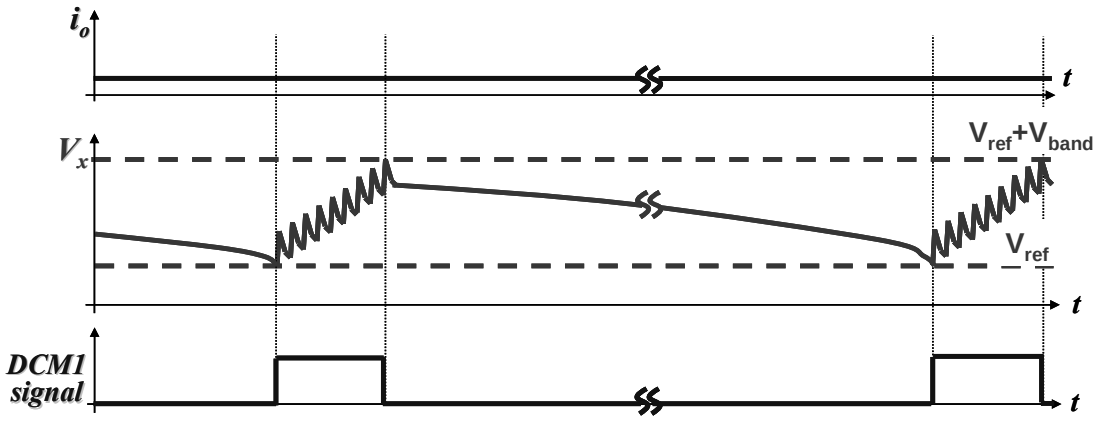

(b)

Figure 7.18 The hysteretic control method to realize the burst-in-DCM1-mode operation in the two-phase coupled-inductor buck converter (a) The two-phase coupled-inductor buck converter (b) The output current i_o, the v_x signal and the DCM1 signal waveforms with the hysteretic control

The detail waveforms of the hysteretic control are shown in Figure 7.19. It can be seen that

$$V_{band} = V_{oripple} + H_v \cdot \Delta V_{ipp} \tag{7.21}$$

The $V_{oripple}$ can be determined by the reqirement in the specific application, e.g. it is 26mV in the laptop CPU VR application [90]. Then, V_{band} can be determined based on the equation (7.21).

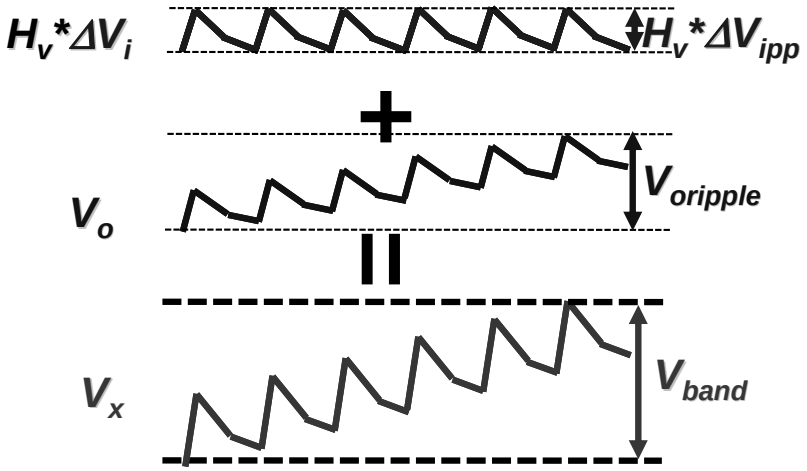

Figure 7.19 The $H_v x \Delta V_i$, the output voltage V_o and the v_x signal waveforms of the two-phase coupled-inductor buck converter with the hysteretic control method

Figure 7.20 shows one method to fully implement the hysteretic control. In Figure 7.20, the burst signal is the signal showing the burst-in-DCM condition. When the circuit is in the constant

on-time control, the burst signal is "0"; when the circuit is in the burst-in-DCM1-mode, it is "1"; the DCM1 signal is the signal showing the state of the circuit in burst-in-DCM condition. When the circuit is in the DCM1 state of the burst-in-DCM-mode condition, the DCM1 signal is "1"; if the circuit is in the idle state of the burst-in-DCM-mode condition or in the constant on-time control condition, it is "0". Figure 7.21 shows the transition from the normal constant on-time control to the burst-in-DCM1-mode control. When the interval of the clock signal d is longer than $0.5T_{crit2}$, the burst-in-DCM1-mode is triggered. Figure 7.22 shows the transition from the burst-in-DCM1-mode control to the normal constant on-time control. If the $v_{1g}+v_{2g}$ control strategy is adopted, Figure 7.23 shows the transition process from the normal constant on-time control to the burst-in-DCM1-mode control. The simulation based on this hysteretic control implementation is shown in Figure 7.24. The simulation result verifies this implementation.

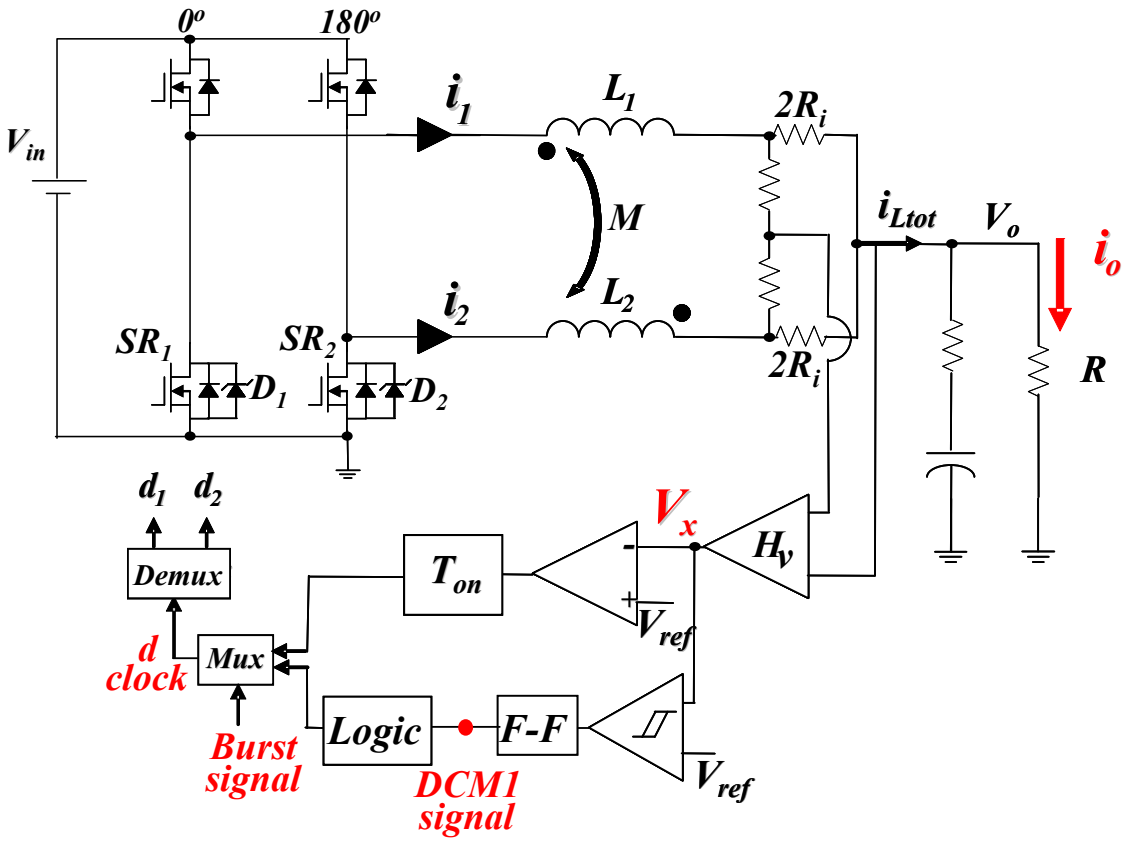

Figure 7.20 One method to implement the above hysteretic control in the two-phase coupled-inductor buck converter

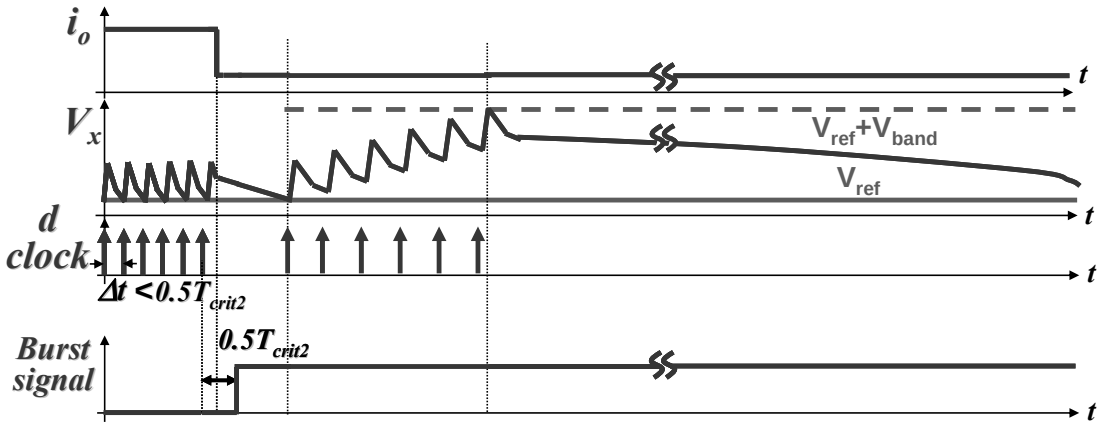

Figure 7.21 The output current i_o, the V_x signal, the clock and the burst signal waveforms of the two-phase coupled-inductor buck converter with the transition from the normal constant on-time control to the burst-in-DCM1-mode control

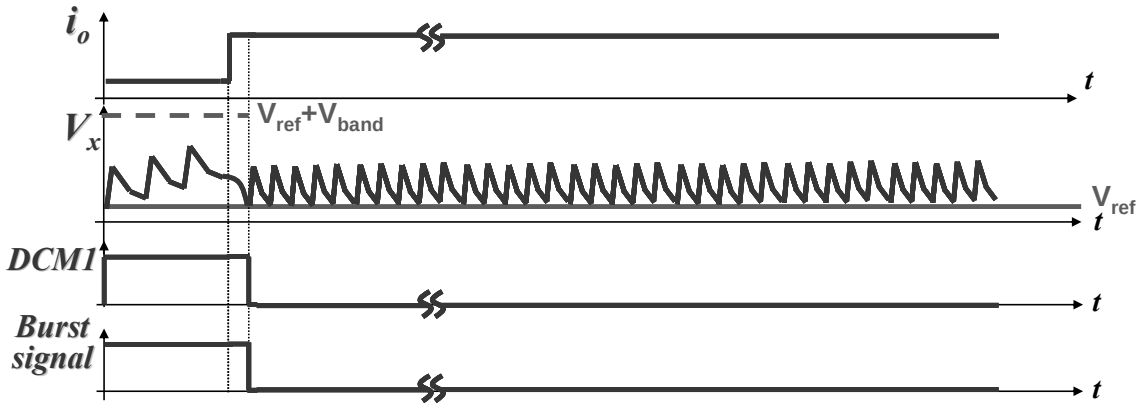

(a)

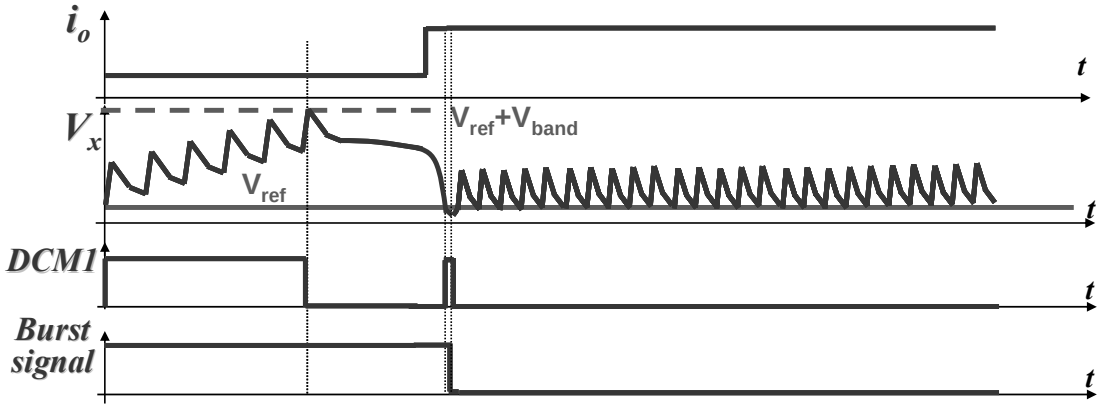

(b)

Figure 7.22 The output current i_o, the V_x signal, the DCM1 signal and the burst signal waveforms of the two-phase coupled-inductor buck converter with the transition from the burst-in-DCM1-mode control to the normal constant on-time control (a) the transition with the i_o stepping up in the DCM1 state (b) the transition with the i_o stepping up in the idle state

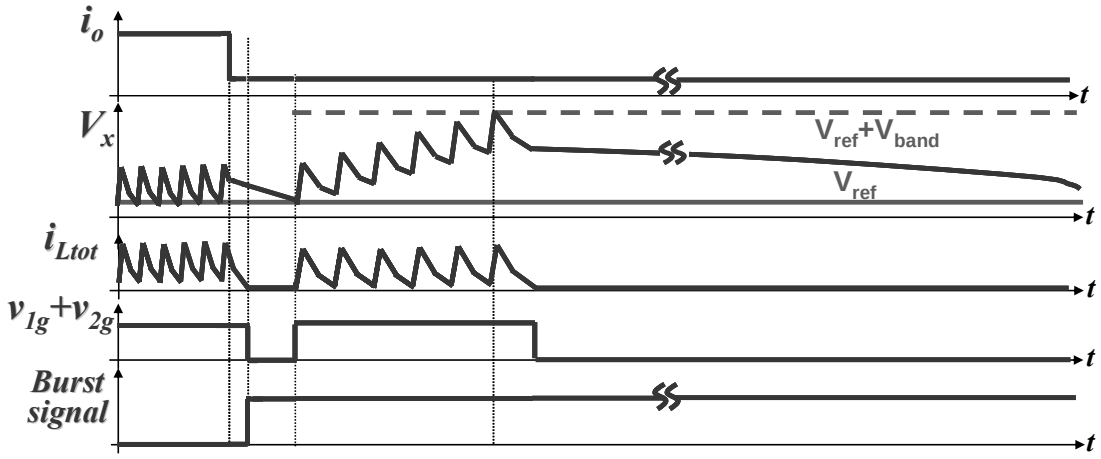

Figure 7.23 The output current i_o, the V_x signal, the inductor total current i_{Ltot}, the $v_{1g}+v_{2g}$ signal and the burst signal waveforms of the two-phase coupled-inductor buck converter during the transient with the $v_{1g}+v_{2g}$ control strategy

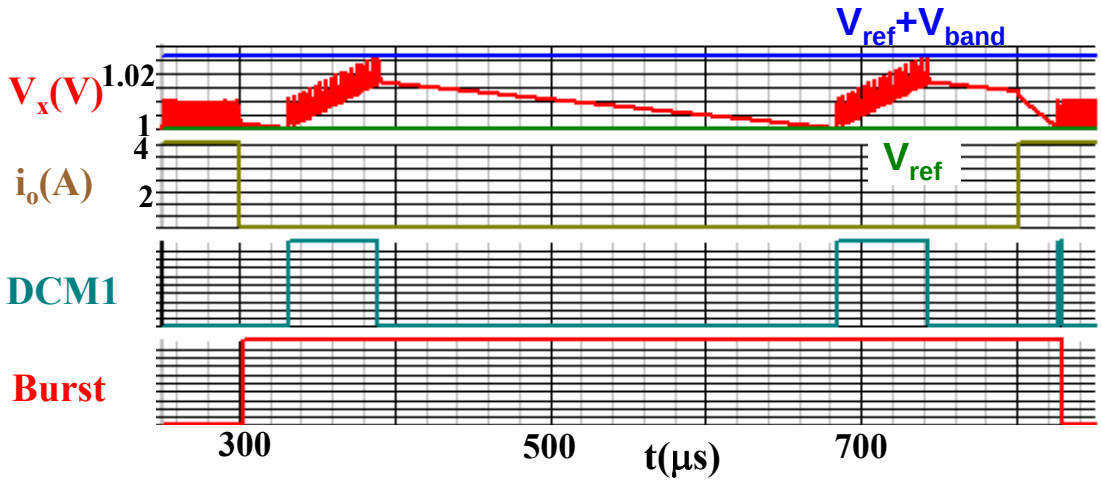

Figure 7.24 The simulated V_x signal, the output current i_o, the DCM1 and the burst signal waveforms of the two-phase coupled-inductor buck converter during the transitions

Figure 7.25 shows the efficiency testing result when the burst-in-DCM1-mode solution is utilized. The efficiency of the coupled-inductor buck converter is similar to that of the non-coupled-inductor buck converter under light-load.

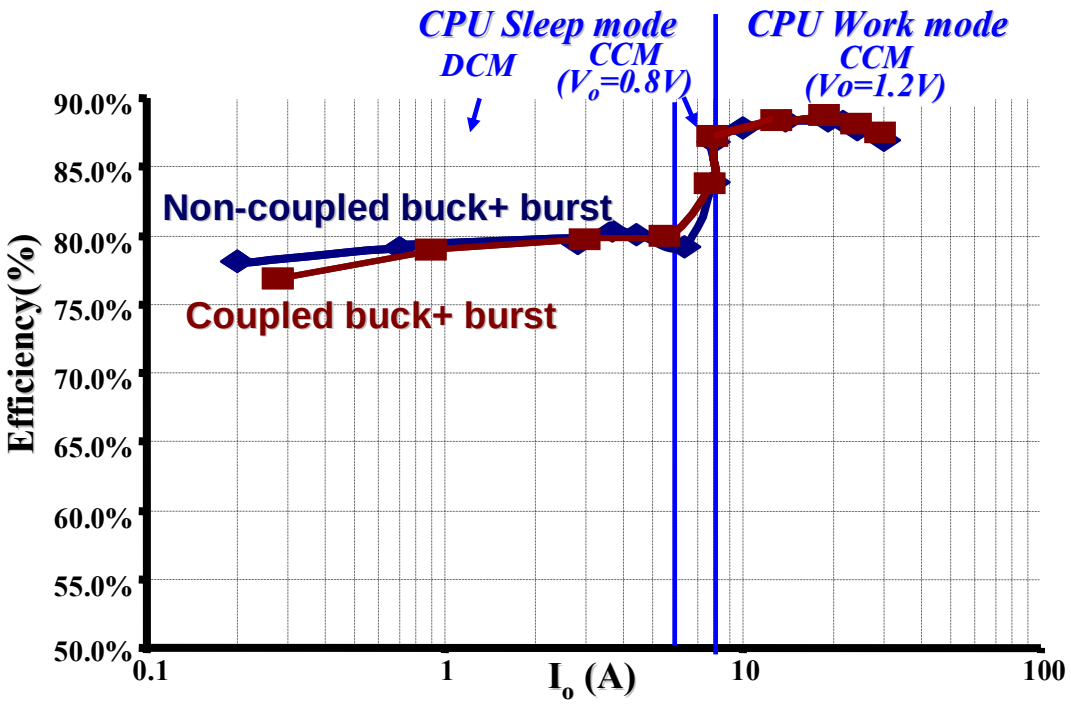

Figure 7.25 The tested efficiency results of the two-phase non-coupled-inductor buck converter with the burst control and the two-phase coupled-inductor buck converter with the burst-in-DCM1-mode control (V_{in}=12V and T_{on}=330ns)

7.5. Summary

In this chapter, the DCM modes of the multiphase coupled-inductor buck converter are investigated for the first time. The two-phase coupled-inductor buck converter has two different DCM modes: DCM1 and DCM2. In DCM1, the phase-currents of the n-phase coupled-inductor buck converter reach zero-current once. In the DCM2 mode, the phase-currents of the n-phase coupled-inductor buck converter reach zero-current more than once, which lowers the efficiency of the n-phase coupled-inductor buck converter. Therefore, the multiphase coupled-inductor buck converter has a lower efficiency than the multiphase non-coupled-inductor buck converter in DCM, keeping the steady-state inductance the same. The solution, burst-in-DCM1-mode, is proposed to solve this issue. With the burst-in-DCM1-mode control, the multiphase coupled-inductor buck converter has a similar efficiency as the multiphase non-coupled-inductor buck converter.

Chapter 8. Conclusion and Future Work

The multiphase coupled-inductor buck converter is a more advanced circuit topology than today's multiphase non-coupled-inductor buck converter. The challeges for the multiphase coupled-inductor buck converter are the limited analysis of this advanced circuit topology, the magnetic structures for this circuit topology, the low light-load efficiency of this toplogy in the DCM and the current sensing methods for this advanced topology. These challeges blockade the widely use of the multiphase coupled-inductor buck converter.

8.1. Summary

This dissertation is engaged in exploring the novel solutions for the above challenges of the multiphase coupled-inductor buck converter. Starting from the comprehensive analysis of the multiphase coupled-inductor buck converter, the analysis theory of the n-phase, whole duty cycle range, any coupling coefficient multiphase coupled-inductor buck converter is established. It is found that although the two-phase coupled-inductor buck can achieve a low FOM (L_{tr}/L_{ss}) around the 0.5 duty cycle, the more-phase coupled inductor buck converter can achieve a low FOM for a wide duty cycle range. This characteristic can be used in the wide-input POL converters to acieve a better efficiency for the whole input voltage range. The asymmetry analysis of the multiphase coupled-inductor buck is also investigated. It is found that the stronger the asymmetry is, the more severe the FOM degration is.

For the low-voltage, high-current applications, one issue for the existing coupled-inductor structure is the long winding path and the corresponding large winding loss and total loss. Several twisted-core coupled-inductors are proposed to solve this issue. With the core twisted, the winding of the coupled-inductors can be made straighter and the winding paths are shorter than the existing coupled inductors. With the tradeoff of the winding loss and the core loss of the twisted core coupled-inductors, the total loss of the low profile twisted-core coupled-inductors can reduce 23 percent compared to that of the existing coupled-inductors. To model and design the twisted-core coupled-inductors, a sophisticated space cutting method is developed to model

the strong 3D fringing fluxes. C. Sullivan proposed the space cutting method for the E-E core transformer before. In the modeling of the twisted-core coupled-inductor, the space cutting method is applied and extended to further separate the fringing fluxes between two perpendicular planes and the fringing fluxes between two parallel planes. The fringing fluxes between the two parallel planes with the changing air gaps are also investigated. The sophisticated space cutting method can also be used to model other magnetic structures with the strong fringing fluxes.

For the integrated POL application, the bottleneck for the high power density is the large inductor size. The coupled-inductor is proposed to reduce the large inductor size and improve the power density of the integrated POL converter. Different integrated coupled-inductor structures are proposed. The side-by-side-winding structure is proved to be better than the top-and-bottom-winding structure in reducing the inductor footprint. This is because the side-by-side-winding structure has a smaller mean magnetic path length than the top-and-bottom-winding structure. The experimental results based on the LTCC process technology shows that the integrated coupled-inductor POL converter doubles the power density. To simplify the modeling and design of the LTCC integrated coupled-inductor, the two-segment approximation of the B-H curve is utilized. This two-segment approximation, or even three-segment approximation, can also be used to model other integrated inductors with a nonlinear B-H curve.

The evalution of the multiphase coupled-inductor buck converter based on the microprocessor VR application is also investigated. When the coupling phase number increases, there is a diminishing return effect on both the efficiency improvement and the transient performance improvement. For the server VR example, the three-phase is an appropriate coupling phase number.

The novel DCR current sensing methods of the multiphase coupled-inductor buck converter are also proposed in this dissertation. With the time constant of the DCR sensing network matching the time constant of the leakge inductance and DCR, the proposed DCR total current sensing method can sense the total current precisely. With a more advanced DCR sensing network, both the phase-current and the total current can be sensed precisely. The proposed DCR current sensing networks are lossless and don’t give additional burden to the power loss of the multiphase coupled-inductor buck converter.

The light-load efficiency of the multiphase coupled-inductor buck converter was expected to be higher than that of the multiphase non-coupled-inductor buck converter. However, it is experimentally found that the light-load efficiency of the multiphase coupled-inductor buck converter is lower that that of its counterpart with the contant on-time control. This is because the phase-current reaches zero-current more-than-once in DCM2 mode. The burst-in-DCM1-mode control is proposed to improve the light-load efficiency of the multiphase coupled-inductor buck converter. With the advanced control method, the efficiency of the multiphase coupled-inductor buck converter is similar to that of the multiphase non-coupled-inductor buck converter.

In conclusion, this dissertation proposed alternative multiphase coupled-inductor structures for the discrete POL application and the side-by-side-winding coupled-inductor structure for the integrated POL application. The analysis, current sensing and the solution for the low light-load efficiency of the multiphase coupled-inductor buck converter are also investigated.

8.2. Future work

In the integrated POL converter in the Chapter 4, the active stage and the passive stage are packaged together. Recently, there is a trend to monolithically integrate the active stage and the passive stage of the integrated POL converter [63] to further increase the power density of the integrated POL converter. In this circumstance, air gaps exist and the multi-turn winding is necessary to achieve an enough inductance because the magnetic core thickness is extremely small due to the process limitation. What the best and symmetric coupled-inductor structure for this application is needs further investigation.

Appendix 1. Analysis of Asymmetric Coupled-inductor Buck Converters

For all the above analyses for the multiphase coupled-inductor buck converter, the multiphase coupled-inductor is assumed to be symmetric. However, as shown in Figure 1.31, the practical n-phase (n>2) coupled-inductor is asymmetric. In this appendix, the effect of asymmetric coupled-inductors on the multiphase coupled-inductor buck converter will be investigated.

Figure A1.1 shows an example of the three-phase asymmetric coupled-inductor and the three-phase asymmetric coupled-inductor buck converter utilizing this coupled-inductor. For this asymmetric coupled-inductor, $L_1=L_3\neq L_2$, $M_{12}=M_{23}\neq M_{13}$.

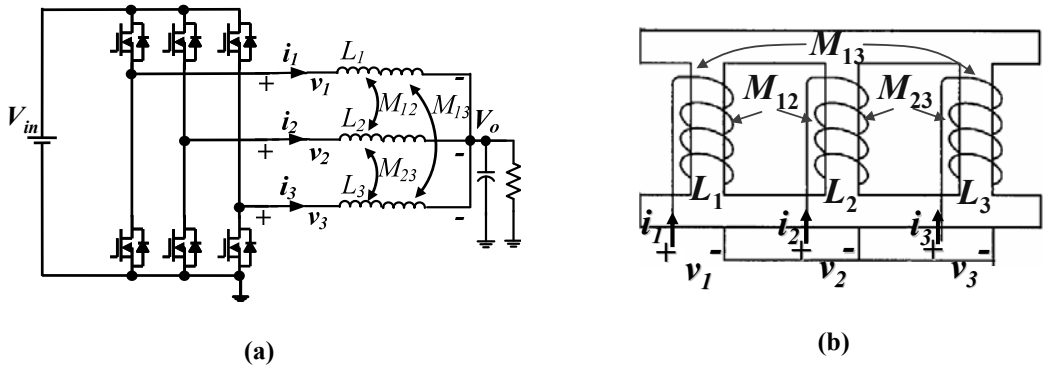

(a) **(b)**

Figure A1.1 The three-phase asymmetric coupled-inductor buck converter (a) The three-phase asymmetric coupled-inductor (b) The three-phase asymmetric coupled-inductor buck converter

The basic electrical equation for the three-phase asymmetric coupled-inductor is

$$\begin{cases} v_1 = L_1 \cdot \dot{i}_1 + M_{12} \cdot \dot{i}_2 + M_{13} \cdot \dot{i}_3 \\ v_2 = M_{12} \cdot \dot{i}_1 + L_2 \cdot \dot{i}_2 + M_{23} \cdot \dot{i}_3 \\ v_3 = M_{13} \cdot \dot{i}_1 + M_{23} \cdot \dot{i}_2 + L_3 \cdot \dot{i}_3 \end{cases} \tag{A1.1}$$

The steady-state inductor voltage and current waveforms are shown in Figure A1.2 when D<1/3. The I_{pp1_nc}, I_{pp2_nc} and I_{pp3_nc} are the inductor current ripples for Phase 1, Phase 2 and Phase 3. L_{ss1}, L_{ss2} and L_{ss3} are the steady state inductances for the three phases

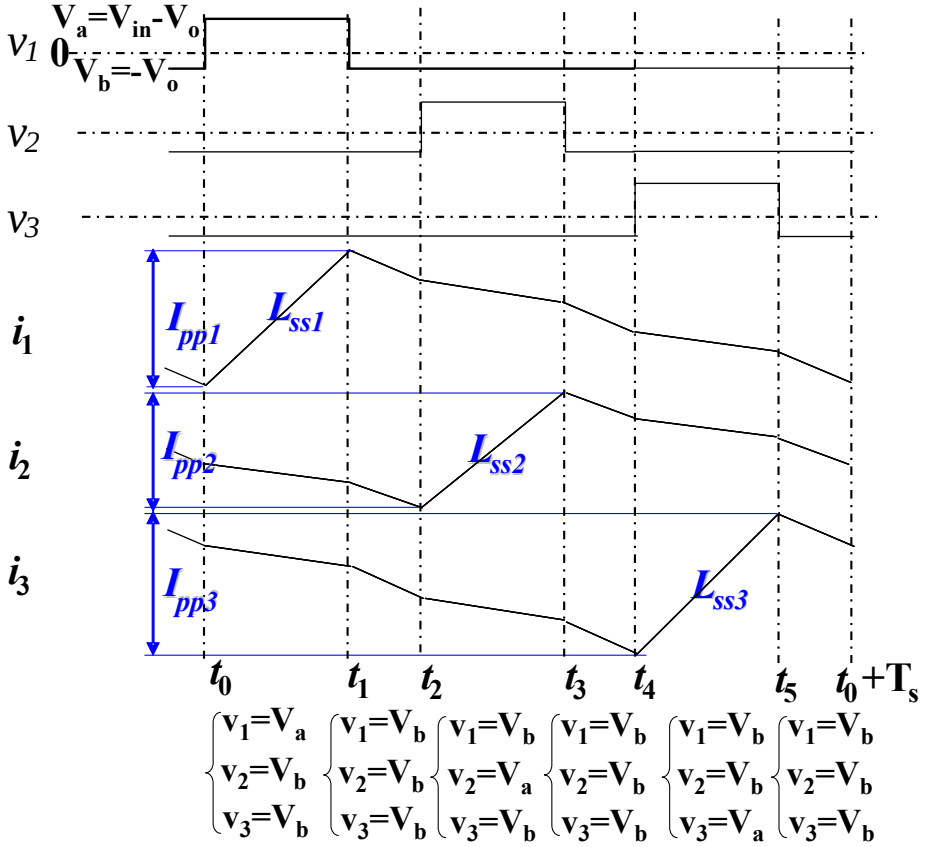

Figure A1.2 The steady-state inductor voltage and current waveforms of the three-phase asymmetric coupled-inductor buck converter

Substituting the inductor voltage combinations into the equation (A1.1), L_{ss1}, L_{ss2} and L_{ss3} when D<1/3 can be found.

$$L_{ss1}=L_{ss3}=\frac{V_{in}-V_o}{I_{pp1}}DT_s=\frac{L_1(L_1L_2-M_{12}^2)-(L_1M_{12}^2-2M_{12}^2M_{13}+L_2M_{13}^2)}{L_1L_2-M_{12}^2+(L_1M_{12}-M_{12}M_{13}-M_{12}^2+L_2M_{13})\frac{D}{D'}} \quad \text{(A1.2)}$$

$$L_{ss2}=\frac{V_{in}-V_o}{I_{pp2}}DT_s=\frac{L_1(L_1L_2-M_{12}^2)-(L_1M_{12}^2-2M_{12}^2M_{13}+L_2M_{13}^2)}{(L_1^2-M_{13}^2)+2(L_1M_{12}-M_{12}M_{13})\frac{D}{D'}} \quad \text{(A1.3)}$$

The steady-state inductances for Phase 1 and Phase 3 are the same, while the steady-state inductance for Phase 2 is different. Figure A1.3 shows the transient inductor voltage and current waveforms for the three-phase asymmetric coupled-inductor buck converter. The transient inductance for Phase 1 is defined as

$$(\frac{di_1}{dt})_{cp} = \frac{\Delta i_1}{T_s} \triangleq \frac{V_{in} \cdot \Delta D}{L_{tr1}} \tag{A1.4}$$

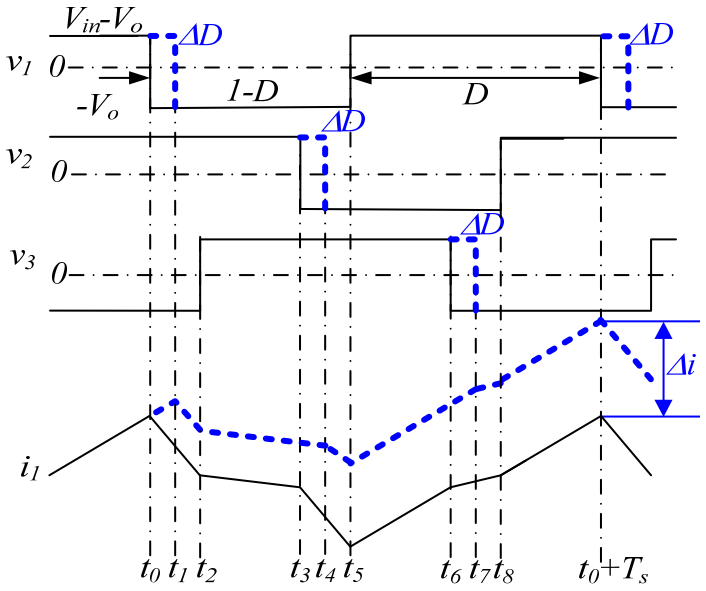

Figure A1.3 The transient inductor voltage and current waveforms for the three-phase asymmetric coupled-inductor buck converter

With a method similar to that used in the previous section, it can be derived that

$$L_{tr1} = \frac{L_1(L_1L_2 - M_{12}^2) - (L_1M_{12}^2 - 2M_{12}^2M_{13} + L_2M_{13}^2)}{L_1L_2 - L_1M_{12} + M_{12}M_{13} - L_2M_{13}} \tag{A1.5}$$

Similarly, L_{tr2} and L_{tr3} can be derived as

$$\begin{aligned} L_{tr2} &= \frac{L_1(L_1L_2 - M_{12}^2) - (L_1M_{12}^2 - 2M_{12}^2M_{13} + L_2M_{13}^2)}{L_1^2 - 2L_1M_{12} + 2M_{12}M_{13} - M_{13}^2} \\ L_{tr3} = L_{tr1} &= \frac{L_1(L_1L_2 - M_{12}^2) - (L_1M_{12}^2 - 2M_{12}^2M_{13} + L_2M_{13}^2)}{L_1L_2 - L_1M_{12} + M_{12}M_{13} - L_2M_{13}} \end{aligned} \tag{A1.6}$$

To characterize the asymmetry of the asymmetric coupled-inductor, several parameters are defined.

$$k = \frac{L_1}{L_2},\ \alpha_1 = \frac{M_{12}}{\sqrt{L_1L_2}},\ \alpha_2 = \frac{M_{13}}{\sqrt{L_1L_3}} = \frac{M_{13}}{L_1} \tag{A1.7}$$

k represents the difference in the phase self inductances. α_1 and α_2 are the coupled coefficients. The values k=1 and $\alpha_1 = \alpha_2$ represents the symmetric coupled-inductor.

With the equations (A1.2), (A1.6) and (A1.7), the FOM for Phase 1 when D<1/3 can be derived

$$\frac{L_{tr1}}{L_{ss1}} = \frac{1-\alpha_1^2+(\alpha_1\sqrt{k}-\alpha_1\alpha_2\sqrt{k}-\alpha_1^2+\alpha_2)\dfrac{D}{D'}}{1-\alpha_1\sqrt{k}+\alpha_1\alpha_2\sqrt{k}-\alpha_2} \tag{A1.8}$$

The relationship in the equation (A1.8) is plotted in Figure A1.4 when D=0.1, and k=1. The FOMs of the two-phase symmetric coupled-inductor and three-phase symmetric coupled-inductor are also shown.

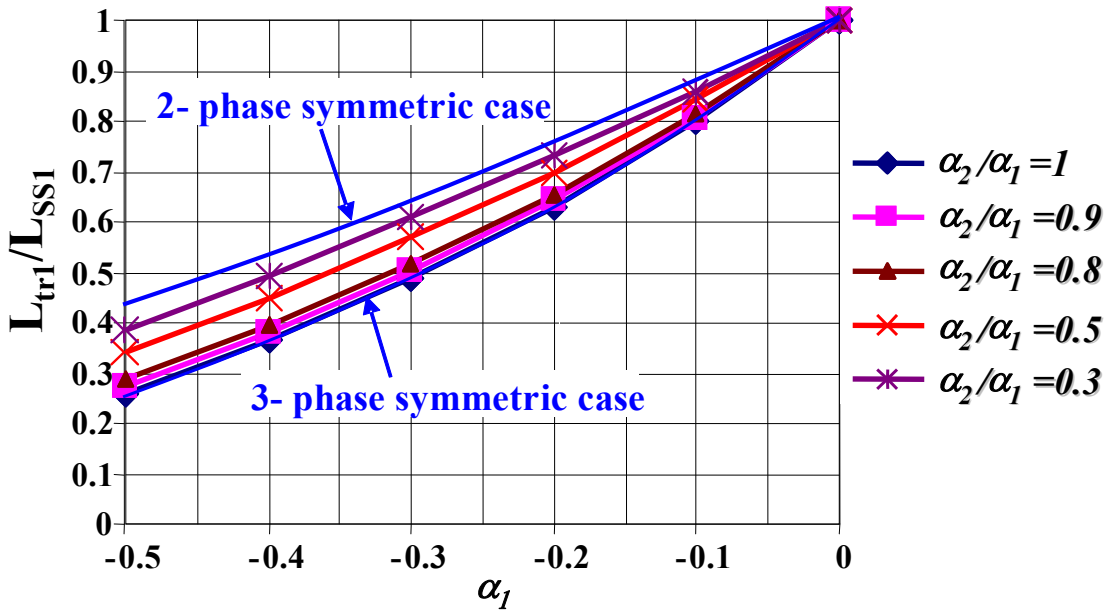

Figure A1.4 The effect of asymmetry on the L_{tr1}/L_{ss1} in the three-phase asymmetric coupled-inductor buck converter (D=0.1)

It can be seen from Figure A1.4 that when the FOM of the three-phase asymmetric coupled-inductor is larger than that of the three-phase symmetric coupled-inductor; i.e. the benefits of the three-phase asymmetric coupled-inductor are degraded. The more asymmetric the inductor is, the more benefits it will degrade. When the asymmetry is very strong, the performance of the three-phase coupled-inductor is similar to that of the two-phase symmetric coupled-inductor.

When $1/3 \leqslant D<2/3$, the steady-state inductance and transient inductances can also be derived.

$$L_{ss1} = L_{ss3} = \frac{L_1(L_1L_2 - M_{12}^2) - (L_1M_{12}^2 - 2M_{12}^2M_{13} + L_2M_{13}^2)}{(L_1L_2 - L_2M_{13} - L_1M_{12} + M_{12}M_{13}) + \frac{1}{3DD'}(L_1M_{12} + L_2M_{13} - M_{12}^2 - M_{12}M_{13})} \tag{A1.9}$$

$$L_{ss2} = \frac{L_1(L_1L_2 - M_{12}^2) - (L_1M_{12}^2 - 2M_{12}^2M_{13} + L_2M_{13}^2)}{(L_1^2 - M_{13}^2) - 2(L_1 - M_{13})M_{12}(1 - \frac{1}{3D}) + M_{12}(L_1 - M_{13})\frac{2}{3D'}} \tag{A1.10}$$

$$\begin{aligned} L_{tr2} &= \frac{L_1(L_1L_2 - M_{12}^2) - (L_1M_{12}^2 - 2M_{12}^2M_{13} + L_2M_{13}^2)}{L_1^2 - 2L_1M_{12} + 2M_{12}M_{13} - M_{13}^2} \\ L_{tr3} &= L_{tr1} = \frac{L_1(L_1L_2 - M_{12}^2) - (L_1M_{12}^2 - 2M_{12}^2M_{13} + L_2M_{13}^2)}{L_1L_2 - L_1M_{12} + M_{12}M_{13} - L_2M_{13}} \end{aligned} \tag{A1.11}$$

Therefore the FOM for Phase 1 when $1/3 \leqslant D<2/3$ can be derived.

$$\frac{L_{tr1}}{L_{ss1}} = \frac{(1 - \alpha_2 - \alpha_1\sqrt{k} + \alpha_1\alpha_2\sqrt{k}) + \frac{1}{3DD'}(\alpha_1\sqrt{k} + \alpha_2 - \alpha_1^2 - \alpha_1\alpha_2\sqrt{k})}{1 - \alpha_1\sqrt{k} + \alpha_1\alpha_2\sqrt{k} - \alpha_2} \tag{A1.12}$$

When $2/3 \leqslant D \leqslant 1$, the steady-state inductance and transient inductances are as follows.

$$L_{ss1} = L_{ss3} = \frac{L_1(L_1L_2 - M_{12}^2) - (L_1M_{12}^2 - 2M_{12}^2M_{13} + L_2M_{13}^2)}{L_1L_2 - M_{12}^2 + (L_1M_{12} - M_{12}M_{13} - M_{12}^2 + L_2M_{13})\frac{D'}{D}} \tag{A1.13}$$

$$L_{ss2} = \frac{L_1(L_1L_2 - M_{12}^2) - (L_1M_{12}^2 - 2M_{12}^2M_{13} + L_2M_{13}^2)}{(L_1^2 - M_{13}^2) + 2(L_1M_{12} - M_{12}M_{13})\frac{D'}{D}} \tag{A1.14}$$

$$\begin{aligned} L_{tr2} &= \frac{L_1(L_1L_2 - M_{12}^2) - (L_1M_{12}^2 - 2M_{12}^2M_{13} + L_2M_{13}^2)}{L_1^2 - 2L_1M_{12} + 2M_{12}M_{13} - M_{13}^2} \\ L_{tr3} &= L_{tr1} = \frac{L_1(L_1L_2 - M_{12}^2) - (L_1M_{12}^2 - 2M_{12}^2M_{13} + L_2M_{13}^2)}{L_1L_2 - L_1M_{12} + M_{12}M_{13} - L_2M_{13}} \end{aligned} \tag{A1.15}$$

Therefore the FOM for Phase 1 when $2/3 \leqslant D \leqslant 1$ is

$$\frac{L_{tr1}}{L_{ss1}} = \frac{1-\alpha_1^2+(\alpha_1\sqrt{k}-\alpha_1\alpha_2\sqrt{k}-\alpha_1^2+\alpha_2)\dfrac{D'}{D}}{1-\alpha_1\sqrt{k}+\alpha_1\alpha_2\sqrt{k}-\alpha_2} \tag{A1.16}$$

The relationships in the equations (A1.8), (A1.12) and (A1.16) are plotted in Figure A1.5 when α_1=-0.4, and k=1. The FOMs of the two-phase symmetric coupled-inductor and three-phase symmetric coupled-inductor are also shown. It can be seen that when the multiphase coupled inductor is more asymmetric, the FOM increases and the benefits from the more-phase coupling are degrading.

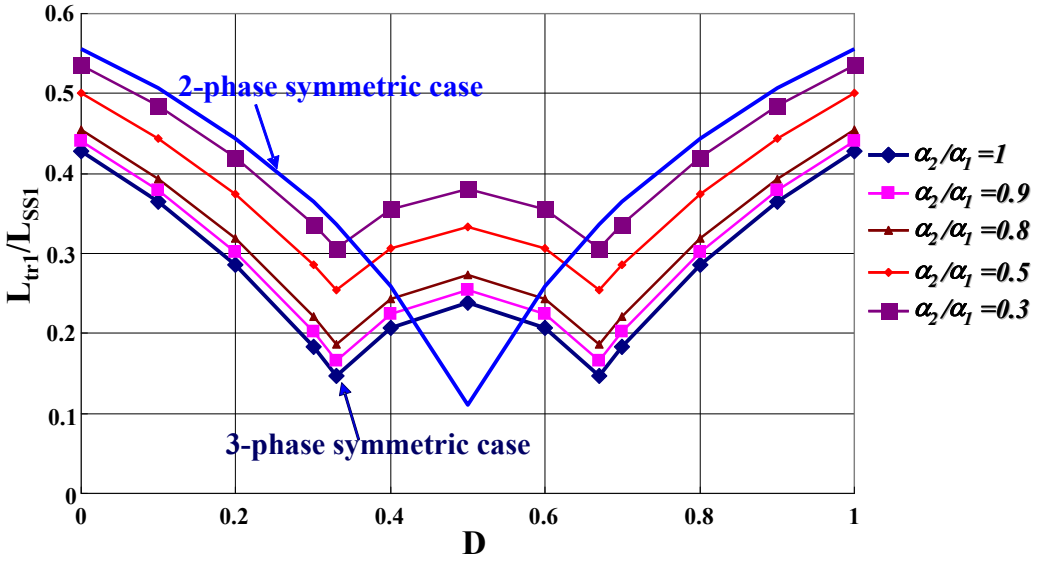

Figure A1.5 The effect of asymmetry on the L_{tr1}/L_{ss1} in the three-phase asymmetric coupled-inductor buck converter (α_1=-0.4)

Appendix 2. Reluctance Models of Alternative Coupled-inductor Structures

A2.1 Twisted-core Coupled-inductor

According to the equations (1.10), (1.11), (1.13) and (1.16), the steady-state inductance and the transient inductance of the coupled-inductor buck converter (D<0.5) are

$$L_{ss} = \frac{L_{self}^2 - (L_{self} - L_k)^2}{L_{self} - \frac{D}{D'} \cdot (L_{self} - L_k)} \tag{A2.1}$$

$$L_{tr} = L_{self} - M = L_k \tag{A2.2}$$

$$L_{self} = \frac{R_{mid\_airgap} + R_{core} + R_{airgap1}}{(R_{core} + R_{airgap1})(2R_{mid\_airgap} + R_{core} + R_{airgap1})} + \frac{1}{R_{air}} \tag{A2.3}$$

$$L_k = \frac{1}{2R_{mid\_airgap} + R_{core} + R_{airgap1}} + \frac{1}{R_{air}} \tag{A2.4}$$

The reluctances in L_{self} and L_k can be derived from the reluctance model of the twisted-core coupled-inductor. In the following, the reluctance model of the twisted-core coupled-inductor will be derived in detail.

Figure A2.1 shows the reluctance model of the twisted-core coupled-inductor. The loop of I, R_{core}, $R_{airgap1}$, R_{core} and $R_{airgap1}$ represents the main flux path, while the paths of R_{mid_airgap} and R_{air} represent the two main leakage flux paths.

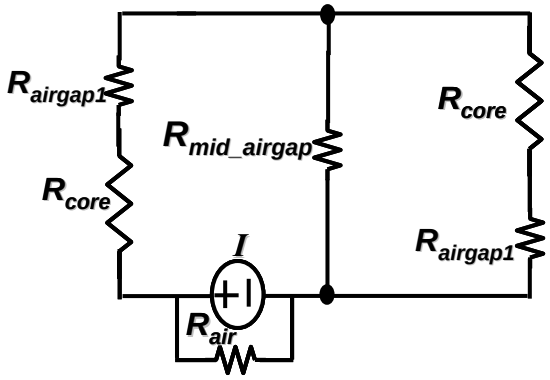

Figure A2.1 The simplified reluctance model of the twisted-core coupled-inductor structure

In the reluctance model, the two most difficult reluctances to be calculated are the middle-pole airgap reluctance R_{mid_airgap} and the air-around-the-winding reluctance R_{air}. In the following two subsections, the calculations of these two reluctances, R_{mid_airgap} and R_{air}, will be discussed. The dimensions of the twisted-core coupled-inductor are defined in Figure A2.2.

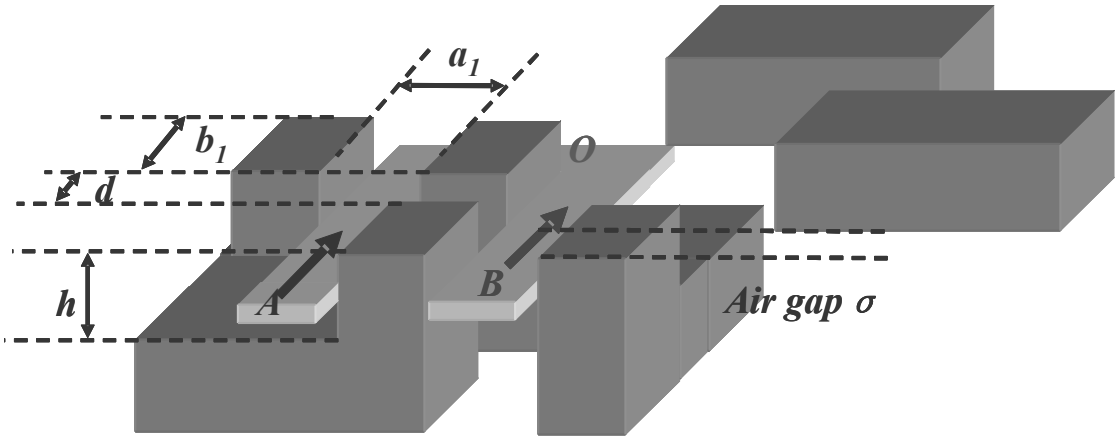

Figure A2.2 The dimension definition of the twisted-core coupled-inductor structure (a_1, b_1, h, d and σ)

A2.1.1 The Middle-pole Air Gap Reluctance R_{mid_airgap}

In Chapter 3, by extending C. Sullivan's space cutting concept, the middle-pole air gap reluctance can be divided into gap, face 1, face 2, face 3 and corner areas. (Figure A2.3). If the reluctances related to the face1 area, the face2 area and the face3 area are defined as R_{face1}, R_{face2} and R_{face3} respectively; and the reluctances related to the gap and corner areas are defined as R_{gap} and R_{corner}, then

$$R_{mid\_airgap} = R_{gap} // 0.25R_{face1} // 0.5R_{face2} // R_{face3} // R_{corner} \quad \text{(A2.5)}$$

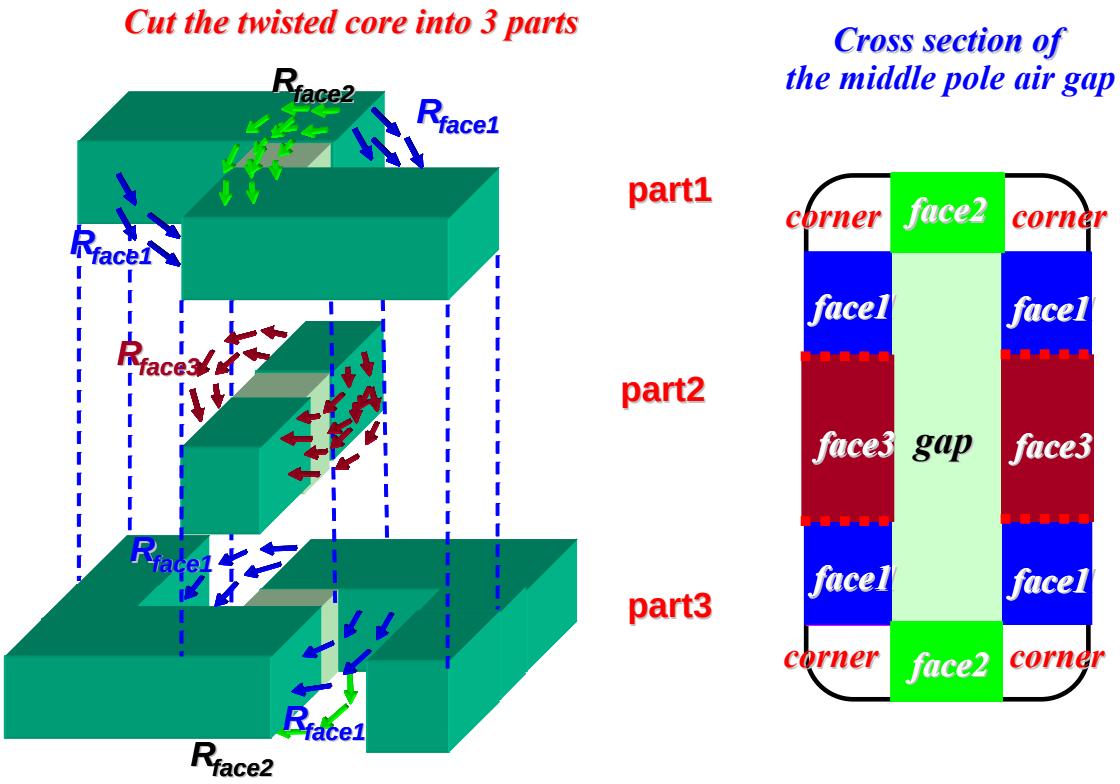

Figure A2.3 The three component parts of the twisted-core coupled-inductor after two horizontal cuts and the cross section view of the middle pole air gap after the two cuts

a. The calculation of the reluctance R_{gap}

R_{gap} is simple and can be calculated based on the simple one dimensional reluctance equation. The R_{gap} calculation equation is

$$R_{gap} = \frac{d}{\mu_o b_1 (2b_1 + h + \sigma)} \quad \text{(A2.6)}$$

b. The calculation of the reluctance R_{face1} calculation

Figure A3.4 The inductor voltage v1 and capacitor current ic waveforms of the two-phase coupled-inductor buck converter in the DCM2 mode (a) The two-phase coupled buck converter (b) the shows the face1 fringing effect flux area. (For symmetry, only one face1 fringing effect flux area and the half of the part1 are shown.) If we look at half of the part1 magnetic core from top to bottom, we can get the cross section view shown at the bottom of Figure A3.4 The

inductor voltage v1 and capacitor current ic waveforms of the two-phase coupled-inductor buck converter in the DCM2 mode (a) The two-phase coupled buck converter (b) the . It is clear that the face1 fringing effect flux is the fringing flux between two perpendicular planes.

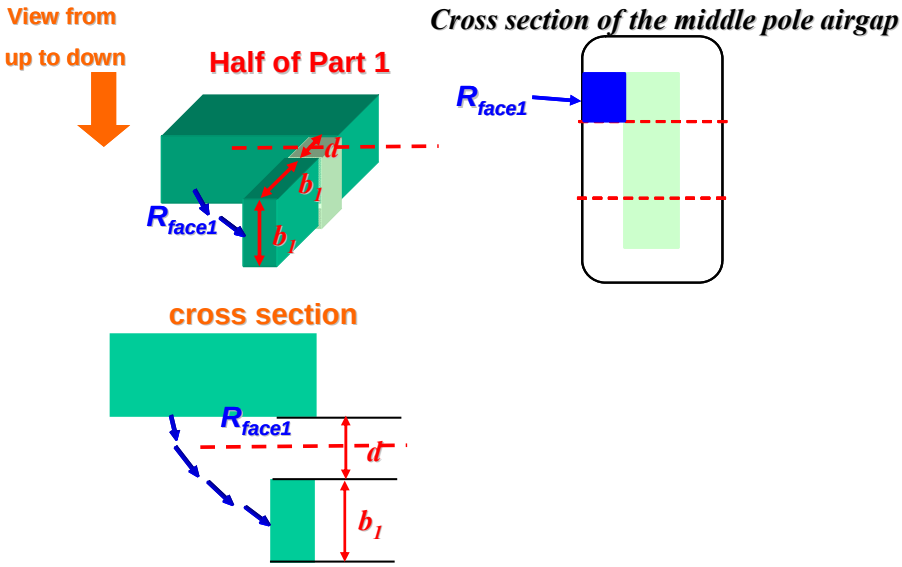

Figure A2.4 The face 1 fringing effect flux area between two perpendicular planes and the top view of the face 1 fringing effect flux area

The airgap here is the middle-pole airgap and is quite large. Calculating the fringing flux between two perpendicular planes when the airgap is larger is very difficult. In [55](Figure A2.5), it is found that R_{face1} fulfills the following complex-variable equation after using the Schwarz–Christoffel transformation.

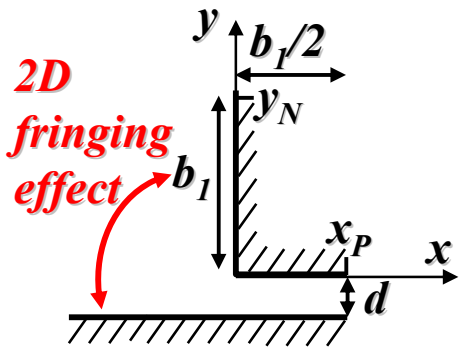

Figure A2.5 The 2D finging effect flux between two perpendicular planes

$$R_{face1} = \frac{1}{b_1(\frac{\mu_0(\ln(z_{1P}) + \ln(z_{1N}))}{\pi} - \frac{\mu_0 b_1}{2d})} \tag{A2.7}$$

where Z_{lP} and Z_{lN} are the Schwarz–Christoffel transformations of the points x_P and y_N and can be found through the following complex equations respectively

$$z_{1P} \approx e^{[\frac{\pi b_1}{2d} + 2(1-\ln 2)]} \tag{A2.8}$$

$$ib_1 = \frac{d}{\pi}[2\ln(1+\sqrt{1-z_{1N}}) - \ln(z_{1N}) - 2\sqrt{1-z_{1N}}] \tag{A2.9}$$

From the equation (A3.9), it can be easily got that

$$ib1 = \frac{d}{\pi}[\ln(\frac{1+\sqrt{1-z_{1N}}}{1-\sqrt{1-z_{1N}}}) - 2\sqrt{1-z_{1N}}] \tag{A2.10}$$

It is equivalent to

$$ib1 = \frac{d}{\pi}[\ln(\frac{1-i\sqrt{z_{1N}-1}}{1+i\sqrt{z_{1N}-1}}) + 2i\sqrt{z_{1N}-1}] \tag{A2.11}$$

Changing the form of the ln(·) function,

$$ib1 = -\frac{d}{\pi}\{i[\pi - 2\sin^{-1}(\frac{\sqrt{z_{1N}-1}}{\sqrt{z_{1N}}})] - 2i\sqrt{z_{1N}-1}\} \tag{A2.12}$$

Considering the basic trigonometric equation

$$\sin(2\alpha) = 2\sin\alpha\cos\alpha \tag{A2.13}$$

The equation (A2.12) can be expressed as

$$ib1 = -i\frac{d}{\pi}[\pi - \sin^{-1}(2\sqrt{\frac{1}{z_{1N}} - \frac{1}{z_{1N}^2}}) - 2\sqrt{z_{1N}-1}] \tag{A2.14}$$

Assume

$$\sin^{-1}(2\sqrt{\frac{1}{z_{1N}} - \frac{1}{z_{1N}^2}}) \approx 2\sqrt{\frac{1}{z_{1N}} - \frac{1}{z_{1N}^2}} \tag{A2.15}$$

then substituting the equation (A2.15) into the equation (A2.14) and rearranging the terms,

$$\sqrt{z_{1N}-1}+\frac{2\sqrt{z_{1N}-1}}{z_{1N}}=\frac{\pi}{2}(1+\frac{b1}{d}) \tag{A2.16}$$

Therefore,

$$Z_{1N}\approx[\frac{\frac{\pi}{2}(1+\frac{b_1}{d})+\sqrt{\frac{\pi^2}{4}(1+\frac{b_1}{d})^2-2}}{2}]^2+1 \tag{A2.17}$$

This is an approximate solution of the equation (A2.9)

Substituting the equations (A2.8) and (A2.9) into the equation (A2.7),

$$R_{face1}\approx\frac{\pi}{b_1\mu_o[0.614+\ln(M^2(\frac{b_1}{d})+1)]} \tag{A2.18}$$

where the function $M(\cdot)$ can be expressed as

$$M(\frac{b_1}{d})=\frac{\frac{\pi}{2}(1+\frac{b_1}{d})+\sqrt{\frac{\pi^2}{4}(1+\frac{b_1}{d})^2-2}}{2}) \tag{A2.19}$$

c. The calculation of the reluctance R_{face2}

Figure A2.6 shows the face2 fringing effect flux area. For symmetry, only one face2 fringing effect flux area is shown. If we look at the magnetic core from left to right, we can get the cross section view that appears at the bottom of Figure A2.6.

The face2 finging effect is the plane-to-plane finging effect (Figure A2.7). Accoding to the mirror theorem, the face2 finging flux reluctance is twice of the finging flux reluctance between two perpendicular planes with the perpendicular plane length to be b_1 and the distance between the two perpendicular planes to be d/2. Therefore, according to the equation (A2.18), the R_{face2} can be calculated to be

$$R_{face2}\approx\frac{2\pi}{b_1\mu_o(0.614+\ln(M^2(\frac{2b_1}{d})+1))} \tag{A2.20}$$

where function $M(\cdot)$ can be expressed as

$$M(\frac{2b_1}{d})=\frac{\frac{\pi}{2}(1+\frac{2b_1}{d})+\sqrt{\frac{\pi^2}{4}(1+\frac{2b_1}{d})^2-2}}{2}) \tag{A2.21}$$

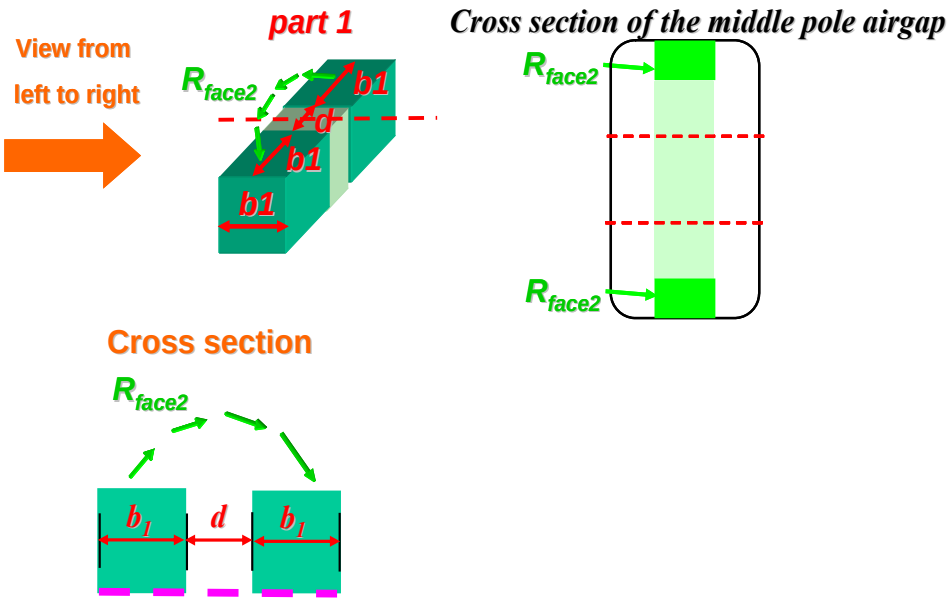

Figure A2.6 The face 2 fringing effect flux area between two perpendicular planes and the top view of the face 2 fringing effect flux area

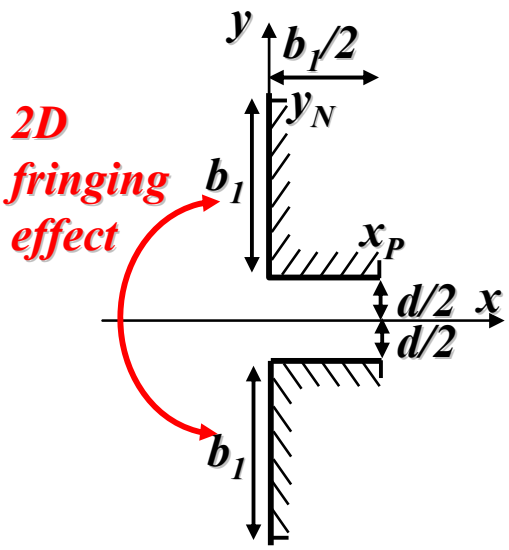

Figure A2.7 The 2D fringing effect flux between two parallel planes

d. The calculation of the reluctance R_{face3}

Figure A2.8 shows the face3 fringing effect flux area. If we look at the magnetic core from top to bottom, we can get the cross section view that appears at the bottom of Figure A2.8.

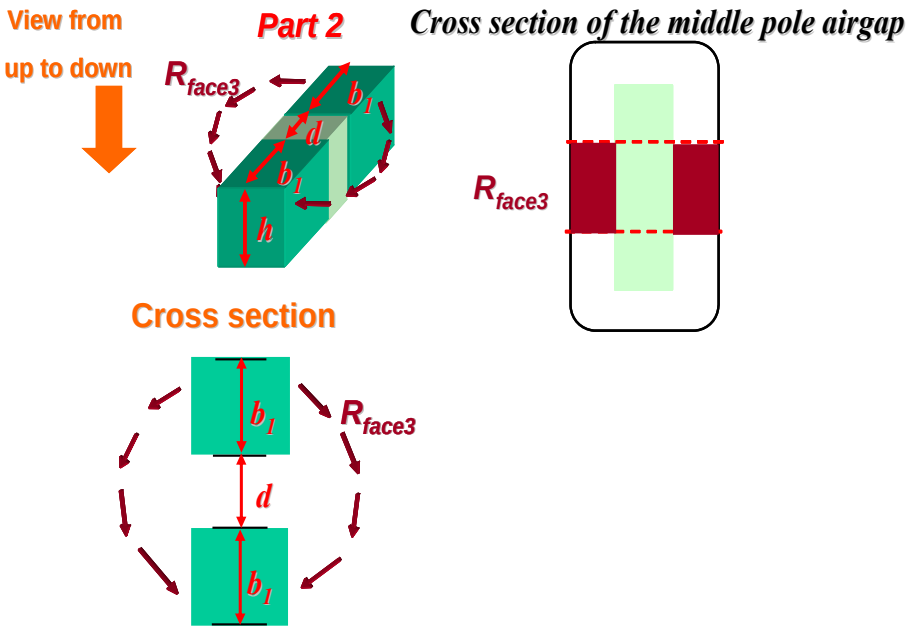

Figure A2.8 The face 3 fringing effect flux area between two perpendicular planes and the top view of the face 3 fringing effect flux area

According to the mirror theorem, the face3 fringing effect flux related reluctance, R_{face3}, is half of the finging flux reluctance between two parallel planes with the distance between the two perpendicular planes to be d and each parallel plane length to be b_1. According to the equation (A3.20), R_{face3} can be calculated to be

$$R_{face3} = \frac{\pi}{h\mu_o[0.614 + \ln(M^2(\frac{2b_1}{d}) + 1)]} \tag{A2.22}$$

where function $M(\cdot)$ can be expressed as

$$M(\frac{2b_1}{d}) = \frac{\frac{\pi}{2}(1+\frac{2b_1}{d}) + \sqrt{\frac{\pi^2}{4}(1+\frac{2b_1}{d})^2 - 2}}{2}) \tag{A2.23}$$

e. The calculation of the reluctance R_{corner}

We have derived the reluctance expressions of the face fringing effect fluxes, and we will derive the reluctance expression of the corner fringing effect flux. Figure A2.9 shows the corner fringing effect flux area. Calculating the corner fringing effect related reluctance, R_{corner}, is also not easy. Fortunately, [56] gives an approximate calculating method for R_{corner}.

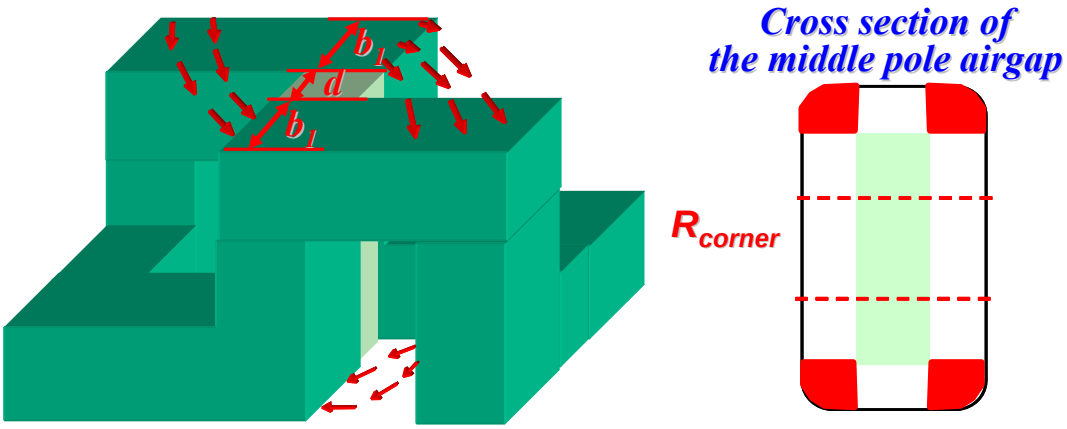

Figure A2.9 The corner fringing effect flux area in the twisted-core coupled-inductor and in the cross section of the middle pole air gap

$$R_{corner} = \frac{1}{8}(R_{SQ} // R_{QSS}) \tag{A2.24}$$

where

$$R_{SQ} = \frac{1}{0.077\mu_o d} \tag{A2.25}$$

$$R_{QSS} = \frac{4}{\mu_o b_1} \tag{A2.26}$$

A2.1.2 The Air-around-the-winding Reluctance R_{air}

Figure A2.10 shows the air-around-the-winding flux. It can be seen that the fringing flux can be looked as the fringing flux between two perpendicular planes. If the reluctance related to the air-around-the-winding flux is called R_{air},

$$R_{air} = \frac{1}{\mu_o \frac{b_1}{\pi}\{0.614 + \ln\{\frac{[\frac{\pi}{2}(1+\frac{b_1}{a_1}) + \sqrt{\frac{\pi^2}{4}(1+\frac{b_1}{a_1})^2 - 2}]^2}{4} + 1\}\}} \tag{A2.27}$$

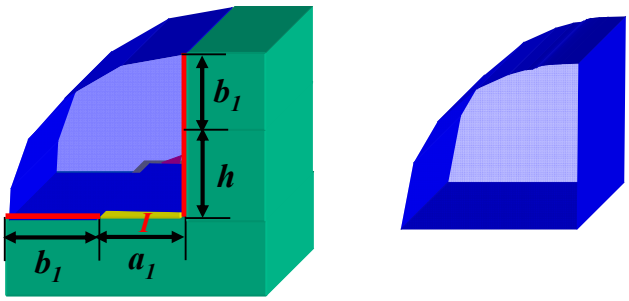

Figure A2.10 The air-around-the-winding fringing flux region in the twisted core coupled inductor and the air-around-the-winding fringing flux area

A2.1.3 The Core Reluctance R_{core} and The Airgap1 Reluctance $R_{airgap1}$

a. The calculation of the core reluctance R_{core}

For calculating R_{core}, we just use the one dimensional reluctance model. Here is the calculation equation

$$R_{core} = 2R_v + R_h \tag{A2.28}$$

where

$$R_v = \frac{1}{\mu_o \mu_r b_1}\left(\frac{h}{b_1} + \frac{\pi}{2}\right) \tag{A2.29}$$

$$R_h = \frac{1}{\mu_o \mu_r b_1}\left(\frac{d + 2a_1}{b_1} + \frac{\pi}{4}\right) \tag{A2.30}$$

b. The calculation of the airgap1 reluctance $R_{airgap1}$

Since the air gap reluctance model considering the 3D fringing effects has been discussed in the calculation of the middle-pole air gap reluctance R_{mid_airgap}, the calculation of the airgap1 reluctance can be done in the same way.

$$R_{airgap1} = R_{1gap} // R_{1face} // R_{1corner} \tag{A2.31}$$

where

$$R_{1gap} = \frac{2\sigma}{\mu_o b_1^{\,2}} \tag{A2.32}$$

$$R_{1\,face} = 2(R_{1\,face1} // 0.5R_{1\,face21} // R_{1\,face22}) \tag{A2.33}$$

$$R_{1\,face1} = \frac{\pi}{b_1\mu_o[0.614 + \ln(M^2(\frac{h+b_1}{\sigma}) + 1)]} \tag{A2.34}$$

$$R_{1\,face21} = \frac{2\pi}{b_1\mu_o(0.614 + \ln(M^2(\frac{2b_1}{\sigma}) + 1))} \tag{A2.35}$$

$$R_{1\,face22} = \frac{2\pi}{b_1\mu_o(0.614 + \ln(M^2(\frac{2h}{\sigma}) + 1))} \tag{A2.36}$$

$$R_{1corner} = \frac{1}{3}(R_{1SQ} // R_{1QSS}) \tag{A2.37}$$

$$R_{1SQ} = \frac{1}{0.077\mu_o\sigma} \tag{A2.38}$$

$$R_{1QSS} = \frac{4}{\mu_o\sigma} \tag{A2.39}$$

The detail reluctance model of the twisted-core coupled inductor is shown in Figure A2.11. The simple reluctance model without considering the fringing effect can be got from the above reluctance model by setting the R_{face}, R_{corner}, R_{air}, R_{1face1} and $R_{1corner1}$ to be infinity.

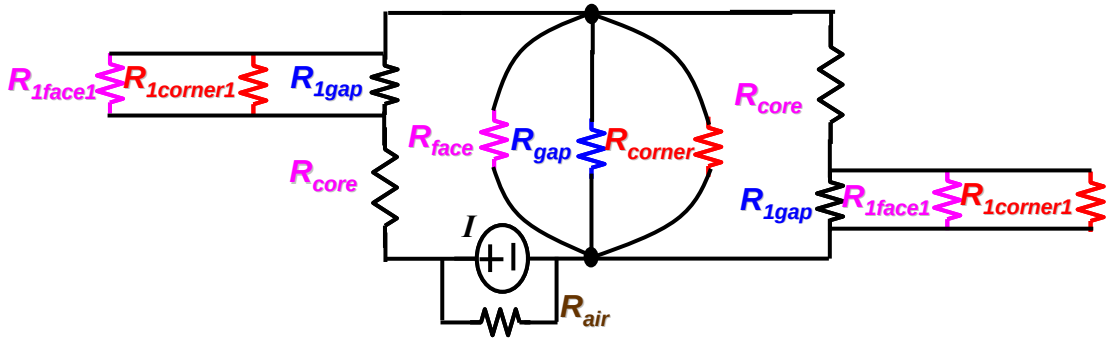

Figure A2.11 The detail reluctance model of the twisted-core coupled-inductor

The derived reluctance model can be used to identify the minimum inductor total loss point of the low-profile twisted-core coupled-inductor. Figure A2.12 shows the low-profile twisted-core coupled-inductor and Figure A2.13 shows the block diagram to achieve the minimum-loss low-profile twisted-core coupled-inductor.

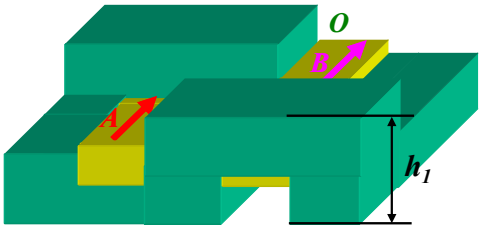

Figure A2.12 The low profile twisted-core coupled-inductor

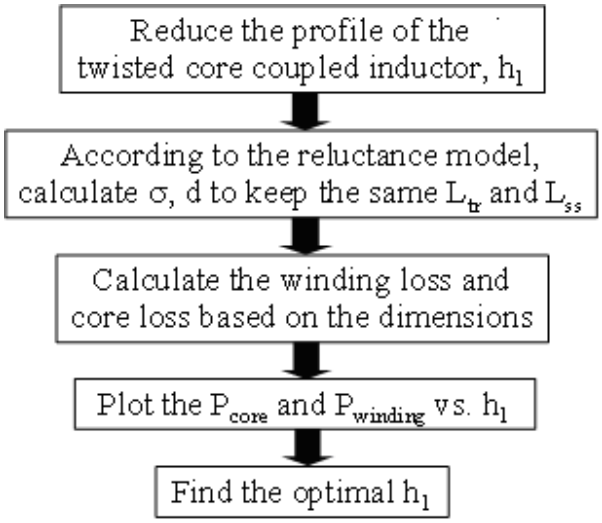

Figure A2.13 The block diagram of finding the minimum-loss low-profile twisted-core coupled-inductor

Figure A2.14 shows the $P_{winding}$, and P_{core} vs. h_1 for the I_{phase}=30A case. The minimum-loss low-profile twisted point for the I_{phase}=30A case is shown in Figure A2.15. The minimum-loss low-profile twisted point for the I_{phase}=20A case is also shown in the Figure A2.15. It can be seem that when the phase current level is higher, the minimum-loss low-profile twisted-core coupled-inductor is more twisted. This can be explained in this way. When the current level is higher, the winding loss is more important in the inductor total loss and the core loss is less important in the inductor total loss. Therefore it is better is to minimize the winding loss and to make the winding more straight. Accordingly, the core is more twisted.

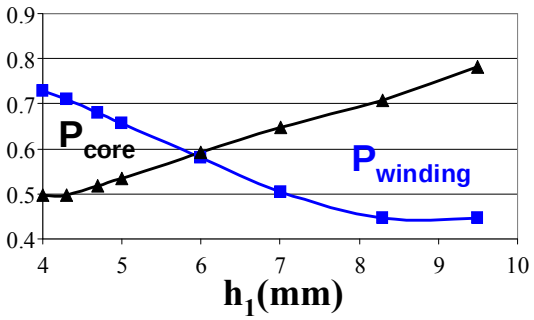

Figure A2.14 The $P_{winding}$, P_{core} vs. h_1 @I_{phase}=30A

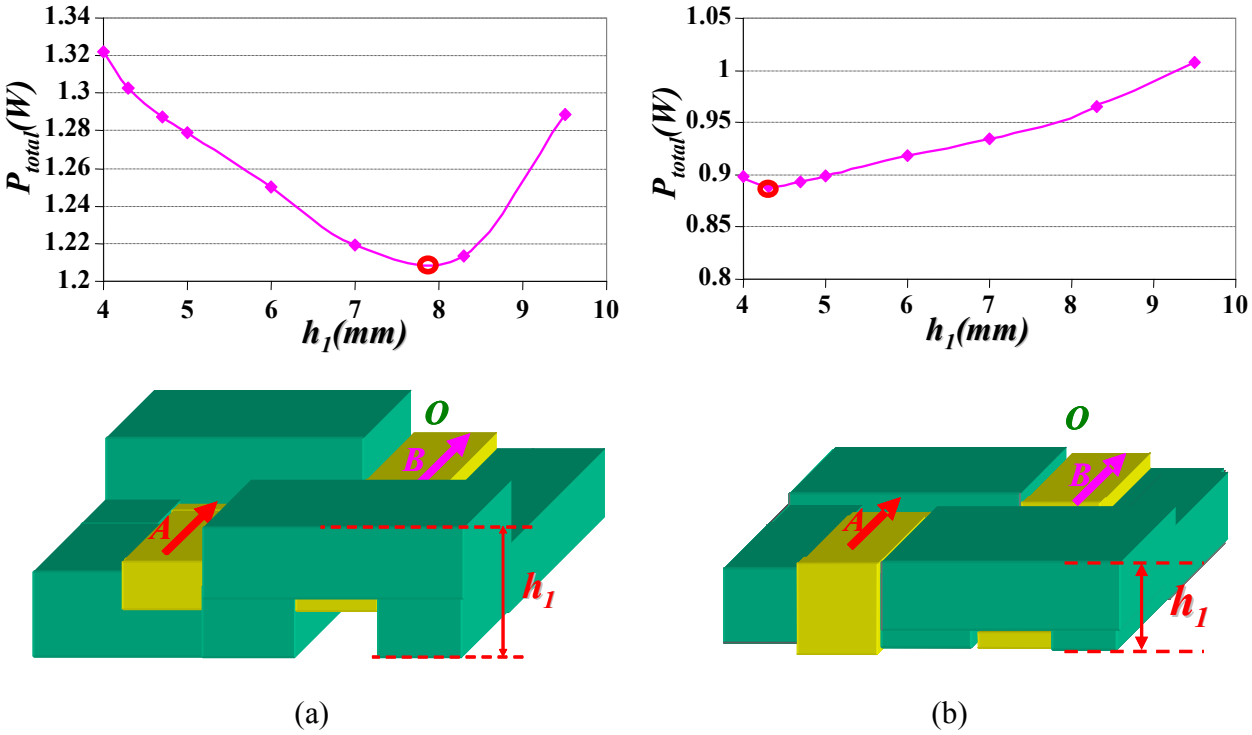

Figure A2.15 The minimum-loss low-profile twisted-core coupled-inductors (a) I_{phase}=30A (b) I_{phase}=20A

A2.2 Low Profile Twisted-core Coupled-inductor

The model of the low profile twisted-core coupled-inductor is a simplified case of the model of the twisted-core coupled-inductor. Therefore, the equations for the low profile twisted-core coupled-inductors can be listed in the following.

Figure A2.16 shows the dimension definition of the low profile twisted-core coupled-inductor. Figure A2.17 shows the reluctance model of the low profile twisted-core coupled-

inductor. The simple reluctance model without considering the fringing effect can be got from this reluctance model by setting the R_{face}, R_{corner}, R_{air}, R_{1face1} and $R_{1corner1}$ to be infinity.

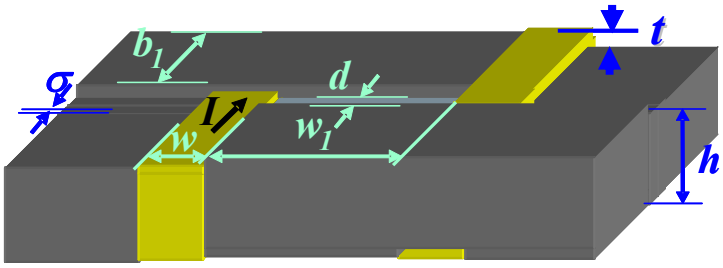

Figure A2.16 The dimension definition of the low profile twisted-core coupled-inductor structure

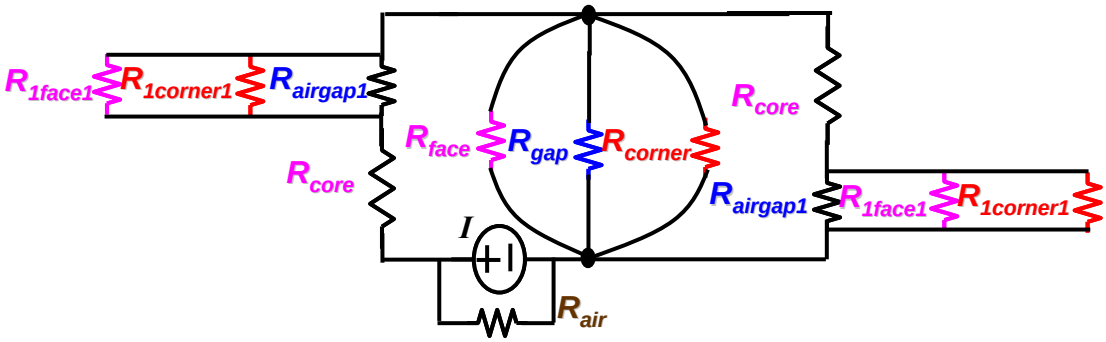

Figure A2.17 The detail new reluctance model of the twisted-core coupled-inductor considering the strong 3D fringing effect

The steady-state inductance and the transient inductance can be expressed as

$$L_{ss} = \frac{2L_{self}L_k - L_k^2}{L_{self} - \frac{D}{D'}(L_{self} - L_k)}, \quad L_{tr} = L_k \tag{A2.40}$$

and

$$L_{self} = \frac{R_{mid\_airgap} + R_{core} + R_{airgap1}}{(R_{core} + R_{airgap1})(2R_{mid\_airgap} + R_{core} + R_{airgap1})} + \frac{1}{R_{air}} \tag{A2.41}$$

$$L_k = L_{k\_midpole} + L_{k\_air} = \frac{1}{2R_{mid\_airgap} + R_{core} + R_{airgap1}} + \frac{1}{R_{air}} \tag{A2.42}$$

a. The middle-pole air gap reluctance R_{mid_airgap}

The middle-pole airgap reluctance can be divided into 3 parts: R_{gap}, R_{face} and R_{corner} (Figure A2.18). R_{gap} is calculated with the one dimensional reluctance model (Figure A3.15); R_{face} is calculated by the method proposed in the precious section (Figure A3.15); R_{corner} is calculated by the method proposed in [56].

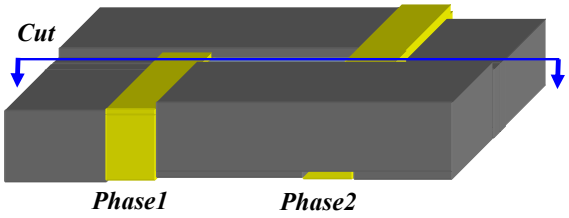

(a)

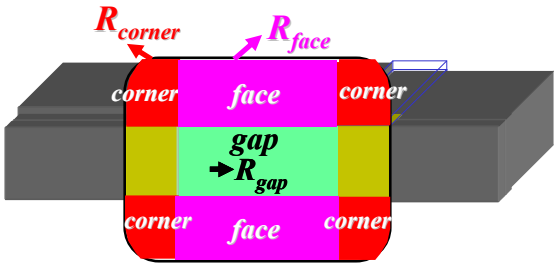

(b)

Figure A2.18 The separation of the middle-pole airgap fringing fluxes (a) Cut at the middle of the middle-pole air gap (b) The gap, face and corner flux areas in the cutting cross section of the middle-pole air gap

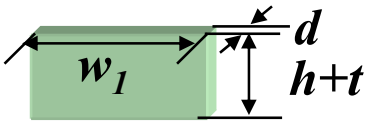

(a)

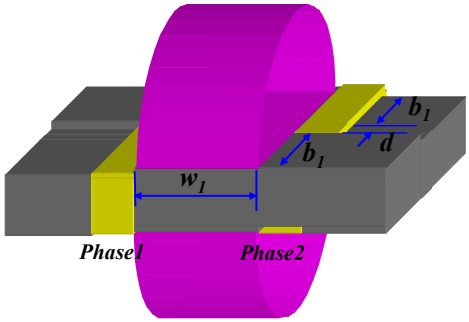

(b)

Figure A2.19 The gap magnetic flux area and face fringing flux area of the low profile twisted-core coupled-inductor (a) The gap magnetic flux area (b) the face fringing flux area

$$R_{mid\_airgap} = R_{gap} // R_{face} // R_{corner} \tag{A2.43}$$

$$R_{gap} = \frac{d}{\mu_o w_1 (h+t)} \tag{A2.44}$$

$$R_{face} = \frac{\pi}{w_1 \mu_o (0.614 + \ln(M^2 (\frac{2b_1}{d}) + 1))}, \tag{A2.45}$$

$$R_{corner} = \frac{1}{8}(R_{SQ} // R_{QSS}), \tag{A2.46}$$

$$R_{SQ} = \frac{1}{0.077 \mu_o d}, \tag{A2.47}$$

$$R_{QSS} = \frac{4}{\mu_o b_1}, \tag{A2.48}$$

b. The air-around-the-winding reluctance R_{air}

The around-the-winding reluctance R_{air} can be divided into three parts: R_{top}, R_{front} and R_{bottom} (Figure A2.20(a)). Figure A2.20(b) shows the flux area of R_{top}. R_{top} is the fringing effect reluctance between two parallel planes. Using the method proposed in the previous section, we can calculate R_{top}. Calculations of R_{front} and R_{bottom} are similar to R_{top}.

$$R_{air} = R_{top} // R_{front} // R_{bottom} \tag{A2.49}$$

$$R_{top} = \frac{2}{\mu_o \frac{b_1}{\pi} \{0.614 + \ln\{\frac{[\frac{\pi}{2}(1+\frac{2b_1}{w}) + \sqrt{\frac{\pi^2}{4}(1+\frac{2b_1}{w})^2 - 2}]^2}{4} + 1\}\}}. \tag{A2.50}$$

$$R_{front} = \frac{2}{\mu_o \frac{h}{\pi} \{0.614 + \ln\{\frac{[\frac{\pi}{2}(1+\frac{2b_1}{w}) + \sqrt{\frac{\pi^2}{4}(1+\frac{2b_1}{w})^2 - 2}]^2}{4} + 1\}\}} \tag{A2.51}$$

$$R_{bottom} = R_{top} \tag{A2.52}$$

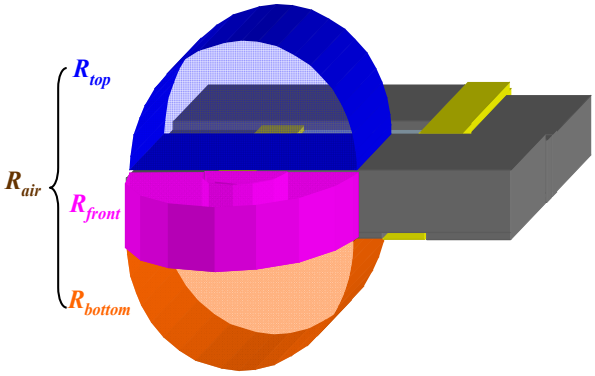

(a) R_{air} reluctance

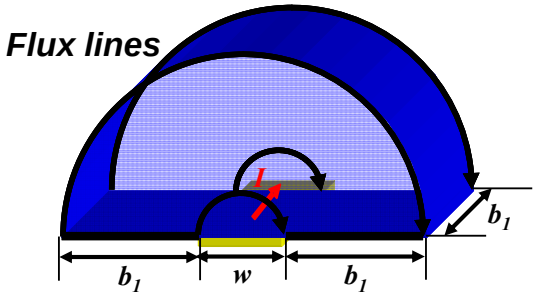

(b) R_{top} reluctance

Figure A2.20 The air-around-the-winding fringing flux area (a) the top, front and bottom fringing flux areas (b) the top fringing flux area with the dimensions marked

c. The core reluctance R_{core} and the airgap1 reluctance $R_{airgap1}$

The R_{core} and $R_{airgap1}$ are shown in Figure A2.21. They can be modeled with the one dimensional reluctance model.

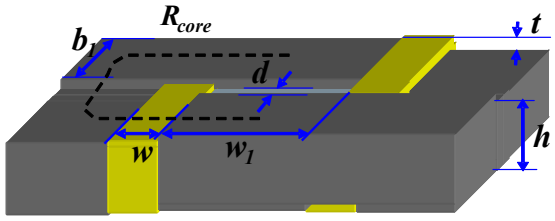

(a) R_{core}

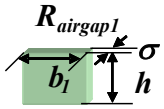

(b) $R_{airgap1}$

Figure A2.21 The magnetic core reluctance R_{core} and the air gap 1 reluctance $R_{airgap1}$ (a) The magnetic core reluctance (b) the air gap1 reluctance

$$R_{core} = \frac{1}{\mu_o \mu_r h}\left(\frac{d + 2w + w_1}{b_1} + \frac{\pi}{2}\right) \tag{A2.53}$$

$$R_{airgap1} = \frac{\sigma}{\mu_o b_1 h} \tag{A2.54}$$

A2.3 Three-phase ET-core Coupled-inductor

The reluctance model of the three-phase ET-core coupled-inductor is built in the similar method as that of the low profile twisted-core coupled-inductor. The equations for the three-phase ET-core coupled-inductor are listed in the following.

Figure A2.22 shows the three-phase ET-core coupled-inductor dimensions. Figure A2.23 shows the reluctance model of three-phase ET-core coupled-inductor.

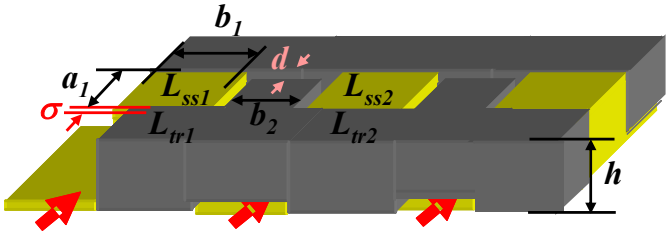

Figure A2.22 The dimension definition of the three-phase ET-core coupled-inductor

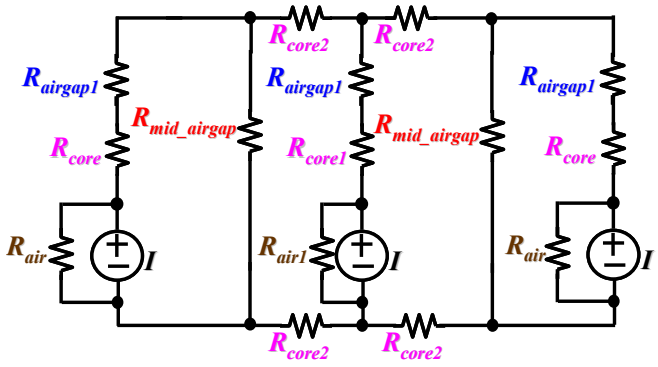

Figure A2.23 The reluctance model of the three-phase ET-core coupled-inductor considering the strong 3D fringing flux effect

$$L_{self1} = \frac{1}{R_{self1}} + \frac{1}{R_{air}} \tag{A2.55}$$

$$L_{self\,2} = \frac{2}{R_{half} + 2R_1} + \frac{1}{R_{air1}} \tag{A2.56}$$

$$L_{k1} = \frac{1}{R_{self\,1}} \cdot \frac{1}{R_{more} + R_{mid\_airgap}} \cdot \{R_{more} + R_{mid\_airgap} \cdot \frac{R_1}{R_{half} + R_1} \cdot \frac{R}{R + R_{mid\_airgap}}\} + \frac{1}{R_{air}} \tag{A2.57}$$

$$L_{k2} = \frac{2}{R_{half} + 2R_1} \cdot \frac{R}{R + R_{mid\_airgap}} + \frac{1}{R_{air1}} \tag{A2.58}$$

where

$$R_{self\,1} = R_{more} \,//\, R_{mid\_airgap} + R \tag{A2.59}$$

$$R_{more} = R_{half} \,//\, R_1 + 2R_{core2} \tag{A2.60}$$

$$R_{half} = R \,//\, R_{mid\_airgap} + 2R_{core2} \tag{A2.61}$$

$$R = R_{core} + R_{airgap1} \tag{A2.62}$$

$$R_1 = R_{core1} + R_{airgap1} \tag{A2.63}$$

a. The core reluctances R_{core}, R_{core1}, R_{core2} and the airgap1 reluctance $R_{airgap1}$

The R_{core} and $R_{airgap1}$ reluctances are shown in Figure A2.24.

$$R_{airgap1} = \frac{\sigma}{\mu_o h \cdot b_1} \tag{A2.64}$$

$$R_{core} = \frac{b_2 + a_1}{\mu_o \mu_r h \cdot b_1} + \frac{\pi}{2\mu_o \mu_r h} \tag{A2.65}$$

(a) **(b)**

Figure A2.24 The air gap 1 reluctance $R_{airgap1}$ and the magnetic core reluctance R_{core} (a) The air gap 1 reluctance $R_{airgap1}$ (b) the magnetic core reluctance R_{core}

The R_{core1} and R_{core2} reluctances are shown in Figure A2.25.

$$R_{core1} = \frac{a_1 + b_1}{\mu_o \mu_r h \cdot b_1} \tag{A2.66}$$

$$R_{core2} = \frac{b_1 + b_2}{2\mu_o \mu_r h \cdot b_1} \tag{A2.67}$$

(a) **(b)**

Figure A2.25 The magnetic core 1 reluctance R_{core1} and the magnetic core 2 reluctance R_{core2} (a) The magnetic core 1 reluctance R_{core1} (b) the magnetic core 2 reluctance R_{core2}

b. The middle-pole air gap reluctance R_{mid_airgap}

The R_{mid_airgap} is shown in Figure A3.22. It is similar to the middle-pole air gap reluctance in the two-phase low profile twisted-core coupled-inductor. Following the same method, we can get the equations

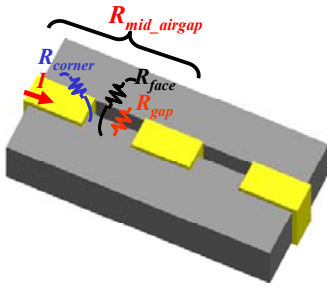

Figure A2.26 The middle-pole airgap reluctance R_{mid_airgap} and its components (R_{gap}, R_{face} and R_{corner}) with the space cutting method in the three-phase ET core coupled-inductor

$$R_{mid\_airgap} = R_{gap} // R_{face} // R_{corner} \tag{A2.68}$$

$$R_{gap} = \frac{d}{\mu_o b_2 h} + \frac{a_1 - d}{\mu_o \mu_r b_2 h} \tag{A2.69}$$

$$R_{face} = \frac{\pi}{b_2 \mu_o [0.614 + \ln(M^2 (\frac{2b_1}{d}) + 1)]} \tag{A2.70}$$

$$R_{corner} = \frac{R_{SQ} // R_{QSS}}{8} \tag{A2.71}$$

$$R_{SQ} = \frac{1}{0.077 \mu_o d} \tag{A2.72}$$

$$R_{QSS} = \frac{4}{\mu_o b_1} \tag{A2.73}$$

c. The air-around-the-winding reluctance R_{air}

The R_{air} and R_{air1} are shown in Figure A2.27. Following the same method used in the two-phase low profile twisted-core coupled-inductor, we can get

$$R_{air} = R_{top} // R_{front} // R_{bottom} \tag{A2.74}$$

$$R_{air1} = R_{top} // R_{bottom} \tag{A2.75}$$

$$R_{top} = R_{bottom} = \frac{2}{\mu_o \frac{b_1}{\pi} \{0.614 + \ln\{\frac{[\frac{\pi}{2}(1+\frac{2b_1}{a_1}) + \sqrt{\frac{\pi^2}{4}(1+\frac{2b_1}{a_1})^2 - 2}]^2}{4} + 1\}\}} \tag{A2.76}$$

$$R_{front} = \frac{2}{\mu_o \frac{h}{\pi} \{0.614 + \ln\{\frac{[\frac{\pi}{2}(1+\frac{2b_1}{a_1}) + \sqrt{\frac{\pi^2}{4}(1+\frac{2b_1}{a_1})^2 - 2}]^2}{4} + 1\}\}} \tag{A2.77}$$

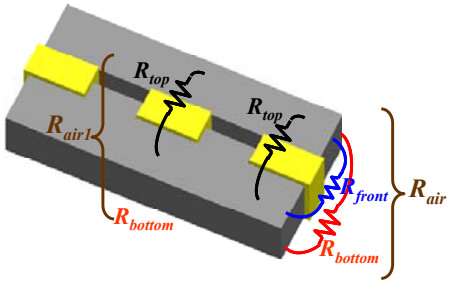

Figure A2.27 The air-around-the-winding fringing flux reluctances for the side pole and the middle pole in the three-phase ET core coupled-inductor: R_{air} and R_{air1}

A2.4 Z-core Coupled-inductor

The reluctance model of the Z-core coupled-inductor can also be built based on the extended space cutting method. Figure A2.28 shows the Z-core coupled-inductor dimensions. Figure A2.29 shows the reluctance model of the Z-core coupled-inductor. The equations for the reluctance model are shown in the following.

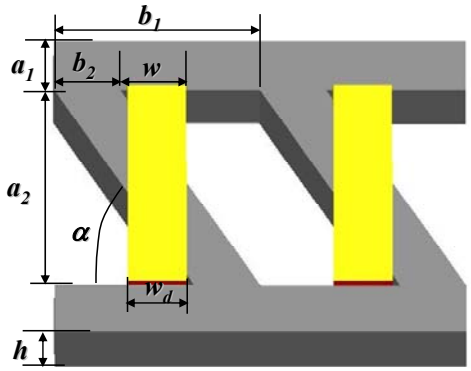

Figure A2.28 The dimension definition of the Z-core coupled-inductor

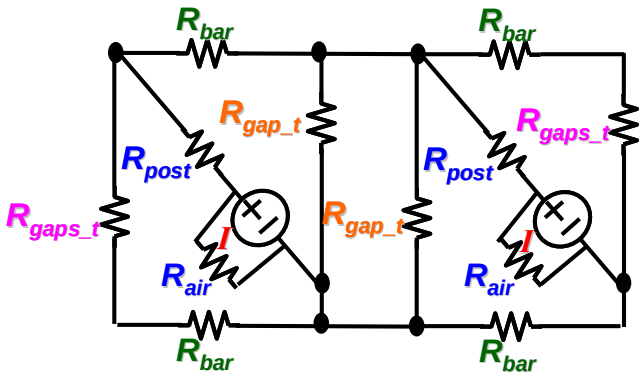

Figure A2.29 The reluctance model of the Z-core coupled-inductor considering the strong 3D fringing effect fluxes

$$L_{self} = \frac{1}{R_{post} + (R_{gaps\_t} + R_{bar2}) // R_{more}} + \frac{1}{R_{air}} \tag{A2.78}$$

$$L_k = \frac{1}{R_{post} + (R_{gaps\_t} + R_{bar2}) // R_{more}} \cdot [1 - \frac{R_{gaps\_t} + R_{bar2}}{R_{gaps\_t} + R_{bar2} + R_{more}} \cdot \frac{0.5R_{gap\_t}}{0.5R_{gap\_t} + R_{bar1} + R_{post} // (R_{gaps\_t} + R_{bar2})} \cdot \frac{R_{gaps\_t} + R_{bar2}}{R_{post} + R_{gaps\_t} + R_{bar2}}] + \frac{1}{R_{air}} \tag{A2.79}$$

where

$$R_{more} = R_{bar1} + 0.5R_{gap\_t} //[R_{bar1} + R_{post} //(R_{gaps\_t} + R_{bar2})] \tag{A2.80}$$

a. The magnetic core reluctances R_{bar} and R_{post}

The R_{bar} and R_{post} reluctances are shown in Figure A2.30.

(a) (b)

Figure A2.30 The magnetic core reluctances R_{bar} and R_{post} (a) The reluctance of the magnetic bar R_{bar} (b) the reluctance of the magnetic post R_{post}

$$R_{bar} = \frac{b_1}{\mu_0 \mu_r a_1 h} \tag{A2.81}$$

$$R_{post} = \frac{a_2}{\mu_0 \mu_r b_2 h} + \frac{\sigma}{\mu_0 b_2 h} \tag{A2.82}$$

b. The air gap reluctances R_{gaps_t} and R_{gap_t}

The R_{gaps_t} reluctance can be broken down into several reluctance components: R_{gap}, R_{face} and R_{corner} (Figure A2.31). R_{gap}, R_{corner}, and R_{face} are shown in Figure A2.32(a), Figure A2.32(b) and Figure A2.33 respectively.

(a) (b)

Figure A2.31 The side air gap reluctance considering the 3D fringing flux effect (a) The side air gap reluctance R_{gaps_t} (b) the components of the side air gap reluctance R_{gaps_t}: R_{gap}, R_{face} and R_{corner}

(a) (b)

Figure A2.32 The calculation of the gap reluctance R_{gap} and the corner fringing flux reluctance R_{corner} (a) The gap reluctance R_{gap} (b) the corner fringing flux reluctance R_{corner}

$$R_{gaps\_t} = R_{gap} \,//\, R_{face} \,//\, R_{corner} \tag{A2.83}$$

$$R_{gap} = \frac{2w_1^2 tg\alpha}{\mu_0 h(w_1 - w + w_1 \sec\alpha)^2} \tag{A2.84}$$

where

$$w_1 = 2b_2 + 2w - w_d \tag{A2.85}$$

$$\alpha = \tan^{-1}\frac{a_2}{b_2 + 2w - w_d} \tag{A2.86}$$

$$R_{corner} = \frac{R_{SQ} \,//\, R_{QSS}}{2} \tag{A2.87}$$

where

$$R_{SQ} = \frac{1}{0.077\mu_o w_1 tg\alpha} \tag{A2.88}$$

$$R_{QSS} = \frac{4}{\mu_o a_1} \tag{A2.89}$$

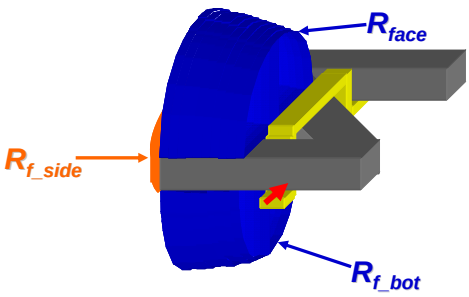

(a)

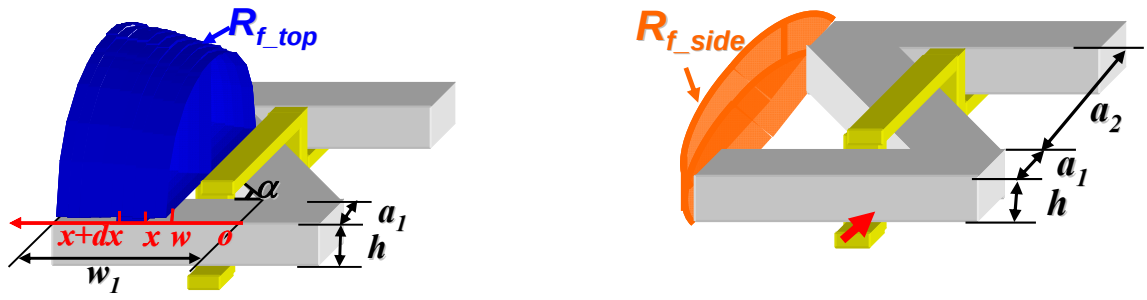

(b) (c)

Figure A2.33 The face fringing flux reluctance R_{face} (a) The three components of the face fringing flux reluctance: R_{f_side} and R_{f_bot} (b) The calculation of the R_{f_top} reluctance (c) The calculation of the R_{f_side} reluctance

$$R_{face} = R_{f\_side} // R_{f\_top} // R_{f\_bot} = R_{f\_side} // 0.5R_{f\_top} \tag{A2.90}$$

where

$$R_{f\_top} = \frac{2\pi}{\mu_0 \int_w^{w_1} 0.614 + \ln[M^2(\frac{2a_1}{x \cdot tg\alpha}) + 1]dx} \tag{A2.91}$$

$$R_{f\_side} = \frac{2\pi}{\mu_0 \cdot h \cdot \{0.614 + \ln[M^2(\frac{2a_1}{a_2}) + 1]\}} \tag{A2.92}$$

The R_{gap_t} reluctance is the simplified version of R_{gaps_t}. It can be calculated as

$$R_{gap\_t} = R_{gap} // 0.5R_{f\_top} \tag{A2.93}$$

c. The air-around-the-winding reluctance R_{air}

The R_{air} is shown in Figure A2.34 The calculation of the air-around-the-winding fringing flux reluctance R_{air}. According to the calculation method in the two-phase low profile twisted-core coupled inductor,

$$R_{air} = \frac{\pi}{\mu_o b_2 \sin\alpha \{0.614 + \ln\{\frac{[\frac{\pi}{2}(1 + \frac{2(w_1 - w)\sec\alpha}{w_d \sec\alpha}) + \sqrt{\frac{\pi^2}{4}(1 + \frac{2(w_1 - w)\sec\alpha}{w_d \sec\alpha})^2 - 2]^2}}{4} + 1\}\}} \tag{A2.94}$$

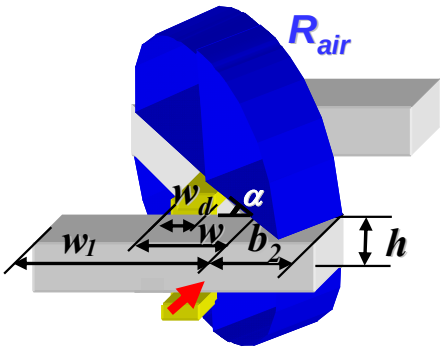

Figure A2.34 The calculation of the air-around-the-winding fringing flux reluctance R_{air} in the Z-core coupled-inductor

Figure A2.35 shows the precision of the Z-core reluctance model when a_1=4mm, a_2=16.5mm, b_1=14mm, b_2=4.5mm, h=4mm, α=60.07°, w=4.5mm, and w_d=4mm. It can be seen that the reluctance model can achieve around 75 percent precision in the steady-state inductance L_{ss} and the transient inductance L_{tr}. This reluctance model can be used to design the Z-core coupled-inductor.

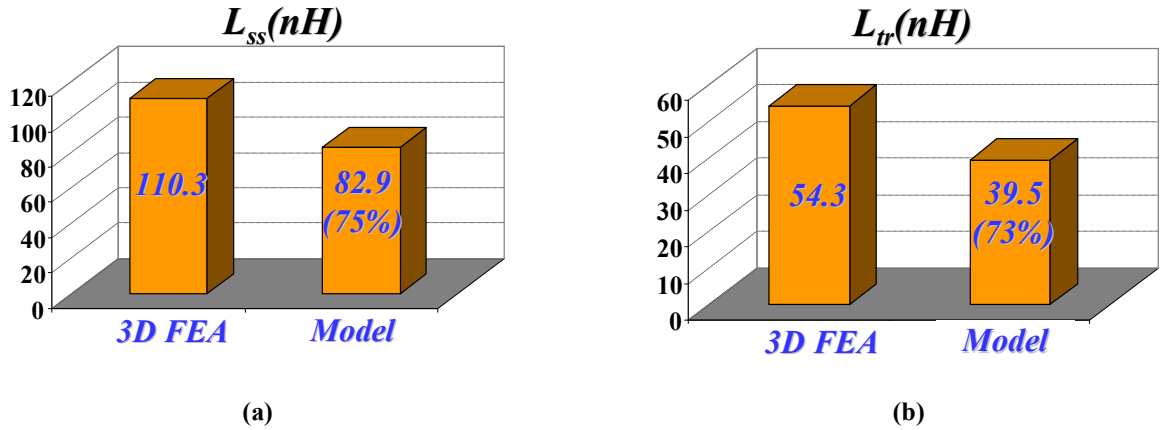

Figure A2.35 The precision of the steady-state inductance L_{ss} and the transient inductance L_{tr} calculated by the Z-core reluctance model considering the 3D fringing flux

Appendix 3. Derivation of Conversion Ratio Equations for Multiphase Coupled-inductor Buck Converters in DCM

A3.1 The 2-phase Coupled-inductor Buck Converter

Figure A3.1 shows a 2-phase coupled inductor buck. Figure A3.2 shows the phase current waveforms of the 2-phase strong coupled inductor buck in the CCM and DCM when the output load current reduces. For the simplicity of further analysis, the waveforms are drawn with the constant-on time control method implemented in the coupled inductor buck. It can be seen that there are two different DCM modes (DCM1 mode and DCM2 mode) for the 2-phase coupled inductor buck. In the following subsections, the conversion ratio equations for the two DCM modes will be investigated.

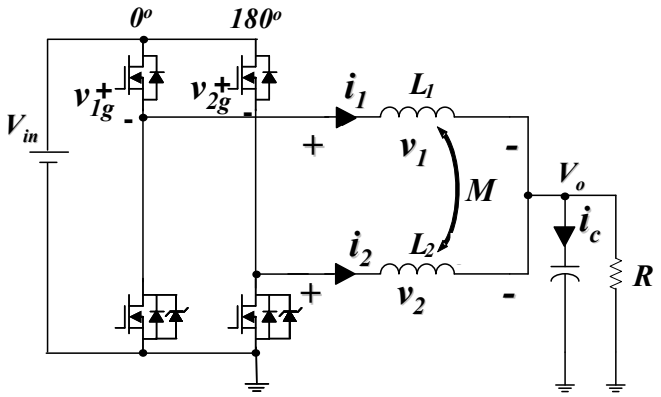

Figure A3.1 The two-phase coupled-inductor buck converter with the phase currents marked

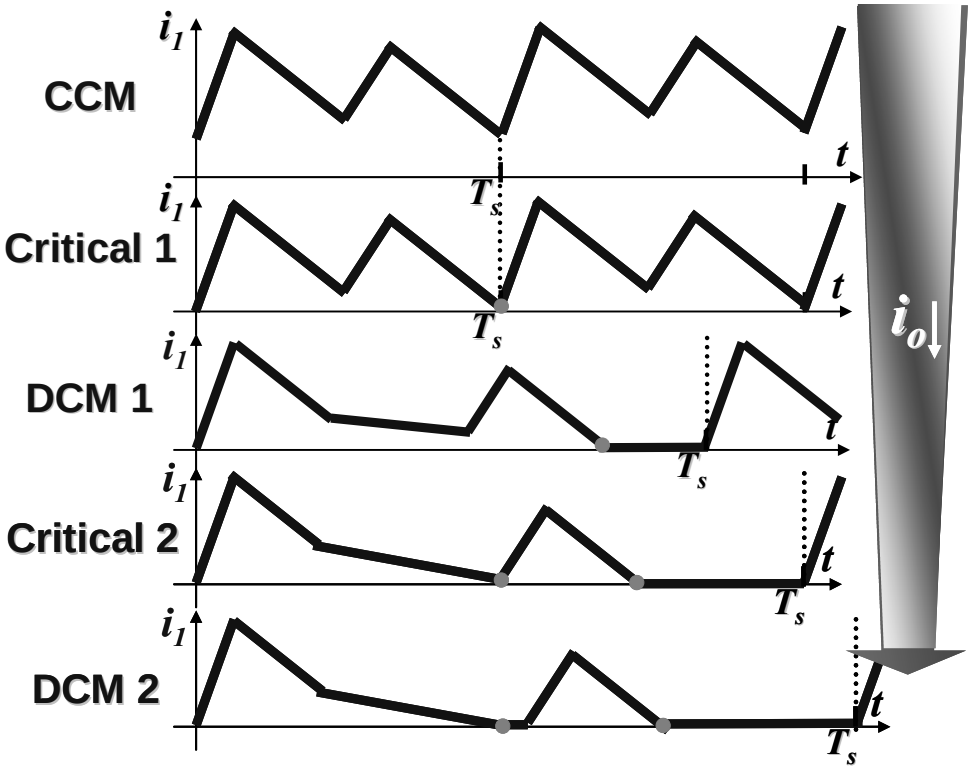

Figure A3.2 The phase-current waveforms of a two-phase coupled-inductor buck converter under different load conditions

a. The DCM1 Mode

The V_o/V_{in} and f_s relationship of the coupled-inductor buck converter is necessary for the control of the two-phase coupled-inductor buck converter in DCM1. Since the relationship has not been investigated in the literature, it is discussed below.

Figure A3.3 shows the inductor voltage v_1 and the capacitor current i_c waveforms of the two-phase coupled-inductor buck converter in the DCM1 mode. Here M<0 for the inverse coupling.

Based on the inductor volt-second balance and the capacitor charge balance,

$$\int_0^{T_s} v_1 dt = 0 \tag{A3.1}$$

$$\int_0^{T_s} i_c dt = \int_0^{T_s} i_1 dt + \int_0^{T_s} i_2 dt - \frac{V_o T_s}{R} = 0 \tag{A3.2}$$

assuming $L=L_1=L_2$, then it can be derived that

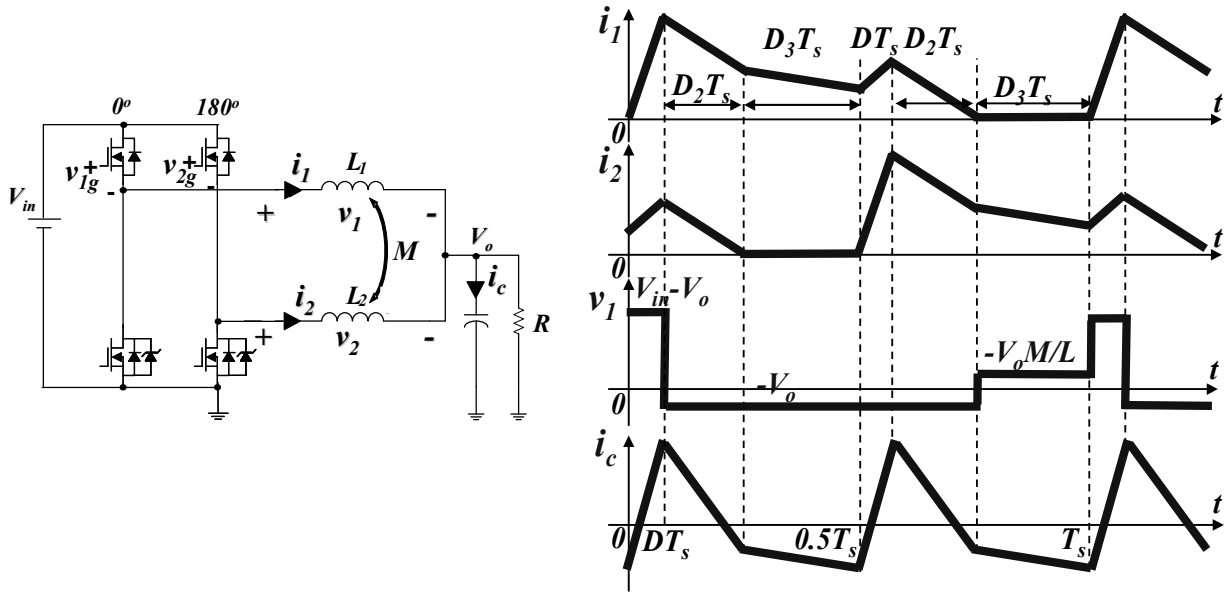

(a) **(b)**

Figure A3.3 The inductor voltage v_1 and capacitor current i_c waveforms of the two-phase coupled-inductor buck converter in the DCM1 mode (a) The two-phase coupled buck converter (b) The inductor currents i_1, i_2, the inductor voltage v_1 and the capacitor current i_c waveforms

$$r^2+\frac{RD^2T_s}{L(1+\frac{M}{L})}r-\frac{RD^2T_s}{L(1-\frac{M^2}{L^2})}=0 \tag{A3.3}$$

Therefore, the expression of the voltage conversion ratio V_o/V_{in} in the coupled-inductor buck converter in DCM1 mode is

$$r=\frac{V_o}{V_{in}}=\frac{2}{(1-\alpha)+\sqrt{(1-\alpha)^2+4\frac{(1-\alpha^2)L}{D^2RT_s}}} \tag{A3.4}$$

where α is the coupling coefficient of the two-phase coupled-inductor, $\alpha=M/L$, $-1\le\alpha\le 0$, and M is the mutual inductance of the coupled-inductor.

Redefining the L_{ss} to be

$$L_{ss} = \frac{L^2 - M^2}{L + \frac{r}{1-r}M} \tag{A3.5}$$

Here, r is defined as the V_o/V_{in} ratio.

$$r = \frac{V_o}{V_{in}} \tag{A3.6}$$

Substituting the equation (A3.5) into the equation (A3.4),

$$r = \frac{V_o}{V_{in}} = \frac{2}{1 + \sqrt{1 + 4\frac{L_{ss}}{D^2 R T_s}}} \tag{A3.7}$$

and

$$f_s = \frac{1}{T_s} = \frac{r^2 L_{ss}}{(1-r){T_{on}}^2 R} \tag{A3.8}$$

Recalling that, for the non-coupled-inductor buck converter, the V_o/V_{in} and f_s relationship is

$$\frac{V_o}{V_{in}} = \frac{2}{1 + \sqrt{1 + 4\frac{K}{D^2}}}, \qquad K = \frac{L_{nc}}{R T_{s\_nc}} \tag{A3.9}$$

and

$$f_{s\_nc} = \frac{r^2 L_{nc}}{(1-r){T_{on}}^2 R} \tag{A3.10}$$

Comparing the equations (A3.7), (A3.8), (A3.9) and (A3.10), it can be found that the V_o/V_{in} and f_s relationship of the two-phase coupled-inductor buck in DCM1 is the same as that of the non-coupled-inductor buck if L_{ss} replaces L_{nc} in the equation.

b. The DCM2 Mode

The V_o/V_{in} and f_s relationship of the coupled-inductor buck converter is necessary for the control of the two-phase coupled-inductor buck converter in DCM2. Since the relationship has not been investigated in the literature, it is discussed below.

Figure A3.4 shows the inductor voltage v_1 and the capacitor current i_c waveforms of the coupled-inductor buck converter in the DCM2 mode. Here M<0 for the inverse coupling.

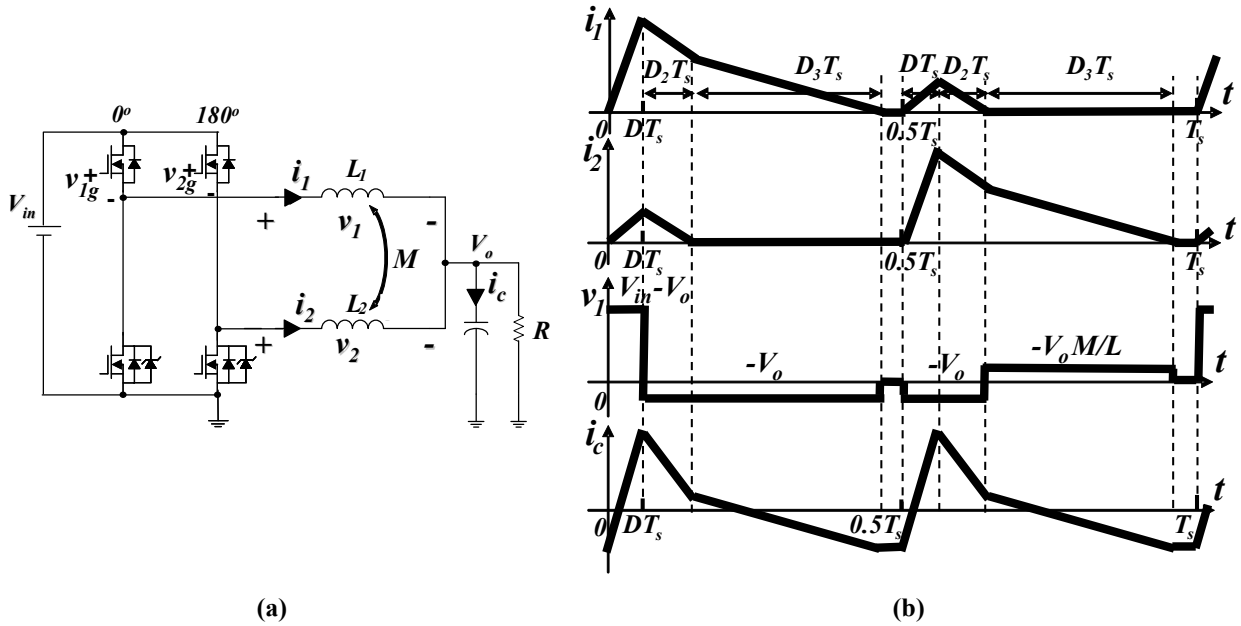

Figure A3.4 The inductor voltage v_1 and capacitor current i_c waveforms of the two-phase coupled-inductor buck converter in the DCM2 mode (a) The two-phase coupled buck converter (b) the inductor currents i_1, i_2, the inductor voltage v_1 and the capacitor current i_c waveforms

Based on the inductor volt-second balance and the capacitor charge balance,

$$\int_0^{T_s} v_1 dt = 0 \tag{A3.11}$$

$$\int_0^{T_s} i_c dt = \int_0^{T_s} i_1 dt + \int_0^{T_s} i_2 dt - \frac{V_o T_s}{R} = 0 \tag{A3.12}$$

Assuming $L=L_1=L_2$, then it can be derived that

$$r^2 + \frac{RD^2T_s}{L(1+\frac{M}{L})}r - \frac{RD^2T_s}{L(1-\frac{M^2}{L^2})} = 0 \tag{A3.13}$$

Therefore, the expression of the voltage conversion ratio V_o/V_{in} in the coupled-inductor buck converter in DCM2 mode is

$$r = \frac{V_o}{V_{in}} = \frac{2}{(1-\alpha)+\sqrt{(1-\alpha)^2+4\frac{(1-\alpha^2)L}{D^2RT_s}}} \tag{A3.14}$$

where α is the coupling coefficient of the two-phase coupled-inductor, α=M/L, $-1 \le \alpha \le 0$, and M is the mutual inductance of the two-phase coupled-inductor.

The equation (A3.14) can be rewritten as

$$r = \frac{V_o}{V_{in}} = \frac{2}{(1-\alpha)+\sqrt{(1-\alpha)^2+4\frac{(1-\alpha^2)L}{T_{on}^2Rf_s}}} \tag{A3.15}$$

Substituting the equation (A3.5) into the equation (A3.15),

$$r = \frac{V_o}{V_{in}} = \frac{2}{1+\sqrt{1+4\frac{L_{ss}}{D^2RT_s}}} \tag{A3.16}$$

and

$$f_s = \frac{1}{T_s} = \frac{r^2L_{ss}}{(1-r){T_{on}}^2R} \tag{A3.17}$$

Comparing the equations (A3.9), (A3.10), (A3.16) and (A3.17), it can be found that the V_o/V_{in} and f_s relationship of the two-phase coupled-inductor buck converter in DCM1 is the same as that of the two-phase coupled-inductor buck converter in DCM2.

Comparing the equations (A3.9), (A3.10), (A3.16) and (A3.17), it can be found that the V_o/V_{in} and f_s relationship of the two-phase coupled-inductor buck converter in DCM2 is the same as that of the non-coupled-inductor buck converter if L_{ss} replaces L_{nc} in the equation.

For the equation (A3.5), when $M \to 0$

$$L_{ss} = \frac{L^2 - M^2}{L + \frac{r}{1-r}M} \to L \tag{A3.18}$$

Therefore, the equation (A3.14) can be found that

$$r = \frac{V_o}{V_{in}} = \frac{2}{1+\sqrt{1+4\frac{L_{ss}}{D^2 RT_s}}} \to \frac{2}{1+\sqrt{1+4\frac{L}{D^2 RT_s}}} \quad \text{when } M \to 0 \tag{A3.19}$$

The V_o/V_{in} and f_s relationship of the non-coupled-inductor buck converter in DCM is a special case of that of the two-phase coupled-inductor buck converter in DCM.

The V_o/V_{in} and α, f_s relationship of the two-phase coupled-inductor buck converter in DCM in the equation (A3.15) is shown in Figure A3.5. In the simulation, L=300nH, R=0.5Ω, and T_{on}=100ns.

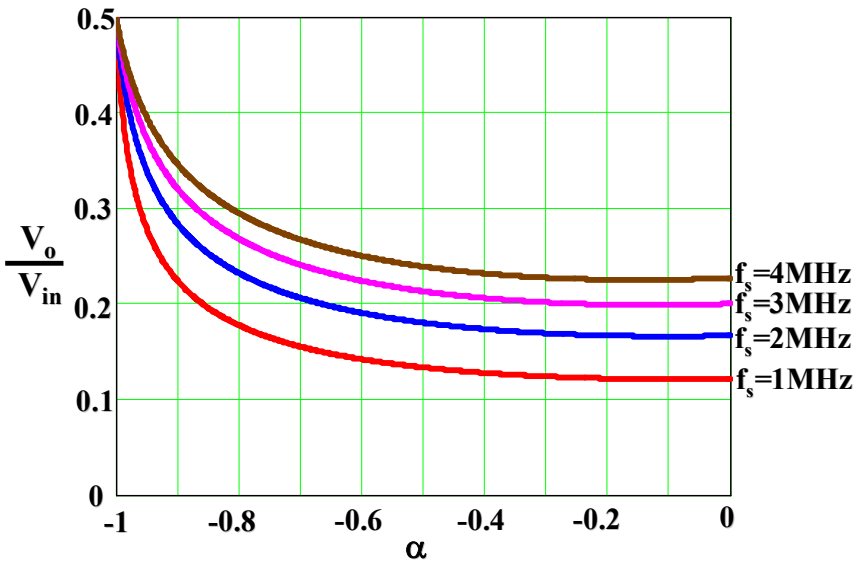

Figure A3.5 The curves of the conversion ratio V_o/V_{in} vs. the coupling coefficient α and the switching frequency f_s for the two-phase coupled-indcutor buck converter in DCM

The V_o/V_{in} and α, D relationship of the two-phase coupled-inductor buck converter in DCM in the equation (A3.14) is also shown in Figure A3.6. In Figure A3.6, $L/(RT_s)$=0.6. The

simulation result (Figure A3.7) verifies the V_o/V_{in} and α, D relationship of the two-phase coupled-inductor buck converter in DCM.

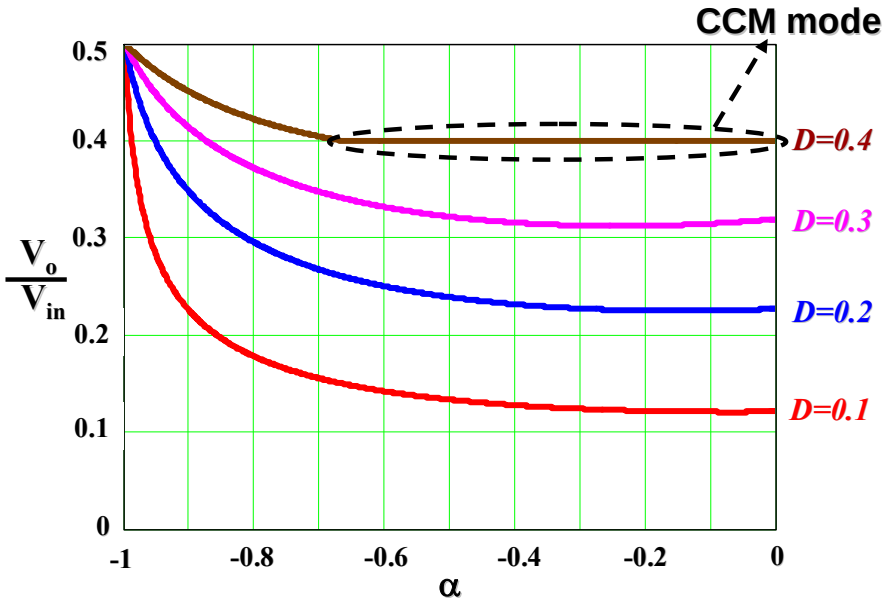

Figure A3.6 The curves of the conversion ratio V_o/V_{in} vs. the coupling coefficient α and the duty cycle D for the two-phase coupling-inductor buck converter in DCM

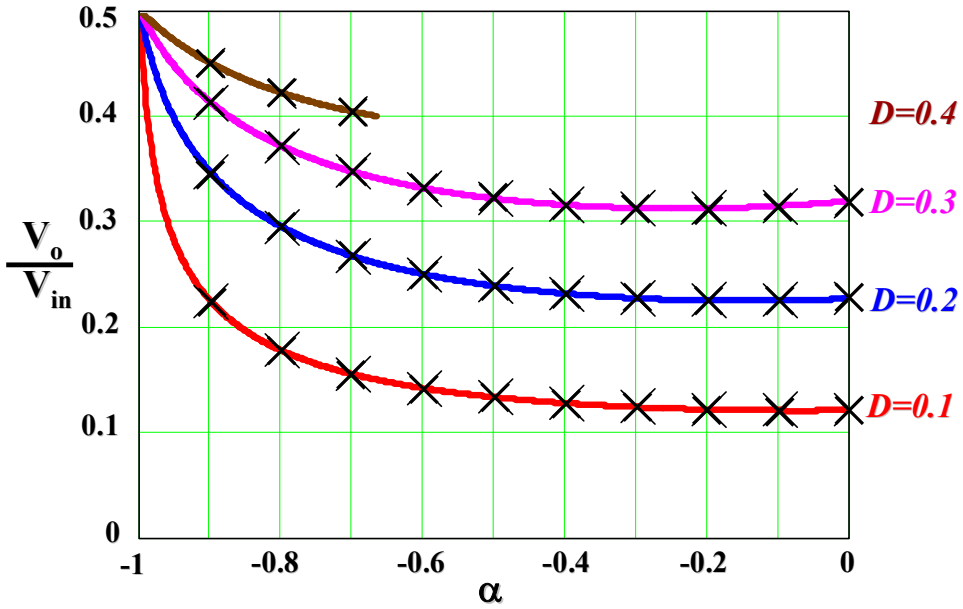

Figure A3.7 The simulation verification of the curves of the conversion ratio V_o/V_{in} vs. the coupling coefficient α and the duty cycle D for the two-phase coupled-idnuctor buck converter

Based on the equation (A3.16), the criteria of the boundary between the CCM and the DCM can be derived. In CCM mode,

$$\frac{V_o}{V_{in}} = D \tag{A3.20}$$

By equalizing the equations (A3.16) and (A3.20), it can be found that

$$R = \frac{L_{ss}}{(1-D)T_s} \tag{A3.21}$$

A3.2 The 3-phase Coupled-inductor Buck Converter

Figure A3.8 shows a 3-phase coupled inductor buck. Figure A3.9 shows the phase current waveforms of the 3-phase strong coupled inductor buck in the CCM and DCM when the output load current reduces. For the simplicity of further analysis, the waveforms are drawn with the constant-on time control method implemented in the coupled inductor buck. It can be seen that there are three different DCM modes (DCM1 mode, DCM2 mode and DCM3 mode) for the 3-phase coupled inductor buck. In the following subsections, the three DCM modes will be investigated in detail.

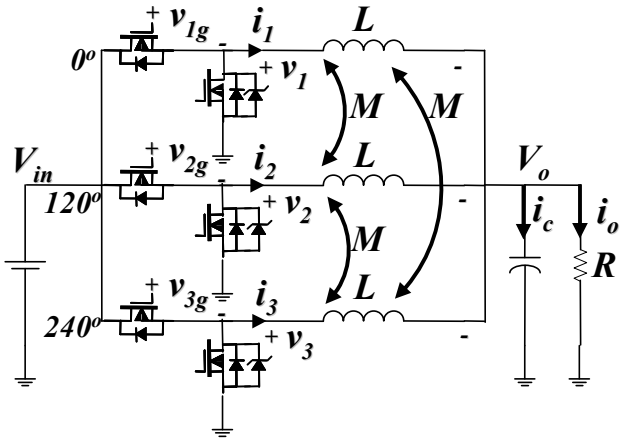

Figure A3.8 The 3-phase coupled inductor buck converter with the phase current marked

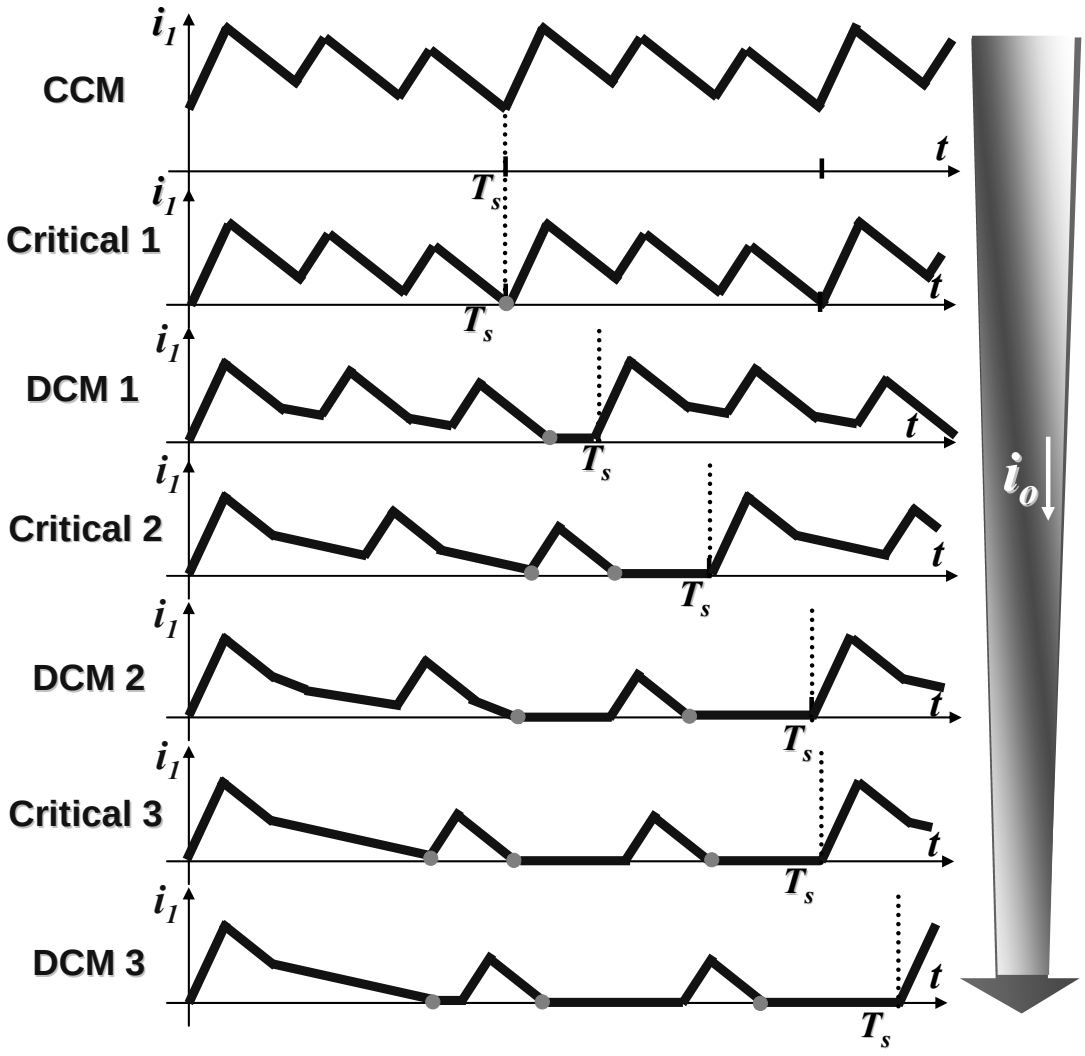

Figure A3.9 The phase-current waveforms of a three-phase coupled-inductor buck converter under different load conditions

a. The DCM1 Mode

When a coupled inductor buck is in the DCM1 mode, the phase current reaches zero only once in one switching period. The key waveforms of the coupled inductor buck in the DCM1 mode are shown in Figure A3.10.

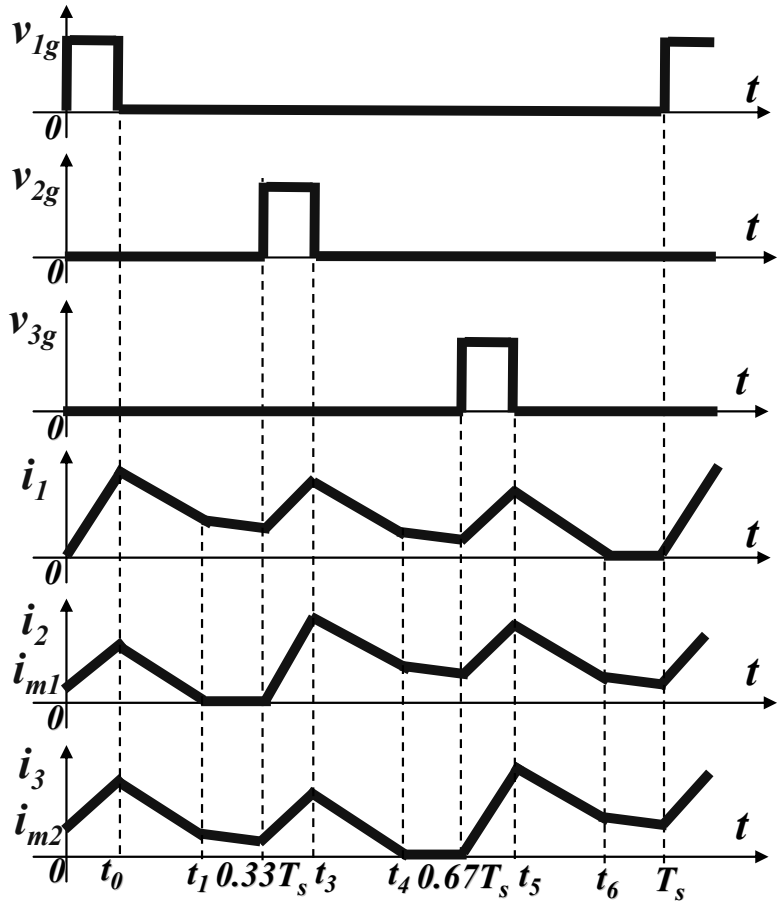

Figure A3.10 The gate driving voltage v_{1g}, v_{2g} and v_{3g}, and the phase current i_1, i_2 and i_3 waveforms of the 3-phase coupled inductor buck converter in DCM1

At the time 0, the phase 1 inductor current i_1 is zero and the other phase inductor currents i_2 and i_3 are at the intermediate values i_{m1}.and i_{m2}, respectively. During the time range [0, t_0], the phase 1 top switch is turned on and the top switches of the phase 2 and phase 3 are turned off. During this time range, the i_1 increases from 0 to the maximum value. For the coupling effect, the i_2 and i_3 also increase. During the time range [t_0, t_1], all the top switches of the three phases are turned off and the phase currents i_1, i_2 and i_3 decrease until i_2 touches zero at t_1. During [0, t_1], all the three phase inductor currents are coupled. During the time range [t_1, $0.33T_s$], only the phase 1 inductor current i_1 and the phase 3 inductor current i_3 are coupled. The phase currents i_1 and i_3 decrease until they reach the inter-mediate value i_{m2} and i_{m1} at the time $0.33T_s$. The phase 2 synchronous rectifier is turned off at time t_1 to avoid that the phase 2 current i_2 goes to a negative value and to achieve the DCM. The phase 2 current i_2 stays at zero during the time range [t_1, $0.33T_s$].

During the time range [$0.33T_s$, $0.67T_s$] and [$0.67T_s$, T_s], the 3-phase coupled inductor buck follows the working principle in [0, $0.33T_s$], except that the conditions of the phase 1, the phase 2 and the phase 3 change with each other. In summary, the three phase inductor currents i_1, i_2 and i_3 couple and the two phase inductor currents couple alternatively in one switching period in the DCM1 mode of the 3-phase coupled inductor buck.

To verify the above analysis, the simulation is implemented. Figure A3.11 shows the phase current waveforms of the 3-phase coupled inductor buck in DCM1. Three phase currents couple and the two phase currents couple alternatively.

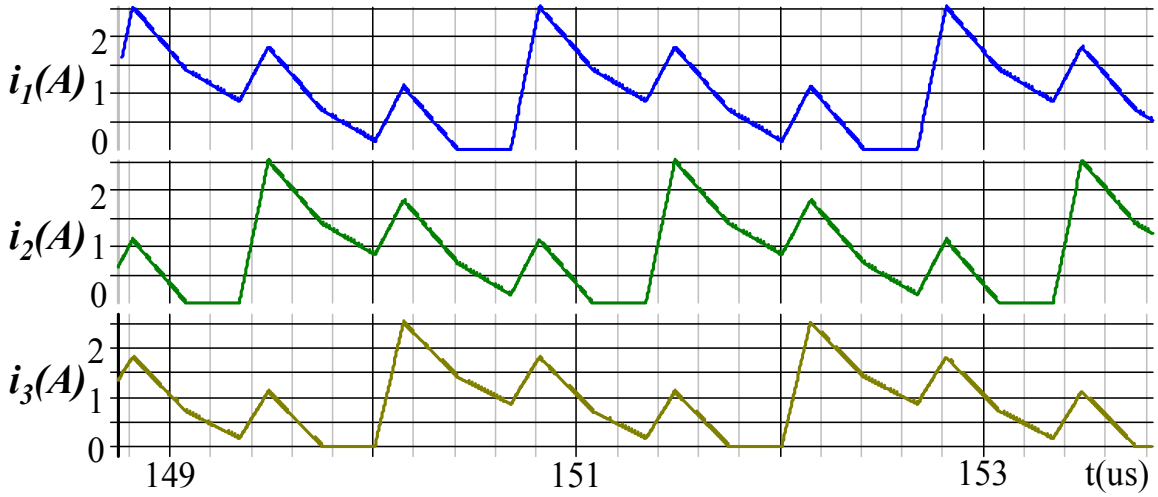

Figure A3.11 The simulated phase current i_1, i_2 and i_3 waveforms of the 3-phase coupled inductor buck converter in DCM1

The V_o/V_{in} and f_s relationship of the coupled inductor buck is necessary in control of the 3-phase coupled inductor buck in DCM1. It will be discussed in detail in the following paragraphs.

Figure A3.12 shows the inductor voltage v_1 and the capacitor current i_c waveforms of the 3-phase coupled inductor buck in the DCM1 mode. Here M<0 for the inverse coupling.

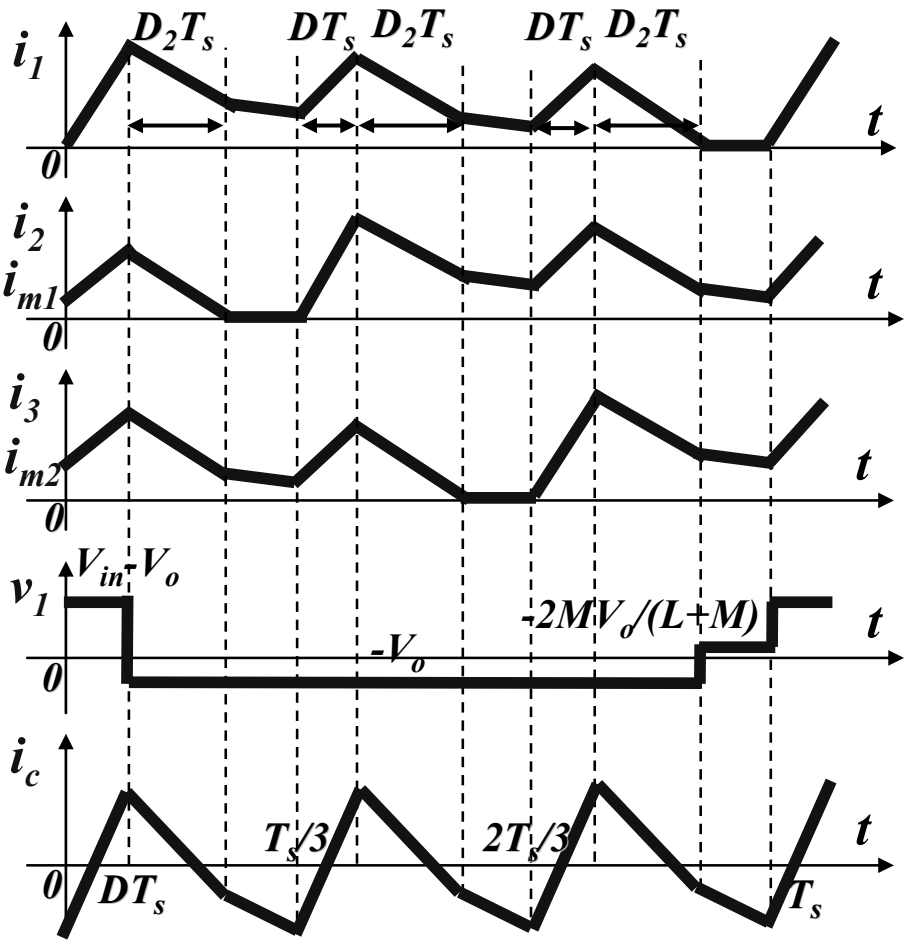

Figure A3.12 The inductor current i_1, i_2 and i_3, the inductor voltage v_1 and the capacitor current i_c waveforms of the 3-phase coupled inductor buck converter in the DCM1 mode

Based on the inductor volt-second balance and the capacitor charge balance,

$$\int_0^{T_s} v_1 dt = 0 \tag{A3.22}$$

$$\int_0^{T_s} i_c dt = \int_0^{T_s} i_1 dt + \int_0^{T_s} i_2 dt + \int_0^{T_s} i_3 dt - \frac{V_o T_s}{R} = 0 \tag{A3.23}$$

i.e.

$$(V_{in} - V_o)DT_s - V_o(0.67 + D_2)T_s - V_o \frac{2M}{L+M}(0.33 - D - D_2)T_s = 0 \tag{A3.24}$$

$$3[0.5\frac{V_{in}-V_o}{L_{eq1}}(DT_s)^2+0.5(2\frac{V_{in}-V_o}{L_{eq1}}DT_s-\frac{V_o}{L_{eq2}}D_2T_s)D_2T_s$$
$$+0.5(\frac{V_{in}-V_o}{L_{eq1}}DT_s-\frac{V_o}{L_{eq2}}D_2T_s+i_{m2})(0.33-D-D_2)T_s+0.5(2i_{m2}-\frac{V_o}{L_{eq3}}DT_s)DT_s$$
$$+0.5(2i_{m2}-\frac{2V_o}{L_{eq3}}DT_s-\frac{V_o}{L_{eq2}}D_2T_s)D_2T_s$$
$$+0.5(i_{m2}-\frac{V_o}{L_{eq3}}DT_s-\frac{V_o}{L_{eq2}}D_2T_s+i_{m1})(0.33-D-D_2)T_s+0.5(i_{m1}+\frac{V_o}{L_{eq2}}D_2T_s)DT_s$$
$$+0.5\frac{V_o}{L_{eq2}}(D_2T_s)^2]-\frac{V_oT_s}{R}=0 \tag{A3.25}$$

where,

$$i_{m1}=\frac{V_o}{L_{eq2}}D_2T_s+\frac{V_o}{L_{eq3}}DT_s \tag{A3.26}$$

$$i_{m2}=\frac{V_{in}-V_o}{L_{eq1}}DT_s-\frac{V_o}{L_{eq2}}D_2T_s-\frac{V_o}{L+M}(0.33-D-D_2)T_s \tag{A3.27}$$

$$L_{eq1}=\frac{(L-M)(L+2M)}{L+(1+2\frac{r}{1-r})M} \tag{A3.28}$$

$$L_{eq2}=L+2M \tag{A3.29}$$

$$L_{eq3}=\frac{(L-M)(L+2M)}{L+\frac{1-r}{r}M} \tag{A3.30}$$

Here, r is defined as the V_o/V_{in} ratio.

$$r = \frac{V_o}{V_{in}} \tag{A3.31}$$

Substituting the equations (A3.31) and (A3.25) into the equation (A3.24) and rearranging terms, it can be got that

$$r^2 + \frac{nRD^2T_s}{2\dfrac{(L-M)(L+2M)}{L+(1+2\dfrac{r}{1-r})M}}r - \frac{nRD^2T_s}{2\dfrac{(L-M)(L+2M)}{L+(1+2\dfrac{r}{1-r})M}} = 0 \tag{A3.32}$$

Therefore, the expression of the voltage conversion ratio V_o/V_{in} in the coupled inductor buck in the DCM1 mode is

$$r = \frac{V_o}{V_{in}} = \frac{2(1+\dfrac{\alpha}{2})}{(1-\dfrac{\alpha}{2}) + \sqrt{(1-\dfrac{\alpha}{2})^2 + 8\dfrac{(1-\dfrac{\alpha}{2})(1+\alpha)(1+\dfrac{\alpha}{2})L}{3D^2RT_s}}} \tag{A3.33}$$

where, $\alpha = 2M/L$ is the coupling coefficient. The equation (A3.33) can be rewritten as

$$r = \frac{V_o}{V_{in}} = \frac{2(1+\dfrac{\alpha}{2})}{(1-\dfrac{\alpha}{2}) + \sqrt{(1-\dfrac{\alpha}{2})^2 + 8\dfrac{(1-\dfrac{\alpha}{2})(1+\alpha)(1+\dfrac{\alpha}{2})L}{3T_{on}^2Rf_s}}} \tag{A3.34}$$

b. The DCM2 Mode

When a coupled inductor buck is in the DCM2 mode, the phase current reaches zero twice in one switching period. The key waveforms of the coupled inductor buck in the DCM2 mode are shown in Figure A3.13.

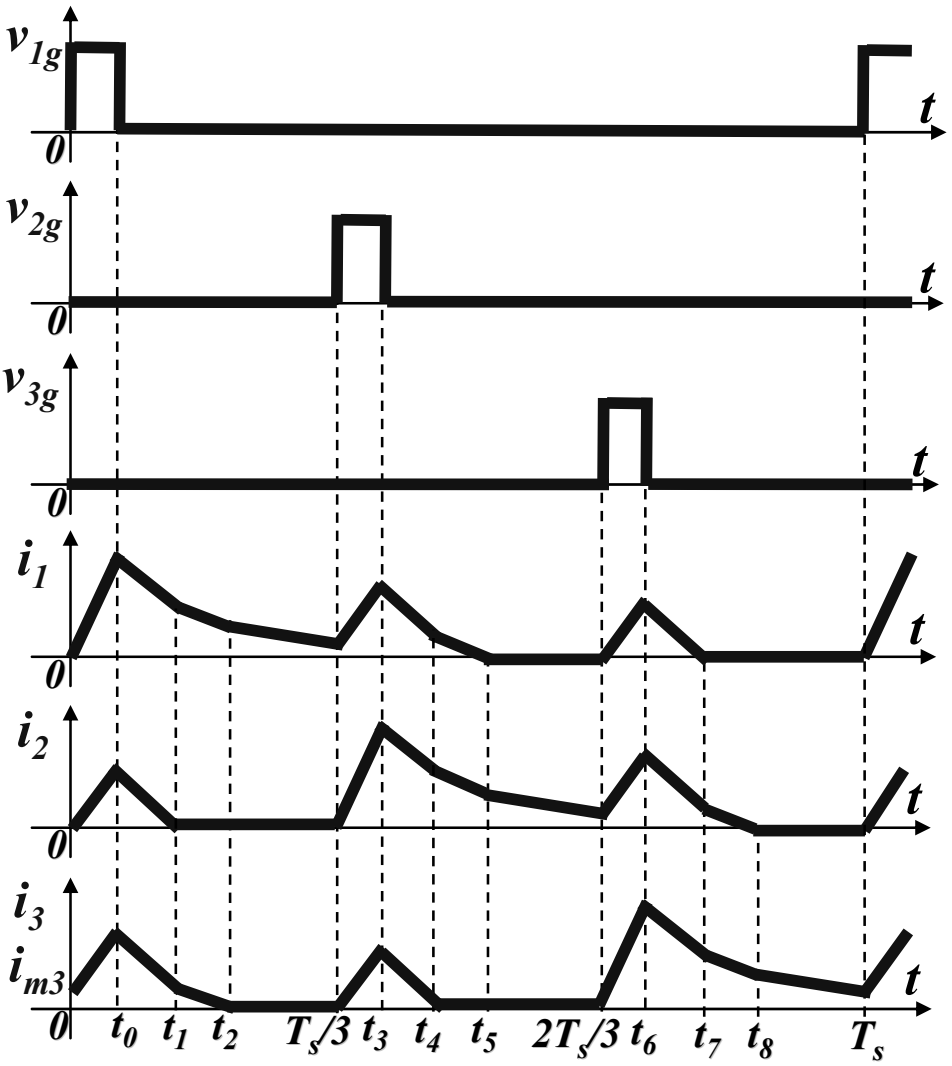

Figure A3.13 The gate driving voltage v_{1g}, v_{2g} and v_{3g}, and the phase current i_1, i_2 and i_3 waveforms of the 3-phase coupled inductor buck converter in DCM2

At the time 0, the phase 1 inductor current i_1 and the phase 2 inductor current i_2 are zero and the phase 3 inductor current i_3 is at an intermediate value i_{m3}. During the time range $[0, t_0]$, the phase 1 top switch is turned on and the top switches of the phase 2 and phase 3 are turned off. During this time range, the i_1 increases from 0 to the maximum value. For the coupling effect, the i_2 and i_3 also increase. During the time range $[t_0, t_1]$, all the top switches of the three phases are turned off and the phase currents i_1, i_2 and i_3 decrease until i_2 touches zero at t_1. During $[0, t_1]$, all the three phase inductor currents are coupled. During the time range $[t_1, t_2]$, only the phase 1 inductor current i_1 and the phase 3 inductor current i_3 are coupled. The phase currents i_1 and i_3 decrease until the phase 3 inductor current i_3 touches zero. The phase 2 synchronous rectifier is

turned off at time t_1 to avoid that the phase 2 current i_2 goes to a negative value and to achieve the DCM. The phase 2 current i_2 stays at zero during the time range $[t_1, t_2]$. During the time range $[t_2, 0.33T_s]$, all the three phase currents decouple. The phase 1 inductor works as a non-couled inductor with its self inductance L and its current i_1 decreases until i_1 reaches the intermediate value i_{m3} at $T_s/3$. The phase 3 synchronous rectifier is turned off at time t_2. The phase 2 current i_2 and the phase 3 current i_3 stay at zero during the time range $[t_2, 0.33T_s]$.

During the time range $[T_s/3, 2T_s/3]$ and $[2T_s/3, T_s]$, the 3-phase coupled inductor buck follows the working principle in $[0, T_s/3]$, except that the conditions of the phase 1, the phase 2 and the phase 3 change with each other. In summary, the three phase inductor currents i_1, i_2 and i_3 fully couple, the two phase inductor currents couple and the three phase currents decouple alternatively in one switching period in the DCM2 mode of the 3-phase coupled inductor buck.

To verify the above analysis, the simulation is implemented. Figure A3.14 shows the phase current waveforms of the 3-phase coupled inductor buck in DCM2. Three phase currents couple, the two phase currents couple and the three phase currents decouple alternatively.

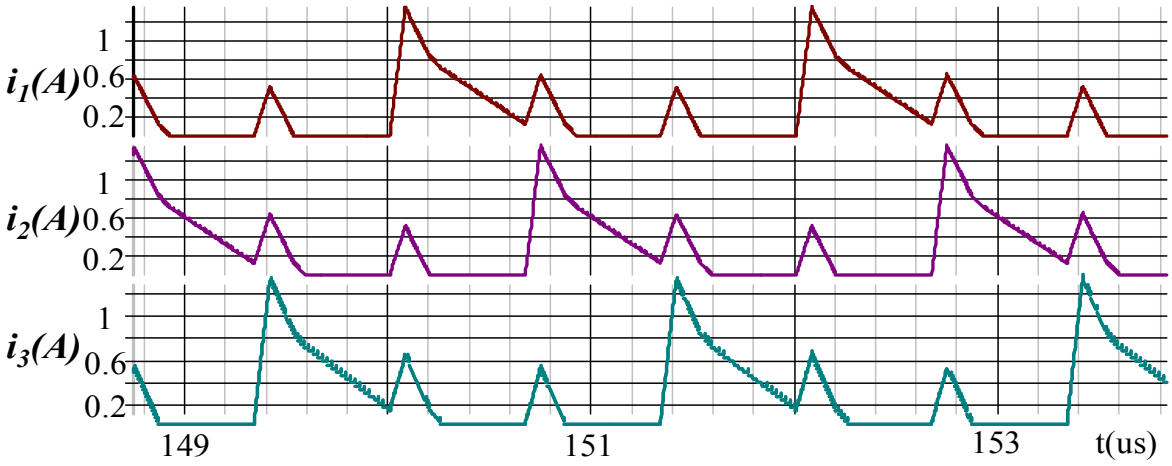

Figure A3.14 The simulated phase current i_1, i_2 and i_3 waveforms of the 3-phase coupled inductor buck converter in DCM2

The V_o/V_{in} and f_s relationship of the coupled inductor buck is necessary in control of the 3-phase coupled inductor buck in DCM2. It will be discussed in detail in the following paragraphs.

Figure A3.15 shows the inductor voltage v_1 and the capacitor current i_c waveforms of the 3-phase coupled inductor buck in the DCM2 mode. Here M<0 for the inverse coupling.

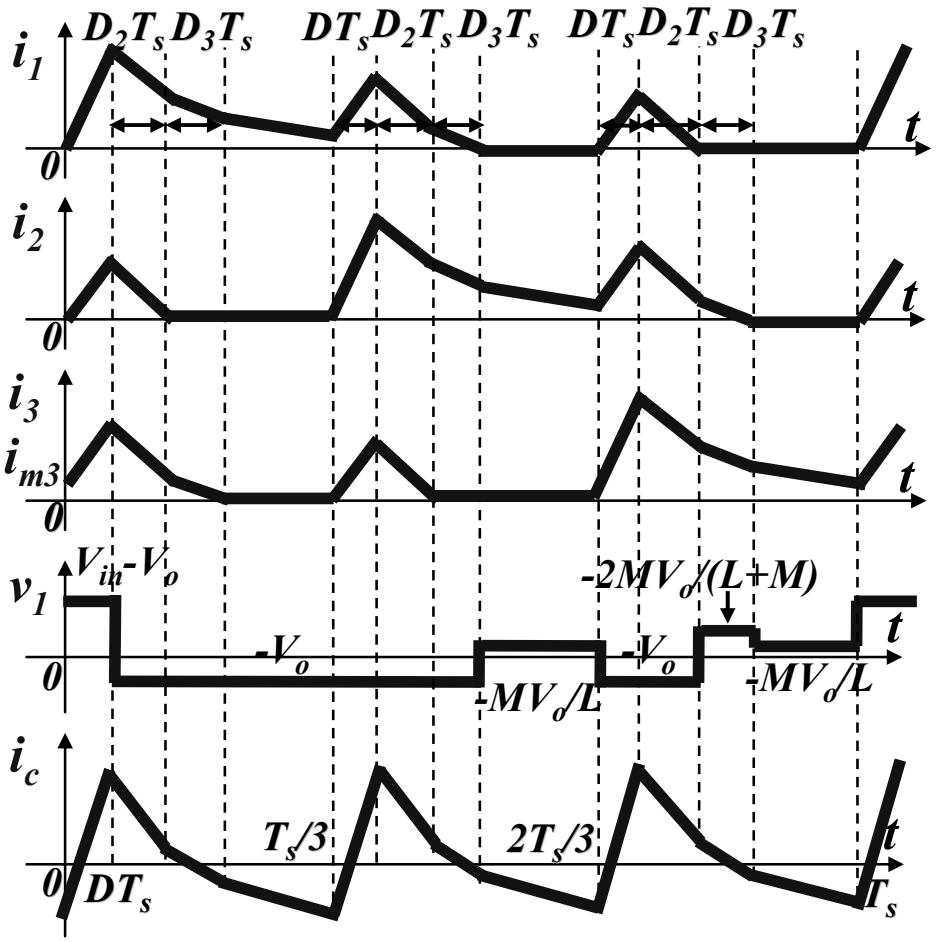

Figure A3.15 The inductor current i_1, i_2 and i_3, the inductor voltage v_1 and the capacitor current i_c waveforms of the 3-phase coupled inductor buck converter in the DCM2 mode

Based on the inductor volt-second balance and the capacitor charge balance,

$$\int_0^{T_s} v_1 dt = 0 \tag{A3.35}$$

$$\int_0^{T_s} i_c dt = \int_0^{T_s} i_1 dt + \int_0^{T_s} i_2 dt + \int_0^{T_s} i_3 dt - \frac{V_o T_s}{R} = 0 \tag{A3.36}$$

i.e.

$$(V_{in}-V_o)DT_s - V_o(0.33+D+2D_2+D_3)T_s - V_o\frac{M}{L}2(0.33-D-D_2-D_3)T_s$$
$$-V_o\frac{2M}{L+M}D_3T_s = 0$$

(A3.37)

$$3[0.5\frac{V_{in}-V_o}{L_{eq1}}(DT_s)^2 + 0.5(2\frac{V_{in}-V_o}{L_{eq1}}DT_s - \frac{V_o}{L_{eq2}}D_2T_s)D_2T_s$$
$$+0.5(2\frac{V_{in}-V_o}{L_{eq1}}DT_s - 2\frac{V_o}{L_{eq2}}D_2T_s - \frac{V_o}{L+M}D_3T_s)D_3T_s$$
$$+0.5(i_{m3}+\frac{V_{in}-V_o}{L_{eq1}}DT_s - \frac{V_o}{L_{eq2}}D_2T_s - \frac{V_o}{L+M}D_3T_s)(0.33-D-D_2-D_3)T_s$$
$$+0.5(2i_{m3} - \frac{V_o}{L_{eq3}}DT_s)DT_s$$
$$+0.5(2i_{m3} - \frac{2V_o}{L_{eq3}}DT_s - \frac{V_o}{L_{eq2}}D_2T_s)D_2T_s$$
$$+0.5\frac{V_o}{L+M}(D_3T_s)^2 - 0.5\frac{V_o}{L_{eq3}}(DT_s)^2$$
$$+0.5\frac{V_o}{L_{eq2}}(D_2T_s)^2] - \frac{V_oT_s}{R} = 0$$

(A3.38)

where,

$$i_{m3} = \frac{V_{in}-V_o}{L_{eq1}}DT_s - \frac{V_o}{L_{eq2}}D_2T_s - \frac{V_o}{L+M}D_3T_s - \frac{V_o}{L}(0.33-D-D_2-D_3)T_s \quad \text{(A3.39)}$$

$$L_{eq1} = \frac{(L-M)(L+2M)}{L+(1+2\frac{r}{1-r})M} \quad \text{(A3.40)}$$

$$L_{eq2} = L + 2M \tag{A3.41}$$

$$L_{eq3} = \frac{(L-M)(L+2M)}{L + \frac{1-r}{r}M} \tag{A3.42}$$

$$-\frac{V_o}{L_{eq3}} DT_s = \frac{V_o}{L_{eq2}} D_2 T_s \tag{A3.43}$$

Here, r is defined as the V_o/V_{in} ratio.

$$r = \frac{V_o}{V_{in}} \tag{A3.44}$$

Substituting the equations (A3.38) and (A3.43) into the equation (A3.37) and rearranging terms, it can be got that

$$r^2 + \frac{nRD^2T_s}{2\frac{(L-M)(L+2M)}{L+(1+2\frac{r}{1-r})M}} r - \frac{nRD^2T_s}{2\frac{(L-M)(L+2M)}{L+(1+2\frac{r}{1-r})M}} = 0 \tag{A3.45}$$

Therefore, the expression of the voltage conversion ratio V_o/V_{in} in the coupled inductor buck in the DCM2 mode is

$$r = \frac{V_o}{V_{in}} = \frac{2(1+\frac{\alpha}{2})}{(1-\frac{\alpha}{2}) + \sqrt{(1-\frac{\alpha}{2})^2 + 8\frac{(1-\frac{\alpha}{2})(1+\alpha)(1+\frac{\alpha}{2})L}{3D^2RT_s}}} \tag{A3.46}$$

where $\alpha = 2M / L$ is the coupling coefficient. The equation (A3.46) can be rewritten as

$$r = \frac{V_o}{V_{in}} = \frac{2(1+\frac{\alpha}{2})}{(1-\frac{\alpha}{2}) + \sqrt{(1-\frac{\alpha}{2})^2 + 8\frac{(1-\frac{\alpha}{2})(1+\alpha)(1+\frac{\alpha}{2})L}{3T_{on}^2 R f_s}}} \quad \text{(A3.47)}$$

c. The DCM3 Mode

When a coupled inductor buck is in the DCM3 mode, the phase current reaches zero three times in one switching period. The key waveforms of the coupled inductor buck in the DCM3 mode are shown in Figure A3.16.

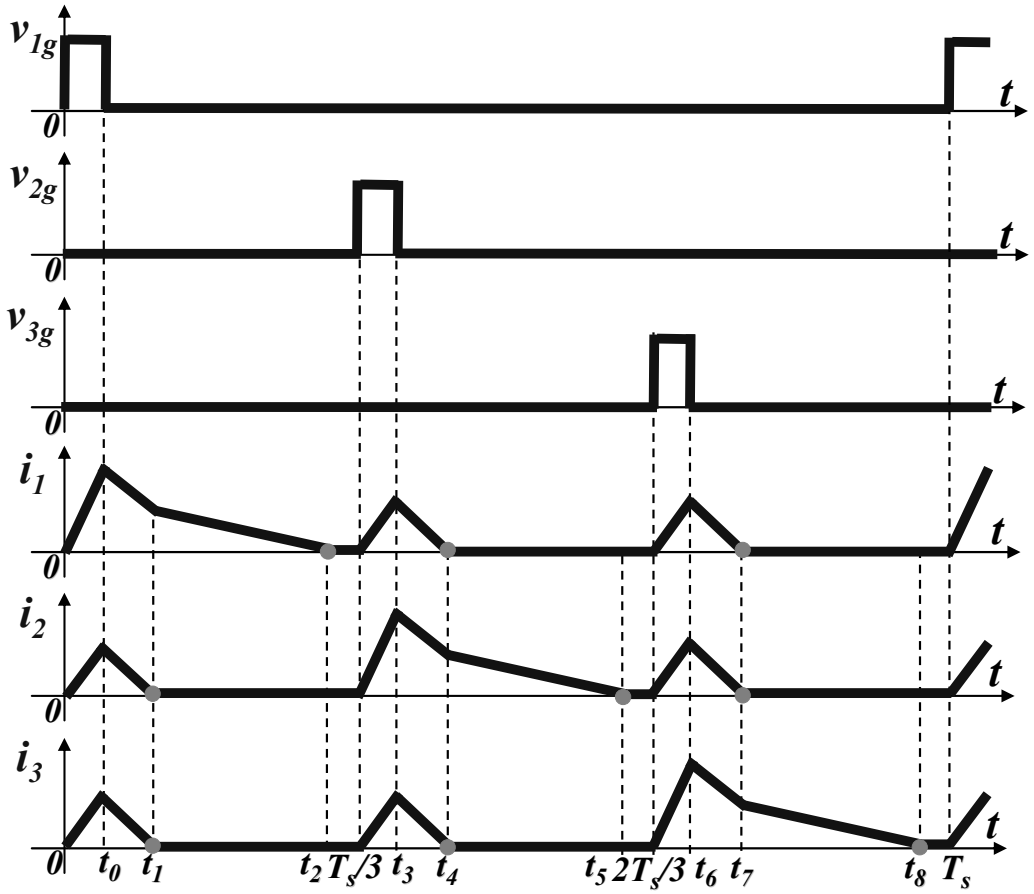

Figure A3.16 The gate driving voltage v_{1g}, v_{2g} and v_{3g}, and the phase current i_1, i_2 and i_3 waveforms of the 3-phase coupled inductor buck converter in DCM3

At the time 0, all the phase inductor currents are zero. During the time range [0, t_0], the phase 1 top switch is turned on and the top switches of the phase 2 and phase 3 are turned off. During this time range, the i_1 increases from 0 to the maximum value. For the coupling effect,

the i_2 and i_3 also increase. During the time range $[t_0, t_1]$, all the top switches of the three phases are turned off and the phase currents i_1, i_2 and i_3 decrease until i_2 and i_3 touch zero at t_1. During $[0, t_1]$, all the three phase inductor currents are coupled. During the time range $[t_1, t_2]$, the phase 1 inductor current i_1 decreases until i_1 touches zero at t_2. The phase 2 and phase 3 synchronous rectifiers are turned off at time t_1 to avoid that the phase 2 current i_2 and the phase 3 current i_3 go to a negative value and to achieve the DCM. The phase 2 current i_2 and the phase 3 current i_3 stay at zero during the time range $[t_1, t_2]$. At t_2, the phase 1 synchronuous rectifier is turned off. During the time range $[t_2, 0.33T_s]$, all the three phase currents are kept at zero. The whole 3-phase coupled inductor buck seems to stop except that the output capacitor provides current to the output load.

During the time range $[T_s/3, 2T_s/3]$ and $[2T_s/3, T_s]$, the 3-phase coupled inductor buck follows the working principle in $[0, T_s/3]$, except that the conditions of the phase 1, the phase 2 and the phase 3 change with each other. In summary, the three phase inductor currents i_1, i_2 and i_3 fully couple, decouple and stop alternatively in one switching period in the DCM3 mode of the 3-phase coupled inductor buck.

To verify the above analysis, the simulation is implemented. Figure A3.17 shows the phase current waveforms of the 3-phase coupled inductor buck in DCM3. Three phase currents couple, decouple and stop alternatively.

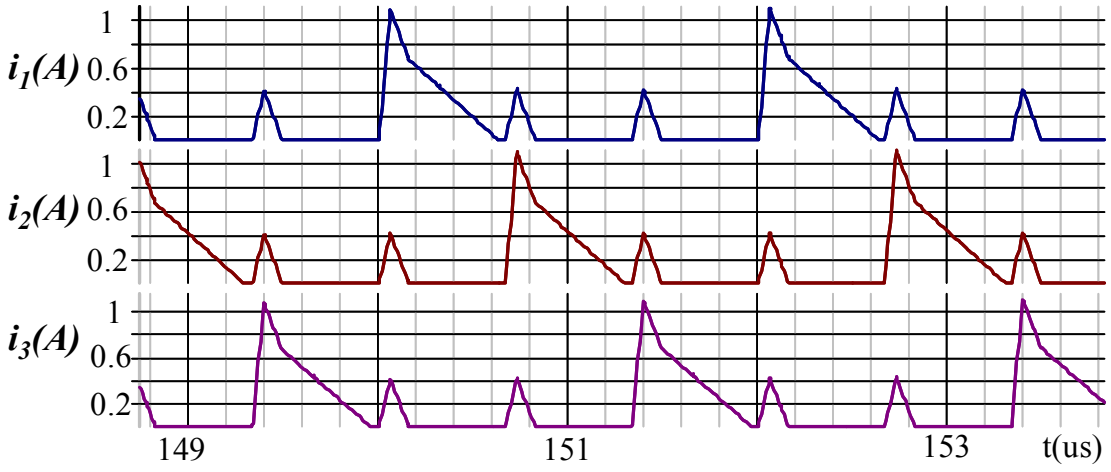

Figure A3.17 The simulated phase current i_1, i_2 and i_3 waveforms of the 3-phase coupled-inductor buck converter in DCM3

The V_o/V_{in} and f_s relationship of the coupled inductor buck is necessary in control of the 3-phase coupled inductor buck in DCM3. It will be discussed in detail in the following paragraphs.

Figure A3.18 shows the inductor voltage v_1 and the capacitor current i_c waveforms of the 3-phase coupled inductor buck in the DCM3 mode. Here M<0 for the inverse coupling.

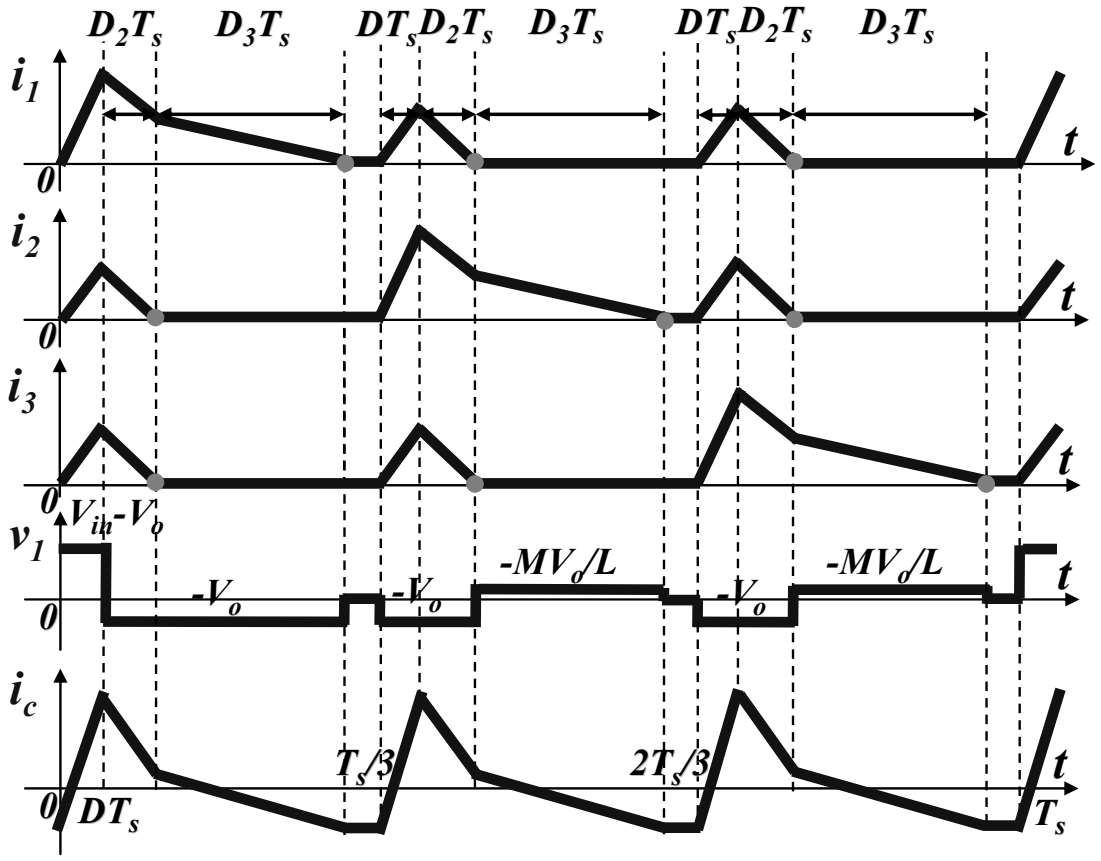

Figure A3.18 The inductor current i_1, i_2 and i_3, the inductor voltage v_1 and the capacitor current i_c waveforms of the 3-phase coupled inductor buck converter in the DCM3 mode

Based on the inductor volt-second balance and the capacitor charge balance,

$$\int_0^{T_s} v_1 dt = 0 \tag{A3.48}$$

$$\int_0^{T_s} i_c dt = \int_0^{T_s} i_1 dt + \int_0^{T_s} i_2 dt + \int_0^{T_s} i_3 dt - \frac{V_o T_s}{R} = 0 \tag{A3.49}$$

i.e.

$$(V_{in}-V_o)DT_s - V_o(D_2+D_3+2D+2D_2)T_s - V_o\frac{M}{L}2D_3T_s = 0 \tag{A3.50}$$

$$3[0.5\frac{V_{in}-V_o}{L_{eq1}}(DT_s)^2 + 0.5(2\frac{V_{in}-V_o}{L_{eq1}}DT_s - \frac{V_o}{L_{eq2}}D_2T_s)D_2T_s \tag{A3.51}$$
$$+0.5\frac{V_o}{L}(D_3T_s)^2 - 2\cdot 0.5\frac{V_o}{L_{eq3}}DT_s(D+D_2)T_s] - \frac{V_oT_s}{R} = 0$$

where,

$$L_{eq1} = \frac{(L-M)(L+2M)}{L+(1+2\frac{r}{1-r})M} \tag{A3.52}$$

$$L_{eq2} = L+2M \tag{A3.53}$$

$$L_{eq3} = \frac{(L-M)(L+2M)}{L+\frac{1-r}{r}M} \tag{A3.54}$$

$$-\frac{V_o}{L_{eq3}}DT_s = \frac{V_o}{L_{eq2}}D_2T_s \tag{A3.55}$$

Here, r is defined as the V_o/V_{in} ratio.

$$r = \frac{V_o}{V_{in}} \tag{A3.56}$$

Substituting the equations (A3.51) and (A3.55) into the equation (A3.50) and rearranging terms, it can be got that

$$r^2 + \frac{nRD^2T_s}{2\frac{(L-M)(L+2M)}{L+(1+2\frac{r}{1-r})M}}r - \frac{nRD^2T_s}{2\frac{(L-M)(L+2M)}{L+(1+2\frac{r}{1-r})M}} = 0 \tag{A3.57}$$

Therefore, the expression of the voltage conversion ratio V_o/V_{in} in the coupled inductor buck in the DCM3 mode is

$$r = \frac{V_o}{V_{in}} = \frac{2(1+\frac{\alpha}{2})}{(1-\frac{\alpha}{2}) + \sqrt{(1-\frac{\alpha}{2})^2 + 8\frac{(1-\frac{\alpha}{2})(1+\alpha)(1+\frac{\alpha}{2})L}{3D^2RT_s}}} \tag{A3.58}$$

where $\alpha = 2M / L$ is the coupling coefficient. The equation (A3.58) can be rewritten as

$$r = \frac{V_o}{V_{in}} = \frac{2(1+\frac{\alpha}{2})}{(1-\frac{\alpha}{2}) + \sqrt{(1-\frac{\alpha}{2})^2 + 8\frac{(1-\frac{\alpha}{2})(1+\alpha)(1+\frac{\alpha}{2})L}{3T_{on}^2Rf_s}}} \tag{A3.59}$$

Comparing the equations (A3.34), (A3.47) and (A3.59), it can be found that the V_o/V_{in} and f_s relationships of the 3-phase coupled inductor buck in DCM1, DCM2 and DCM3 are the same.

Since

$$L_{ss} = \frac{(L-M)(L+2M)}{L+(1+2\frac{r}{1-r})M} \tag{A3.60}$$

Substituting the equation (A3.60) into the equation (A3.59),

$$r = \frac{V_o}{V_{in}} = \frac{2}{1+\sqrt{1+8\frac{L_{ss}}{3D^2RT_s}}} \tag{A3.61}$$

and

$$f_s = \frac{1}{T_s} = \frac{2r^2L_{ss}}{3(1-r){T_{on}}^2R} \tag{A3.62}$$

Recalling that, for the 3-phase non-coupled inductor buck, the V_o/V_{in} and f_s relationship is

$$\frac{V_o}{V_{in}} = \frac{2}{1+\sqrt{1+4\frac{K}{D^2}}}, \qquad K = \frac{2L_{nc}}{3RT_{s\_nc}} \tag{A3.63}$$

and

$$f_{s\_nc} = \frac{2r^2 L_{nc}}{3(1-r){T_{on}}^2 R} \tag{A3.64}$$

Comparing the equations (A3.63), (A3.64), (A3.61) and (A3.62), it can be found that the V_o/V_{in} and f_s relationships of the 3-phase coupled inductor buck in DCM is similar as that of the 3-phase non-coupled inductor buck except that the L_{ss} replaces L_{nc}.

Considering the equation (A3.60)

$$L_{ss} = \frac{(L-M)(L+2M)}{L+(1+2\frac{r}{1-r})M} \to L \quad \text{when } M \to 0 \tag{A3.65}$$

the equation (A3.61)

$$r = \frac{V_o}{V_{in}} = \frac{2}{1+\sqrt{1+8\frac{L_{ss}}{3D^2 RT_s}}} \to \frac{2}{1+\sqrt{1+8\frac{L}{3D^2 RT_s}}} \quad \text{when } M \to 0 \tag{A3.66}$$

The V_o/V_{in} and f_s relationship of the 3-phase non-coupled inductor buck in DCM is a special case of that of the 3-phase coupled inductor buck in DCM.

The V_o/V_{in} and α, f_s relationship of the 3-phase coupled inductor buck in DCM shown in the equation (A3.59) is drawn in Figure A3.19. In the simulation, L=300nH, R=0.5ohm, T_{on}=100ns. The V_o/V_{in} and α, D relationship of the 3-phase coupled inductor buck in DCM shown in the equation (A3.58) is drawn in Figure A3.20. In Figure A3.20, $L/(RT_s)$=0.6.

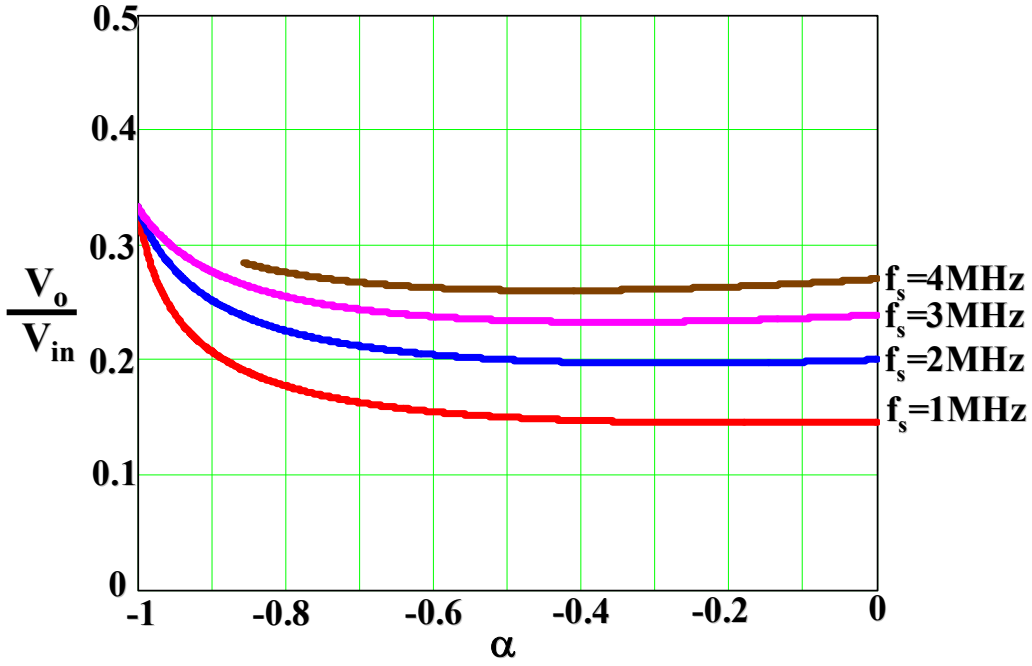

Figure A3.19 The curves of the conversion ratio V_o/V_{in} vs. the coupling coefficient α and the switching frequency f_s in the 3-phase coupled inductor buck converter in DCM

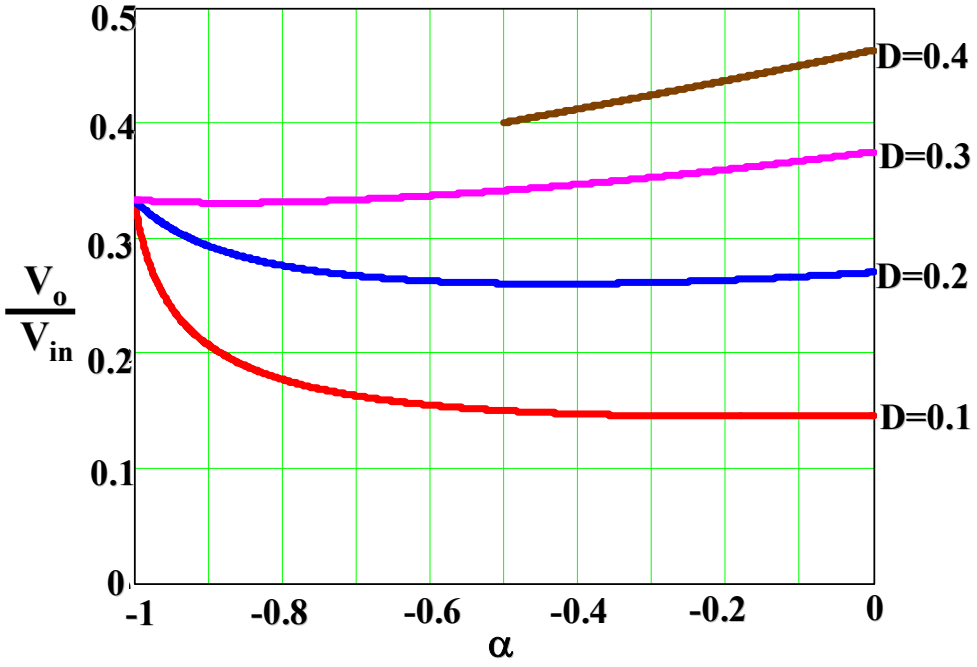

Figure A3.20 The curves of the conversion ratio V_o/V_{in} vs. the coupling coefficient α and the duty cycle D in the 3-phase coupled inductor buck converter in DCM

It has been seen that the V_o/V_{in} equation of the multipase coupled inductor buck in DCM is similar as that of the multiphase non-coupled inductor buck in DCM for 2-phase and 3-phase cases. This can be explained in the following. The input currents of the 3-phase coupled inductor buck in DCM and the 3-phase non-coupled inductor buck in any DCM are shown in Figure A3.21.

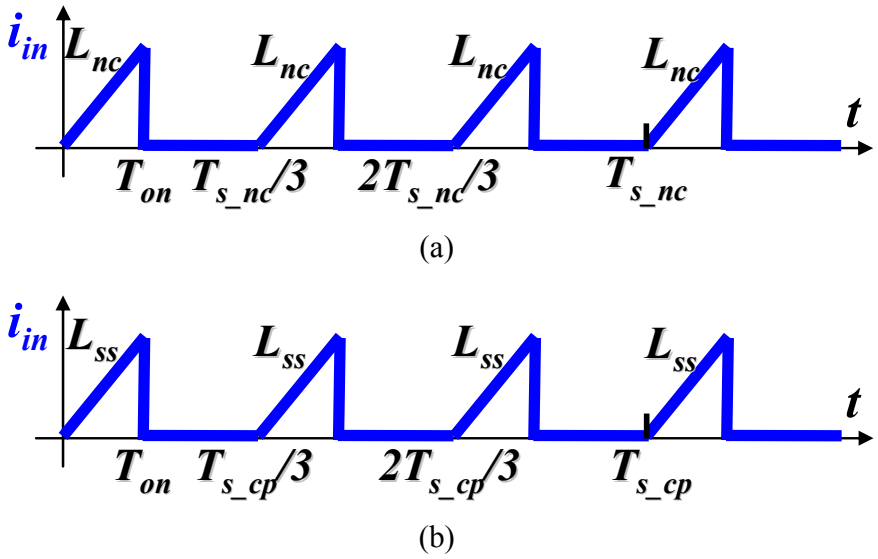

Figure A3.21 The input current waveforms of the 3-phase non-coupled and coupled buck converter in DCM (a) the input current waveform of the 3-phase non-coupled-inductor buck converter (b) the input current waveform of the 3-phase coupled-inductor buck converter

Assume the V_{in}, V_o and i_o of the 3-phase coupled inductor buck in DCM and the 3-phase non-coupld inductor buck in DCM are the same. Since the input power of the converter is equal to the output power of the converter, neglecting the loss in the converter,

$$V_{in} \cdot 3 \cdot 0.5 \cdot \frac{V_{in} - V_o}{L_{nc}} \cdot (T_{on})^2 / T_{s\_nc} = V_o \cdot i_o \tag{A3.67}$$

$$V_{in} \cdot 3 \cdot 0.5 \cdot \frac{V_{in} - V_o}{L_{ss}} \cdot (T_{on})^2 / T_{s\_cp} = V_o \cdot i_o \tag{A3.68}$$

Comparing the equations (A3.67) and (A3.68), it can be seen that, when $L_{nc}=L_{ss}$,

$$T_{s\_nc} = T_{s\_cp} \tag{A3.69}$$

This means that the V_o/V_{in} conversion ratio equation of the 3-phase coupled inductor buck in DCM is the same as that of the 3-phase non-coupled inductor buck in DCM except that the L_{nc} is replaced by L_{ss}.

Based on the equation (A3.61), the criteria of the boundary between the CCM and the DCM for the 3-phase coupled inductor buck can be derived. In CCM mode,

$$\frac{V_o}{V_{in}} = D \tag{A3.70}$$

By equalizing the equation (A3.61) and the equation (A3.70), it can be found that

$$R = \frac{2L_{ss}}{3(1-D)T_s} \tag{A3.71}$$

A3.3 The N-phase Coupled-inductor Buck Converter

Figure A3.22 shows the n-phase coupled inductor buck. Figure A3.23 shows the phase current waveforms of the n-phase strong coupled inductor buck in the CCM and DCM when the output load current reduces. For the simplicity of further analysis, the waveforms are drawn with the constant-on time control method implemented in the coupled inductor buck. It can be seen that there are n different DCM modes (DCM1 mode, DCM2 mode,… and DCMn mode) for the n-phase coupled inductor buck.

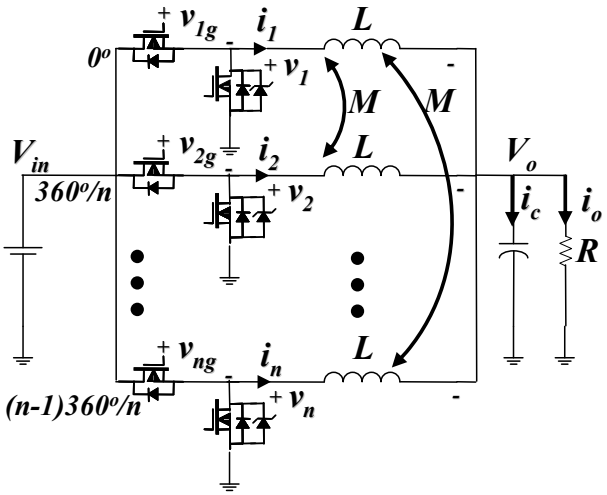

Figure A3.22 The n-phase coupled-inductor buck converter with the phase current marked

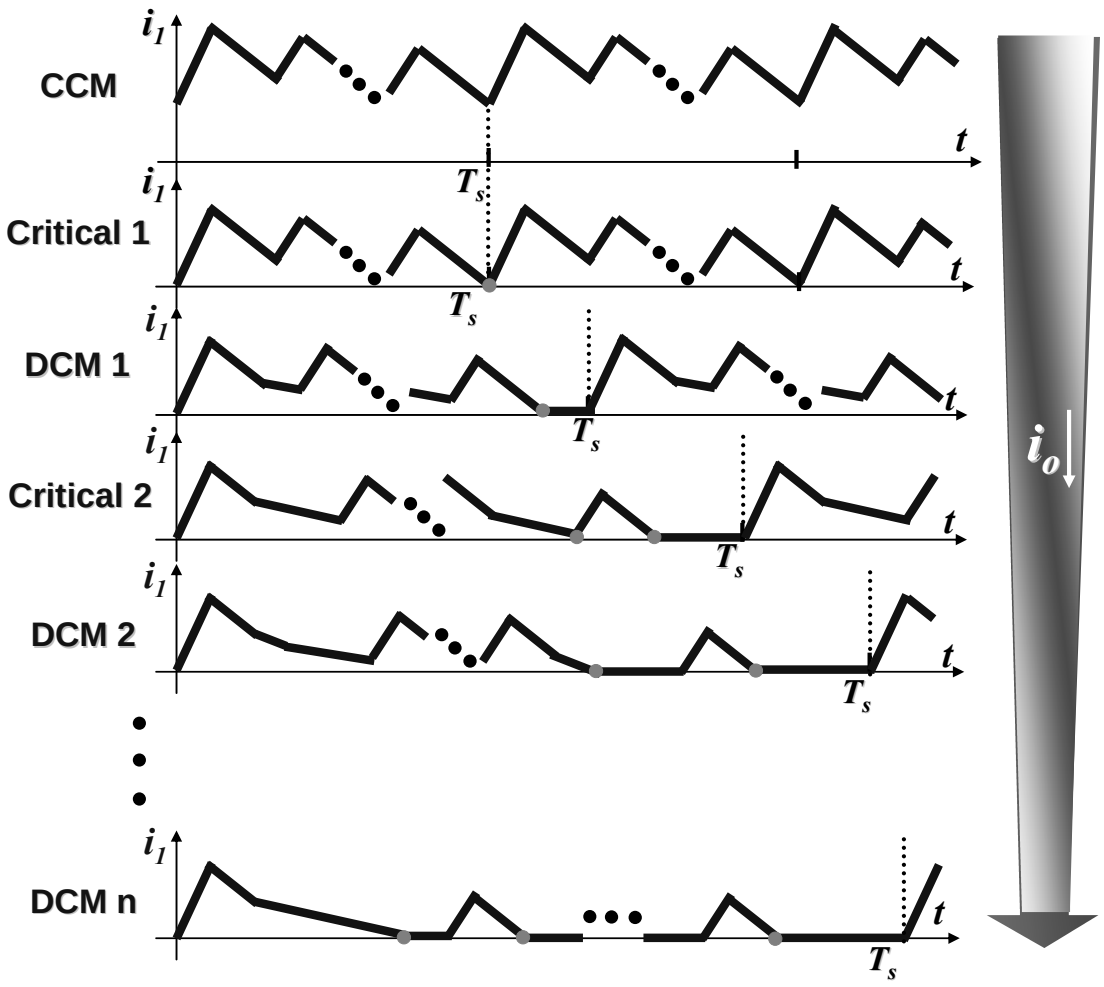

Figure A3.23 The phase-current waveforms of an n-phase coupled-inductor buck converter under different load conditions

In the DCM1, the n phase currents couple and the (n-1) phase currents couple alternatively in one switching period. In the DCM2 mode, the n phase currents couple, the (n-1) phase currents couple and the (n-2) phase currents couple alternatively in one switching period. In the DCM3 mode, the n phase currents couple, the (n-2) phase currents couple and the (n-3) phase currents coupled alternatively in one switching period. In the DCM n mode, the n phase currents couple, the n phase currents decouple and the n phase currents keep at zero altermatively in one switching period.

Figure 6.29 shows the input current waveforms of the n-phase non-coupled inductor buck in DCM and the n-phase coupled inductor buck in any DCM mode. Assume the V_{in}, V_o and $i_o(R)$ of the n-phase coupled inductor buck in any DCM mode and the n-phase non-coupld inductor buck

in DCM are the same. Since the input power of the converter is equal to the output power of the converter, neglecting the loss in the converter,

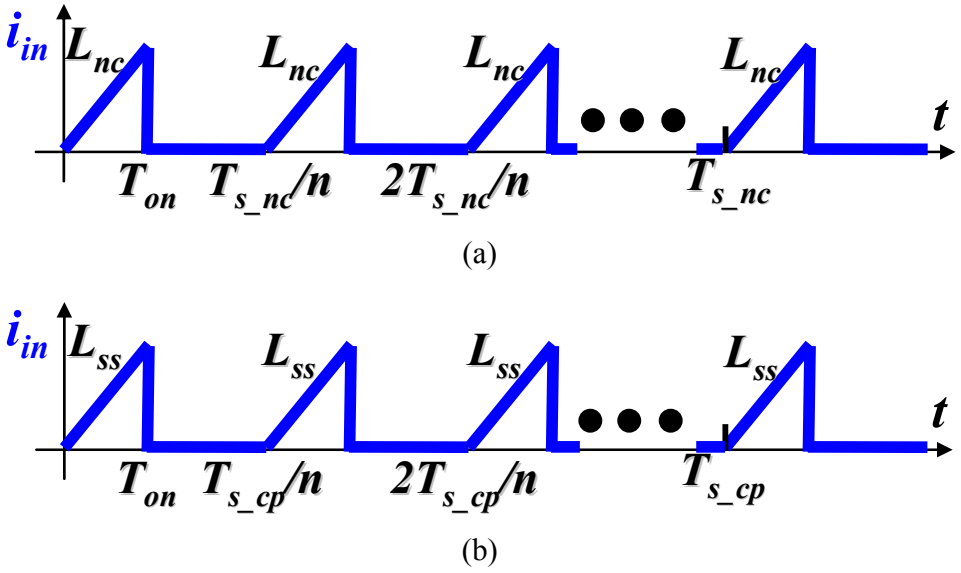

Figure A3.24 The input current waveforms of the n-phase non-coupled and coupled buck converter in DCM (a) the input current waveform of the n-phase non-coupled-inductor buck converter (b) the input current waveform of the n-phase coupled-inductor buck converter

$$V_{in} \cdot n \cdot 0.5 \cdot \frac{V_{in} - V_o}{L_{nc}} \cdot (T_{on})^2 / T_{s\_nc} = V_o \cdot i_o \tag{A3.72}$$

$$V_{in} \cdot n \cdot 0.5 \cdot \frac{V_{in} - V_o}{L_{ss}} \cdot (T_{on})^2 / T_{s\_cp} = V_o \cdot i_o \tag{A3.73}$$

Comparing the equations (A3.67) and (A3.68), it can be seen that, when L_{nc}=L_{ss},

$$T_{s\_nc} = T_{s\_cp} \tag{A3.74}$$

This means that the V_o/V_{in} conversion ratio equation of the 3-phase coupled inductor buck in DCM is the same as that of the 3-phase non-coupled inductor buck in DCM except that the L_{nc} is replaced by L_{ss}.

Recalling that, for the n-phase non-coupled inductor buck, the V_o/V_{in} ratio is

$$\frac{V_o}{V_{in}} = \frac{2}{1+\sqrt{1+4\frac{K}{D^2}}}, \qquad K = \frac{2L_{nc}}{nRT_{s\_nc}} \tag{A3.75}$$

Therefore, the V_o/V_{in} conversion ratio for the n-phase coupled inductor buck in any DCM mode is

$$r = \frac{V_o}{V_{in}} = \frac{2}{1+\sqrt{1+8\frac{L_{ss}}{nD^2RT_s}}} \tag{A3.76}$$

where,

$$L_{ss} = \frac{(L-M)[L+(n-1)M]}{L+[(n-2)+(n-1)\frac{r}{1-r}]M} \tag{A3.77}$$

Rearranging the terms,

$$f_s = \frac{1}{T_s} = \frac{2r^2L_{ss}}{n(1-r){T_{on}}^2R} \tag{A3.78}$$

Substituting the equation (A3.77) into the equation (A3.76) and rearranging the terms,

$$r = \frac{V_o}{V_{in}} = \frac{2(1+\frac{n-2}{n-1}\alpha)}{(1-\frac{\alpha}{n-1})+\sqrt{(1-\frac{\alpha}{n-1})^2+8\frac{(1-\frac{\alpha}{n-1})(1+\alpha)(1+\frac{n-2}{n-1}\alpha)L}{nD^2RT_s}}} \tag{A3.79}$$

where $\alpha = (n-1)M/L$ is the coupling coefficient. The equation (A3.79) can be rewritten as

$$r = \frac{V_o}{V_{in}} = \frac{2(1+\frac{n-2}{n-1}\alpha)}{(1-\frac{\alpha}{n-1}) + \sqrt{(1-\frac{\alpha}{n-1})^2 + 8\frac{(1-\frac{\alpha}{n-1})(1+\alpha)(1+\frac{n-2}{n-1}\alpha)L}{nT_{on}^2 R f_s}}} \tag{A3.80}$$

Based on the equation (A3.76), the criteria of the boundary between the CCM and the DCM for the n-phase coupled inductor buck can be derived. In CCM mode,

$$\frac{V_o}{V_{in}} = D \tag{A3.81}$$

By equalizing the equation (A3.81) and the equation (A3.76), it can be found that

$$R = \frac{2L_{ss}}{n(1-D)T_s} \tag{A3.82}$$

References

Introduction

[1] Sunlin Chou, "Innovation and integration in the nanoelectronics era," Presented at International Solid-state Circuit Conference, Feb. 2005. Available at ftp://download.intel.com/research/silicon/Sunlin-ISSCC-020705-foils.pdf

[2] Intel document, "Moore's law: Made real by Intel innovation," Available at http://www.intel.com/technology/timeline.pdf.

[3] G. Marcyk, "Breaking barriers to Moore's Law," Presentation at Intel Developer Forum, Spring 2002. Available at ftp://download.intel.com/research/silicon/MarcykIDF022802.pdf.

[4] E. Stanford, "Power delivery challenges in computer platforms," Special Session Presentation of IEEE APEC, 2006.

[5] R. Gonzalez, B. M. Gordon, M. A. Horowitz, "Supply and threshold voltage scaling for low ower CMOS," IEEE Journal of Solid State Circuits, 32(8), August 1997.

[6] S. Saewong, R. Raikumar, "Practical voltage scaling for fixed-priority RT-systems," Nineth IEEE real-time and embedded technology and application symposium, May 2003, pp. 106-115.

[7] Kisun Lee, "Advanced control schemes for voltage regulators," Ph. D dissertation, Virginia Tech, VA, Mar., 2008.

Multiphase Buck Converter

[8] X. Zhou, P.-L. Wong, R. Watson, L. Amoroso, X. Sun, H. Wu, P. Xu, B. Yang, W. Chen, M. Donati, F. C. Lee, and A. Q. Huang, "Voltage regulator module for future generation of processors," Tutorial of VPEC Annual Seminar, 1998.

[9] X. Zhou, "Low-voltage high-efficiency fast-transient voltage regulator module," Ph.D Dissertation, Virginia Tech, Blacksburg, 1999.

[10] P. Wong, F.C. Lee, X. Zhou and J. Chen, "VRM transient study and output filter design for future processors," Proc. of IEEE IECON, 1998, pp. 410-415.

[11] P. Wong, F.C Lee, X. Zhou and J. Chen, "Voltage regulator module (VRM) transient modeling and analysis," Proc. of IEEE IAS, 1999, pp. 1669-1676.

[12] R. Miftakhutdinov, “Optimal design of interleaved synchronous buck converter at high slew-rate load current transients,” Proc. of IEEE PESC, 2001, pp. 1714-1718.

[13] J. Zhou, “High frequency, high current density voltage regulators,” Ph.D Dissertation, Virginia Tech, Blacksburg, VA, Apr. 2005.

[14] G. J. Mehas, K. D. Coonley and C. R. Sullivan, “Converter and inductor design for fast-response microprocessor power delivery,” Proc. of IEEE PESC, 2001, pp. 1621-1626.

[15] Y. Qiu, J. Sun, M. Xu, K. Lee, and F. C. Lee, “high-bandwidth designs for voltage regulators with peak-current control”, Proc. of IEEE APEC, 2006, pp. 24–30.

[16] P. L. Wong, F. C. Lee, P. Xu, and K. Yao, “Critical inductance in voltage regulator modules,” IEEE Transactions of Power Electronics, vol. 17, no. 4, Jul. 2002, pp. 485–492.

[17] Y. Ren, K. Yao, M. Xu, and F. C. Lee, “Analysis of the power delivery path from the 12-V VR to the microprocessor,” IEEE Transactions of Power Electronics, vol. 19, no. 6, Nov. 2004, pp. 1507–1514.

[18] Y. Ren, “High Frequency, High Efficiency Two-Stage Approach for Future Microprocessors,” Ph.D. Dissertation, Virginia Tech, Blacksburg, VA, Apr., 2005.

[19] Y. Panvo and M. M. Jovanovic, “Design consideration for 12-V/1.5-V, 50-A voltage regulator modules,” IEEE Transactions on Power Electronics, vol. 16, no. 6, Jan. 2002, pp. 776–783.

[20] W. Qiu and Z. Liang, “Practical design considerations of current sharing control for parallel VRM applications”, Proc. of IEEE APEC, 2005, pp. 281–286.

[21] Jinghai Zhou, Ming Xu, Fred. C. Lee, “Small signal modeling of a high bandwidth voltage regulator using coupled-inductors,” Proc. of IEEE PESC 2005, pp.2790-2796.

[22] K. Yao, “High-frequency and high performance VRM design for the next generations of processors,” Ph.D Dissertation, Virginia Tech, Blacksburg, VA, Apr., 2004.

[23] J. Sun, “Investigation of alternative power architactures for CPU voltage regulators,” Ph.D Dissertation, Virginia Tech, Blacksburg, VA, Nov. 2008.

[24] Intel document, “Voltage regulator module (VRM) and enterprise voltage regulator-down (EVRD) 10.2 design guidelines,” Available at ftp://download.intel.com/design/Xeon/XeonMP/devtools/30676001.pdf.

[25] Intel document, “Voltage regulator-down (VRD) 11 design guide for desktop LGA775 socket,” Available at http://www.intel.com/Assets/PDF/designguide/313214.pdf.

[26] A.Waizman and C.Y. Chung, "Resonant free power network design using extended adaptive voltage positioning (EAVP) methodology," IEEE Transactions on. Advanced Packaging, vol. 24, pp. 236-244, Aug. 2001.

[27] S.A. Chickamenahalli, S. Mahadevan, E. Stanford and K. Merley, "Effect of target impedance and control loop design on VRM stability," Proc. of IEEE APEC, 2002, pp. 196-202.

[28] K. Yao, M. Xu, Y. Meng, and F. C. Lee, "Design considerations for VRM transient response based on the output impedance," IEEE Transactions on Power Electronics, vol. 18, no. 6, Nov. 2003, pp. 1270–1277.

[29] Yang Qiu, J. Sun, M. Xu, K. Lee, and F. C. Lee, "High-Bandwidth Designs for Voltage Regulators with Peak-Current Control," Proc. of IEEE APEC, 2006, pp.24-30.

[30] W. Chen, F. C. Lee, X. Zhou and P. Xu, "Integrated planar inductor scheme for multi-module interleaved quasi-square-wave (QSW) DC/DC converter," Proc. of IEEE PESC, 1999, pp. 759-762.

[31] J. Sun, "Dynamic Performance Analyses of Current Sharing Control for DC/DC Converters," Ph.D Dissertation, Virginia Tech, Blacksburg, VA, Jun., 2007.

[32] Muruta VCN60/70 Series DC/DC converter datasheet, Jan., 2008. Available at

http://www.murata-ps.com/data/power/mdc_vcn60_70.pdf

[33] Texas Instrument PTV08T250W datasheet, Nov., 2008. Available at

http://focus.ti.com/lit/ds/symlink/ptv08t250w.pdf

[34] Junhong Zhang, "Bidirectional DC-DC power converter design optimization, modeling and control," Ph.D dissertation, Virginia Tech, Blacksburg, VA, Jan., 2008.

[35] P. Wong, "Performance improment of multi-channel interleaving voltage regulator modules with integrated coupling inductors", Ph.D dissertation, Virginia Tech, Blacksburg, VA, Mar., 2001.

Multiphase Coupled-inductor Bucks

[36] I. G. Park, S. I. Kim, "Modeling and analysis of multi-interphase transformers for connecting power converters in parallel," Proc. of IEEE PESC, 1997, pp.1164-1170, Jun. 22-27, 1997.

[37] P. Wong, Q. Wu, P. Xu, B. Yang, and F.C. Lee, "Investigating coupling inductor in interleaving QSW VRM," Proc. of IEEE APEC, 2000, pp.973-978.

[38] P. Wong, P. Xu, B. Yang and F. C. Lee, "Performance improvements of interleaving VRMs with coupling inductors," Proc. CPES Annual Seminar, 2000, pp.317-324.

[39] P. Wong, P. Xu, P. Yang, and F.C. Lee, "Performance improvements of interleaving VRMs with coupling inductors", IEEE Trans. on Power Electronics, vol. 16, no. 4, pp. 499–507, Jul., 2001.

[40] J. Li, A. Stratakos, A Schultz, C. R. Sullivan, "Using coupled-inductors to enhance transient performance of multi-phase buck converters," in Proc. IEEE APEC '04, Feb. 22-26, 2004, Anaheim, CA, pp. 1289–1293.

[41] Jieli Li, Charles R. Sullivan, Aaron Schultz, "Coupled-inductor design optimization for fast-response low-voltage DC-DC converters", in Proceedings of APEC 2002 - Applied Power Electronics Conf., pp. 817–823 vol.2.

[42] A. M. Schultz and C. R. Sullivan, "Voltage converter with coupled inductive windings and associated methods", U.S. Patent 6,362,986, Mar. 26, 2002, Volterra Semiconductor Corp.

[43] A. V. Ledenev, et al., "Multiple power converter system using combining transformers," US patent 6,545,450 B1, Apr. 8, 2003, Advanced Energy Inc.

[44] Zumel P., Garcia O., J. Cobos J.A., Uceda J.,"Magnetic integration for interleaved converters", Applied Power Electronics Conference, 2003, APEC'03

[45] P. Zumel, O. Garcia, J. A. Cobos and J. Uceda, "Tight magnetic coupling in multiphase interleaved converters based on simple transformers," in Proc. IEEE APEC 2005.

[46] Ming Xu, Yucheng Ying, Qiang Li, "Novel coupled-inductor multiphase VRs," in Proc. IEEE APEC, 2007.

[47] Z. Lu, W. Chen, "Multi-phase inductor coupling scheme with balancing winding in VRM applications", in Proc. IEEE APEC, 2007, pp.731-735.

[48] Jinghai Zhou, Ming Xu, Fred. C. Lee, "Small signal modeling of a high bandwidth voltage regulator using coupled-inductors," in Proc. IEEE PESC 2005, pp.2790-2796.

[49] Wenkai Wu, Nai-Chi Lee, George Schuellein, "Multi-phase buck converter design with two-phase coupled-inductors," in Proc. IEEE APEC 2006, Mar. 19-23, 2006, Austin, TX, pp.487-492.

[50] Y. Dong, F. C. Lee, J. Zhou, M. Xu, S. Wang, "The twisted-core coupled-inductor VRs", in Proc. IEEE PESC, 2007, Jun. 17-21, 2007, Orlando, FL, pp.2536-2545.

[51] Y. Dong, M. Xu, F.C. Lee, "Short winding path coupled-inductor VRs", IEEE APEC 2008, Feb. 24-28, Austin, TX, 2008, pp.1446-1452.

[52] Y. Dong, M. Xu, F.C. Lee, "Evaluation of multiphase coupled-inductor VRs", IEEE APEC 2008, Feb. 24-28, Austin, TX, 2008, pp.831-837.

[53] Jieli Li, T. Abdallah, and C.R. Sullivan, "Improved calculation of core loss with non-sinusoidal waveforms", in Proc. IEEE IAS 2001, pp.2203-2210.

[54] A. Hoke and C. R. Sullivan, "An Improved two-dimensional numerical modeling method for E-core transformers," in Proc. IEEE APEC '02, Mar. 10-14, 2002, Dallas, TX, pp. 151 - 157.

[55] B. A. Joines W T, and T. G. Wilson, "Air-gap reluctance and inductance calculations for magnetic circuits using a Schwarz-Christoffel transformation", IEEE Transactions on Power Electronics, vol. 12, no 4., pp. 654-63, Jul., 1997.

[56] H.C. Roters, Electromagnetic Devices. John Wiley & Sons Inc.:1943, pp.130-143.

Integrated POL Converter

[57] Product ISL 8540 datasheet, Intersil.

[58] Product LM3200 datasheet, National Semiconductor Corp.

[59] Product TPS62300 datasheet, Texas Instrucment.

[60] Product MAX8640Z datasheet, Maxim.

[61] Product EN5360 datasheet, Enpirion.

[62] Product FB6831 datasheet, Fuji Electronics.

[63] P. Galle, X. Wu, L. Milner, S. Kim, P. Johnson, P. Smeys, P. Hopper, K. Hwang, and M. Allen, "Ultra-compact power conversion based on a CMOS-compatible microfabricated power inductor with minimized core losses," Electronic Components and Technology Conference, 2007, pp.1889-1894.

[64] K. Exel and J. Schulz-Harder, Water cooled DBC direct bonded copper substrates. Eschenbach, Germany: Curamik Electronics GmbH, 2005.

[65] J. Schulz-Harder, Direct bonded copper substrates for semiconductor power devices. Eschenbach, Germany: Curamik Electronics GmbH, 2005.

[66] Mariya Ivanova, Yvan Avenas, Christian Schaeffer, Jean-Bernard Dezord, and Juergen Schulz-Harder, "Heat pipe integrated in direct bonded copper (DBC) technology for cooling of power electronics packaging," IEEE Transactions on Power Electronics, Vol. 21, No. 6, November 2006, pp. 1541-1546.

[67] Schulz-Harder J., Dezord J., Schaeffer, Avenas, Puig O., Rogg. A., "DBC (Directed Bonded Copper) substrate with integrated flat heat pipe," EMPC 2005, June 12-15, Brugge, Belgium.

[68] P. Cadre, A. Petitbon, N. Changey, E. Ranchiy, "New encapsulation technique using standard DBC substrate technology", Alcatel Alsthom Recherche, IEEE 1998, pp. 2103-2107.

[69] Dr. Jurgen Schulz-Harder, "DBC substrates as a base for power MCMs," 2000 Electronics Packaging Technology Conference, 2000, pp. 315-320

[70] James M. Fusaro, Guillermo L. Romero, Pablo Rodrigucz and Joe L. Martincz, Jr., "Thermal characterization of DBC and MMC stacks for power modules," IEEE 1996, pp. 1411-1417.

[71] A.Ball, M. H. Lim, A. Gilham, F.C.Lee, "System design of a 3D integrated non-isolated point of load converter," in Proc. CPES Annual Seminar 2008, pp.52-58.

[72] A. Ball, M. Lim, D. Gilham, F.C. Lee, "System design of a 3D integrated non-isolated point-of-load converter," in Proc. IEEE APEC 2008, pp. 181-186, Feb., 24-28, 2008.

[73] A. Ball, “Thermal and electrical considerations for the design of highly-integrated point-of-load converters,”, Ph.D dissertation, Virginia Tech, Blacksburg, VA, Nov., 2001.

Current Sensing

[74] D. R. Pacholok, “Novel current-sense technique boosts converter efficiency,” PCIM Mag., pp. 30–32, July 1990.

[75] B. Carsten, “Designing high frequency current shunts and current transformers,” in Proc. 9th Int. High Frequency Power Conversion Conf., San Jose, CA, Apr. 17–21, 1994, pp. 539–550.

[76] R. Lenk, “Application bulletin AB-20 optimum current sensing techniques in CPU converters,” Fairchild semiconductor application notes, 1999.

[77] X. Zhou, P. Xu and F.C. Lee, “A high power density, high efficiency and fast transient voltage regulator module with a novel current sensing and current sharing technique,” IEEE APEC’99, pp. 289–294.

[78] X. Zhou, P. Xu and F. C. Lee, “A novel current-sharing control technique for low-voltage high-current voltage regulator module applications,” IEEE Transaction on Power Electronics, November 2000, pp. 1153-1162.

[79] E. Dallago, M. Passoni and G. Sassone, “Lossless current sensing in low voltage high current DC/DC modular supplies,” IEEE Trans. Industrial Electronics, vol. 47, pp. 1249-1252, Dec. 2000.

[80] M. Walters, C.Hawkes, “DC-to-DC converter with inductor current sensing and related methods,” US patent 5,982,160, Nov. 9, 1999.

[81] K. Xing, “Inductor current sensing scheme for PWM regulator,” US patent 7,106,035, Sep.12, 2006.

[82] Chin Chang, “Lossless current sensing and its application in current mode control,” in Proc. IEEE PESC 2008, Jun.15-19, 2008, Rhodes, Greece, pp.4086-4091.

[83] Y. Dong, M. Xu, F.C. Lee, “DCR current sensing method for achieving adaptive voltage positioning (AVP) in voltage regulators with coupled-inductors,” in Proc. IEEE PESC, 2006, pp.18-22.

Light-load efficiency

[84] Julu Sun, Yuancheng Ren, Ming Xu, Fred. C. Lee, “Light-load efficiency improvement for laptop VRs,” in Proc. IEEE APEC, 2007.

[85] J. Wei, F. C. Lee, "Two-stage voltage regulator for laptopcomputer CPUs and the corresponding advanced controlschemes to improve light-load performance," in IEEE Proc.APEC, 2004.

[86] Julu Sun, Ming Xu and Fred C. Lee, “High power density, high efficiency system two-stage power architecture for laptop computers,” in Proc. IEEE PESC 2006.

[87] Ming Xu, Julu Sun and Fred C. Lee, "Voltage divider and its application in the two-stage power architecture," in Proc. IEEE APEC 2006, pp.499-505.

[88] Maxl545 datasheet, Maxim.

[89] Yan Dong, Julu Sun, Ming Xu, Fred C. Lee, Milan M. Jovanovic, "The light-load issue of coupled-inductor laptop voltage regulators and its solutions", in Proc. IEEE APEC, 2007, pp.1581 - 1587.

[90] Intel core duo processor and Intel core solo processor datasheet, Intel document number: 309221-004.